SUPRAMOLECULAR INTERACTIONS AS A BASIS

FOR DIFFERENTIAL SENSING APPLICATIONS

by

MICHAEL H. IHDE

MARCO BONIZZONI, COMMITTEE CHAIR
MICHAEL P. JENNINGS
SHANE C. STREET
STEPHEN A. WOSKI
ADAM J. HAUSER

A DISSERTATION

Submitted in partial fulfillment of the requirements
for the degree of Doctor of Philosophy
in the Department of Chemistry and Biochemistry
in the Graduate School of The University of Alabama

TUSCALOOSA, ALABAMA

2021

Copyright Michael Ihde 2021
ALL RIGHTS RESERVED

ABSTRACT

In this work, we used supramolecular interactions to construct systems that respond to analytical stimuli and report on specific chemical species in solution using optical spectroscopic techniques (e.g. absorbance and fluorescence spectroscopy), affording low cost and high sensitivity. To obtain selectivity, we used cross-reactive sensors (organic dyes, conjugated polymers) to generate differential response patterns when exposed to families of subtly different analytes of interest. The differential responses produced large data sets that were interpreted using well-established pattern recognition algorithms, such as linear discriminant analysis (LDA) and principal component analysis (PCA).

We first report on conditions and methods based on linear discriminant analysis to predict the identity and composition of samples containing metal ion mixtures without prior physical separation, a common shortcoming of these systems. We also report on a higher-sensitivity metal ion sensing array composed of novel fluorene-based conjugated polymers with high affinity groups to detect nine divalent metal cations down to 500 pM in freshwater, and to 100 nM in seawater samples collected from the Gulf of Mexico. This robust system was sufficiently sensitive for detection below the maximum mandated concentrations set by the US Environmental Protection Agency (EPA) for toxic metals in drinking water and aquatic ecosystems.

Similar highly sensitive, fluorene-based conjugated polymers were used again to detect pollutants with intrinsic characteristic light absorption such as polycyclic aromatic hydrocarbons (PAHs) and azo textile dyes. Instead of chemical interaction with these analytes, the polymers

displayed good spectral overlap with the absorbance spectra of the targets, leading to changes in their optical spectrum caused by the inner filter effect, where the analytes themselves acted as "chemical filters".

Finally, we investigated the nature of the binding interactions between PAH probes and amine-terminated poly(amidoamine) (PAMAM) dendrimers. Using time-resolved fluorescence, fluorescence anisotropy, and selective quenching experiments, we used two probes, anthracene and pyrene, to highlight distinct binding modes and locations to the polycationic, macromolecular PAMAM hosts, paving the way for future applications of such charged polymers with interesting affinity towards hydrophobic guests.

LIST OF ABBREVIATIONS AND SYMBOLS

AC	alizarin complexone
AO7	acid orange 7
AO10	acid orange 10
AR1	acid red 1
AR14	acid red 14
AR27	acid red 27
AR88	acid red 88
AR112	acid red 112
ARS	alizarin red S
CF	5(6)-carboxyfluorescein
CHTC	1,3,5-cyclohexanetricarboxylate
CI	confidence interval
COP	cyclo-olefin polymer
CR	congo red
DI	deionized
DMF	*N*,*N*-dimethylformamide
DNA	deoxyribonucleic acid
DP	displacer
DR2	direct red 2
DR80	direct red 80
DWH	Deepwater Horizon

EDTA	ethylenediaminetetraacetic acid
EPA	United States Environmental Protection Agency
FMO	frontier molecular orbital
FRET	fluorescence resonance energy transfer
GC	gas chromatography
GC-MS	gas chromatography-mass spectrometry
GCR	glycine cresol red
HEPES	2-[4-(2-hydroxyethyl)piperazin-1-yl]ethanesulfonic acid
HPLC	high performance liquid chromatography
IFE	inner filter effect
$K_{eq.}$	equilibrium constant
K_{SV}	Stern-Volmer constant
LC	liquid chromatography
LC-MS	liquid chromatography-mass spectrometry
LDA	linear discriminant analysis
LED	light emitting diode
LOD	limit of differentiation
M^{II}	divalent metal ion
MeO	methyl orange
MeOH	methanol
MCL	maximum contaminant level
MTB	methylthymol blue
NYS	naphthol yellow S
PAH	polycyclic aromatic hydrocarbon
PAMAM	poly(amidoamine)

PCA	principal component analysis
PEI	poly(ethylenimine)
Ph-AA	poly[2,7-(9,9-di((aminodiacetate)propyl)-fluorene)-*alt*-1,4-phenylene]
Ph-PA	poly[2,7-(9,9-di((aminodipropionate)propyl)-fluorene)-*alt*-1,4-phenylene]
pIFE	primary inner filter effect
PMT	photomultiplier tube
ppb	parts per billion
ppt	parts per trillion
PTFE	polytetrafluoroethylene
PV	pyrocatechol violet
S-V	Stern-Volmer
sIFE	secondary inner filter effect
SYFCF	sunset yellow FCF
TC-SPC	time-correlated single photon counting
UK	unknown
UV	ultraviolet
UV-vis	ultraviolet-visible spectroscopy
XO	xylenol orange
yne-AA	poly[2,7-(9,9-di((aminodiacetate)propyl)-fluorene)-*alt*-1,4-ethynylene]

ACKNOWLEDGEMENTS

First and foremost, I gratefully acknowledge my research advisor, Prof. Marco Bonizzoni, for his constant support and guidance with the studies described in this dissertation. As a research scientist, the collection of skills and intellectual attributes that I have gained under his instruction is too immense to convey here.

I would also like to thank the members of my dissertation committee, Prof. Michael P. Jennings, Prof. Shane C. Street, Prof. Stephen A. Woski, and Prof. Adam J. Hauser for their valuable time, attention, and advice throughout my graduate studies. I am also grateful for all of the lab mates and co-workers that I have met within my research group and in the department.

I would like to acknowledge all of the funding sources throughout my time in the graduate program, including the University of Alabama and the National Science Foundation for their financial support. I also thankfully acknowledge the Department of Education for their financial support during my time as a GAANN fellow. I would also like to thank Dr. Blackstock, Dr. Woski, and Dr. Shaughnessy for their guidance and training to become a better instructor and educator within the GAANN program.

Finally, I would like to thank my family and friends for their patience, love, and support throughout my time at The University of Alabama. I sincerely could not thank everyone in my life enough for their kind words of encouragement over the years. Especially, I dedicate this dissertation to my parents, Richard and Mary Ihde, and to my siblings Thomas and Kristin.

CONTENTS

ABSTRACT ii

LIST OF ABBREVIATIONS AND SYMBOLS iv

ACKNOWLEDGEMENTS vii

LIST OF TABLES xii

LIST OF FIGURES xiii

LIST OF SCHEMES xxi

CHAPTER 1 INTRODUCTION 1

1.1 SUPRAMOLECULAR CHEMISTRY 1

1.1.1 Metal-ligand coordination 2

1.1.2 Electrostatic interactions 2

1.1.3 Cation-π and polar-π interactions 2

1.1.4 π-π interactions 4

1.1.5 The hydrophobic effect 4

1.2 MOLECULAR SENSING METHODS 5

1.2.1 Cross-reactive sensing 5

1.2.2 Array-based sensing 6

1.3 CHEMOMETRIC PATTERN RECOGNITION AND DATA INTERPRETATION METHODS 8

1.3.1 Linear discriminant analysis (LDA) 8

1.3.2 Principal component analysis (PCA) 9

1.4 POLYELECTROLYTES 10

1.4.1 Conjugated polymers 11

1.4.2 Poly(fluorene) co-polymers 13

CHAPTER 2 CHEMICAL FINGERPRINTING OF METAL CATION MIXTURES 15

2.1 INTRODUCTION: THE PROBLEM OF MIXTURES 15

2.2 PROJECT DESIGN 17

2.3 QUALITATIVE RESULTS 27

2.4 QUANTITATIVE RESPONSE 37

2.5 ANALYSIS OF MIXTURES 39

2.6 PROJECTION OF UNKNOWN AND UNTRAINED-FOR MIXTURES 42

2.7 IDENTIFICATION OF QUATERNARY MIXTURES AND RESPONSE TO CHANGING TOTAL [M^{II}] 46

2.8 CONCLUSIONS 50

2.9 EXPERIMENTAL DETAILS 52

2.9.1 Materials 52

2.9.2 Instrumentation 52

2.9.3 Microwell plate setup: qualitative differentiation experiments 53

2.9.4 Microwell plate setup: quantitative experiments 53

2.9.5 Metal ion mixtures: training set experiments 54

2.9.6 Metal ion mixtures: projected test set experiments 54

2.9.7 Multivariate data analysis 55

CHAPTER 3 CONJUGATED POLYMERS AS TRACE METAL CATION SENSORS IN SEAWATER 57

3.1 INTRODUCTION 57

3.2 POLYMER SYNTHESIS AND SENSOR DESIGN 60

3.3 METAL CATION BINDING AND EXPERIMENTAL CONSIDERATIONS 62

3.4 CHEMICAL FINGERPRINTING OF METAL CATIONS AT PICOMOLAR CONCENTRATIONS 69

3.5 DETECTION IN SEAWATER SAMPLES 75

3.6 CONCLUSIONS 84

3.7 EXPERIMENTAL DETAILS 85

3.7.1 Materials 85

3.7.2 Instrumentation 86

3.7.3 Benchtop titrations 87

3.7.4 Multivariate data analysis 88

CHAPTER 4 BINDING INTERACTIONS OF HYPERBRANCHED POLYELECTROLYTES WITH AROMATIC HYDROPHOBICS IN WATER 91

4.1 INTRODUCTION 91

4.1.1 Thin-film dissolution experiments 95

4.2 STRICT CONTROL OF BULK SOLUTION PROPERTIES 102

4.3 FLUORESCENCE ANISOTROPY 103

4.4 TIME-RESOLVED FLUORESCENCE 107

4.5 SELECTIVE QUENCHING EXPERIMENTS 111

4.6 CONCLUSIONS 115

4.7 EXPERIMENTAL DETAILS 117

4.7.1 Materials 117

4.7.2 Instrumentation 118

4.7.3 Thin film experimental setup 119

CHAPTER 5 ARRAY SENSING OF OPTICALLY DENSE COMPOUNDS USING THE INNER-FILTER EFFECT 121

5.1 INTRODUCTION 121

5.2 POLYMER DESIGN AND OPTICAL CHARACTERIZATION 123
5.3 EVIDENCE FOR THE IFE 127
5.4 PATTERN RECOGNITION OF PAHS USING CONJUGATED POLYMERS 129
5.5 AZO DYE DETECTION USING CONJUGATED POLYMERS AND THE IFE 137
5.6 PATTERN RECOGNITION OF AZO DYES 144
5.7 CONCLUSIONS 151
5.8 EXPERIMENTAL DETAILS 152
5.8.1 Materials 152
5.8.2 Instrumentation 153
5.8.3 Benchtop titration design 154
5.8.4 Multivariate data analysis 154
CHAPTER 6 SUMMARY AND PERSPECTIVE 159
6.1 SUMMARY 159
6.2 PERSPECTIVE 160
REFERENCES 161

LIST OF TABLES

Table 2-1 Binding constants for 2:1, 1:1, and 1:2 dye:metal complexes obtained from non-linear fitting of the absorption profiles from the titration of metal(II) chlorides into dye solutions in buffered water..... 27

Table 2-2 Unknown metal ion mixtures that were prepared separately and added randomly to the array. The set of unknown ("UK") solutions include seven binary mixtures and one equimolar ternary mixture..... 44

Table 3-1 Constituents for a 1 kg artificial seawater solution prepared and used as a metal ion sensing medium. 79

Table 4-1 Time-resolved fluorescence decay parameters from tri-exponential fittings of the emission decay profile data for anthracene and pyrene in Figure 4-11 ([G*n*] = 0.1 mM). 108

Table 4-2 Time-resolved fluorescence decay parameters from tri-exponential fitting of the emission decay profiles for anthracene and pyrene in Figure 4-12 ([G*n*] = 0.84 mM). . 111

Table 5-1 Time-resolved fluorescence decay parameters from single exponential fitting of the decay profile data for **P7-P9** and a mixture of each polymer and Congo Red (CR). 143

Table 5-2 Individual fluorescence measurements for each polymer in the 15 μM data set and their corresponding percentage contributions to factors 1 and 2. 157

LIST OF FIGURES

Figure 2-1 Depictions of the linear (green) vs. nonlinear (red) relationship between a 1:1 mixture of analytes A and B and the response of its pure components. 16

Figure 2-2 Absorbance spectra of various dyes (ARS, 30 μM; AC, 30 μM; PV, 30 μM; CF, 30 μM; NYS, 50 μM; and GCR, 20 μM), upon titration with $NiCl_2$..... 19

Figure 2-3 (A) Representative absorbance spectra acquired over the course of the titration of XO (5 μM) with $NiCl_2$ (0-14.4 μM) and corresponding isotherm from the same titration at 578 nm. (B) Representative absorbance spectra acquired over the course of the titration of MTB (7.5 μM) with $NiCl_2$ (0-21.7 μM) and corresponding isotherm from the same titration at 604 nm. 21

Figure 2-4 Absorbance spectra of XO (5 μM), upon addition of (A) $CoCl_2$, (B) $NiCl_2$, (C) $MnCl_2$, (D) $CuCl_2$, (E) $CdCl_2$, (F) $HgCl_2$, (G) $PbCl_2$, and (H) $ZnCl_2$ (0-33.0 μM).... 23

Figure 2-5 Absorbance spectra of MTB (7.5 μM), upon addition of (A) $CoCl_2$, (B) $NiCl_2$, (C) $MnCl_2$, (D) $CuCl_2$, (E) $CdCl_2$, (F) $HgCl_2$, (G) $PbCl_2$, and (H) $ZnCl_2$ (0-36.5 μM).... 24

Figure 2-6 Binding isotherms from the titration of aliquots of eight metal(II) chlorides into solutions of xylenol orange (XO, 5 μM, top) and methylthymol blue (MTB, 7.5 μM, bottom). 25

Figure 2-7 Representative titration profiles upon addition of $NiCl_2$ into XO at 578 nm (left) and MTB at 604 nm (right), along with the corresponding nonlinear fit obtained using the *HypSpec* software. 26

Figure 2-8 Representative absorbance spectra of XO (left; 20 μM) and MTB (right; 30 μM), upon addition of (A) NaCl, (B) $BaCl_2$, and (C) $MgCl_2$. 30

Figure 2-9 Representative absorption spectra of XO (left, 20 μM) and MTB (right, 30 μM) solutions, upon titration with $NiCl_2$. 31

Figure 2-10 Layout of a 384-well microplate for a typical qualitative multivariate experiment (left), and a picture of the 384-well microplate with all solutions added (right). 32

Figure 2-11 Left: Two-dimensional plot of the LDA scores for the qualitative discrimination of divalent metal ions using all instrumental variables in the raw data set ([metal] = 30 μM, [XO] = 20 μM, [MTB] = 30 μM). Right: Corresponding loadings

plot of the complete data set. Inset: table of variable contributions to the first three LDA factors (F1, F2, and F3). 33

Figure 2-12 Left: Two-dimensional plot of the LDA scores for the qualitative differentiation of divalent metal ions. Right: The corresponding LDA loadings plot, indicating the relative contributions of each instrumental variable to the calculated LDA factors ([metal] = 30 μM, [XO] = 20 μM, [MTB] = 30 μM). 34

Figure 2-13 Absorbance titration profiles monitored at 578 nm and 604 nm for the XO (left; 20 μM) and MTB (right; 30 μM) dyes, respectively at various pH values in H_2O. 36

Figure 2-14 Left: Two-dimensional plot of the LDA scores for the qualitative differentiation of divalent metal ions at 500 nM. Right: LDA scores plot at a total metal concentration of 250 nM ([metal] = 250 or 500 nM, [XO] = 20 μM, [MTB] = 30 μM). 37

Figure 2-15 Two-dimensional plot of the LDA scores (left) and loadings (right) for the quali-quantitative differentiation of Cd^{II}, Hg^{II}, Pb^{II}, Cu^{II} at five concentrations ([M^{II}] = 1 μM, 2.5 μM, 5 μM, 7.5 μM, and 10 μM; [XO] = 5, 20, 40 μM and [MTB] = 10, 30, 60 μM). 39

Figure 2-16 Two-dimensional plot of LDA scores for the separation of metal ion mixtures (Ni^{II}, Pb^{II}, and Hg^{II}) ([XO] = 20 μM, [MTB] = 30 μM, total [M^{II}] = 30 μM). 40

Figure 2-17 Two-dimensional plot of LDA scores for the differentiation of metal ion mixtures (Co^{II}, Cu^{II}, and Cd^{II}) ([XO] = 20 μM, [MTB] = 30 μM, total [M^{II}] = 30 μM). . 42

Figure 2-18 Two-dimensional plot of the LDA scores for the "test set" including 8 unknown metal ion mixtures (UK1-8, see Table 2-2) projected onto the mixtures training set from Figure 2-16 ([XO] = 20 μM, [MTB] = 30 μM, total [M^{II}] = 30 μM). .. 43

Figure 2-19 Two-dimensional plot of the LDA scores for the "ternary test set", projecting four unequal ternary metal ion mixtures onto the mixtures training set from Figure 2-16 ([XO] = 20 μM, [MTB] = 30 μM, and total [M^{II}] = 30 μM). 46

Figure 2-20 Three-dimensional plot of LDA scores for the differentiation of divalent metal ion mixtures (Cu^{II}, Cd^{II}, Pb^{II}, and Hg^{II}) ([XO] = 20 μM, [MTB] = 30 μM, total [M^{II}] = 36 μM). 47

Figure 2-21 Two-dimensional LDA scores plot for the separation of metal ion mixtures at 15 μM (Ni^{II}, Pb^{II}, and Hg^{II}) ([XO] = 20 μM, [MTB] = 30 μM, total [M^{II}] = 15 μM). 48

Figure 2-22 Three-dimensional scores plot from the LDA analysis for the combined 15 μM (blue) and 30 μM (red) metal ion mixtures data sets (Ni^{II}, Pb^{II}, and Hg^{II}). 49

Figure 2-23 PCA scores plot of the NaCl replicate set, with 95% confidence ellipsoid shown as a dotted grey line. 56

Figure 3-1 Representative steady-state fluorescence titration spectra for (a) **Ph-AA** ($\lambda_{exc.}$ = 380 nm) upon the addition of $CuCl_2$ (0-8.1 µM), (b) **yne-AA** ($\lambda_{exc.}$ = 400 nm) upon the addition of $CuCl_2$ (0-3.7 µM), and (c) **Ph-PA** ($\lambda_{exc.}$ = 380 nm) upon the addition of $CuCl_2$ (0-3.2 µM).. 62

Figure 3-2 Fluorescence spectra for the **Ph-AA** polymer ($\lambda_{exc.}$ = 380 nm), upon the addition of (a) $CuCl_2$, (b) $CoCl_2$, (c) $NiCl_2$, (d) $MnCl_2$, (e) $CdCl_2$, (f) $HgCl_2$, and (g) $ZnCl_2$. 63

Figure 3-3 Fluorescence spectra for the **yne-AA** polymer ($\lambda_{exc.}$ = 400 nm), upon the addition of (a) $CuCl_2$, (b) $CoCl_2$, (c) $NiCl_2$, (d) $MnCl_2$, (e) $CdCl_2$, (f) $HgCl_2$, and (g) $ZnCl_2$. 64

Figure 3-4 Fluorescence spectra for the **Ph-PA** polymer ($\lambda_{exc.}$ = 380 nm), upon the addition of (a) $CuCl_2$, (b) $CoCl_2$, (c) $NiCl_2$, (d) $MnCl_2$, (e) $CdCl_2$, (f) $HgCl_2$, and (g) $ZnCl_2$. 65

Figure 3-5 Fluorescence binding profiles for (a) **Ph-AA** ($\lambda_{exc.}$ = 380 nm, $\lambda_{em.}$ = 418 nm), (b) **Ph-PA** ($\lambda_{exc.}$ = 380 nm, $\lambda_{em.}$ = 412 nm), and (c) **yne-AA** ($\lambda_{exc.}$ = 400 nm, $\lambda_{em.}$ = 444 nm), upon the addition of $CuCl_2$, $CoCl_2$, $NiCl_2$, $HgCl_2$, $CdCl_2$, $MnCl_2$, and $ZnCl_2$. 66

Figure 3-6 Normalized fluorescence titration profiles of the three conjugated polymers, upon the addition of aliquots of (a) $CuCl_2$, (b) $MnCl_2$, and (c) $NiCl_2$ ($\lambda_{exc.}$ = 380 nm for **Ph-AA** and **Ph-PA** and $\lambda_{exc.}$ = 400 nm for **yne-AA**). 66

Figure 3-7 Stern-Volmer (S-V) plots for (a) **Ph-AA** ($\lambda_{exc.}$ = 380 nm, $\lambda_{em.}$ = 418 nm), (b) **Ph-PA** ($\lambda_{exc.}$ = 380 nm, $\lambda_{em.}$ = 412 nm), and (c) **yne-AA** ($\lambda_{exc.}$ = 400 nm, $\lambda_{em.}$ = 444 nm), upon the addition of aliquots of Cu^{II}, Co^{II}, Ni^{II}, and Mn^{II}. 68

Figure 3-8 (a) A general schematic of a multi-well microplate used for a typical multivariate experiment. (b) Raw experimental fluorescence data for the **Ph-AA**, **yne-AA**, and **Ph-PA** polymers in the presence of metal cations ($[M^{II}]$ = 500 pM), using the following band-pass filter combination: $\lambda_{exc.}$ = 380 ± 10 nm, $\lambda_{em.}$ = 450 ± 25 nm..... 71

Figure 3-9 (a) Two-dimensional plot of the PCA scores for the attempted differentiation of nine divalent metal ions using all instrumental measurements in the raw data set ([metal] = 500 pM). (b) Two-dimensional plot of LDA scores for the differentiation of nine divalent metal ions using the same data set. 71

Figure 3-10 Two-dimensional plot of LDA loadings from the scores plot in Figure 3-9b, displaying the high amount of superfluous instrumental measurements that could be removed (black circles). 72

Figure 3-11 A graphical representation of the process by which we removed 14 instrumental measurements from the raw 500 pM data set. 73

Figure 3-12 (a) Two-dimensional plot of the LDA scores for the successful differentiation of nine divalent metal cations at 500 pM using only the **Ph-AA** and **yne-AA** polymers. (b) Corresponding LDA loadings plot for the differentiation of divalent metal ions at

500 pM, indicating the relative contributions of each instrumental measurement to the first two LDA factors. 74

Figure 3-13 Two-dimensional plot of PCA scores for the differentiation of nine divalent metal cations at 500 pM, using the ten most important instrumental measurements. 75

Figure 3-14 (a) A map of the Deepwater Horizon location in the Gulf of Mexico, identifying the coordinates of sample collection (red star, 29°18'22.0"N, 88°29'29.2"W) used as the matrix for metal ion sensing. (b) Raw experimental fluorescence data for the **Ph-AA**, **yne-AA**, and **Ph-PA** polymers in the presence of metal cations ($[M^{II}]$ = 500 nM) in Deepwater Horizon ("DWH3") seawater media, using the following band-pass filter combination: $\lambda_{exc.}$ = 380 ± 10 nm, $\lambda_{em.}$ = 450 ± 25 nm. 77

Figure 3-15 (a) Two-dimensional plot of LDA scores for the differentiation of nine divalent metal cations dissolved in a seawater sample matrix using conjugated polymers **Ph-AA**, **yne-AA**, and **Ph-PA** ($[M^{II}]$ = 500 nM). (b) Corresponding LDA loadings plot, indicating the relative contributions of each instrumental measurement to the first two factors. 78

Figure 3-16 Two-dimensional plot of PCA scores for the differentiation of nine divalent metal cations at 500 nM in natural seawater, using the ten most important instrumental measurements. 79

Figure 3-17 (a) Two-dimensional plot of LDA scores for the differentiation of nine divalent metal cations at 500 nM in artificial seawater media. (b) Corresponding LDA loadings plot, indicating the relative contributions of each instrumental measurement to the first two factors. 80

Figure 3-18 (a) Two-dimensional plot of LDA scores for the differentiation of nine divalent metal cations dissolved in an artificial seawater matrix using conjugated polymers **Ph-AA**, **yne-AA**, and **Ph-PA** ($[M^{II}]$ = 100 nM). (b) Corresponding LDA loadings plot, indicating the relative contributions of each instrumental measurement to the first two factors. 81

Figure 3-19 Two-dimensional plot of PCA scores for the differentiation of nine divalent metal cations at 100 nM in artificial seawater. 82

Figure 3-20 Three-dimensional plot of LDA scores for the differentiation of nine divalent metal cations at $[M^{II}]$ = 100 nM in artificial seawater media, using the same data set from the 2D plot shown in Figure 3-18a. 83

Figure 3-21 Representative absorbance (solid lines) and fluorescence spectra (dotted lines) for **Ph-AA** (red , $\lambda_{exc.}$ = 380 nm, 400 μL added stock solution), **yne-AA** (blue, $\lambda_{exc.}$ = 400 nm, 200 μL added stock solution), and **Ph-PA** (green, $\lambda_{exc.}$ = 380 nm, 400 μL added stock solution). 88

Figure 3-22 PCA score plot for replicates of the Cu(II) analyte in the 500 pM replicate data set, with a calculated 95% confidence ellipsoid shown as a grey line. 89

Figure 4-1 Fluorescence intensity isotherm from the titration of a G5-CF_n complex with trimesate and 1,3,5-cyclohexanetricarboxylate trianion displacers (DPs).[156] 93

Figure 4-2 Left: Representative fluorescence spectra of anthracene brought into solution from a thin film in buffered water as a function of increasing concentration of G4 amine-terminated PAMAM dendrimer. Right: Comparing fluorescence emission profiles for anthracene as a function of increasing concentration of G3-G5 PAMAM added. 96

Figure 4-3 Fluorescence spectra for anthracene brought into solution from a thin film in H_2O as a function of increasing concentrations of G3 PAMAM (left) and G5 PAMAM (right) dendrimers. 97

Figure 4-4 Left: Representative fluorescence emission spectra of pyrene brought into solution from a thin film in buffered water as a function of increasing concentration of G4 amine-terminated PAMAM dendrimer. Right: Profiles of the normalized fluorescence emission of pyrene's excimer as a function of increasing concentration of G3-G5 PAMAM. 99

Figure 4-5 Fluorescence spectra of pyrene brought into solution from a thin film in H_2O as a function of increasing concentrations of G3 PAMAM (left) and G5 PAMAM (right) dendrimers. 99

Figure 4-6 Thin film experiments of anthracene (left) and pyrene (right), comparing the effectiveness of positively (G4) and negatively (G3.5) charged poly(amidoamine) (PAMAM) dendrimers (emission spectrum from a saturated solution of free PAH is included as a reference. 101

Figure 4-7 Fluorescence emission spectra of anthracene (left) and pyrene (right) solution in equilibrium with a thin film of the respective solid in the presence of a constant concentration of dendrimer and methanol. 102

Figure 4-8 Intrinsic fluorescence emission spectra of PAMAM dendrimers, upon the addition of (a) G3 PAMAM (0-1.90 mM) and (b) G4 PAMAM (0-0.12 mM) dendrimers..... 104

Figure 4-9 Fluorescence anisotropy of (a) anthracene at 404 nm (black) and 426 nm (red) and (b) pyrene at 374 nm (black), 394 nm (red), and 430 nm (blue), upon the addition of G3 PAMAM dendrimer..... 105

Figure 4-10 Fluorescence anisotropy data for anthracene (left) and pyrene (right), with constant concentration of G3-G5 PAMAM dendrimer ([G*n*] = 0.1 mM)..... 106

Figure 4-11 Time-resolved fluorescence decay profiles for anthracene (left) and pyrene (right) with constant concentrations of G3-G5 PAMAM dendrimer ([G*n*] = 0.10 mM). 108

Figure 4-12 Fluorescence emission decay profiles for anthracene (left) and pyrene (right) with and without G4 PAMAM dendrimer (gold and red lines, respectively; [G4] = 0.84 mM). 111

Figure 4-13 Stern-Volmer plots for anthracene (left) and pyrene (right) containing equal concentrations of G3-G5 PAMAM dendrimer ([G*n*] = 0.10 mM), upon the titration of CsCl. 114

Figure 4-14 Stern-Volmer plots for anthracene (left) and pyrene (right), upon the titration of CsCl in the presence (gold squares) vs. absence (red circles) of G4 PAMAM dendrimer ([G4] = 0.84 mM). 115

Figure 5-1 Normalized absorbance and fluorescence emission spectra of **P1-P6** in DMF. 125

Figure 5-2 (a) Overlap between excitation and emission spectra of **P2** with the absorbance spectrum of anthracene, providing the basis for an IFE. (b) Representative fluorescent spectra of **P2** (15 mg L^{-1}) upon the titration with anthracene ([anthracene] = 0-9.4 mM). 126

Figure 5-3 (a) Fluorescence titration profiles of **P1-P4** upon the addition of aliquots of anthracene, acenaphthylene, and pyrene in DMF. (b) Wavelength dependence of molar extinction coefficient for anthracene, acenaphthylene, and pyrene. 127

Figure 5-4 (a) Emission decay of **P2** (15 mg L^{-1}) before and after the addition of anthracene (500 µM) in DMF. (b) UV-vis absorption spectra of **P2**, anthracene, a mixture of **P2** and anthracene, compared to a simulated spectrum, calculated from sum of the individual experimental absorbance spectra. 128

Figure 5-5 Fluorescence anisotropy as **P5** is titrated into anthracene (100 µM) in DMF. 129

Figure 5-6 Normalized UV-vis absorption spectra of **P2** (solid line, [**P2**] = 15 mg L^{-1}) and **P6** (dashed line, [**P6**] = 15 mg L^{-1}) overlaid with the absorption spectra of (a) two- and three-membered PAHs, (b) four- and five-membered PAHs, and (c) five- and six-membered PAHs in DMF ([PAHs] = 10 µM). 130

Figure 5-7 (a) Two-dimensional plot of LDA scores for the differentiation of 16 PAHs with **P1-P6** ([PAH] = 500 µM; [**P1-P6**] = 15 mg L^{-1}). (b) Zoom-in on the LDA scores plot from Figure 5-7a for 14 PAHs, displaying less-than-ideal inter-cluster spacing for these analytes. All confidence ellipsoids are drawn to 95% confidence level. (c) LDA loadings plot for the differentiation of 16 PAHs shown in Figure 5-7a, displaying the relative contributions of each instrumental measurement to the first two LDA factors. 132

Figure 5-8 A representative example of one information-rich (green, < 420 nm) vs. an information-poor (red, ≥ 420 nm) measurement channel for all 16 PAH analytes. 133

Figure 5-9 (a) Two-dimensional plot of LDA scores for the differentiation of 16 PAHs with polymers **P1-P6** ([PAH] = 500 µM); [**P1-P6**] = 15 mg L^{-1}), using the 79

most important instrumental measurements. (b) LDA loadings plot for the differentiation of 16 PAHs shown in Figure 5-9a, displaying the relative contributions of each instrumental measurement to the first two LDA factors. 134

Figure 5-10 Three-dimensional plot of LDA scores for the differentiation of 16 PAHs with polymers **P1-P6**, using the same data set from Figure 5-9. 135

Figure 5-11 (a) LDA scores plot for the attempted differentiation of 16 PAHs without the inclusion of the polymers, **P1-P6** ([PAH] = 500 μM). (b) LDA loadings plot for the attempted differentiation of 16 PAHs without the polymers shown in Figure 5-11a. Inset: UV-vis absorbance spectra of naphthalene, fluorene, acenaphthene, and phenanthrene. 136

Figure 5-12 Two-dimensional PCA scores plot for the (a) differentiation of 16 PAHs using **P1-P6** and (b) attempted differentiation of 16 PAHs without **P1-P6** ([PAH] = 500 μM; [**P1-P6**] = 15 mg L^{-1}). 137

Figure 5-13 (a) Normalized excitation and emission spectra of **P8** overlaid with the absorbance spectrum of Congo Red, providing a good basis for the IFE. (b) Fluorescence spectra of **P8** (10 μM) upon the titration with Congo Red. 140

Figure 5-14 (a) Absorbance spectra of **P7-P9** ([polymer] = 10 μM) overlaid with that of Congo Red ([CR] = 10 μM). (b) Normalized emission spectra of **P7-P9** ([polymer] = 10 μM) compared to the normalized absorbance spectrum of Congo Red ([CR] = 10 μM). (c) Fluorescence titration profiles for **P7-P9**, upon the addition of aliquots of Congo Red. 141

Figure 5-15 (a) Chemical structures of 12 target azo dye analytes identified as hazardous pollutants. (b) Wavelength dependence of molar absorptivity for 12 target azo dye analytes in aqueous solution. 142

Figure 5-16 (a) Emission decay profile of **P8** (10 μM) before and after the addition of Congo Red (CR) (15 μM) in DI H_2O. (b) UV-vis absorption of **P8** (20 μM), CR (15 μM), and a mixture of **P8** and CR, compared to a simulated spectrum calculated from the sum of the individual experimental spectra. 143

Figure 5-17 (a) UV-vis absorption of **P7** (20 μM), Congo Red (CR) (15 μM), and a mixture of **P7** and CR, compared to a simulated spectrum calculated from the sum of the individual experimental spectra. (b) UV-vis absorption of **P9** (20 μM), CR (15 μM), and a mixture of **P9** and CR, compared to a simulated spectrum calculated from the sum of the individual experimental spectra. 144

Figure 5-18 (a) Two-dimensional plot of LDA scores for the differentiation of 12 azo dyes with **P7-P9** in DI H_2O ([dye] = 15 μM, [**P7-P9**] = 10 μM). (b) Corresponding LDA loadings plot for the differentiation of 12 azo dyes, indicating the relative contributions of each instrumental measurement to the first two LDA factors. Inset: Absorbance and emission spectra of **P7** and **P8**, with the wavelengths of maximum contribution outlined. 145

Figure 5-19 Two-dimensional PCA scores plot for the differentiation of azo dyes at 15 µM using **P7-P9** (10 µM). 146

Figure 5-20 (a) Two-dimensional plot of LDA scores for the differentiation of 12 azo dyes ([dye] = 500 nM) with **P7-P9** ([polymer] = 375 nM) in DI H_2O. (b) Two-dimensional plot of PCA scores for the differentiation of 12 azo dyes with **P7-P9** at 500 nM in DI H_2O. 147

Figure 5-21 LDA loadings plot for the differentiation of 12 azo dyes shown in Figure 5-20a, indicating the relative contributions of each instrumental measurement to the first two LDA factors. Inset: UV-vis absorbance and fluorescence spectra of **P9**, highlighting the spectral regions of maximum contribution. 148

Figure 5-22 (a) Two-dimensional plot of LDA scores for the attempted differentiation of 12 azo dyes without **P7-P9** at 500 nM in DI H_2O. (b) Two-dimensional plot of PCA scores for the attempted differentiation of 12 azo dyes without **P7-P9** at 500 nM in DI H_2O. 149

Figure 5-23 Two-dimensional plot of the (a) LDA and (b) PCA scores for the attempted differentiation of six azo dyes at 15 µM using **P7-P9** (10 µM) in artificial seawater media, using the 30 most important fluorescence measurements. 150

Figure 5-24 (a) Two-dimensional plot of LDA scores for the differentiation of six azo dyes at 15 µM using **P7-P9** (10 µM) in artificial seawater media, using the 58 most important absorbance and fluorescence measurements. (b) Corresponding PCA scores plot for the differentiation of azo dyes at 15 µM in artificial seawater using the same instrumental measurements. 151

Figure 5-25 PCA scores plot of the (a) pyrene and (b) AR27 replicate sets, with 95% confidence ellipsoids shown as a dashed line. 155

Figure 5-26 A representative visual example of an information-poor instrumental measurement ("P7 450/528") for all 12 azo dye analytes, containing more experimental noise than discriminatory capacity. 156

Figure 5-27 A graphical representation of the process by which we removed nine fluorescence measurements from the azo dye data set (15 µM). 158

LIST OF SCHEMES

Scheme 1-1 The stabilizing interaction between a potassium cation (K^+, left) and primary ammonium cation (NH_3^+, right) and the face of a benzene molecule..... 3

Scheme 1-2 The attractive interaction between a polarized C-H bond (α-carbon of ammonium group) and the face of a benzene molecule. 3

Scheme 1-3 The favorable displaced (or slipped) stacking of two benzene molecules..... 4

Scheme 1-4 The hydrophobic effect, displaying a greater number of water molecules being freed up when two hydrophobic solute molecules are brought together, causing an entropic gain and lower overall free energy of the system. 5

Scheme 1-5 A visual representation of a cross-reactive sensing array with non-selective receptors, whose exposure to four different analytes (A-D) provides distinct response patterns (i.e. "chemical fingerprints") that can be interpreted to successfully detect all four analytes..... 7

Scheme 1-6 Structural representation of linear (left) and hyperbranched (right) cationic polyelectrolytes..... 10

Scheme 1-7 Representative examples of well-known polyelectrolytes:[67] (left) hyaluronic acid, (right) poly(ethylenimine) (PEI). 11

Scheme 1-8 Chemical structures of representative conjugated polymer backbones: (left) poly(*p*-phenylene) and (right) poly(phenylene-ethynylene)..... 11

Scheme 1-9 Traditional chemosensor whose analytical sensitivity is related to the concentration of bound receptor (binding constant, $K_{eq.}$) vs. receptors wired in series, whose collective response leads to signal amplification and sensitivity enhancement (adapted from Swager et al.)[16] 12

Scheme 1-10 Chemical structures of fluorene monomer and poly(fluorene)..... 13

Scheme 1-11 Chemical structure of novel poly(fluorene) alternating co-polymers with examples of π-spacers used in this work..... 14

Scheme 2-1 Chemical structures of xylenol orange (XO) and methylthymol blue (MTB) in their likely protonation state in neutral water solution (pH = 7.4)..... 20

Scheme 3-1 Chemical structures and general synthetic scheme for the three conjugated polymers (**Ph-AA**, **yne-AA**, and **Ph-PA**) used in a metal ion sensing array..... 59

Scheme 3-2 Chemical structure of ethylenediaminetetraacetic acid in its neutral form. 60

Scheme 4-1 Chemical structure of a first generation (G1) amine-terminated poly(amidoamine) (PAMAM) dendrimer. 92

Scheme 4-2 Chemical structures of anthracene (left) and pyrene (right) as representative PAHs used as guest binding probes with amine-terminated PAMAM dendrimers..... 95

Scheme 4-3 A representation of the possible interaction modes between Cs^+ with a surface-bound PAH probe (left) vs. an internally encapsulated probe (right). 113

Scheme 5-1 Chemical structure and synthetic scheme of conjugated polymers, **P1-P6**, used for the detection of PAHs. 124

Scheme 5-2 The chemical structures of all 16 PAH analytes identified by the EPA as priority pollutants of interest. 130

Scheme 5-3 Chemical structures and synthetic scheme of conjugated polyelectrolytes, **P7-P9**, used for the detection of azo dyes. 139

CHAPTER 1

INTRODUCTION

1.1 Supramolecular chemistry

Supramolecular chemistry is the study of molecular assemblies and intermolecular interactions in artificial systems.[1] Over 30 years ago, Jean-Marie Lehn, Donald Cram, and Charles Pedersen brought significant attention to the field of supramolecular chemistry, winning the Nobel Prize in chemistry in 1987. Since then, considerable research involving intermolecular interactions and molecular self-assembly has been undertaken for many applications.[1-3] Early in this field, common systems studied involved a variety of molecular recognition processes,[4] including electrostatic interactions, hydrogen bonding, and cation-π interactions, providing relatively weak interactions that are easily reversible under thermodynamic control using mild conditions.[5] In fact, even reversible covalent interactions have also been introduced as systems with similar features to non-covalent supramolecular chemistry; namely reversible bond or adduct formation, generating products at continuous thermodynamic equilibrium.[6]

Given the many types of intermolecular interactions accessible for the molecular assembly of multiple chemical species, it is often the case that supramolecular systems benefit from a variety of possible interactions relating to the host, guest, and bulk surroundings. Therefore, it is important to outline and summarize each of the covalent and non-covalent supramolecular interactions that are relevant to this work.

1.1.1 Metal-ligand coordination

Metal-ligand coordinative interactions are unique, in that they can have electrostatic characteristics, but are primarily driven by the covalent nature between a metal acceptor (Lewis acid) and an organic donor (Lewis base).[7-8] Therefore, these interactions have found widespread use in supramolecular chemistry thanks to their well-defined and well-known geometries, compared to weaker non-covalent interactions. Owing to the highly predictable nature of transition metal coordination with labile ligands, self-assembly of small molecules using these coordinative interactions offers greater control over design, sizes, and dimensions of the desired supramolecular ensembles.[9]

1.1.2 Electrostatic interactions

Electrostatics are among the strongest non-covalent interactions, ranging between 5-250 kJ mol^{-1}.[5] Generally, they involve either an attractive force between oppositely charged species or a repulsive force between species with the same charge. These interactions can range from full formal charged species to weaker dipole-dipole interactions.

1.1.3 Cation-π and polar-π interactions

Generally, π systems within a molecule are associated with regions of electron density above and below the plane of the σ bonding scaffold. Therefore, they can readily interact with positively charged cations, with relative strength (see Scheme 1-1); in fact, this attractive interaction can be on the same order as a hydrogen bond with strengths between 5-80 kJ mol^{-1}.[5,10]

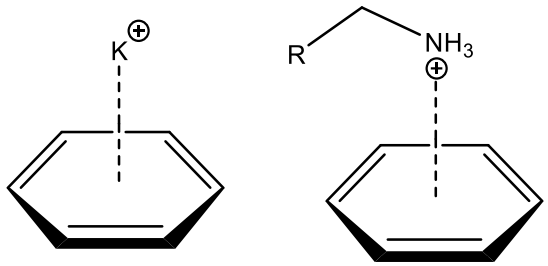

Scheme 1-1 The stabilizing interaction between a potassium cation (K^+, left) and primary ammonium cation (NH_3^+, right) and the face of a benzene molecule.

Given its quadrupolar nature, benzene and other aromatic compounds can also interact with polarized hydrogen bonds (such as water or ammonia).[5] Like cation-π interactions, this involves an attractive force between the partially negative charge of the π system with the partially positive hydrogen atoms. This interaction can also occur between an aromatic moiety and a polarized C-H bond, such as that shown in Scheme 1-2. An example of a practical application using these kinds of interactions is writing and erasing on paper with a graphite pencil, in which the aromatic graphite interacts with the polysaccharide (cellulose) of the paper through polar-π interactions, and the rubber eraser removes these interactions via competitive C-H-π interactions with the graphite.[11-12]

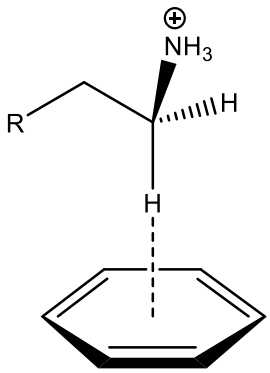

Scheme 1-2 The attractive interaction between a polarized C-H bond (α-carbon of ammonium group) and the face of a benzene molecule.

1.1.4 π-π interactions

π-π and aromatic-aromatic interactions (also termed "π stacking") are an attractive interaction between the negative region of a πsystem (e.g. face of an aromatic ring) with the region of positive electrostatic potential (typically the edges of the σ bonding scaffold).[5,13] These interactions can be quite prominent, especially when mostly non-polar aromatic compounds are introduced into water, incorporating a large hydrophobic component to the system. Contrary to the common term, "π-stacking", the two π systems are not directly stacked; in fact they must be displaced to allow the appropriate regions of the molecules to attain an attractive interaction (direct stacking would be highly unfavorable and repulsive, see Scheme 1-3).

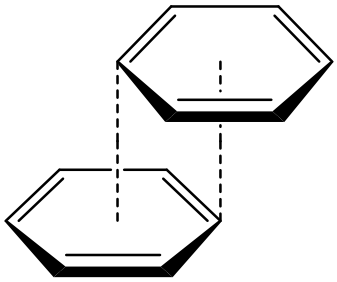

Scheme 1-3 The favorable displaced (or slipped) stacking of two benzene molecules.

1.1.5 The hydrophobic effect

Using more polar solvents (such as water) can force non-polar molecules together, even in the absence of appropriate functional groups for intermolecular binding. As shown in Scheme 1-4, the basis for this phenomenon is a favorable entropic gain by the solvent, as forcing the aggregation of hydrophobic molecules frees up many more solvent molecules from having to solvate each hydrophobic molecule individually, thereby lowering the overall free energy of the system.[5,14]

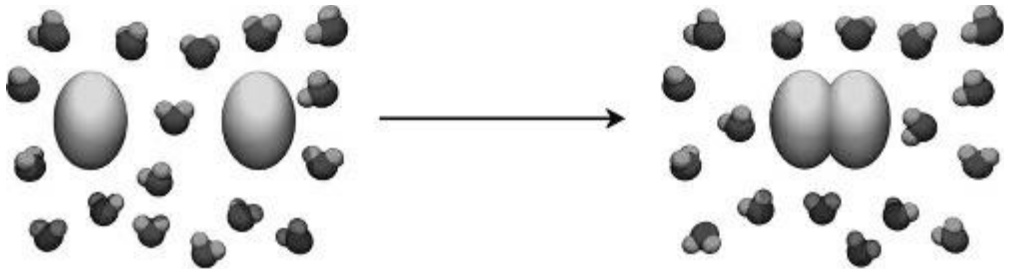

Scheme 1-4 The hydrophobic effect, displaying a greater number of water molecules being freed up when two hydrophobic solute molecules are brought together, causing an entropic gain and lower overall free energy of the system.

1.2 Molecular sensing methods

Molecular sensing refers to the aspects of supramolecular chemistry and molecular recognition that are coupled with a detectable change in a measurable macroscopic property of the system, resulting in an analytical signal.[2] This signal modulation can be challenging, requiring distinct molecular recognition receptors that can change the chemical or physical properties of the molecular environment upon exposure to structurally similar analytes (good selectivity), while at the same time transforming the perturbations into useful signal changes at the desired concentrations (good sensitivity).[15] Common signal transduction methods use either optical spectroscopy or electrochemical approaches, and for many years, fluorescence spectroscopy has led the way as one of the most sensitive optical signal transduction techniques.[16] Moreover, UV-vis absorption, although less sensitive, has also been extensively studied because of its extreme ruggedness, wide availability, and ease of use. In this work, we will focus mainly on absorbance and fluorescence spectroscopic signal transduction.

1.2.1 Cross-reactive sensing

Typical sensor design uses a “lock and key” strategy, in which a single purpose-built receptor is used to selectively bind a specific analyte. However, this process for molecular sensing can be cost intensive and time consuming if one attempts to target multiple analytes,

requiring the design and synthesis of specialized receptors for each analyte. Therefore, differential molecular sensing has been extensively used as an alternative approach,[17] designed to mimic the olfactory and gustatory sensing systems, in which non-specific sensors generate responses that produce recognizable patterns for analyte classification and identification.[18-19] Akin to biological chemosensory systems, the individual receptors themselves are not highly selective for any one stimulus; instead multiple receptors respond differentially to a single analyte (e.g. an odorant in mammalian olfactory systems), and also any one receptor responds to many analytes.[20-21] These kinds of promiscuous, non-selective chemical sensory systems, also termed cross-reactive, have gained widespread interest over the last 20 years in the chemical sensing community with the advent of chemical or electronic noses or tongues.[22-23]

1.2.2 Array-based sensing

Given the built-in non-selectivity of cross-reactive sensing, a series of receptors are arranged in an array style format, whose collective and chemically diverse response leads to the discrimination of many similar analytes, designed and developed by many researchers, such as Anslyn, Anzenbacher, and others (see Scheme 1-5).[24-25]

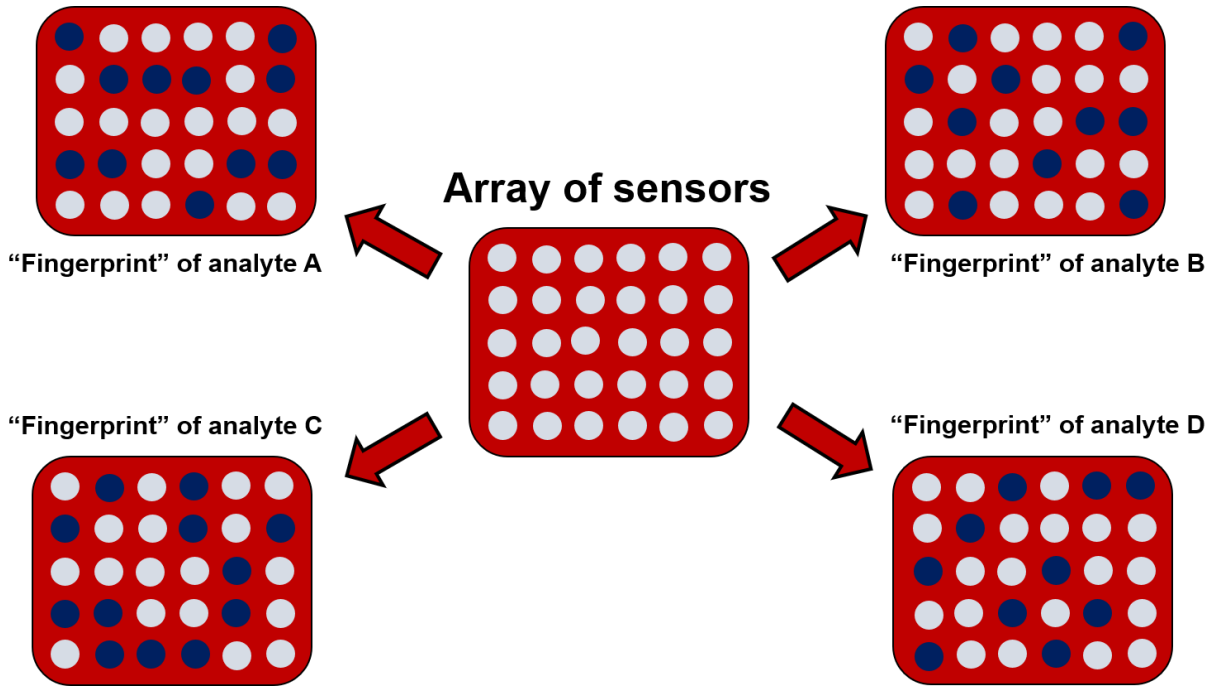

Scheme 1-5 A visual representation of a cross-reactive sensing array with non-selective receptors, whose exposure to four different analytes (A-D) provides distinct response patterns (i.e. "chemical fingerprints") that can be interpreted to successfully detect all four analytes.

More specifically, colorimetric and fluorometric sensing arrays often combine the good selectivity from array sensing with high sensitivity from optical spectroscopic methods, and are recognized as high throughput and inexpensive detection methods of many analytes in a single experiment.[26-29] In recent years, pattern recognition methods have been developed by other research groups for the detection of an assortment of analytes including small organic molecules,[30-41] gases,[42-44] proteins,[45-47] nanoparticles,[48] and bacteria in biofilm matrices.[49] In fact, chemical fingerprinting has even been extended to the identification of more complex chemical processes, such as molecular aggregation and enzyme activity.[50-51] Array sensing approaches invariably produce complex responses, often leading to multivariate data sets. The resulting large data sets are typically interpreted using well-established data processing and automated pattern recognition techniques, as described below.

1.3 Chemometric pattern recognition and data interpretation methods

The response patterns generated from the data collected in sensing arrays are often too cumbersome to be interpreted by simple analytical calibration methods; instead, the wealth of information is interpreted using multivariate methods, which aid in reducing the dimensionality of the information contained in the large data sets.[52-54] The two methods used primarily throughout this dissertation are linear discriminant analysis (LDA) and principal component analysis (PCA). Analysis using LDA is a *supervised* technique, meaning that the samples are classified before data processing is carried out, whereas PCA is considered to be *unsupervised*, since sample identity is classified as a result of the analysis. Therefore, these two methods are often run in tandem to ensure that the results from the more "aggressive", supervised LDA analysis are representative of strong underlying chemical responses of the array components. In the following sections, we will discuss these two multivariate techniques in more detail.

1.3.1 Linear discriminant analysis (LDA)

The LDA algorithm operates on a data set to generate a new set whose descriptor variables are linear combinations of the original instrumental variables, constructed so that maximum separation between sample clusters is achieved, while at the same time minimizing separation between replicate measurements for the same analyte.[55-56] The descriptor variables, called *factors*, are returned in decreasing order of information content. This important feature allows for straightforward dimensionality reduction, where one can drastically reduce the size of the data set by retaining only the first few, most important, factors with minimal loss of information. After retaining only the first two factors, each sample in the transformed data set is now associated with only a pair of numbers, its *factor scores*, which can be used as data points in a two-dimensional plot, called a *scores plot*. Also provided by the LDA analysis are the *factor*

loadings; i.e. the contributions of each raw measurement to the LDA factors. Since we will most commonly reduce our results down to two dimensions, we will typically be most interested in the makeup of the first two factors, which will be presented by a two-dimensional *loadings plot*. For these reasons, LDA has become an increasingly popular multivariate data processing method, used by top researchers for the detection of explosives,[57-58] peptides,[59] and proteins.[60]

1.3.2 Principal component analysis (PCA)

Principal component analysis (PCA) is one of the most common statistical treatments used for the interpretation of sensor array data sets.[61-62] Unlike LDA, the unsupervised PCA method interprets the data by preserving the variances within the data, without classification beforehand. Specifically, PCA reorganizes the data by finding linear combinations of the original data, generating *principal components* (PCs), which are the corresponding eigenvectors that lie in the direction of maximum variance within the data set. Similar to LDA, the PCs are also reported in decreasing order of their degree of variance. Thus, PCA merely summarizes and highlights latent features in the raw data set.

From the standpoint of array sensing, successful PCA results should provide clear clustering of replicates for the same sample, while maximizing the differences between different samples, using two or three relevant PCs. This concept is not a foregone conclusion of PCA, although it is an intrinsic aspect of the LDA algorithm. Therefore, a successful PCA can not only report directly on the discriminatory power of the sensing system, but also on the quality of the array's response. As such, PCA has received considerable interest as a frequently used multivariate data processing method for many important array sensing applications for a variety of relevant analytes.[63-64]

1.4 Polyelectrolytes

Polyelectrolytes are polymers whose repeat units contain charged functional groups; polyanions and polycations refer to polymers with multiple negative and positive charges, respectively. Structurally, polyelectrolytes can take many forms and architectures, including linear, branched, or hyperbranched polymers, as shown in Scheme 1-6. They have found many practical applications (Scheme 1-7) in water treatment,[65] drug delivery systems,[66] among many others.[67] One major advantage of polyelectrolytes is the large number of charged groups that increase their solubility and usability in water solution, which depends on the size of the polymer and the number, location, and density of the solubilizing groups. Some of these polymers have a hydrophobic backbone as is the case for many conjugated polyelectrolytes.

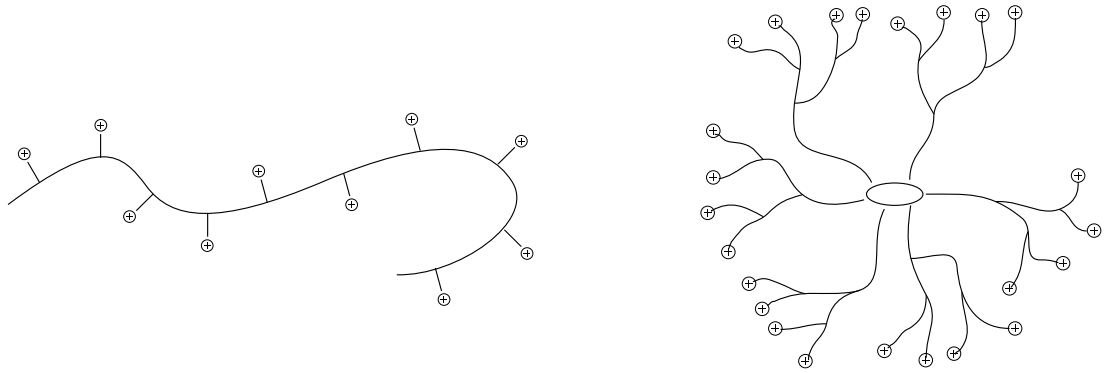

Scheme 1-6 Structural representation of linear (left) and hyperbranched (right) cationic polyelectrolytes.

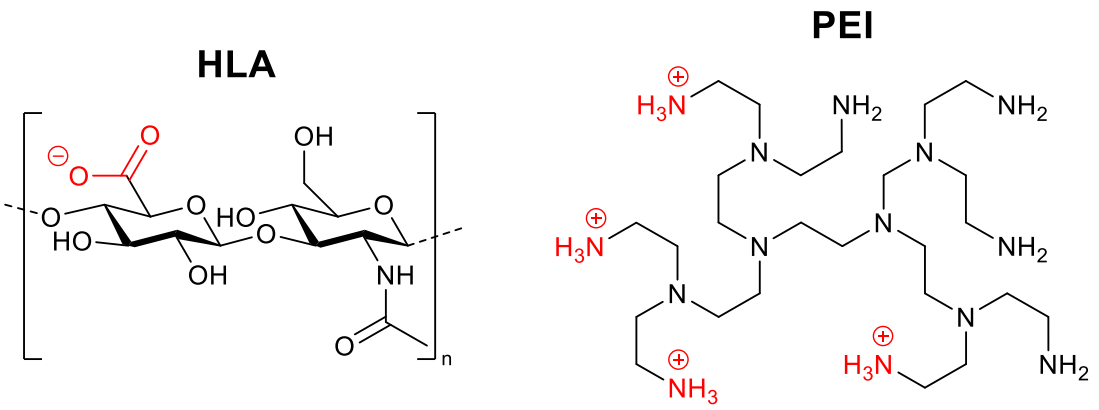

Scheme 1-7 Representative examples of well-known polyelectrolytes:[67] (left) hyaluronic acid, an anionic polyelectrolyte used as a lubricant to alleviate joint pain; (right) poly(ethylenimine) (PEI) is a cationic polyelectrolyte that is used in industrial waste treatments. Red fragments denote charged functional groups on each polyelectrolyte.

1.4.1 Conjugated polymers

Conjugated polymers, two of which are displayed in Scheme 1-8, are macromolecules with a conjugated backbone, whose extended π-systems leads to unique electronic (e.g. conductivity) and optical properties. They offer significant advantages over their small-molecule counterparts, such as more cooperative, high affinity analyte-receptor and non-specific interactions, as well as amplified collective responses to the intermolecular interactions.[68] Therefore, conjugated polymers have been extensively studied over the last 25-30 years; among their many applications, their use as emergent fluorescent chemosensory materials to improve the analytical sensitivity of typical fluorescence sensors has been widely exploited (see Scheme 1-9).

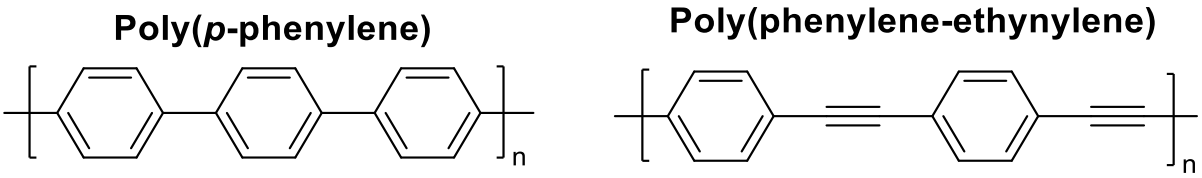

Scheme 1-8 Chemical structures of representative conjugated polymer backbones: (left) poly(*p*-phenylene) and (right) poly(phenylene-ethynylene).

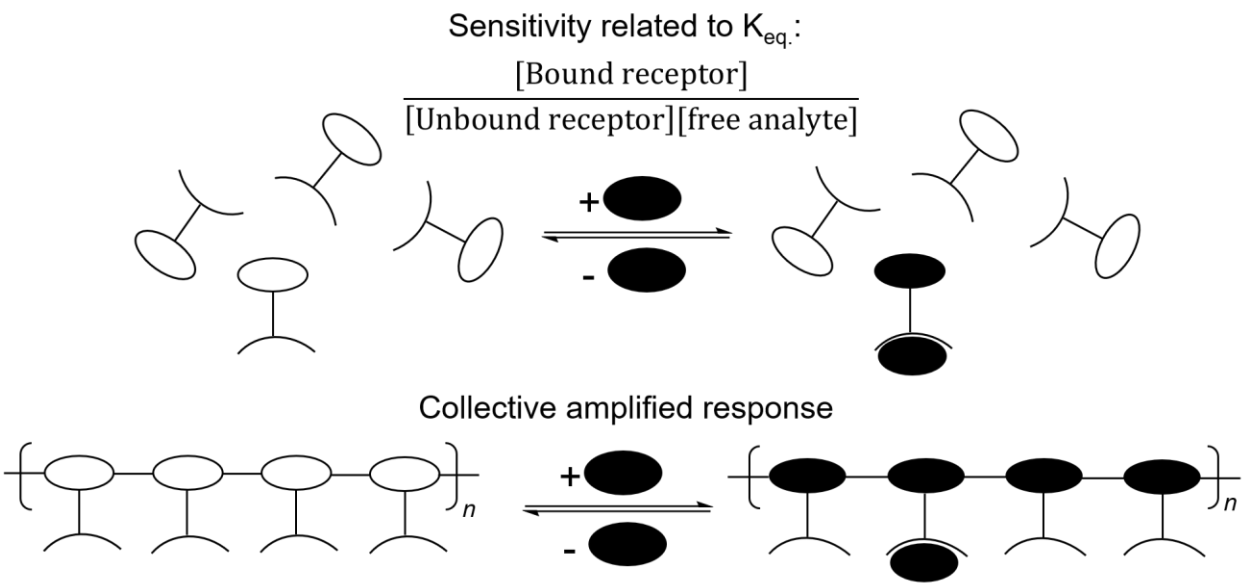

Scheme 1-9 Traditional chemosensor whose analytical sensitivity is related to the concentration of bound receptor (binding constant, $K_{eq.}$) vs. receptors wired in series, whose collective response leads to signal amplification and sensitivity enhancement. This scheme was adapted from Swager et al.[16]

The enhanced sensitivity is not only attributed to cooperative increase in the association constants from more binding sites, but also to excited state (exciton) migration along the conjugated polymer chain.[69-71] For example, as excitons diffuse along the polymer, they may encounter a bound analyte at a remote binding site, which can act as a quencher and drastically reduce the overall fluorescence signal from the polymer; this collective response has been termed the "molecular wire effect".[72-73] As a representative example, this energy migration to a local minimum was demonstrated by Timothy Swager and co-workers for a poly(phenylene-ethynylene) conjugated polymer, emitting from an anthracene "antenna" end group.[74] In particular for conjugated polyelectrolytes, additional common factors that can also influence emission include quenching induced by polymer aggregation in certain solvents, and also analyte-induced aggregation.[75-76] Given these unique properties, conjugated polymers have found many analytical applications:[77] a variety of such systems have been reported for the

detection of many analytes, including small organic molecules,[30,78-84] metal cations,[85-88] and biologically relevant targets.[89-92]

1.4.2 Poly(fluorene) co-polymers

Poly(fluorene)-based polymers (see Scheme 1-10) are well-known as bright blue emitters with rigid, rod-like structures, analogous to poly(*p*-phenylene)-type polymers.[93-94] The fluorene monomer can be coupled with conjugated spacer groups in an alternating co-polymer assembly to achieve highly tunable (opto)electronic properties. Another advantage of fluorene is the sp^3 carbon atom (highlighted in red in Scheme 1-10) that is available to covalently attach pendant functional groups, often used to add water solubilizing groups to the polymer's hydrophobic backbone.[95-98] Another common conjugated polymer backbone is poly(phenylene-ethynylene), which has been studied extensively by Schanze and co-workers, displaying quantum yields and quenching sensitivity comparable to poly(fluorenes).[99] Despite the many similarities between poly(*p*-phenylene) and poly(fluorene) polymers, the differential quenching responses can often be quite different, owing to their greatly different frontier molecular orbital (FMO) energies, tendencies to aggregate in water, and fluorescence lifetimes, due to structural changes between their ground and excited states.[100-102]

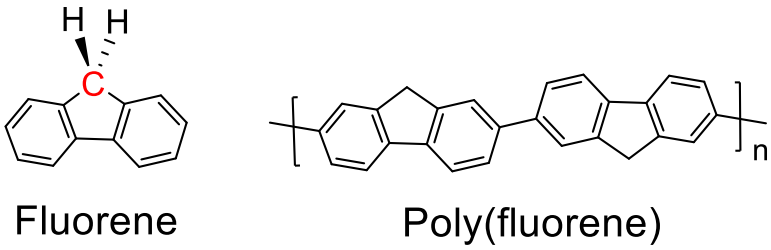

Scheme 1-10 Chemical structures of fluorene monomer and poly(fluorene). The sp^3 carbon atom used to covalently attach metal binding ligands is highlighted in red on the monomer structure.

In the following, we will present a variety of fluorene-based co-polymers for sensing applications that contain conjugated spacer groups, including 1,4-phenylene (*p*-phenylene),

ethynylene, and thiophene groups, covalently linked to make up the monomer that, when polymerized, generates the alternating co-polymer conjugated backbone (see Scheme 1-11). The change in conjugated linker provides an assortment of electronic properties, altering the polymer's corresponding optical spectroscopic properties, whereas the pendent arms (R-groups in Scheme 1-11) can be used to adjust the binding affinity, enhance the polymers' water solubility, and to add appropriate optical modifier groups.

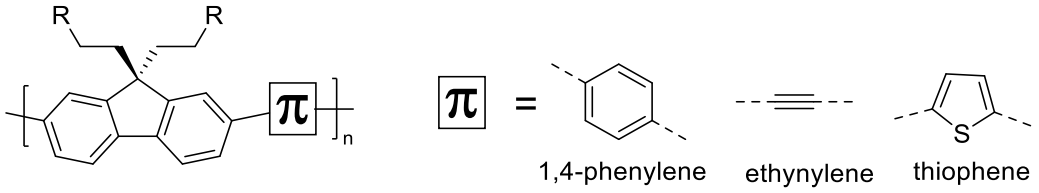

Scheme 1-11 Chemical structure of novel poly(fluorene) alternating co-polymers with examples of π-spacers used to make up the conjugated backbone that will be used in this work for analytical applications.

CHAPTER 2

CHEMICAL FINGERPRINTING OF METAL CATION MIXTURES

2.1 Introduction: the problem of mixtures

Pattern-based array sensing techniques, also known as chemical fingerprinting, have been extensively used in the Bonizzoni research group for the detection of structurally similar analytes. As mentioned previously, these methods offer improved selectivity thanks to the analytes' cross-reactive, differential responses to only a few promiscuous receptors, rather than using one specialized receptor for each analyte. Despite their increased selectivity and high discriminatory power, array sensing systems often falter when exposed to analytes in a mixture. As is the case for other detection methods (i.e. selective recognition methods), often physical separation is needed before the analytes can be successfully differentiated (e.g. GC-MS or HPLC); this is no different for chemical fingerprinting systems. For example, even if an array sensor is able to differentiate two pure analytes, the system may often respond unpredictably to a mixture of the two analytes. This is depicted in Figure 2-1, using a scores plot as a common way of presenting results in pattern recognition.

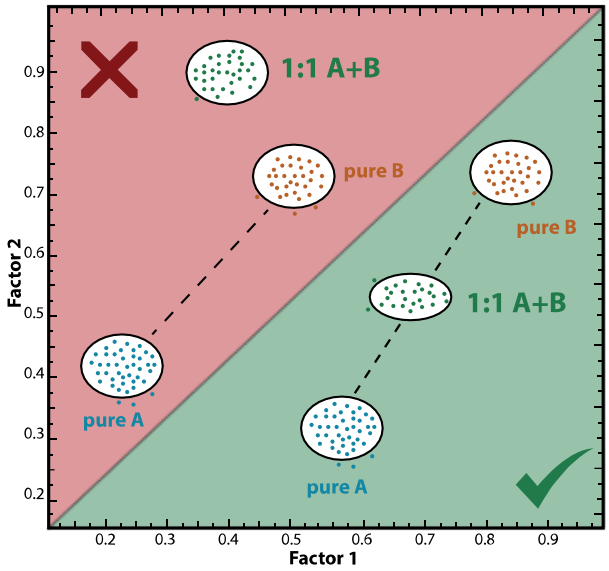

Figure 2-1 Depictions of the linear (green) vs. nonlinear (red) relationship between a 1:1 mixture of analytes A and B and the response of its pure components.

This visual representation displays two separate cases for the response of an array towards a 1:1 binary mixture. One might assume that if one can train a pattern recognition system to recognize pure substances A and B, then the response of a 1:1 mixture of the two would fall halfway between them (a *linear* response, green section). However, this is often not the case in most array sensing systems (red section), due to inherent nonlinearities in the analytical response of the underlying chemical sensors in the array sensing platform. Typically, either the user is operating in a nonlinear portion of the analytical response curve, or the chosen signal transduction method does *not* respond linearly. Consequently, predicting where an unknown mixture would fall based on the response to its pure components is exceedingly difficult. On the other hand, a completely linear response would make unknown mixture analysis remarkably straightforward for all possible mixtures. For example, a 2:1 mixture of A:B should fall two-thirds of the way towards the pure A cluster on a line that connects the A and B clusters. In this chapter, we will discuss the design and development of an array-based sensor that is able

to linearly map pure analytes and their mixtures in a two-dimensional plot. The results were then used to accurately predict the contents of unknown mixture samples. Furthermore, the system was also constructed to respond linearly to changes in varying *total* analyte concentrations, allowing for a simultaneous quali-quantitative determination of the *nature* and *concentration* of an unknown analyte contained in a mixture using only a single experiment without the need for physical separation prior to detection.

2.2 Project design

This chapter will demonstrate that pattern-based analysis of mixtures can be achieved if the array components are carefully controlled so that the underlying chemical interactions, the analytical signal transduction method, and the data processing method respond linearly. For our system, UV-vis absorbance spectroscopy was chosen as the analytical detection method, due to the ease with which a rigorous linear dependence of signal intensity (absorbance) on changes to concentration can be achieved. Moreover, this linear dependence can be retained over a concentration range spanning several orders of magnitude by making simple changes in optical path length. The cross-reactive, chemical receptors needed to be carefully chosen for the array so that their absorbance signals would change significantly, differentially, *and* linearly upon exposure to multiple analytes.

To ensure strong linearity in the receptors' signal changes, organic dyes were chosen as sensors that are well-known to form highly favorable supramolecular complexes with our analytes of interest. These strong interactions would be characterized by binding curves with robust, linear features. Thus, divalent metal cations and their mixtures were chosen as testbed analytes for our design principles. Along with being viable candidates for mixture analysis, metal

cation detection is of great practical importance because of their implications to human health and environmental safety.[103]

After screening several dye candidates for inclusion in a cross-reactive style array (Figure 2-2), two very good metal-binding dyes were found that provided excellent linear characteristics, meeting the desired specifications. The two dyes used in this study, xylenol orange (XO) and methylthymol blue (MTB), are shown in Scheme 2-1 and have long been known to form strong coordination complexes with multiple metal cations.[104-105]

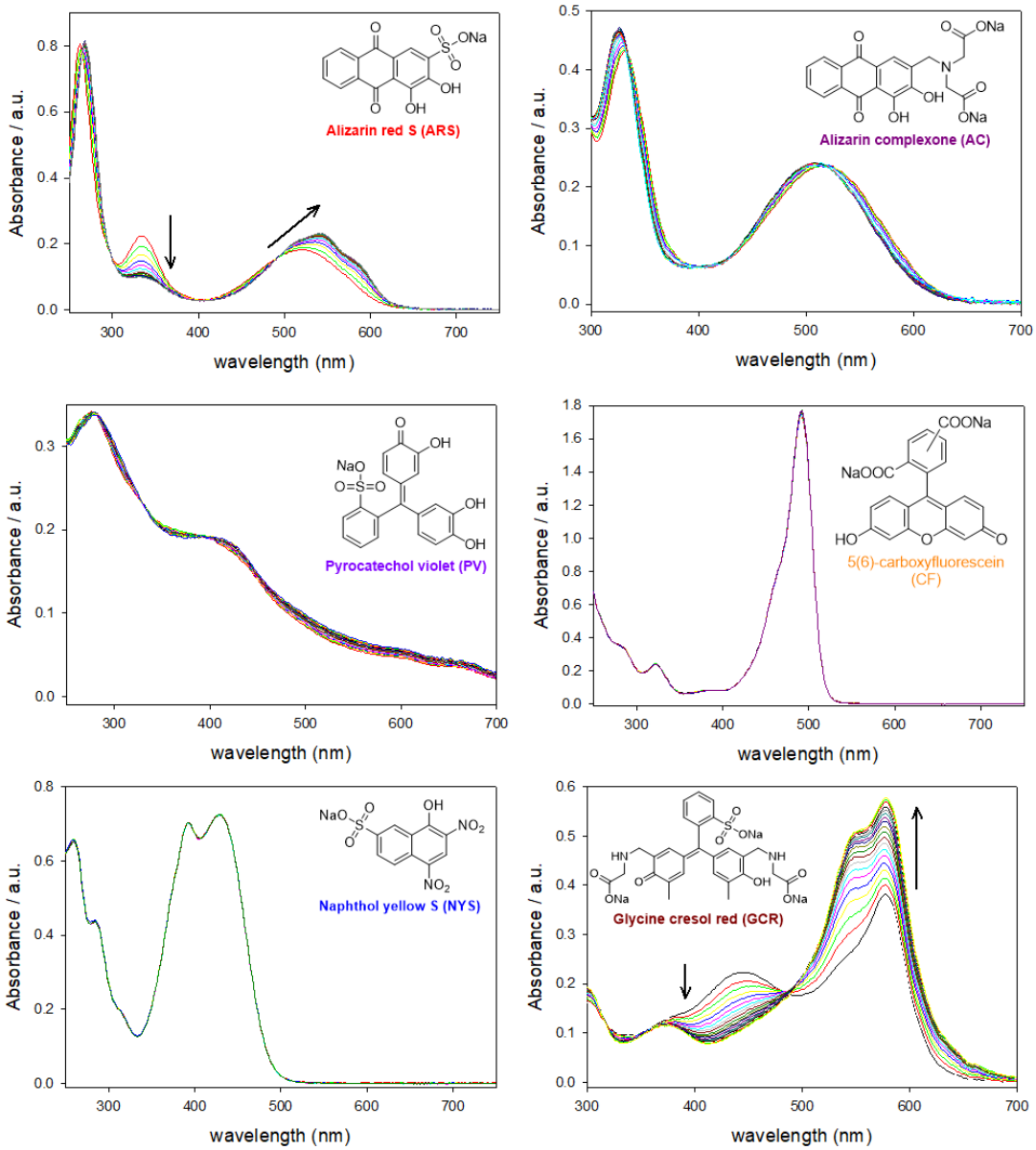

Figure 2-2 Absorbance spectra of various dyes (ARS, 30 µM; AC, 30 µM; PV, 30 µM; CF, 30 µM; NYS, 50 µM; and GCR, 20 µM), upon titration with $NiCl_2$. Measurements conducted in H_2O solution buffered to pH 7.4 with 50 mM HEPES.

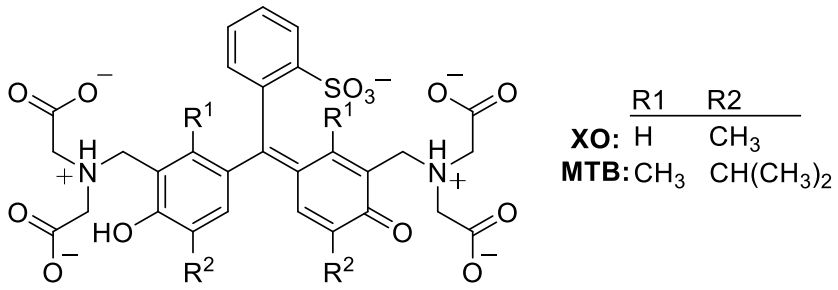

Scheme 2-1 Chemical structures of xylenol orange (XO) and methylthymol blue (MTB) in their likely protonation state in neutral water solution (pH = 7.4).

Finally, linear multivariate data processing methods were selected for the array sensing system, namely linear discriminant analysis (LDA) and principal component analysis (PCA), whose goal is to find *linear combinations* of features in the data that best differentiates the analytes of interest. Indeed, there have been many reported examples in the literature for the differentiation of metal cations using LDA and PCA algorithms for multivariate data analysis, although these examples suffered from the "problem of mixtures".[106-110]

Using metal cations as a valuable proof of principle, we first hoped to demonstrate that the two-dye array could differentiate numerous divalent metal cations qualitatively. As a first step, benchtop absorbance measurements were performed to determine the regions of greatest differential response when metal ions were titrated into each dye. As a representative example, shown in Figure 2-3, Ni(II) displayed vast absorbance signal changes at different regions in the spectrum, as Ni(II) was titrated into each dye. More importantly, based on each dye's binding profile, there are clear regions in the binding curve at 578 and 604 nm for which the response is completely linear with respect to increasing Ni(II) concentration. At lower Ni(II) concentrations, there is a steep linear increase in absorbance, followed by a plateau at high [Ni^{II}].

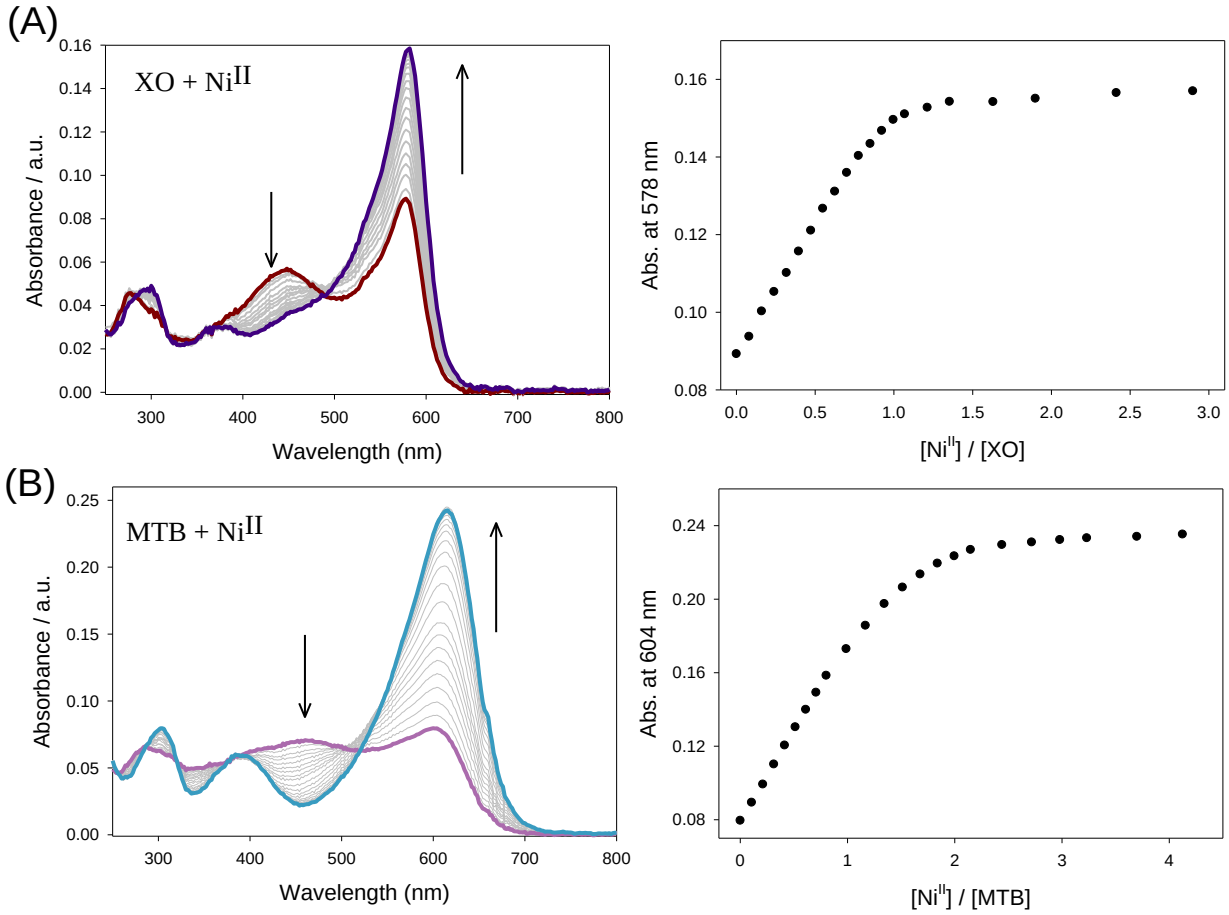

Figure 2-3 (A) Representative absorbance spectra acquired over the course of the titration of XO (5 μM) with $NiCl_2$ (0-14.4 μM) and corresponding isotherm from the same titration at 578 nm. (B) Representative absorbance spectra acquired over the course of the titration of MTB (7.5 μM) with $NiCl_2$ (0-21.7 μM) and corresponding isotherm from the same titration at 604 nm. Measurements were conducted in H_2O solution buffered to pH 7.4 with 50 mM HEPES.

Metal binding titrations were carried out with eight divalent transition and main group metal chloride salts into each dye ($CuCl_2$, $CoCl_2$, $NiCl_2$, $MnCl_2$, $HgCl_2$, $CdCl_2$, $PbCl_2$, and $ZnCl_2$), to ascertain the dyes' cross-reactive behavior and linear response upon exposure to these metal ions. These absorbance titration spectra for XO and MTB dyes are displayed in Figure 2-4 and Figure 2-5, respectively. For consistency, all titrations were carried out in aqueous solution containing 50 mM 2-[4-(2-hydroxyethyl)piperazin-1-yl]ethanesulfonic acid (HEPES buffer) adjusted to pH 7.4. To prevent biasing effects from the metals' counterion, all metal(II) salts

used throughout this study were chloride salts, since Cl^- is a well-solvated and relatively inert anion in neutral water solution.[111] For clarity, a comparison of all eight divalent metal chloride salts titrated into XO and MTB dyes is presented in Figure 2-6 as profiles at 578 nm and 604 nm, respectively. As the metal ion concentration was increased, noticeable differences in behavior were observed. For example, at a M(II):XO ratio of 2:1, very marked differences in the absorbance were apparent for the Zn^{II} vs. Cu^{II} vs. Ni^{II} complex at 578 nm. This varied behavior for all metal ions is a consequence of the underlying differences in binding modes and affinities (e.g. binding geometry, stoichiometry).

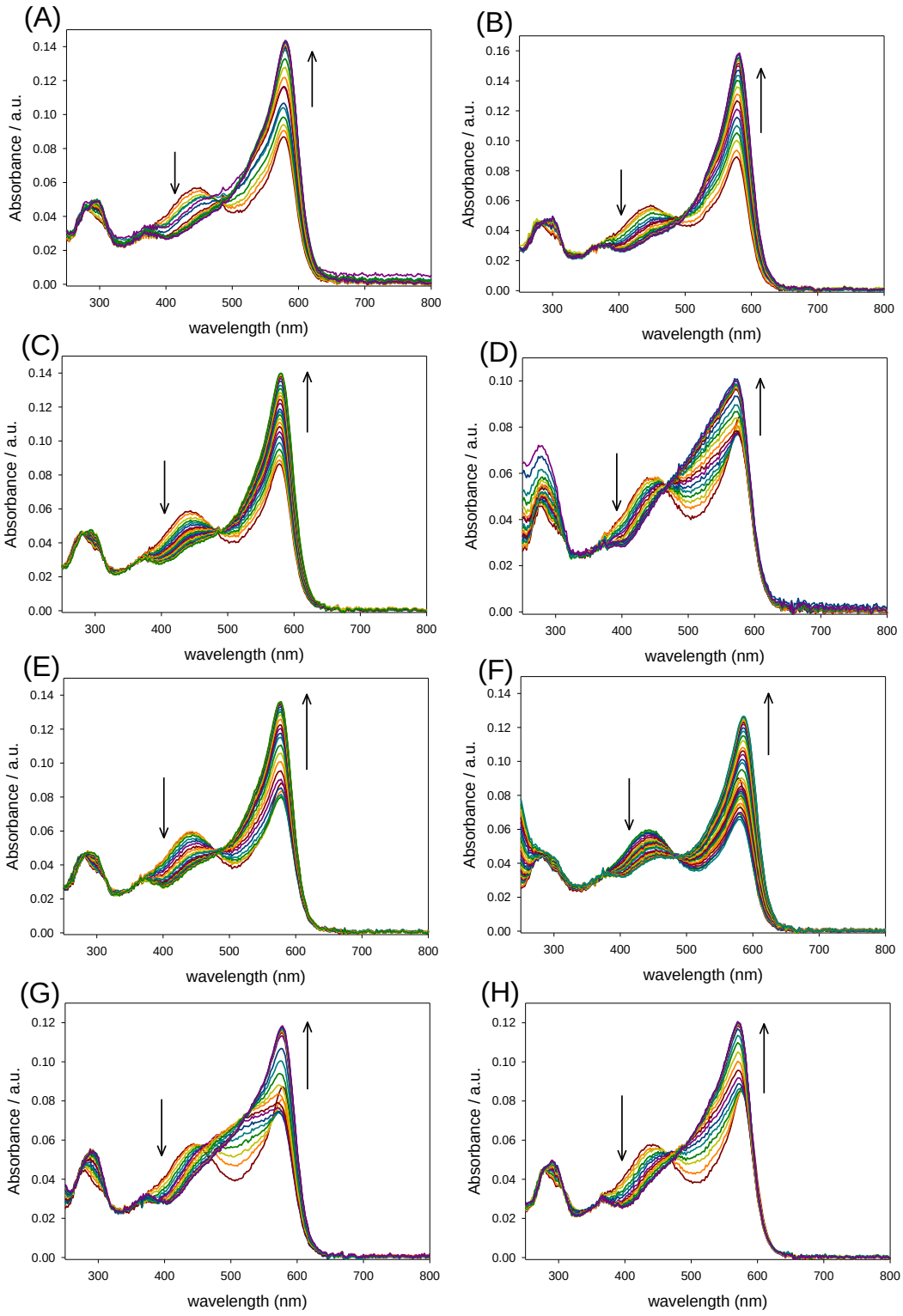

Figure 2-4 Absorbance spectra of XO (5 μM), upon addition of (A) $CoCl_2$, (B) $NiCl_2$, (C) $MnCl_2$, (D) $CuCl_2$, (E) $CdCl_2$, (F) $HgCl_2$, (G) $PbCl_2$, and (H) $ZnCl_2$ (0-33.0 μM). Measurements were conducted in H_2O solution buffered to pH 7.4 with 50 mM HEPES.

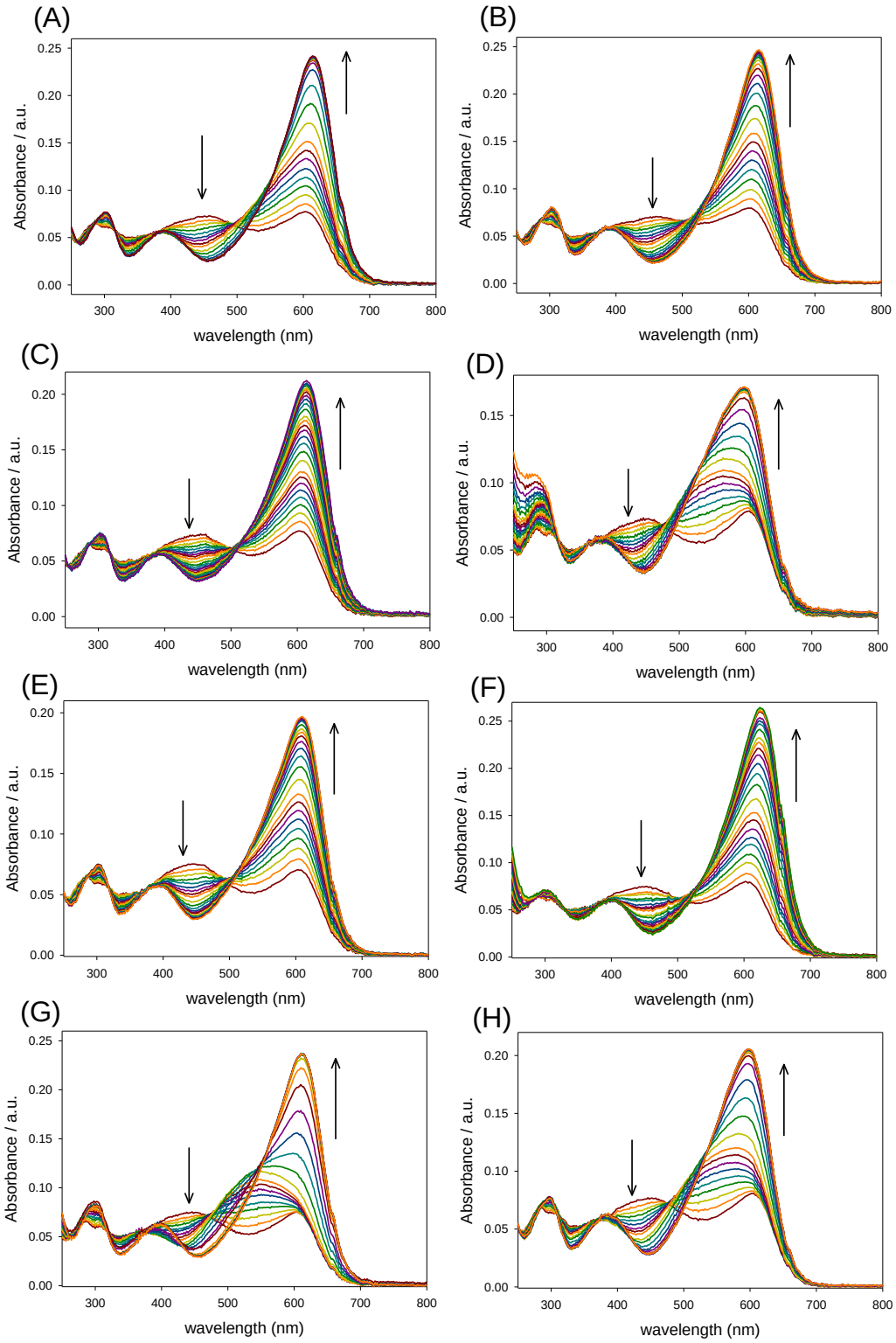

Figure 2-5 Absorbance spectra of MTB (7.5 μM), upon addition of (A) $CoCl_2$, (B) $NiCl_2$, (C) $MnCl_2$, (D) $CuCl_2$, (E) $CdCl_2$, (F) $HgCl_2$, (G) $PbCl_2$, and (H) $ZnCl_2$ (0-36.5 μM). Measurements were conducted in H_2O solution buffered to pH 7.4 with 50 mM HEPES.

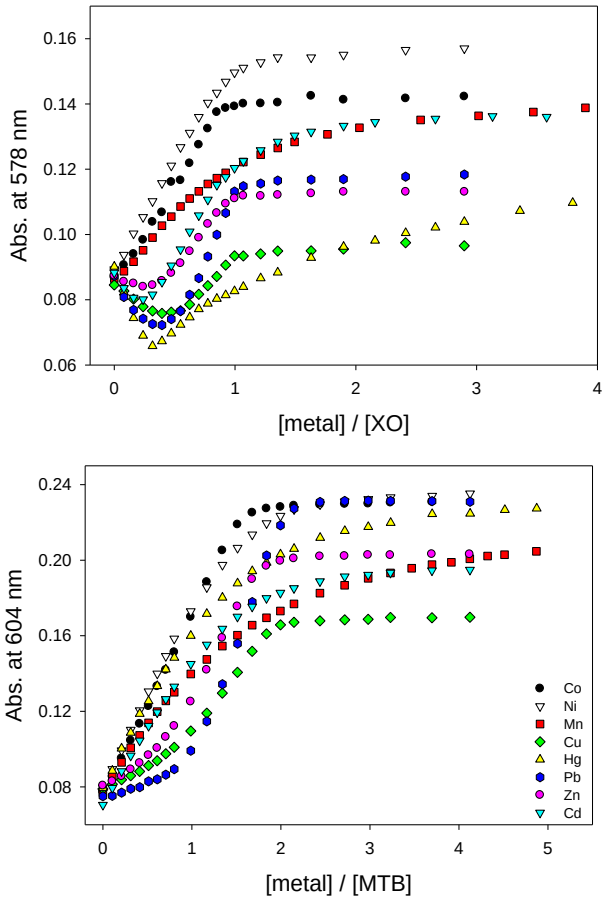

Figure 2-6 Binding isotherms from the titration of aliquots of eight metal(II) chlorides into solutions of xylenol orange (XO, 5 μM, top) and methylthymol blue (MTB, 7.5 μM, bottom) in buffered water (pH 7.4, 50 mM HEPES).

From absorption profiles such as those presented in Figure 2-6, metal-dye binding constants could be determined for the divalent metal ions shown above with XO and MTB dyes. Experimental data was fit to binding models using the *HypSpec2007* software; a representative example for these fittings with Ni(II) into each dye is displayed in Figure 2-7. Absorbance data used for fitting was selected based on the largest observed changes in the spectra (typically from 500-700 nm). These results indicate that the XO and MTB dyes display vastly different stoichiometries; XO tends to form a 1:2 metal:dye complex followed by a 1:1 complex. Surprisingly, a 2:1 complex was not observed for the XO dye. On the other hand, the MTB dye

appears to form a 1:1 metal:dye complex, and a 2:1 metal:dye complex at higher [M^{II}], presumably binding one metal ion on either side of the dye. Given the very similar chemical structure of each of these dyes, this surprising difference in stoichiometry for metal binding was welcome for our proposed system, since each dye can respond differentially *and* uniquely to various divalent metal ions depending on their chemical nature and concentration.

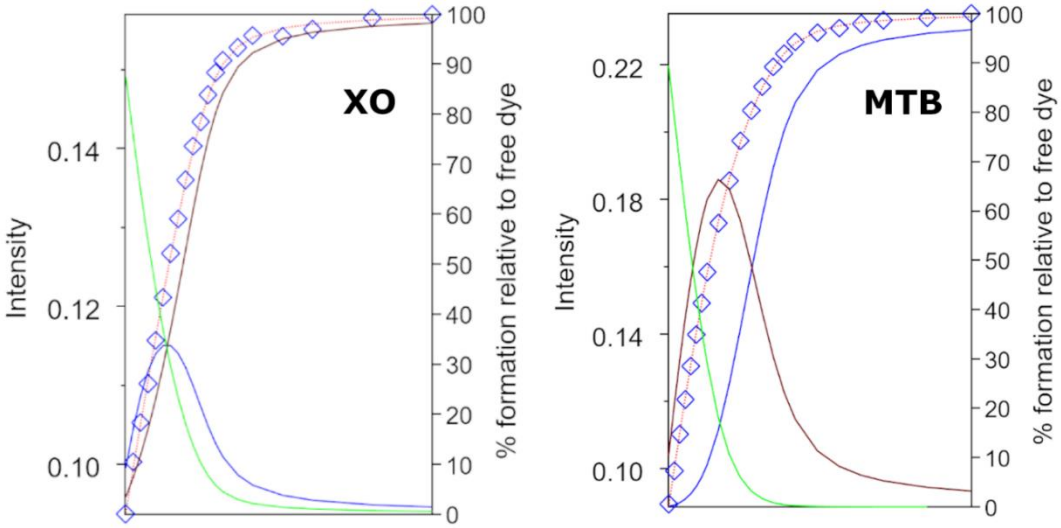

Figure 2-7 Representative titration profiles upon addition of $NiCl_2$ into XO at 578 nm (left) and MTB at 604 nm (right), along with the corresponding nonlinear fit obtained using the *HypSpec* software. Dotted red lines display the profiles obtained from the fit of the blue experimental data points to a 2:1 and 1:1 dye:cation model for XO vs. a 1:1 and 1:2 dye:cation model for MTB. Solid colored lines represent the relative concentrations of free dye (green line), 1:1 dye:Ni^{II} complex (brown line), and the 1:2 MTB:Ni^{II} or 2:1 XO:Ni^{II} complex (blue line) as $NiCl_2$ is added over the course of the titration.

The determined binding constants for all eight divalent metals into each dye are presented in Table 2-1. Comparison of 1:1 binding constants for eight metal ions into each dye gave values ranging from 10^5 to 10^{10} in favor of dye-metal complex formation. These values are indicative of strong binding affinity coupled with widespread variability, spanning several orders of magnitude. The strong affinity assures that binding curves will display near linear behavior over a wide range of metal ion concentrations for all divalent metal ions in this study, while the good

variability provides a basis for successful discrimination using these dyes as cross-reactive receptors in a pattern-based sensing array.

Table 2-1 Binding constants for 2:1, 1:1, and 1:2 dye:metal complexes obtained from non-linear fitting of the absorption profiles from the titration of metal(II) chlorides into dye solutions in buffered water (pH 7.4, 50 mM HEPES).

M^{2+}	XO ($\text{Log}K_{2:1}$ + $\text{Log}K_{1:1}$)	MTB ($\text{Log}K_{1:1}$ + $\text{Log}K_{1:2}$)
Mn	5.46(5) + 6.14(1)	6.00(2) + 4.97(4)
Co	6.3(3) + 7.88(9)	8.6(2) + 6.7(7)
Ni	5.5(2) + 7.36(6)	7.47(3) + 6.27(6)
Cu	6.3(1) + 8.30(4)	9.29(7) + 7.7(2)
Cd	6.6(2) + 7.82(6)	7.06(3) + 5.91(6)
Hg	6.8(1) + 6.35(3)	6.89(4) + 5.52(8)
Pb	5.88(7) + 8.62(2)	8.42(2) + 7.27(5)
Zn	6.8(3) + 9.6(1)	9.8(3) + 7.9(7)

2.3 Qualitative results

In addition to those observed at 578 nm (for XO) and 604 nm (for MTB), further differences were also evident in other parts of the spectrum for each dye-metal complex. This is evident in Figure 2-4 and Figure 2-5 (e.g. changes in absorbance between 400-500 nm). Taken together, these features would in principle allow one to uniquely identify the nature of each metal by analysis of the absorbance spectra at relatively high concentration. However, distinguishing each metal at lower concentrations would become increasingly difficult: instead this wealth of information was interpreted using computational pattern recognition techniques, which could identify the differential behavior observed in the benchtop titrations. Given the strong binding, and therefore, highly linear spectral response with changing metal ion concentration, this system

provided an ideal testbed for our hypothesis that retaining a nearly linear response from all array components will yield a pattern-based sensing system that accurately predicts the nature and concentration of analytes in a mixture without the need for physical separation.

For repeatable acquisition of absorption data at multiple wavelengths on many different metal cations, dyes and metal ion solutions were laid out on 384-well microplates and experiments were conducted on an automated plate reader. For qualitative experiments, plates contained 15 replicates of each metal sample, together with dye reference standards and buffer blanks. For the initial qualitative experiment, the array of XO and MTB dyes was exposed to eleven divalent metal chloride salts: Ba^{II}, Mg^{II}, Fe^{II}, Mn^{II}, Co^{II}, Ni^{II}, Cu^{II}, Hg^{II}, Cd^{II}, Zn^{II}, and Pb^{II}. All conditions for the plate were identical to the benchtop titrations shown earlier, i.e., H_2O solutions buffered to pH 7.4 with 50 mM HEPES and metal chloride salts were used throughout.

In addition to the divalent transition metal ions from the benchtop titrations, Fe^{II} was added to the analyte panel. Iron(II) could not be included in the benchtop titrations shown above because of its instability in aqueous solution. More specifically, iron(II) tends to be slowly oxidized to iron(III) in solution by dissolved oxygen in water.[112] The resulting acidic Fe^{III} aqua complex is then susceptible to pH-dependent hydrolysis to form insoluble precipitates, leading to major inconsistencies in Fe^{II} concentration over time.[113] Therefore, iron(II) was not included in the more time-consuming benchtop titration shown above. However, work could be carried out more quickly and in parallel on microwell plates. Stock solutions could be made fresh and immediately added to plates containing the dyes, preventing unwanted oxidation and hydrolysis. For consistency throughout, all stock solutions (dye and metal chloride stock) were prepared fresh before each experiment.

Relative to the transition and main group divalent metal ions used in this study, each dye was much less responsive to s-block divalent metal cations, such as Mg^{II} and Ba^{II}. Thus, these metal ions were included in the array as negative controls. Similarly, Na^{+} was included in the array as a negative control, since no response from either dye was observed with this metal ion in the preparatory benchtop titrations. In fact, insensitivity to Na^{+} was actually welcome for the current application since it is a ubiquitous interferent in any matrix of practical relevance. The lack of response from XO and MTB in the presence of these s-block metal ions is displayed in Figure 2-8.

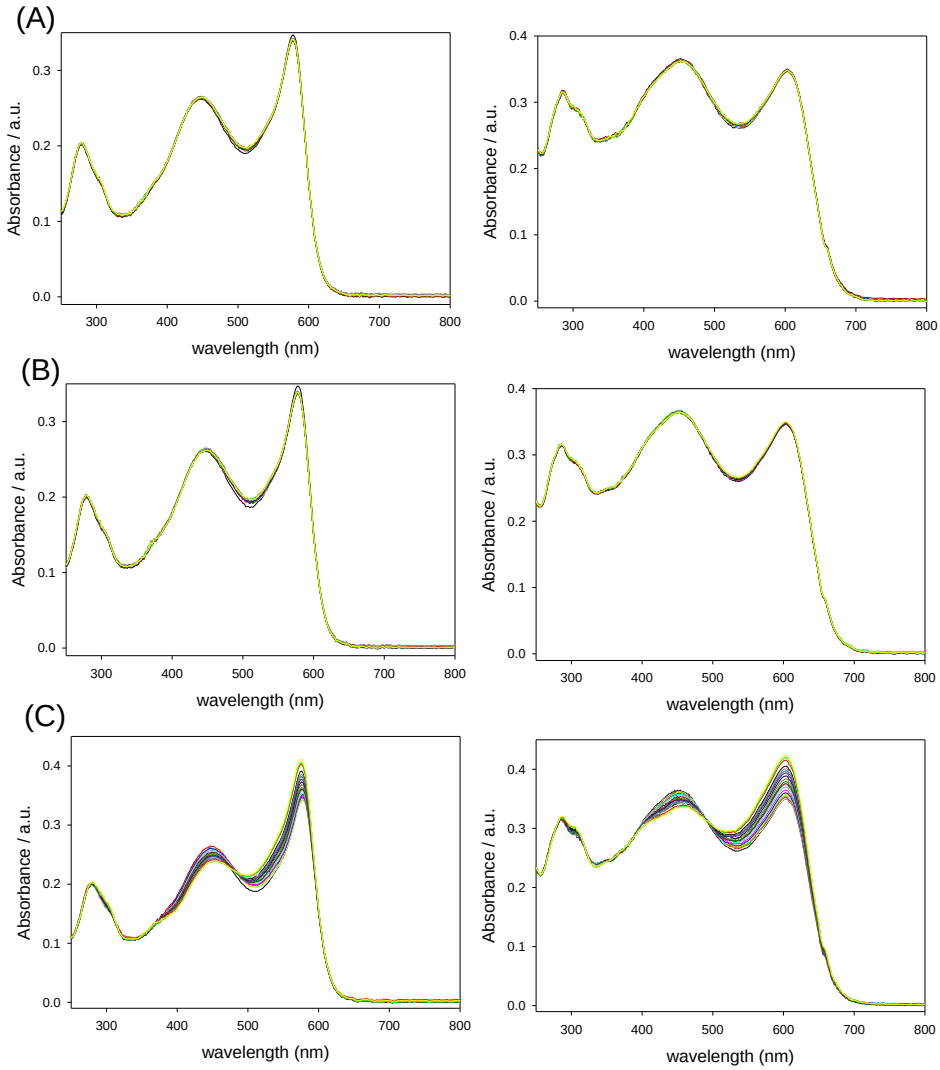

Figure 2-8 Representative absorbance spectra of XO (left; 20 μM) and MTB (right; 30 μM), upon addition of (A) NaCl, (B) $BaCl_2$, and (C) $MgCl_2$ in H_2O solution buffered to pH 7.4 with 50 mM HEPES. Little to no change can be observed in the presence of these metal ions, indicating lack of binding.

For qualitative experiments, absorbance was monitored at 334, 342, 436, 442, 450, 482, 500, 540, 578, 590, and 614 nm, corresponding to the positions of prominent features in the absorbance spectra of the dye-metal complexes formed by the XO and MTB dyes, found through binding titrations described earlier (see Figure 2-9). Metal concentrations were kept constant at 30 μM, XO and MTB concentrations were set to 20 μM and 30 μM, respectively. Dye and metal concentrations were selected based on the dyes' optimal absorbance signal at these

concentrations (ca. 0.3 for each dye), and also to attain metal:dye ratios that were likely to display high discriminatory capabilities based on the behavior observed in each dye's respective metal binding profiles. Fifteen replicates were laid out for each dye-metal sample, which generated a large data set (2 dyes x 12 analytes x 15 replicates = 360 samples), each represented by 11 absorbance measurements (described above) for each dye. Figure 2-10 shows a schematic layout of the qualitative plate used for discrimination of divalent metal cations and a picture of the final microwell plate containing these solutions, highlighting the differential responses from the two dyes to the metal ions of interest.

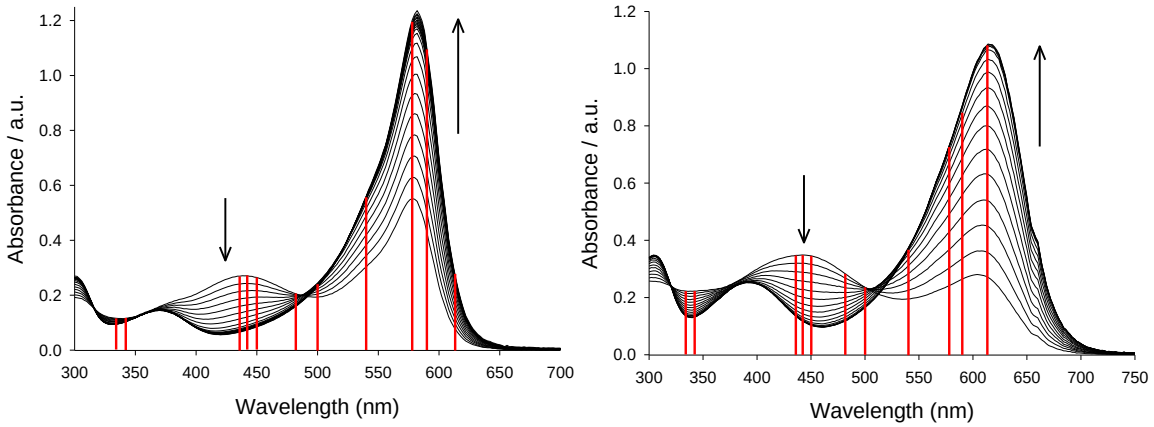

Figure 2-9 Representative absorption spectra of XO (left, 20 µM) and MTB (right, 30 µM) solutions, upon titration with $NiCl_2$. Measurements conducted in H_2O solution buffered to pH 7.4 with 50 mM HEPES. Red lines denote wavelengths that were selected to be measured on the plate reader for array sensing.

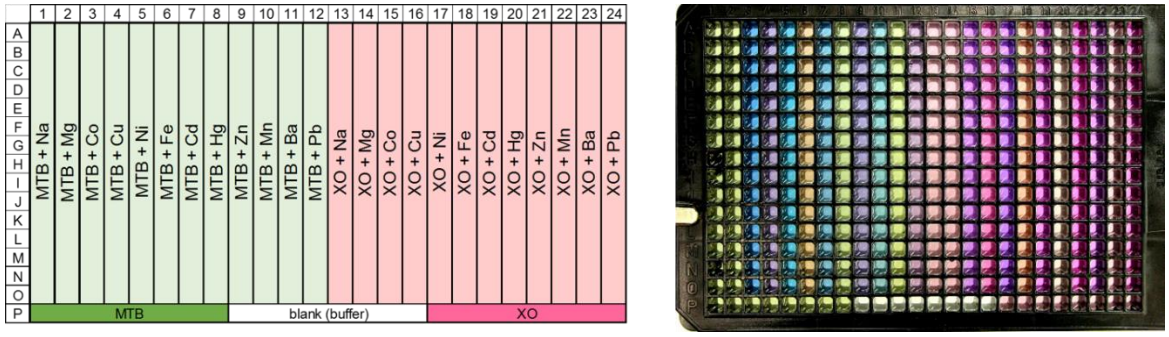

Figure 2-10 Layout of a 384-well microplate for a typical qualitative multivariate experiment (left), and a picture of the 384-well microplate with all solutions added (right), highlighting the differential response of XO and MTB dyes to metal(II) cations.

Linear discriminant analysis (LDA) was then used to carry out data analysis and subsequent dimensionality reduction, as described in Chapter 1. The two-dimensional scores plot and corresponding loadings plot for the complete qualitative data set is given in Figure 2-11. The scores plot displays excellent separation between different analytes and extremely tight intra-cluster spacing; in fact, it is difficult to see distinct replicate data points without zooming in on individual analyte clusters. This is indicative of strong discriminatory power of the array coupled with excellent repeatability, respectively. In short, these dyes were very effective sensors to build a cross-reactive array for discriminating all selected divalent metal ions of analytical interest. Moreover, Na(I), Ba(II), and Mg(II) did not interfere with the discrimination; this was not surprising given that the addition of these s-block metal ions had induced little or no change in the dyes' absorbance signal.

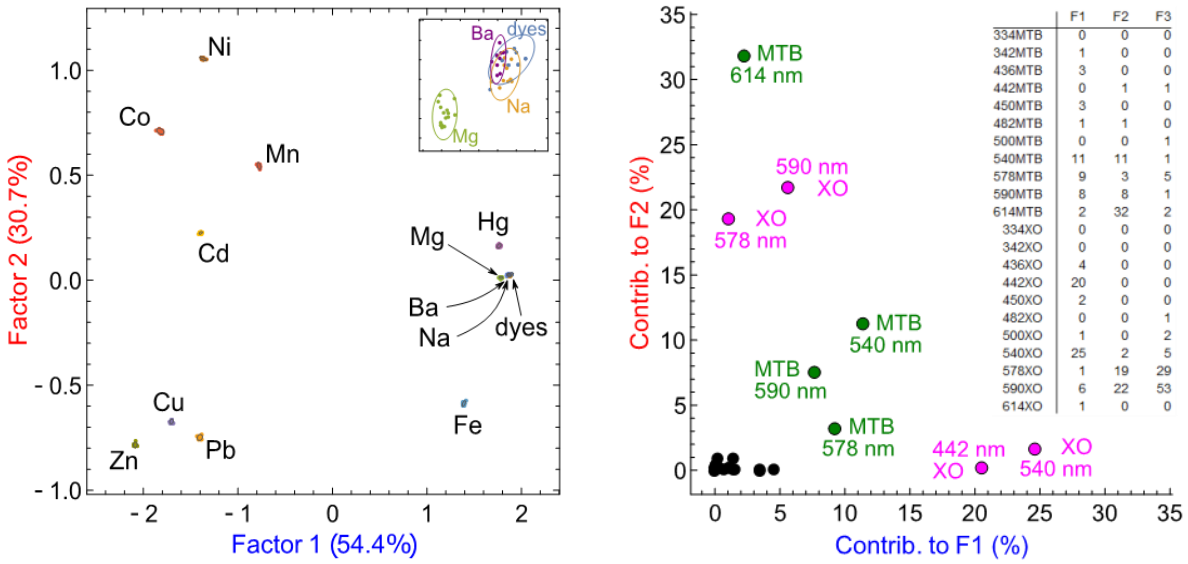

	F1	F2	F3
334MTB	0	0	0
342MTB	1	0	0
436MTB	3	0	0
442MTB	0	1	1
450MTB	3	0	0
482MTB	1	1	0
500MTB	0	0	1
540MTB	11	11	1
578MTB	9	3	5
590MTB	8	8	1
614MTB	2	32	2
334XO	0	0	0
342XO	0	0	0
436XO	4	0	0
442XO	20	0	0
450XO	2	0	0
482XO	0	0	1
500XO	1	0	2
540XO	25	2	5
578XO	1	19	29
590XO	6	22	53
614XO	1	0	0

Figure 2-11 Left: Two-dimensional plot of the LDA scores for the qualitative discrimination of divalent metal ions ([metal] = 30 µM, [XO] = 20 µM, [MTB] = 30 µM in H_2O solution buffered to pH 7.4 with 50 mM HEPES). This plot was generated using all instrumental variables in the raw data set. Inset: magnified portion of the same plot to highlight the similarities between Na^+, Ba^{2+}, Mg^{2+}, and free dyes clusters: these ions display only minimal interaction with the dyes in our array. Confidence ellipsoids are drawn to 95% confidence level. Right: Corresponding loadings plot of the complete data set. Inset: table of variable contributions to the first three LDA factors (F1, F2, and F3) for the complete data set.

Based on the loadings plot (Figure 2-11, right), there were many instrumental measurements that contributed very little to the overall performance of the array in separating metal ions (shown as black dots in Figure 2-11, right). These superfluous instrumental variables introduce noise, require extra acquisition time, and generally lead to a more complicated, less performant system. Therefore, those measurements whose contribution to the separation was negligible were removed, with minimal loss in the array's discriminatory power. This process, typically referred to as "variable reduction", greatly optimizes the sensing system by discarding all measurements whose overall contributions are below a certain user-defined threshold. For this qualitative system, this threshold was set at 5% contribution to both factors, or 10% to one factor. This enabled the removal of 15 out of 22 total instrumental measurements, retaining only 7 measurements (namely, absorbance data at 442, 540, 578, and 590 nm for the XO dye, and at

540, 590, and 614 nm for the MTB dye). LDA analysis was carried out once more on this reduced data set, as described previously. The LDA scores plot and corresponding loadings plot obtained for the reduced data set are shown in Figure 2-12.

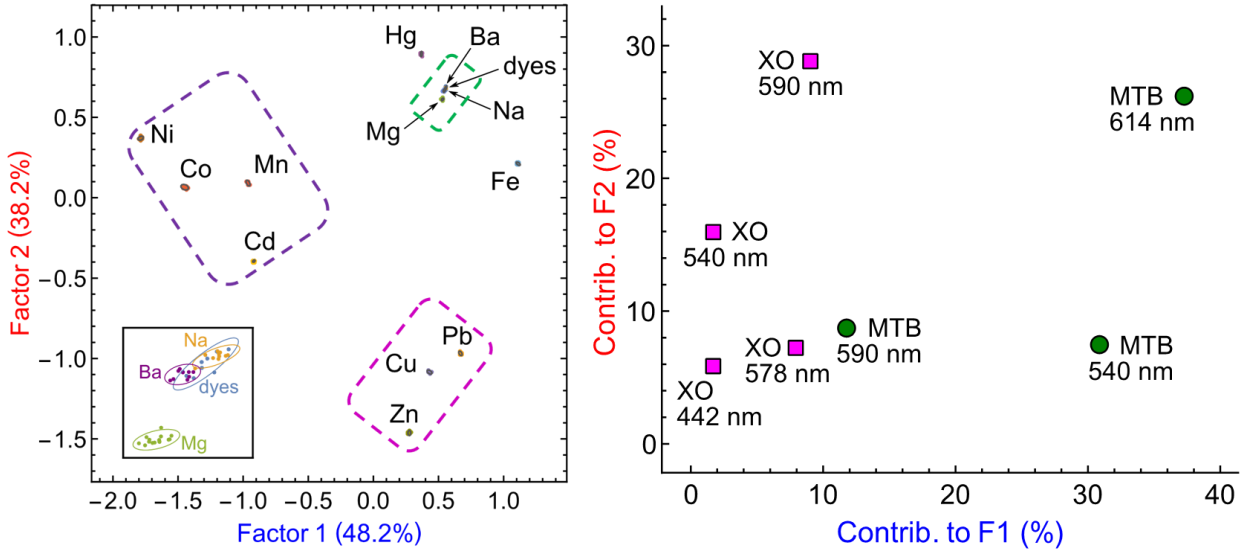

Figure 2-12 Left: Two-dimensional plot of the LDA scores for the qualitative differentiation of divalent metal ions: Purple and pink dashed lines highlight two superclusters corresponding to the pronation state of the dyes' phenol group when the metal is bound. Inset: a magnified portion of the same plot highlights the Na^+, Ba^{2+}, Mg^{2+}, and free dye clusters (green dashed line). Right: The corresponding LDA loadings plot, indicating the relative contributions of each instrumental variable to the calculated LDA factors. Purple squares: contributions from XO-metal complexes; green circles: contributions from MTB-metal complexes. ([metal] = 30 µM, [XO] = 20 µM, [MTB] = 30 µM in H_2O solution buffered to pH 7.4 with 50 mM HEPES; confidence ellipsoids drawn at 95% level).

Based on the scores plot for the reduced data set, it is evident that removal of redundant instrumental variables did not hamper the array's differentiation capabilities. All metal ion analytes retain their tight clustering and good separation, despite removing over half of the original instrumental variables from the data set. Moreover, analysis of the loadings plot from Figure 2-12 showed that, at first approximation, each dye contributes roughly independently to each of the first two factors, with MTB signals contributing most significantly to factor 1, and XO signals to factor 2. In fact, the contributions from both factors are more balanced in the

reduced data set, (48.2% for F1 and 38.2% for F2), indicating that the two dyes are both contributing significantly to the differentiation, an ideal situation for pattern-based sensing procedures.

Samples in the scores plot can be further classified into superclusters according to shared behavior. First is the cluster of s-block metals, which unsurprisingly shows little separation from the free dye reference cluster. Comparison of supercluster composition with spectral data from benchtop titrations indicates that the two other analyte superclusters are likely to be associated with the protonation state of the dyes' phenolic oxygen atom when bound. Since this phenol oxygen atom is part of the chromophore system of each dye, its protonation state has a direct effect on the absorbance characteristics of the dye, causing significant spectral changes with changing protonation state. Comparing the spectral changes observed upon the addition of Mn^{II}, Co^{II}, Ni^{II}, and Cd^{II}, with those observed during an acid-base (pH) titration of these dyes (Figure 2-13) suggest that the phenolic OH groups are deprotonated in the presence of these metal ions, whereas solutions containing Cu^{II}, Zn^{II}, and Pb^{II} appear to bind with dyes in their protonated form. The LDA analysis recognized these effects through these characteristic spectral changes, resulting in sample clusters arranged by chemical similarity in the scores plot. These encouraging similarities validate the underlying hypothesis that cluster distance in the LDA "factor space" can be relied upon to directly reflect similarity in chemical features.

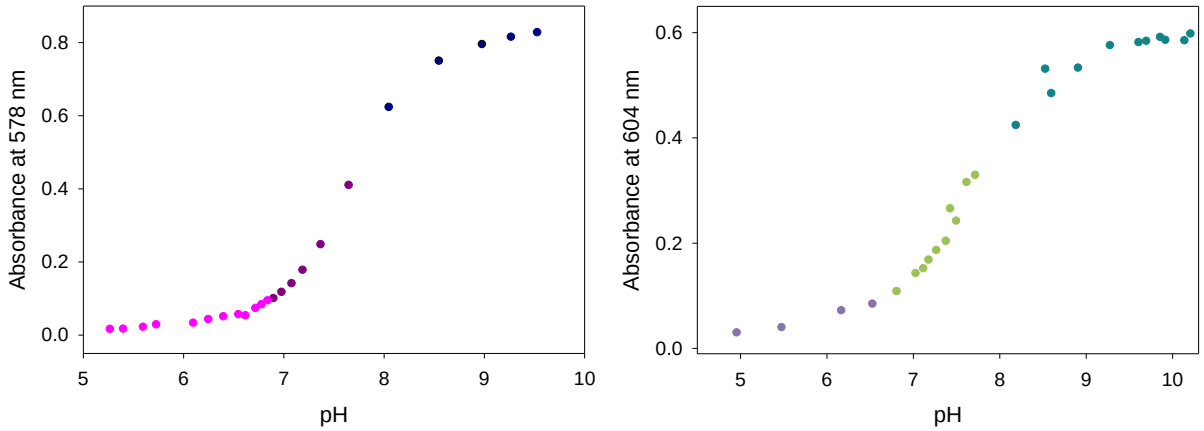

Figure 2-13 Absorbance titration profiles monitored at 578 nm and 604 nm for the XO (left; 20 µM) and MTB (right; 30 µM) dyes, respectively at various pH values in H_2O. The colors of each data point approximates the solution's color at the corresponding pH for each dye.

As a final step for the qualitative analysis, we tested whether the array could retain its performance at much lower concentrations. To determine the limit of differentiation (LOD) for our system, the array was exposed to ten previously considered metal(II) cations at decreasing concentrations until discrimination was lost ([XO] = 20 µM, [MTB] = 30 µM). All measurements and multivariate data analysis were conducted as previously described. Displayed in Figure 2-14 is the LOD study, which showed that differentiation was retained down to 500 nM, but lost at 250 nM. Conservatively, we therefore considered the array's limit of differentiation to be 500 nM. Considering the excellent qualitative results, we moved towards verifying that the system could respond linearly to changes in concentration of metal ions, opening the way to quali-quantitative analytical determinations.

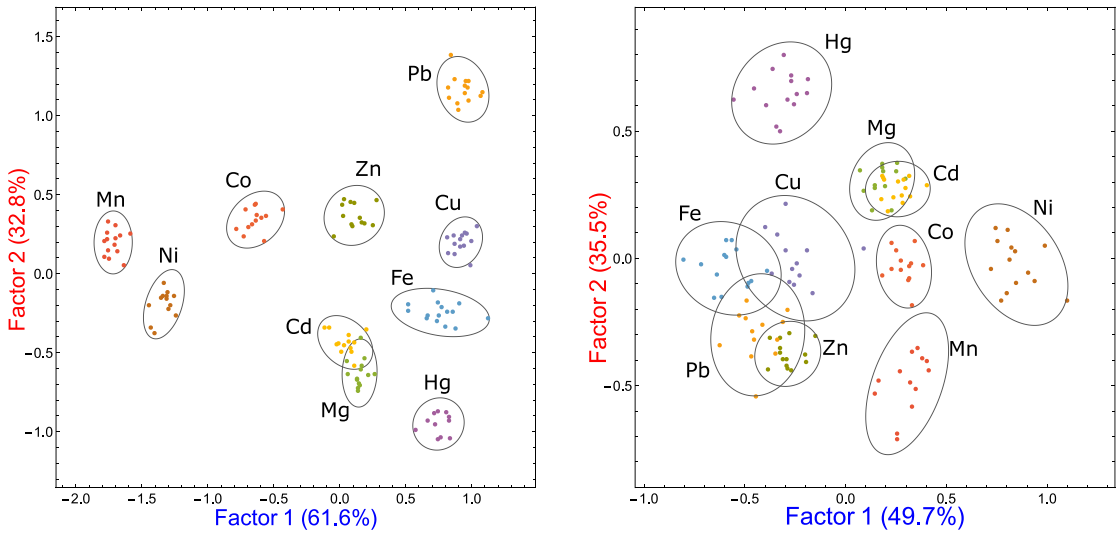

Figure 2-14 Left: Two-dimensional plot of the LDA scores for the qualitative differentiation of divalent metal ions at 500 nM. Right: LDA scores plot at a total metal concentration of 250 nM: at this lower concentration, the array can no longer accurately discriminate between all divalent metal cations. ([metal] = 250 or 500 nM, [XO] = 20 µM, [MTB] = 30 µM in H_2O solution buffered to pH 7.4 with 50 mM HEPES).

2.4 Quantitative response

Critical to the quantitative work was retaining a linear response from the dye-metal complex formation system. However, under the presented conditions, the system responds linearly only over a relatively small range of metal ion concentrations. To pursue a quantitative response, we redesigned the array to include multiple concentrations of each dye, added to the plate in a single experiment. This design helped guarantee that for any concentration of metal ions, one of the multiple dye concentrations would exhibit the desired linear response, whereas other metal ion concentrations would become “silent” (i.e. either unresponsive or saturated), with no significant differential response. Only those metal-dye ratios that fall in the linear region of the relevant binding curve would show different behavior; all other metal-dye ratios would either be too concentrated and therefore give off a uniformly high, saturated signal, or too dilute and insensitive, giving off a uniformly low signal, leading the LDA analysis to automatically discard

these contributions as the “out-of-range” dye solutions because of their lower discriminatory power, i.e. no useful information content for sample discrimination.

For the quantitative analysis, four divalent metal ions were selected (Cd^{II}, Hg^{II}, Pb^{II}, and Cu^{II}) for their biological and environmental importance. On a 384-well microplate, three concentrations for each dye were laid out (5 μM, 20 μM, 40 μM for XO, and 10 μM, 30 μM, and 60 μM for MTB). A series of metal ion samples were then laid out at five concentrations for each metal ion (1 μM, 2.5 μM, 5 μM, 7.5 μM, and 10 μM). Using LDA and the variable reduction method outlined previously, the array was able to differentiate all concentrations of these metal ions with clear linear response. In this case, 54 total instrumental measurements were reduced to only 18, while retaining minimal intra-cluster distance between replicates and maximizing separation between clusters of different metal ions *and* their concentrations. The final quali-quantitative LDA scores plot and corresponding loadings plot are displayed in Figure 2-15. The scores plot displays excellent separation between clusters (strong discriminatory power), while the intra-cluster distance between replicates of the same sample is very low (good repeatability). Furthermore, individual concentrations of metal ions are arranged linearly with respect to their concentration, with increasing concentrations positioned further away from the free dyes cluster. Analysis of the loadings plot reveals that, this time, factor 1 primarily reports on the response from XO, while factor 2 depends mostly on the response from MTB. This gives intuitive information about the origin of the discriminatory power of the array. For example, the response to changes in concentration of Pb^{II} is almost exclusively described by factor 1, which is mostly associated with the XO dye. This indicates that this dye is most responsible for the quantitative detection of Pb^{II}, whereas, factor 2 (associated with MTB) is mostly responsible for the qualitative discrimination of Pb^{II} from all other metals.

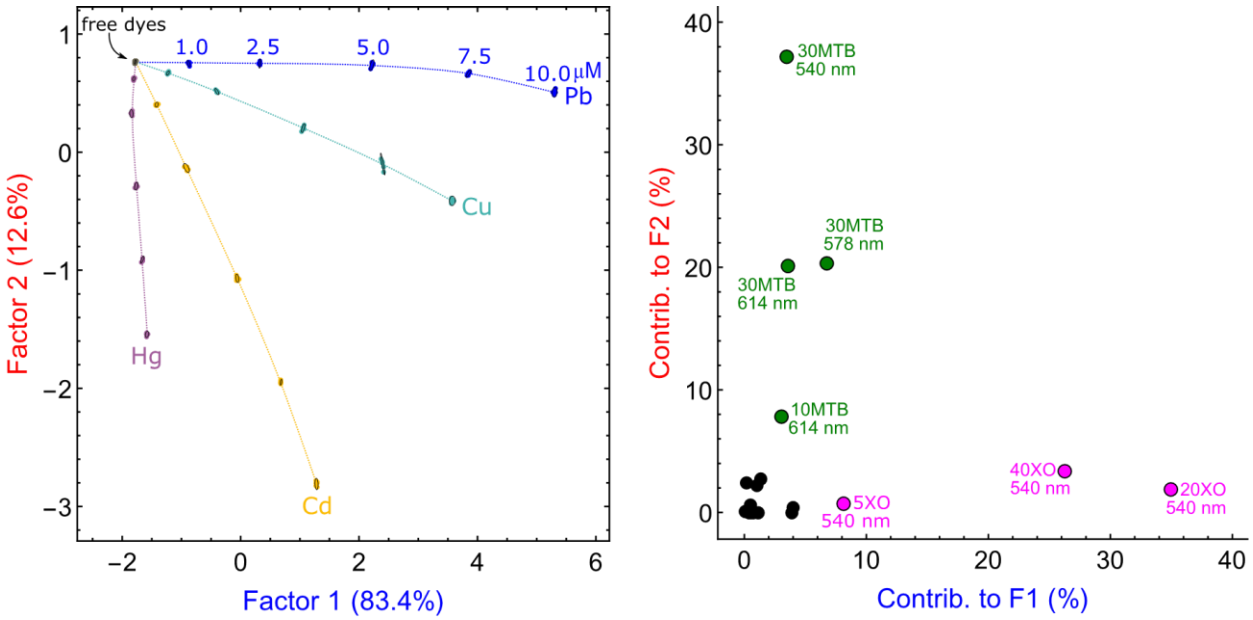

Figure 2-15 Two-dimensional plot of the LDA scores (left) and loadings (right) for the quali-quantitative differentiation of Cd^{II}, Hg^{II}, Pb^{II}, Cu^{II} at five concentrations ([M^{II}] = 1 μM, 2.5 μM, 5 μM, 7.5 μM, and 10 μM; [XO] = 5, 20, 40 μM and [MTB] = 10, 30, 60 μM). Measurements were conducted in H_2O solution buffered to pH 7.4 with 50 mM HEPES.

The results presented here clearly show that the system is well capable of qualitative *and* quantitative differentiation of these metal cations in one experiment. If one were to process an unknown in the same way as these training samples, this scores plot could function effectively as a calibration plot with unknown's position indicating both the *nature* and *concentration* of the metal ion present. The remarkably good discriminatory power coupled with linearity in concentration response obtained in a quantitative study provided the necessary foundation to confront the "problem of mixtures".

2.5 Analysis of mixtures

In the following work, the array was challenged with a series of mixtures of metal(II) cations, with the intention to use its response as a 2D calibration curve for unknown mixture analysis. The differentiation of binary and ternary mixtures containing $NiCl_2$, $HgCl_2$, and $PbCl_2$ was examined. On a 384-well microplate, three solutions containing pure metal ions

([metal] = 30 μM), one equimolar ternary mixture ([metal] = 10 μM each), and six solutions containing 2:1 binary mixture combinations of each metal ion ([metal] = 20 μM and 10 μM in each), were added to the array, in the conditions used for the qualitative work described earlier ([MTB] = 30 μM, [XO] = 20 μM).

After LDA analysis, dimensionality reduction, and retention of the nine most important raw instrumental measurements (out of 24 collected), the resulting LDA scores plot, shown in Figure 2-16, retained 98.7% of the information in the original data set, with tight clusters (high reproducibility) and good separation (high discriminatory power).

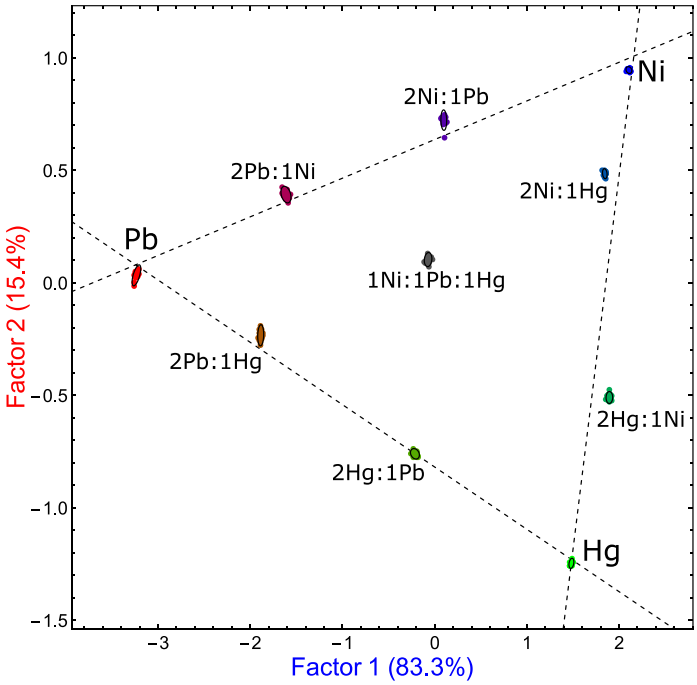

Figure 2-16 Two-dimensional plot of LDA scores for the separation of metal ion mixtures (Ni^{II}, Pb^{II}, and Hg^{II}). The plot was obtained using only the nine most important instrumental measurements and captures 98.7% of the total information content from the original data set ([XO] = 20 μM, [MTB] = 30 μM, total [M^{II}] = 30 μM in H_2O solution buffered to pH 7.4 with 50 mM HEPES).

Encouragingly, the three pure metal ion and their mixture clusters were distributed along the edges of a triangle, with the pure metal ion samples at each vertex. For each pair of metal ions, the positions of the 1:2 and 2:1 mixture clusters were in agreement with where one would

expect them to be located, namely one-third and two-thirds of the way along the corresponding edge, respectively. Furthermore, replicates from the equimolar ternary mixture clustered very close to the center of the triangle identified by the pure metal ion clusters. To highlight the quality of the positional response, we calculated best fit trendlines for each of the triangle's sides; for instance, the trendline on the top left of Figure 2-16 was obtained by drawing a best fit line through the centroids of the clusters for Pb^{II}, $2Pb^{II}$:Ni^{II}, Pb^{II}:$2Ni^{II}$, and Ni^{II}. In short, thanks to the fact that all components were chosen or adjusted to behave linearly in this sensing array (i.e. the chemical transduction mechanism, the instrumental response, and the data analysis algorithm), the system's response was shown to be completely linear with respect to the composition of sample mixtures, thus making determination of unknown mixture samples highly predictable.

To further support the efficacy of this approach, the same array was exposed to mixtures composed of three different metal cations. The same series of 2:1 binary and equimolar ternary mixtures used previously for Ni^{II}, Pb^{II}, and Hg^{II} was prepared using $CoCl_2$, $CuCl_2$, and $CdCl_2$, and added to a 384-well microplate under the same conditions described previously. After LDA analysis, dimensionality reduction, and retention of the eight most important instrumental measurements, the two-dimensional LDA scores plot, shown in Figure 2-17 was generated. Clearly, the plot of LDA scores for this new series of mixtures appears nearly identical to the plot shown for Ni^{II}, Pb^{II}, and Hg^{II} (Figure 2-16): the three pure metal clusters make up the vertices of a triangle, with the 2:1 binary mixtures distributed appropriately along its edges, and the equimolar ternary mixture replicate points clustered near the center of the triangle. Once again, all replicate data points display tight intra-cluster distances (indicating high reproducibility), with large inter-cluster spacing between different clusters (excellent

discriminatory power). The results obtained using a second set of metal ion mixtures confirmed that the previous results were not due to the specific analytes, but in fact to the choice of conditions, leading to a complete linear systematic response and allowing for the discrimination of any mixture of metal cations using these methods.

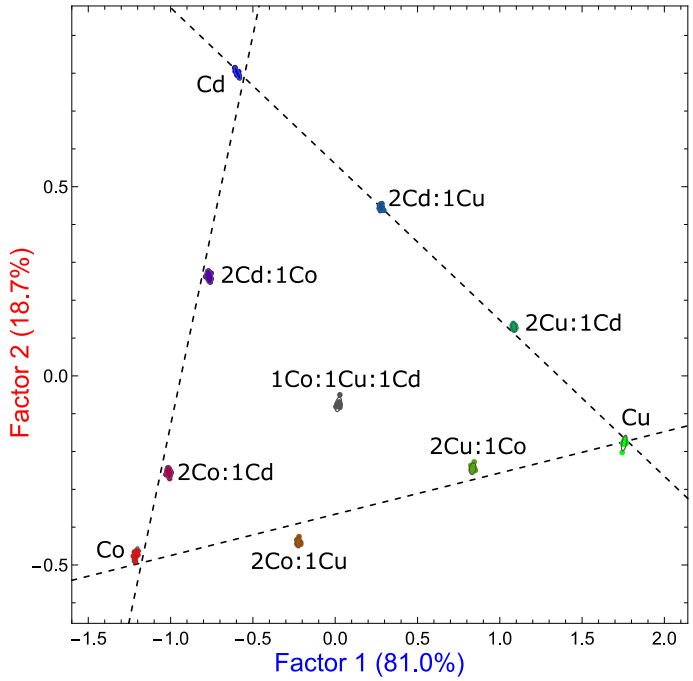

Figure 2-17 Two-dimensional plot of LDA scores for the differentiation of metal ion mixtures (Co^{II}, Cu^{II}, and Cd^{II}). The plot was obtained using the eight most important instrumental measurements and captures 99.7% of the total information content from the original data set ([XO] = 20 µM, [MTB] = 30 µM, total [M^{II}] = 30 µM in H_2O solution buffered to pH 7.4 with 50 mM HEPES).

2.6 Projection of unknown and untrained-for mixtures

Having established conditions in which the system responds linearly to variations in relative composition of these mixtures, the plot in Figure 2-16 was considered further as a potential calibration plot for the identification of unknown mixture samples. More specifically, it was important to determine the array's ability to identify mixture samples for which the system had not been explicitly trained previously. In other words, could the sensing array accurately predict the components of binary mixtures whose metal ions are *not* in 2:1 relative composition?

To address this question, a colleague was asked to prepare eight metal ion mixture solutions of unknown composition, each with a total [M^{II}] = 30 µM, using the same three divalent metal ions from the training set (i.e. Ni^{II}, Pb^{II}, Hg^{II}). The eight solutions were exposed to the array, under the same conditions used in the mixtures training set experiment shown in Figure 2-16. The resultant data set was transformed using the LDA eigenvectors (transformation rules) that had been obtained for the training set data, so the unknown test set could be projected onto the training set scores plot (i.e. Figure 2-16). The results are displayed in Figure 2-18.

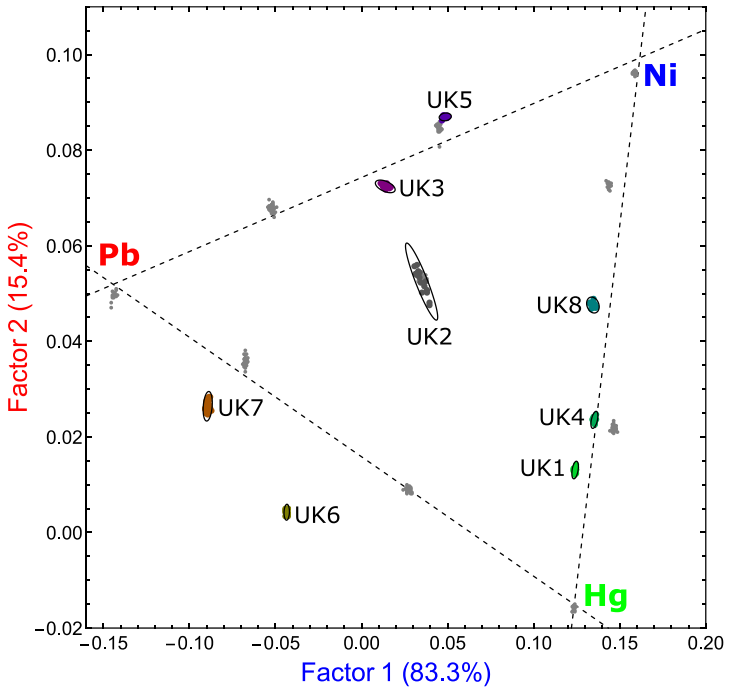

Figure 2-18 Two-dimensional plot of the LDA scores for the "test set" including 8 unknown metal ion mixtures (UK1-8, see Table 2-2) projected onto the mixtures training set from Figure 2-16. The plot was generated using the nine most important instrumental measurements from the training set ([XO] = 20 µM, [MTB] = 30 µM, total [M^{II}] = 30 µM in H_2O solution buffered to pH 7.4 with 50 mM HEPES).

The projection of the unknown challenge set provided an accurate prediction of the composition for all eight unknown sample solutions. The contents of each unknown solution are listed in Table 2-2. Included in the unknown challenge set was an equimolar ternary mixture, which was successfully found to overlap with the same cluster from the training set.

Additionally, all binary mixture clusters from the test set aligned well with their expected positions along the trendlines provided in the training set scores plot. Most notably, this included four binary mixtures that had not been present in the training data (three equimolar binary mixtures and a 5:1 Hg^{II}:Ni^{II} mixture), and yet the system was able to project them in appropriate positions on the calibration plot. This shows that our system is able to overcome the "problem of mixtures" we mentioned earlier. Thus, enforcement of a strictly linear behavior provided a multivariate scores plot with high predictive power capable of extrapolation to identify features for which the system was not trained. Any deviation from linearity in the response or analysis layers would be likely to prevent such an accomplishment for multivariate systems.

Table 2-2 Unknown metal ion mixtures that were prepared separately and added randomly to the array. The set of unknown ("UK") solutions include seven binary mixtures and one equimolar ternary mixture.

Unknown (UK) #	**Contents**
1	25 μM Hg, 5 μM Ni
2	10 μM Ni, 10 μM Pb, 10 μM Hg
3	15 μM Pb, 15 μM Ni
4	20 μM Hg, 10 μM Ni
5	20 μM Ni, 10 μM Pb
6	15 μM Pb, 15 μM Hg
7	20 μM Pb, 10 μM Hg
8	15 μM Ni, 15 μM Hg

Building on the success with binary mixtures, we attempted the identification of four unequal *ternary* mixtures of these three metal cations. It is important to remind the reader that none of these challenge ternary mixtures had been present in the training set. For the following experiment, three solutions containing 20 μM of one metal and 5 μM of the other two metals were prepared. In addition to these, one solution containing 15 μM Ni^{II}, 10 μM Pb^{II}, and

5 μM Hg^{II} was also prepared, and all four unequal ternary mixtures were added to the array described for the training set ([XO] = 20 μM, [MTB] = 30 μM). After taking the same nine absorbance measurements that had been selected as most informative in the training set experiment, and using the training set's LDA eigenvectors to transform the obtained "ternary test set" data, Figure 2-19 shows the resulting projection of the ternary challenge set onto the calibration plot previously shown in Figure 2-16. As a first positive result, all ternary mixtures fall inside the triangle delineated by the lines of best fit on the training set scores plot. The array's ability to distinguish the most abundant metal in each 4:1:1 ternary mixture was particularly impressive indicating the achievement of simultaneous quali-quantitative discrimination. Moreover, the position of the 3:2:1 unequal ternary mixture cluster agrees with the relative position of the equimolar ternary mixture cluster contained in the training set. Based on these results, we validated our hypothesis that, thanks to the overall linearity of its response, this system can correctly identify mixtures of analytes even after having been "trained" on the pure components alone. In fact, very successful projections of unknown binary and ternary mixtures were obtained, leading to the identification of the composition *and* relative abundance of mixtures of three divalent metal cations.

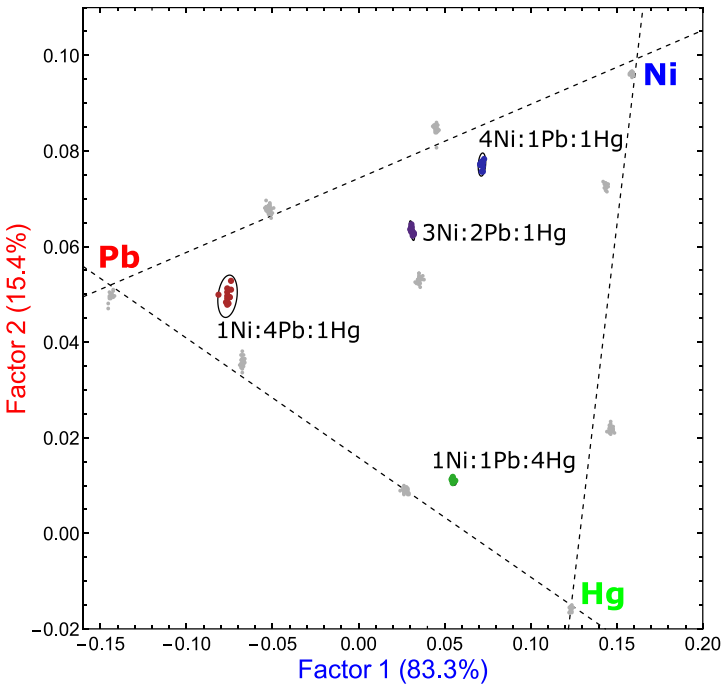

Figure 2-19 Two-dimensional plot of the LDA scores for the "ternary test set", projecting four unequal ternary metal ion mixtures onto the mixtures training set from Figure 2-16 ([XO] = 20 μM, [MTB] = 30 μM, and total $[M^{II}]$ = 30 μM in H_2O solution buffered to pH 7.4 with 50 mM HEPES).

2.7 Identification of quaternary mixtures and response to changing total $[M^{II}]$

The same array ([XO] = 20 μM and [MTB] = 30 μM) was pushed further by exposing it to a series of mixtures composed of *four* metal chlorides (total $[M^{II}]$ = 36 μM, $CuCl_2$, $PbCl_2$, $HgCl_2$, and $CdCl_2$). For this study, the calibration panel included an equimolar quaternary mixture, all twelve possible 2:1 binary mixtures, and the four pure metal samples. After LDA was conducted on the resultant data set, three factor scores were retained for each sample, generating the three-dimensional plot presented in Figure 2-20, in which the equimolar quaternary mixture was found towards the center of a tetrahedron, whose vertices correspond to the pure metal samples. Moreover, the most abundant metal in each 2:1 binary mixture was positioned nearest to the respective pure metal vertex, within the confines of the tetrahedron (i.e. between the pure metal and quaternary mixture clusters). These results further highlight that

carefully controlling the system's response to be linear translates to highly predictable behavior via pattern-based approaches, which can be used for the analytical identification of mixtures.

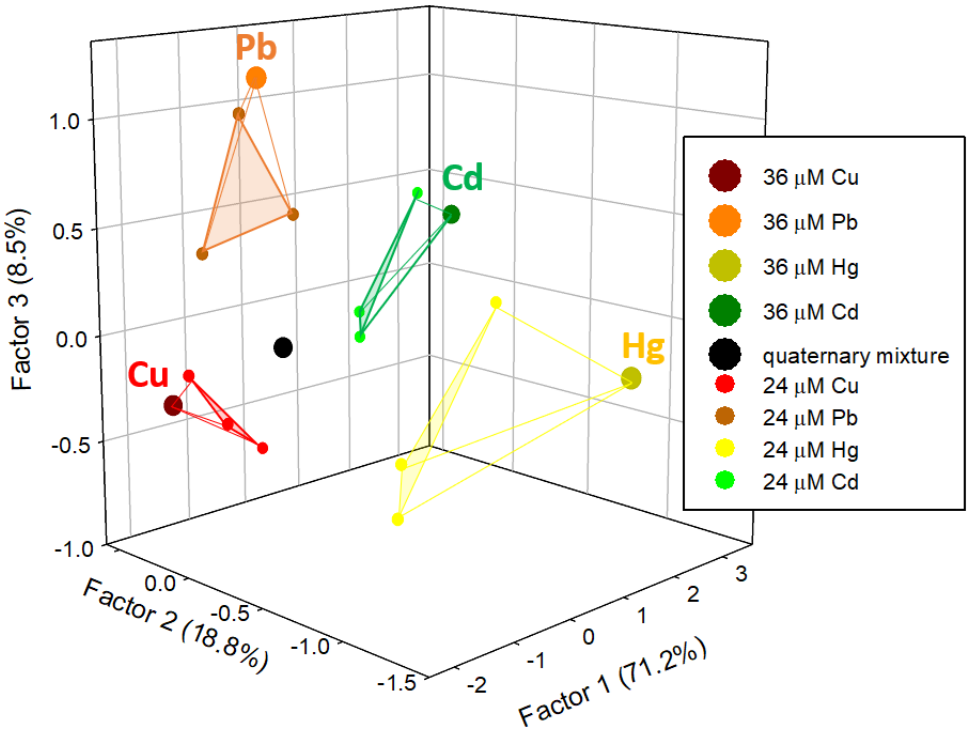

Figure 2-20 Three-dimensional plot of LDA scores for the differentiation of divalent metal ion mixtures. The plot was obtained using the eleven most important instrumental measurements and captures 98.5% of the information from the original data set. For clarity, 2:1 binary mixtures are not explicitly labeled and only replicate cluster centroids are shown (i.e. all replicate sample points have been averaged into a single point) ([XO] = 20 μM, [MTB] = 30 μM, total [M^{II}] = 36 μM in H_2O solution buffered to pH 7.4 with 50 mM HEPES).

Finally, the array's response to variations in total metal ion concentrations was examined. Up to this point, all metal ion mixtures have contained a total metal concentration of 30 μM. Using the same array, we explored the array's response, as a function of total metal ion concentration. We acquired a second training data set at a lower concentration of metal ions, namely 15 μM. As long as the underlying component responses scale linearly with total metal ion concentration, one should be able to determine the *nature, relative concentration, and absolute concentration* of all metal ions under study within a mixture, in a single experiment.

The procedure used to generate the 30 μM training set was repeated for metal ion mixtures where the total metal ion concentration was cut in half, to 15 μM. This 15 μM data set was first evaluated separately to ensure that linearity was still achieved at this working concentration. To that end, LDA analysis and subsequent variable reduction were carried out on the 15 μM data set, with the corresponding two-dimensional scores plot shown in Figure 2-21. Excellent results were obtained, analogous to the LDA scores plot obtained for the 30 μM system (Figure 2-16). These reassuring results confirmed that the array's response was still linear at this concentration and allowed for the combination of the two data sets for the determination of *total* metal ion concentration in mixtures.

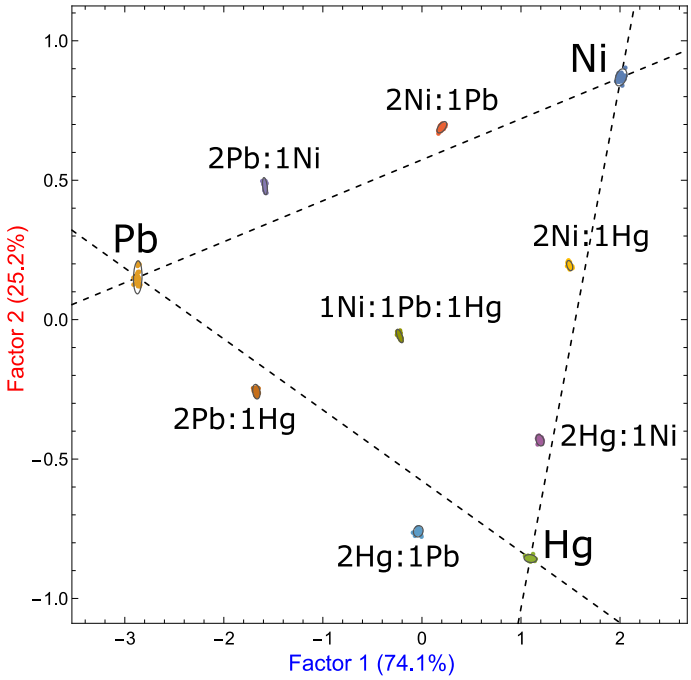

Figure 2-21 Two-dimensional LDA scores plot for the separation of metal ion mixtures at 15 μM. The plot was obtained using the ten most important instrumental measurements and captures 99.3% of the total information content from the original data set ([XO] = 20 μM, [MTB] = 30 μM, total [M^{II}] = 15 μM in H_2O solution buffered to pH 7.4 with 50 mM HEPES).

Upon combination of the 30 μM and 15 μM data sets, subsequent LDA analysis and variable reduction on this larger data set generated a 3D scores plot, shown in Figure 2-22,

displaying very clear separation of the two concentration data sets. Each separate data set retained their signature triangular shape, with the vertices of each triangle identified by the pure metal samples at 15 and 30 μM, and individual mixture clusters still positioned at appropriate intermediate positions along each edge of their representative triangle. Furthermore, the two triangular ensembles of points, corresponding to the two total metal ion concentration values, stacked up well in 3D factor space, highlighting the relationship between the two data sets.

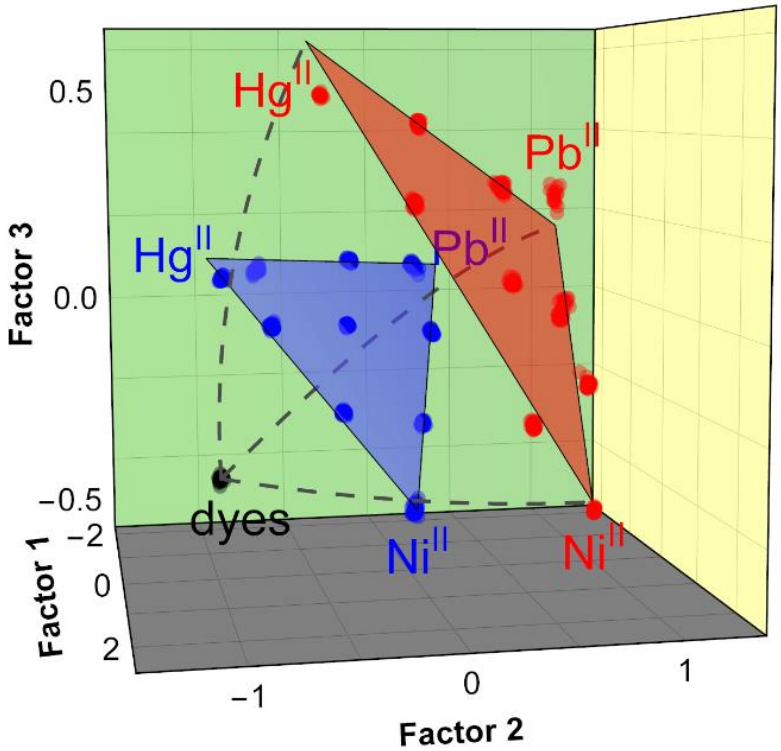

Figure 2-22 Three-dimensional scores plot from the LDA analysis for the combined 15 μM (blue) and 30 μM (red) data sets. Dotted lines connecting corresponding pure metal sample clusters extend to the no-metal cluster at $[M^{II}]$ = 0 μM (labelled "dyes" in the plot).

Connecting the corresponding "pure metal" vertices of the obtained triangles for each metal ion concentration data set also allowed us to extrapolate the array's behavior at infinite sample dilution (i.e. $[M^{II}]$ ~ 0 μM). Indeed, we found that this extrapolated behavior matched with the experimental array samples that contained no metal ions (i.e. $[M^{II}]$ = 0 μM, black dots in Figure 2-22), further confirming that the entire sensing array's response scales linearly with

concentration of these metal ion analytes and allows for successful quantitative prediction. This final analysis demonstrates the array's ability to determine the identity and concentration of a sample containing any mixture of Ni^{II}, Pb^{II}, and Hg^{II} over a range of concentrations between 0-30 μM. In fact, it should be possible to extend the effective concentration range as far as all components of the array's analytical system respond linearly.

2.8 Conclusions

In summary, a simple, cross-reactive sensing array was developed, consisting of two commercially available dyes that were selected to form strong coordination complexes with a variety of divalent metal cations in neutral buffered water. Using rapid UV-visible absorption measurements and multivariate data analysis, the array sensor was able to separate nine transition and main group metal ions (Ni^{II}, Co^{II}, Mn^{II}, Cd^{II}, Cu^{II}, Zn^{II}, Pb^{II}, Hg^{II}, and Fe^{II}), as well as binary and ternary mixtures of two sets of three of those metal ions (Ni^{II}, Pb^{II}, Hg^{II} and Co^{II}, Cu^{II}, Cd^{II}). Using these results as a training set (i.e. calibration plot), accurate identification of unknown mixture samples was accomplished, leading to the correct classification of the nature *and* concentration of the metal ions of interest. As intended the array displayed a consistent linear response with respect to changes in concentration of metal ions. The combination of these results expanded the reach of the system to variations in *total* metal ion concentration; in this case spanning 0-30 μM, with excellent discriminatory power for pure and mixture samples across the whole concentration range.

These achievements were made possible by the stringent design choices of the array components in the array's analytical stack, which enforced a linear behavior throughout. More specifically, these components included the array's chemical binding interaction responsible for its response at the molecular level (i.e. the formation of strong coordinative complexes), the

signal detection method (UV-vis spectroscopy), the operational conditions, and the multivariate data processing technique (linear discriminant analysis). Careful consideration was given to the chemical receptors selected and their working concentrations, to ensure a linear response throughout. For this case, dye selection was critical to obtain strong binding with metal ions, resulting in a linear response over a wide range of metal ion concentrations. UV-visible absorbance spectroscopy was chosen as the detection method due to its simplicity, linear response to concentration when conditions are chosen appropriately, and the ability to adapt its sensitivity over a wide range of concentrations using simple changes in optical path length. Finally, the generated data sets were analyzed using common multivariate systems with intrinsically linear behavior (e.g. LDA).

Presented in this chapter are general guidelines to a robust approach for direct quantitative multivariate sensing for any series of similar analytes, either in their pure form or in a mixture, and a proof-of-principle implementation of such guidelines, applied to a system of practical analytical importance (i.e. metal ion discrimination in H_2O media). We hope to see these design guidelines applied to other multivariate pattern-based sensors for the detection of other analytically relevant targets, sidestepping the need for chemical separation or pre-treatment prior to detection. Once response linearity is achieved, the multivariate sensor can be used to build effective and simple multidimensional “calibration curves” to accurately identify the makeup of unknown analyte mixtures. Separation and detection methods for analyte mixtures, normally envisioned as independent processes, can be integrated in a single system.

2.9 Experimental details

2.9.1 Materials

Xylenol orange (XO) and methylthymol blue (MTB) were purchased from Sigma-Aldrich and used as received. 2-[4-(2-hydroxyethyl)piperazin-1-yl]ethanesulfonic acid (HEPES) was purchased from ICI Scientific. All metal chloride salts were bought from Fluka. For consistency, all stock solutions for dyes and metal chloride salts were prepared fresh before each experiment. All experiments were carried out in a 50 mM HEPES aqueous solution buffered to pH 7.4, prepared by adding an appropriate amount of HEPES free acid to deionized (DI) water; the pH was then adjusted to 7.4 by adding 1.0 M NaOH as needed and monitoring with a combined glass electrode, then bringing up to volume. Stock solutions of xylenol orange (XO) and methylthymol blue (MTB) were prepared in this buffer, taking into consideration the manufacturer specified dye content (90% and 70% for XO and MTB, respectively). All metal chloride salt stock solutions (except $PbCl_2$) were prepared by adding an appropriate amount of salt to 10 mL of buffer. Lead(II) chloride solutions were prepared by dissolving a minimal amount of salt in DI water and diluting an appropriate aliquot of this solution in buffer. To avoid unwanted absorption of water over time, any hygroscopic salts ($ZnCl_2$, $CdCl_2$, $MgCl_2$, $BaCl_2$) were dried to constant weight in an oven set to 110 °C and stored in a desiccator before use.

2.9.2 Instrumentation

Benchtop UV-Vis measurements were performed on a Hewlett-Packard 8452A diode array UV-Vis spectrophotometer. The experimental sample temperature was thermostatted to 25 °C by an external circulating water bath. Multivariate data was acquired on a BioTek *Synergy II* multimode microwell plate reader, equipped with a monochromator to measure absorbance spectra. The sample compartment in this instrument was electrically thermostatted. Experiments

were laid out by hand using Eppendorf Research multichannel pipettors and disposable plastic tips into Greiner BioOne non-treated polystyrene microwell plates with clear flat bottoms in a 384-well configuration. Each well was filled with 100 μL of solution. Plates were read on a multimode plate reader immediately after preparation. Reading time was about 10-15 minutes for each plate. In this time span, no evaporation was observed so the plates did not need to be sealed.

2.9.3 Microwell plate setup: qualitative differentiation experiments

For qualitative experiments, one microwell plate was used. For a typical qualitative experiment, aliquots of each dye stock solution (XO and MTB) were laid out in the wells and 12 freshly prepared metal chloride stock solutions (NaCl, $MgCl_2$, $CoCl_2$, $CuCl_2$, $NiCl_2$, $FeCl_2$, $HgCl_2$, $CdCl_2$, $ZnCl_2$, $MnCl_2$, $BaCl_2$, $PbCl_2$) were added to give 15 replicates of metal-dye samples (see Figure 2-10 for a visual representation of this layout). The total volume in each well was 100 μL. Additionally, 8 replicates of buffer (as blanks), and 8 replicates of each dye solution (as a reference) were added to the plate. Dye concentrations in the wells were kept constant at 20 μM and 30 μM for XO and MTB, respectively. The metal chloride concentration in the wells was kept constant at 30 μM. Absorbance values were collected at the following wavelengths: 334, 342, 436, 442, 450, 482, 500, 540, 578, 590, 614 nm.

2.9.4 Microwell plate setup: quantitative experiments

For quantitative experiments, one plate was prepared for each dye by adding three separate concentrations of each dye to their respective plates (5 μM, 20 μM, 40 μM for XO, and 10 μM, 30 μM, 60 μM for MTB). Four metal chloride stock solutions were prepared ($PbCl_2$, $HgCl_2$, $CuCl_2$, and $CdCl_2$) and appropriate amounts of each stock were laid out to give six replicates of six different metal chloride concentrations (0 μM, 1 μM, 2.5 μM, 5 μM, 7.5 μM, and 10 μM). Additionally, reference wells containing plain dye solutions at each of the working

concentrations were added to the appropriate plate as reference standards; each plate also contained six buffer replicates for blanking. For quantitative experiments, absorbance values were collected at the following wavelengths: 334, 342, 436, 442, 450, 540, 578, 590, 614 nm.

2.9.5 Metal ion mixtures: training set experiments

For experiments on metal ion mixtures, the training set was obtained by preparing two identical plates to increase the number of sample replicates to the desired amount (32 replicates for each sample in the complete data set). Dyes were laid out on the plate so that their concentrations were 20 μM and 30 μM for XO and MTB, respectively. Three metal stock solutions were prepared fresh from $NiCl_2$, $HgCl_2$ and $PbCl_2$. Aliquots of these solutions were added to the plate to generate: three solutions of each pure metal ($[M^{II}]$ = 30 μM); six solutions encompassing all possible 2:1 binary mixtures (e.g. 20 μM $NiCl_2$ and 10 μM $HgCl_2$); and one equimolar ternary mixture including each metal chloride at a concentration of 10 μM. In addition, 16 reference samples for each dye and 32 buffer blanks were added to each plate. For experiments with metal ion mixtures, absorbance measurements were collected at the following wavelengths: 334, 342, 436, 442, 450, 500, 520, 540, 560, 578, 590, and 605 nm, for a total of 12 instrumental measurements per dye. The same experimental procedures and conditions were applied to the second set of three metal ions and their mixtures (Co^{II}, Cu^{II}, and Cd^{II}, total $[M^{II}]$ = 30 μM), using 16 replicates (instead of 32) for each sample. Absorbance measurements were collected at the following wavelengths for each dye: 334, 342, 436, 442, 450, 500, 520, 540, 560, 578, 590, and 604 nm.

2.9.6 Metal ion mixtures: projected test set experiments

For the test set containing eight unknown mixtures, 16 replicates for each sample were laid out on one plate. Dye concentrations were the same as those used on the training plate

([XO] = 20 μM, [MTB] = 30 μM). Metal chloride mixture solutions were prepared by adding appropriate aliquots of pure metal stock solutions to a 10 mL volumetric flask containing buffer and bringing up to volume. The eight solutions were then arbitrarily labelled "1-8" by an undergraduate collaborator Cara Pridmore and the newly labelled solutions were added to the plate. The non-equimolar ternary mixture samples were prepared similarly, from a solution made by adding appropriate aliquots of pure metal chloride stock solutions to a 10 mL volumetric flask and bringing up to volume with buffer. For the test set, eight replicates of each dye were added as reference standards and 16 replicates of buffer were added as blanks. Absorbance values were collected at the same wavelengths used for the training set (334, 342, 436, 442, 450, 500, 520, 540, 560, 578, 590, and 605 nm).

2.9.7 Multivariate data analysis

In order to evaluate the discriminatory power of the sensing array, linear discriminant analysis (LDA) and principal component analysis (PCA) were used to interpret the obtained data sets. LDA and PCA are a statistical treatment commonly used for the interpretation of multidimensional data sets. All multivariate analyses were performed in the *Mathematica* software (release 11.3) published by Wolfram Research Inc, using code developed in-house.

As a first step towards data analysis, principal component analysis (PCA) was applied to each set of metal chloride/dye replicate points. Points well outside a 95% multivariate confidence interval (CI), represented below by a dotted grey ellipsoid, were considered outliers and removed from the raw data set. As an example, see Figure 2-23 for the Na^+ analyte: in this case, replicate 14 in the Na^+ data set lies well outside the 95% CI (dotted grey ellipsoid) and was removed from the data set before further analysis.

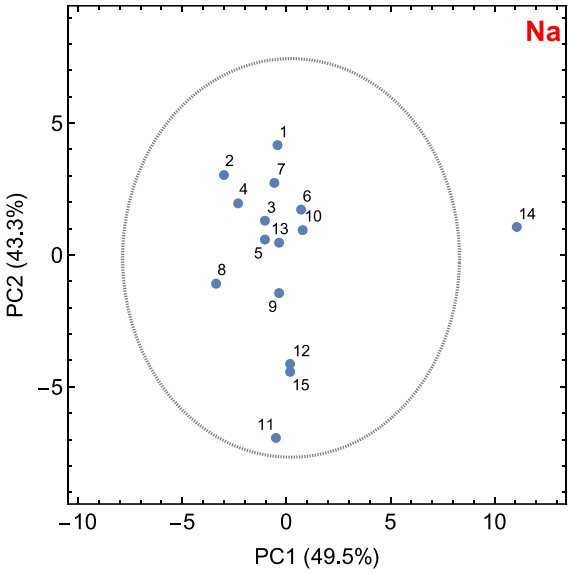

Figure 2-23 PCA scores plot of the NaCl replicate set, with 95% confidence ellipsoid shown as a dotted grey line. Point 14 is clearly outside the confidence interval, and it was removed from the data set before further analysis.

After all outlier data points were removed, LDA analysis was run for the first time. Dimensionality reduction was achieved by retaining the first two or three most information-rich factors and plotting the corresponding factor scores for each sample. Based on the factor loadings from these results, any instrumental measurements that were found to contribute little to the overall differentiation were removed. Displayed in Figure 2-11 and Figure 2-12 are the two-dimensional LDA scores plots for the complete and reduced data sets, respectively.

CHAPTER 3

CONJUGATED POLYMERS AS TRACE METAL CATION SENSORS IN SEAWATER

3.1 Introduction

As was highlighted in the previous chapter, metal cation detection is of great importance due to their negative impacts on human and environmental health, particularly in aqueous solution.[103,114] Recently, there have been many advances for picomolar metal cation sensing using an assortment of analytical methods.[115-120] In particular, fluorescent chemosensory systems have gained increasing interest thanks to their high sensitivity and relative ease of operation.[121] Despite being highly sensitive at sub-nanomolar concentrations, these systems are typically selective for one or two metal cations. As we have shown in the previous chapter, selectivity can alternatively be achieved for a wider scope of analytes by using pattern recognition techniques, in analogy to the principle of operation of many biological sensory systems.[26,28-29,122] In this chapter, an ultra-sensitive sensing array is reported, made up of three poly(fluorene) conjugated polyelectrolyte receptors, capable of detecting *nine* divalent heavy metal cations down to 500 pM in pure water, well below the "Maximum Contaminant Levels" (MCLs) mandated by the United States Environmental Protection Agency (EPA) for toxic metal ions in ground water and drinking water.[123] In addition, the array was also successful in natural seawater samples, collected from the Deepwater Horizon (DWH) region in the Gulf of Mexico. In this complex sensing medium, nine divalent heavy metal ions were detected down to $[M^{II}]$ = 100 nM, which is comparable or lower than the toxic metal ion concentrations (low ppb) set by the EPA for aquatic

life,[124] and many orders of magnitude below the trace elemental distributions found in the DWH samples, in particular.[125] Impressively, this sensing array, made of strongly binding conjugated polyelectrolyte receptors, performed very well in this high-salinity medium, an otherwise challenging analytical matrix.

An early example of poly(fluorene) copolymers used for sensing purposes was provided by Wang and co-workers in 2005, which used a cationic poly(fluorene)-*alt*-(1,4-phenylene) polymer to detect conformational changes in single-stranded DNA.[126] In recent years, the improved selectivity from array sensing techniques has been paired with the high sensitivity from extensively conjugated fluorophores.[127-133] For metal cation detection, Bunz et al. reported a series of very promising systems made up of poly(phenylene-ethynylene) polyelectrolytes with carboxylate groups attached to the phenylene repeat units.[134-136] Later, Tan et al. used four poly(phenylene-ethynylene) polymers with a variety of metal binding groups to differentiate eight transition metal cations, with a limit of detection of 100 nM.[137] However, rarely have conjugated polyelectrolytes with different electronic properties been used in a single array. Therefore, a highly effective poly(fluorene) co-polymer-based metal cation array sensor is introduced in this chapter, relying mostly on electronic variations in each polymers' backbone. All polymers were designed with strong metal binding groups per fluorene repeat unit, such that less importance would be placed on variations in the metal binding affinity of these pendant groups.

Poly(fluorene) co-polymers were synthesized and characterized by our collaborator in the Azoulay research group in the School of Polymer Science and Engineering at the University of Southern Mississippi (see Scheme 3-1). Each fluorene monomer was linked to alternating conjugated spacer groups, either a *p*-phenylene or ethynylene unit. To each of these conjugated

polymer scaffolds, two high affinity metal binding groups (iminodiacetate ligands) were covalently attached to the sp^3 carbon of the fluorene monomer, generating two novel conjugated polyelectrolytes, to probe the differing electronic properties of the polymers. For added variability, a variation in the attached metal binding groups was also examined, adding iminodipropionate ligands to the poly(fluorene)-*alt*-(*p*-phenylene) co-polymer, instead of the iminodiacetate ones. Taken together, these purpose-built supramolecular receptors proved to be highly effective metal ion sensors in aqueous environments, including highly unprecedented and more analytically complex seawater samples collected from the Gulf of Mexico.

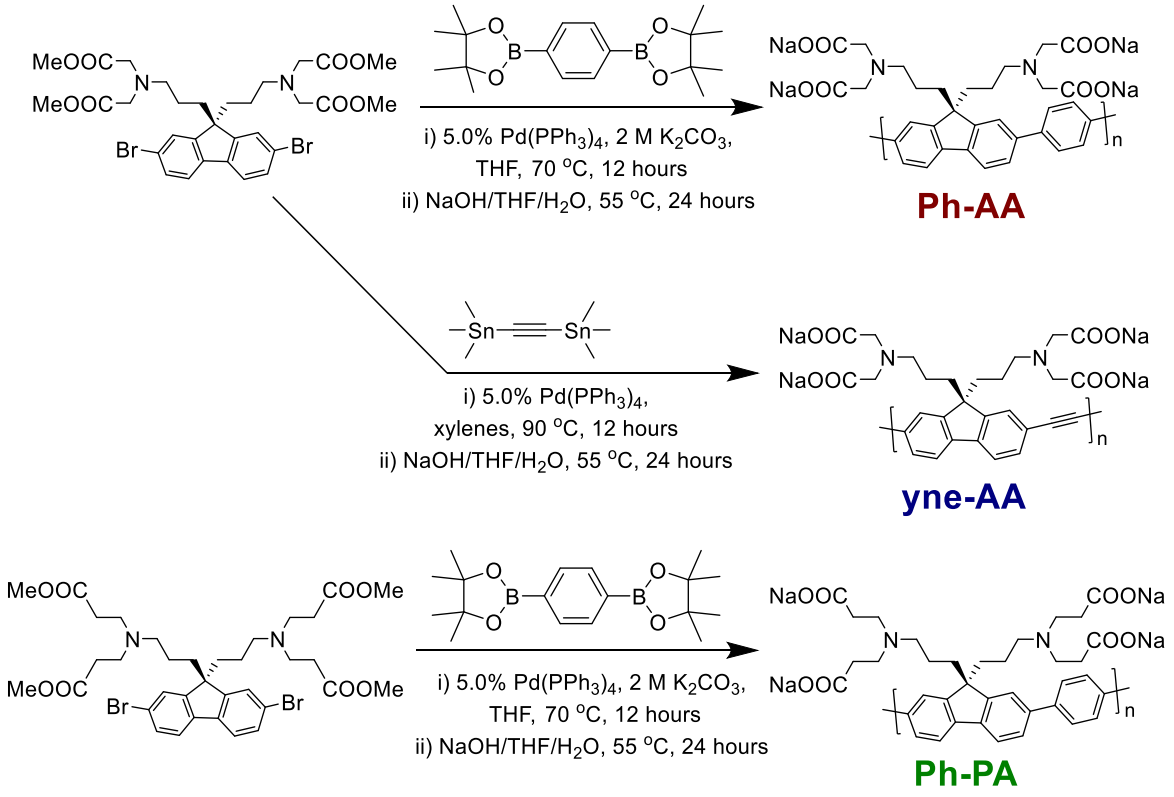

Scheme 3-1 Chemical structures and general synthetic scheme for the three conjugated polymers (**Ph-AA**, **yne-AA**, and **Ph-PA**) used in a metal ion sensing array.

3.2 Polymer synthesis and sensor design

Each polymer contained a common fluorene fluorophore, coupled to a conjugated spacer group capable of altering the electronic features of the conjugated polymer. Thus, each fluorene was covalently linked to either a 1,4-phenylene (*p*-phenylene) or ethynylene group to provide a monomer that, once polymerized, made up the conjugated backbone of the polymers. Each fluorene monomer was modified with two iminodiacetate metal binding appendages attached to the sp^3 carbon of the fluorene repeat units. These groups were inspired by ethylenediaminetetraacetic acid (EDTA), commonly used as a strong metal chelating agent for a variety of metal ions (see Scheme 3-2).[138-139]

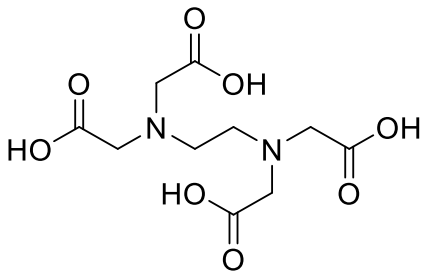

Scheme 3-2 Chemical structure of ethylenediaminetetraacetic acid (EDTA) in its neutral form.

To incorporate diversity in metal binding group as well, the poly(fluorene)-*alt*-*p*-phenylene polymer was equipped with two iminodipropionate functional groups, a conjugated polyelectrolyte previously reported for pH and sugar sensing.[140] As shown in Scheme 3-1, the following conjugated polyelectrolytes were synthesized: poly[2,7-(9,9-di((aminodiacetate)propyl)-fluorene)-*alt*-1,4-phenylene] (with phenylene conjugated spacer and acetate metal binding group, referred to as **Ph-AA**), poly[2,7-(9,9-di((aminodiacetate)propyl)-fluorene)-*alt*-1,4,-ethynylene] (with ethynylene conjugated spacer and acetate metal binding units, **yne-AA**), and

poly[2,7-(9,9-di((aminodipropionate)propyl)-fluorene)-*alt*-1,4,-phenylene] (with phenylene conjugated spacer and propionate metal binding units, **Ph-PA**).

With these materials in hand, our attention turned to identifying optimal conditions for their use as sensors in water. As mentioned previously, many conjugated polyelectrolytes are well-known to form aggregates in aqueous solution, leading to solvent-dependent changes in emission properties.[141-142] Thus, many strategies to break up these assemblies in solution have been attempted, including the use of co-solvent systems or surfactant additives.[143-145] For instance, 1,4-dioxane in ratios of 30-80% by volume was shown to be very effective in breaking up poly(fluorene) aggregates.[146] Therefore, to avoid self-aggregation, polymer stock solutions were prepared as saturated solutions in 50:50 water:1,4-dioxane solution, buffered to pH 7.4 in 25 mM 2-[4-(2-hydroxyethyl)piperazin-1-yl]ethanesulfonic acid (HEPES), followed by centrifugation and filtration. Each saturated polymer stock solution was then diluted appropriately, to give a constant fluorescence emission signal. The similar emission would also allow each polymer to have an equal opportunity for differential response, since the magnitude of the fluorescence responses from each of the polymers in the array would be comparable to start with. Under these conditions, titrations were carried out to study the binding of metal ions to each polymer. Representative spectra for each polymer obtained upon titration with Cu^{II} are shown in Figure 3-1.

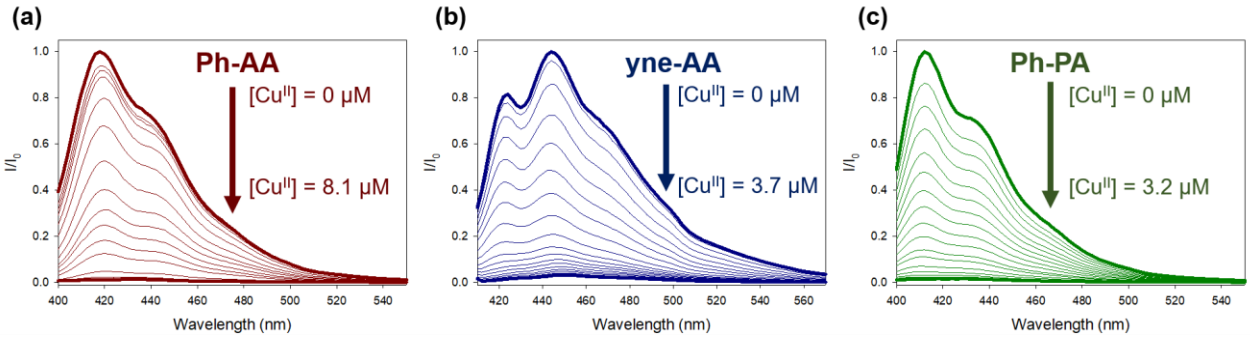

Figure 3-1 Representative steady-state fluorescence titration spectra for (a) **Ph-AA** ($\lambda_{exc.}$ = 380 nm) upon the addition of $CuCl_2$ (0-8.1 μM), (b) **yne-AA** ($\lambda_{exc.}$ = 400 nm) upon the addition of $CuCl_2$ (0-3.7 μM), and (c) **Ph-PA** ($\lambda_{exc.}$ = 380 nm) upon the addition of $CuCl_2$ (0-3.2 μM). All measurements were conducted in 50:50 water:1,4-dioxane buffered to pH 7.4 with 25 mM HEPES.

3.3 Metal cation binding and experimental considerations

In addition to Cu^{II}, benchtop fluorescence titrations were conducted for each polymer with various other divalent metal cations, all as chloride salts for consistency and to avoid unwanted counterion effects, as mentioned in the previous chapter. All metal binding titration spectra are presented in Figure 3-2, Figure 3-3, and Figure 3-4. The binding isotherms for each polymer with seven heavy metal ions are also presented in Figure 3-5, displaying clear differential emission responses at micromolar concentrations of metal ions. Furthermore, comparing the binding isotherms obtained with different metals interacting with the same polymer highlighted the strength of that metal's quenching ability upon binding. For instance, Ni^{II} seemingly quenches the polymer with the *p*-phenylene ("Ph") spacer more effectively than the one with the ethynylene ("yne") spacer; Cu^{II} quenched all three polymers with similar efficacy, and Mn^{II} quenched the emission of the **yne-AA** polymer better than both polymers with the *p*-phenylene ("Ph") spacer. The combined emission profiles for Cu^{II}, Mn^{II}, and Ni^{II} titrated into each polymer is displayed in Figure 3-6.

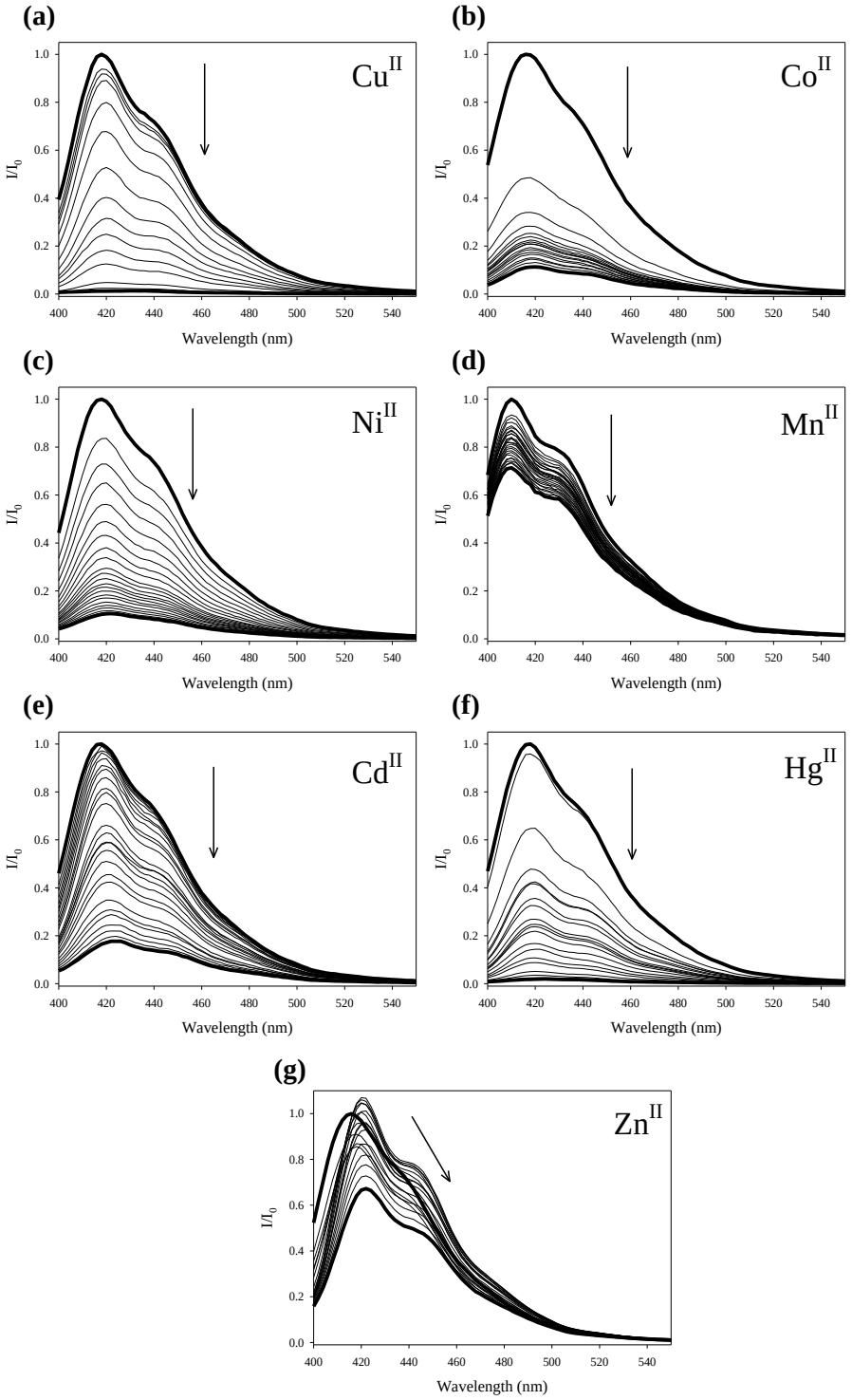

Figure 3-2 Fluorescence spectra for the **Ph-AA** polymer ($\lambda_{exc.}$ = 380 nm), upon the addition of (a) $CuCl_2$, (b) $CoCl_2$, (c) $NiCl_2$, (d) $MnCl_2$, (e) $CdCl_2$, (f) $HgCl_2$, and (g) $ZnCl_2$. All measurements were conducted in 50:50 water:1,4-dioxane buffered to pH 7.4 with 25 mM HEPES.

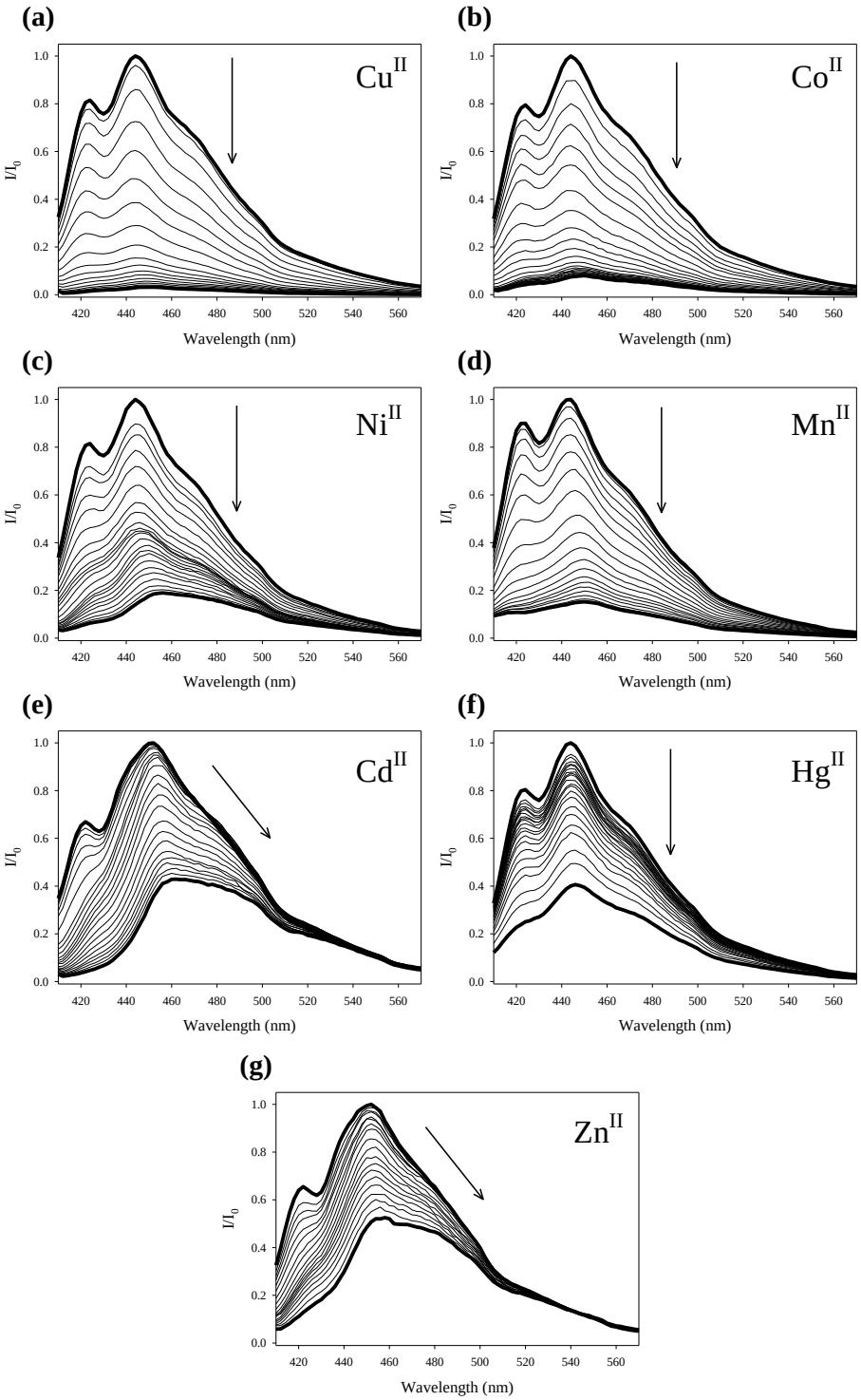

Figure 3-3 Fluorescence spectra for the **yne-AA** polymer ($\lambda_{exc.}$ = 400 nm), upon the addition of (a) $CuCl_2$, (b) $CoCl_2$, (c) $NiCl_2$, (d) $MnCl_2$, (e) $CdCl_2$, (f) $HgCl_2$, and (g) $ZnCl_2$. All measurements were conducted in 50:50 water:1,4-dioxane buffered to pH 7.4 with 25 mM HEPES.

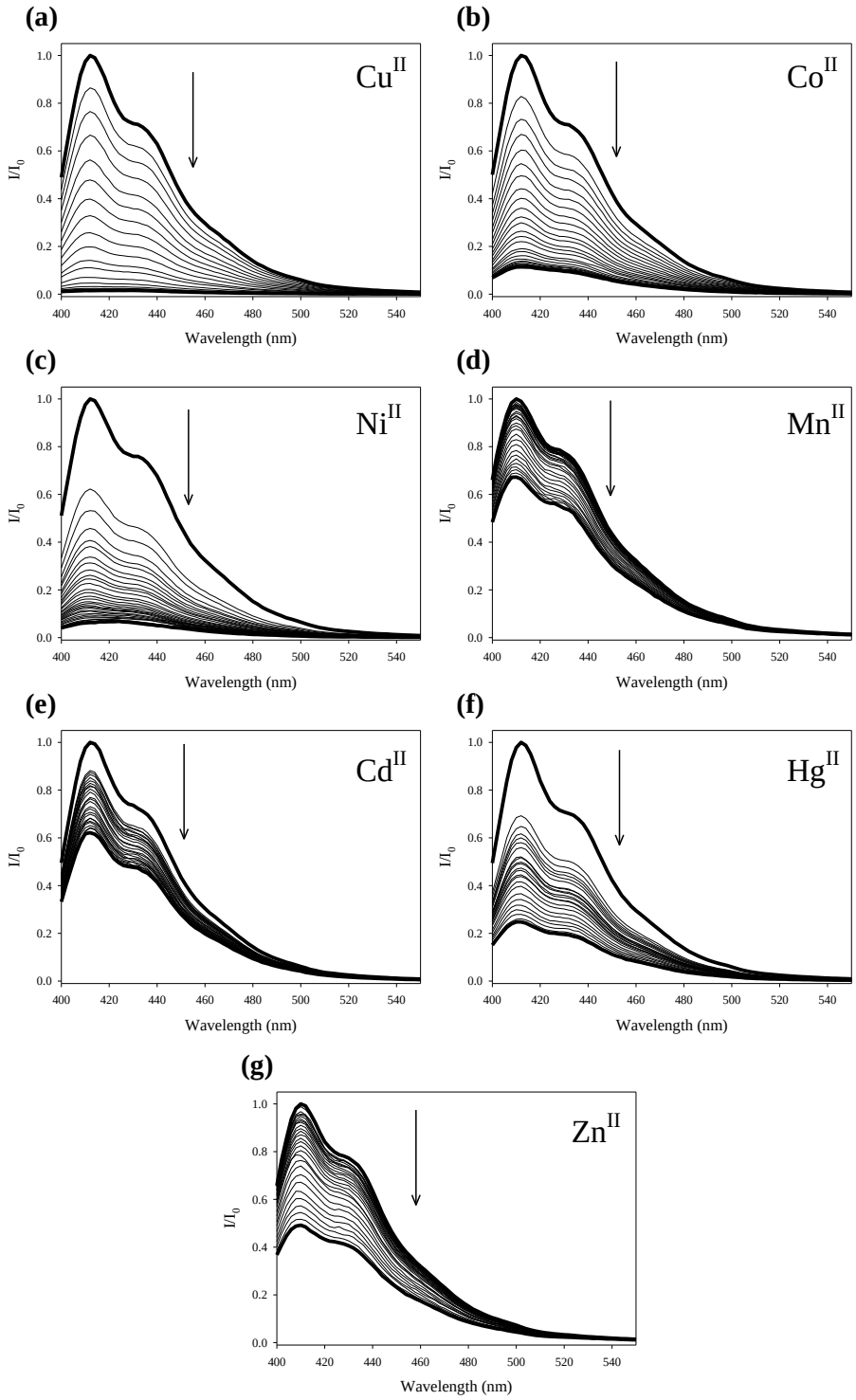

Figure 3-4 Fluorescence spectra for the **Ph-PA** polymer ($\lambda_{exc.}$ = 380 nm), upon the addition of (a) $CuCl_2$, (b) $CoCl_2$, (c) $NiCl_2$, (d) $MnCl_2$, (e) $CdCl_2$, (f) $HgCl_2$, and (g) $ZnCl_2$. All measurements were conducted in 50:50 water:1,4-dioxane buffered to pH 7.4 with 25 mM HEPES.

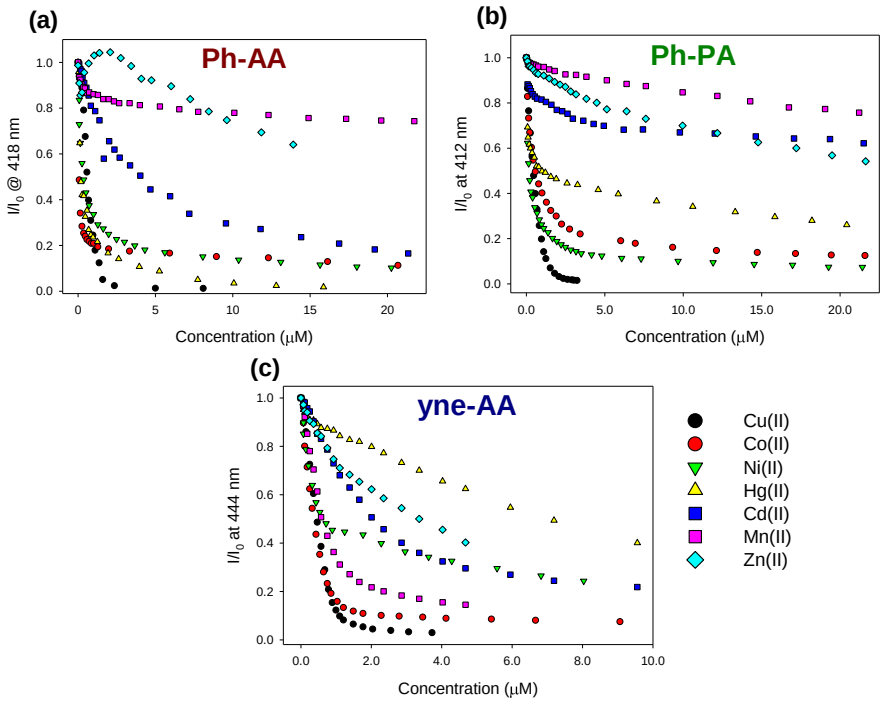

Figure 3-5 Fluorescence binding profiles for (a) **Ph-AA** ($\lambda_{exc.}$ = 380 nm, $\lambda_{em.}$ = 418 nm), (b) **Ph-PA** ($\lambda_{exc.}$ = 380 nm, $\lambda_{em.}$ = 412 nm), and (c) **yne-AA** ($\lambda_{exc.}$ = 400 nm, $\lambda_{em.}$ = 444 nm), upon the addition of $CuCl_2$, $CoCl_2$, $NiCl_2$, $HgCl_2$, $CdCl_2$, $MnCl_2$, and $ZnCl_2$. All measurements were conducted in a 50:50 water:1,4-dioxane solution buffered to pH 7.4 with 25 mM HEPES.

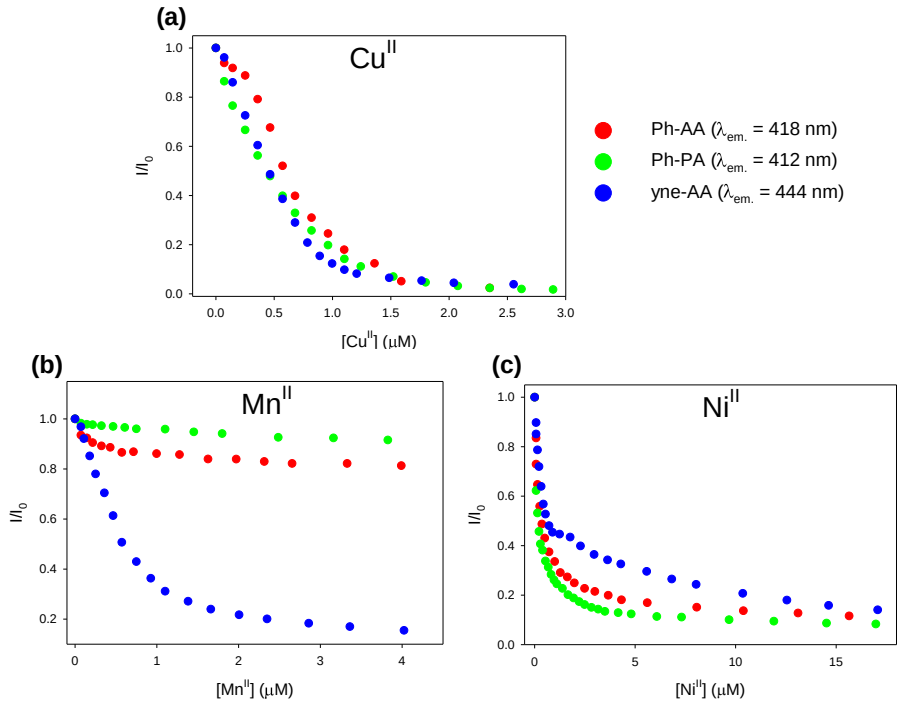

Figure 3-6 Normalized fluorescence titration profiles of the three conjugated polymers, upon the addition of aliquots of (a) $CuCl_2$, (b) $MnCl_2$, and (c) $NiCl_2$ ($\lambda_{exc.}$ = 380 nm for **Ph-AA** and **Ph-PA**

and $\lambda_{exc.}$ = 400 nm for **yne-AA**). Fluorescence profiles are shown at the wavelength of maximum emission for each polymer.

Other forms of quenching, including dynamic (i.e. collisional) quenching and aggregation-induced quenching are possible contributors to the observed amplified quenching. The amplified quenching response typical of conjugated polymers can be elucidated via Stern-Volmer (S-V) plots, in which the changes in the slope of I_0/I as a function of quencher concentration ([Q]) is plotted (i.e. changes Stern-Volmer constant (K_{SV}) (see eq. 1).

$$\frac{I_0}{I} = 1 + K_{SV}[Q] \quad \text{(eq. 1)}$$

In fact, a non-linear S-V plot (i.e. changes in the K_{SV}) is indicative of multiple quenching processes occurring throughout the titration. Additionally, the typical amplified quenching response is associated with an increase in K_{SV}.[71,76] As an illustrative example, Figure 3-7 displays four stacked S-V plots for each polymer with Cu^{II}, Mn^{II}, Co^{II}, and Ni^{II}. Some metal ions display high non-linearity throughout the titration, indicating that more complex quenching mechanisms may be present, whereas weaker quenchers showed more linear responses, indicating the dynamic collisional mechanism as the main driver of the observed quenching. Initially, some metal ions display a steep increase in slope in the Stern-Volmer diagram, which eventually decreases starkly at higher [M^{II}]. This suggests that the first few equivalents of M^{II} binding to specific sites on the polymer lead to strong quenching amplification (high and increasing slope in a Stern-Volmer diagram). Further quenching past the saturation of available metal binding is mostly collisional (corresponding to the linear portion in the Stern-Volmer plot, with lower, constant slope). Similarly, metal ions with weaker affinity for these polymers also display primarily dynamic collisional quenching, with linear Stern-Volmer plots with lower and

constant slope (K_{SV}). It should also be noted that d^{10} metals, namely Zn^{II} and Cd^{II} ions, generated a systematic red-shift in the emission spectrum of the **yne-AA** polymer, suggesting that metal ion induced aggregation quenching is a significant quenching pathway as well, as reported previously for other closed-shell metal ions interacting with conjugated polyelectrolytes (see Figure 3-3).[76] This effect is also evident for Ni^{II} into **yne-AA**, albeit to a lesser extent, and also Zn^{II} into the **Ph-AA** polymer (see Figure 3-2).

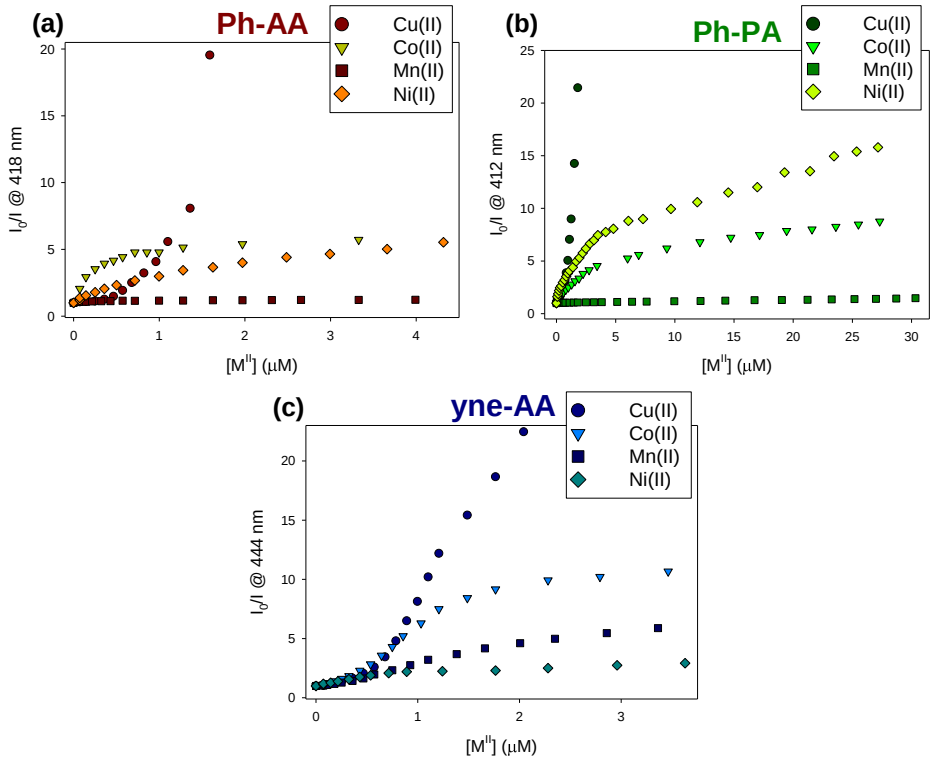

Figure 3-7 Stern-Volmer (S-V) plots for (a) **Ph-AA** ($\lambda_{exc.}$ = 380 nm, $\lambda_{em.}$ = 418 nm), (b) **Ph-PA** ($\lambda_{exc.}$ = 380 nm, $\lambda_{em.}$ = 412 nm), and (c) **yne-AA** ($\lambda_{exc.}$ = 400 nm, $\lambda_{em.}$ = 444 nm), upon the addition of aliquots of Cu^{II}, Co^{II}, Ni^{II}, and Mn^{II}. All measurements were conducted in a 50:50 water:1,4-dioxane solution buffered to pH 7.4 with 25 mM HEPES.

Taken together, these differential quenching responses would allow one to distinguish each of these metal ions at relatively high (e.g. micromolar) concentrations. Direct discrimination at lower, analytically more relevant concentrations (e.g. sub-nanomolar) may still be possible thanks to the high sensitivity of conjugated polymers, but it would become

increasingly difficult to achieve high selectivity for multiple metal ions at smaller concentrations. However, this wealth of information from the highly sensitive signal responses from these conjugated polyelectrolytes can be harnessed using pattern recognition techniques.

3.4 Chemical fingerprinting of metal cations at picomolar concentrations

These three fluorene-based conjugated polyelectrolytes were used to build an array for metal ion detection at sub-nanomolar concentrations against a panel of nine divalent metal ions (Cu^{II}, Co^{II}, Ni^{II}, Mn^{II}, Fe^{II}, Zn^{II}, Cd^{II}, Hg^{II}, and Pb^{II}) at a $[M^{II}]$ = 500 pM, a concentration that is well below the detection limits required by the EPA for toxic metal ions in environmental water samples.[123] Samples were laid out on 384-well microplates. Each metal-polymer combination was added in replicates of 16 to test repeatability, along with polymer reference standards and solvent blanks (see Figure 3-8a). As mentioned previously, polymer stock solutions were prepared as saturated solutions that were centrifuged and filtered in 50:50 water:1,4-dioxane solution buffered to pH 7.4 in 25 mM HEPES. Appropriate aliquots of the saturated polymer solutions were diluted to obtain working solutions with similar fluorescence emission intensities. Divalent metal chloride stock solutions were freshly prepared in DI water from the solid salts. Once again, metal chloride salts were used throughout to prevent anion biasing effects and for chloride's good water solubility and relative inertness at neutral pH.[111] An appropriate aliquot (between 0-25 µL) of each metal chloride solution was then added to volumetric flasks containing the polymers and filled to volume with 50:50 buffered water:1,4-dioxane to give [metal] = 500 pM. Care was taken to ensure that each aliquot of metal ion solution in DI water added would be exactly 1% of the total volume, thereby preventing significant deviation from the 50:50 water:dioxane co-solvent system and also possible differential quenching from unequal solvent composition, instead of the metal ions themselves.

For rapid data acquisition, fluorescence measurements were collected on an automated plate reader using a series of band-pass filters ($\lambda_{exc.}/\lambda_{em.}$): 330/450 nm, 330/460 nm, 330/485 nm, 330/516 nm, 380/450 nm, 380/460 nm, 380/485 nm, 380/516 nm, corresponding to the maximum excitation and emission wavelengths of the polymers. In total, eight fluorescence measurements were taken for each polymer, giving a total of 24 instrumental variables. Absorbance measurements were not taken, since the polymer concentrations in the working solution were low enough that their absorbance was well below the detection limit of the instrument. The raw instrumental data from the plate reader using the 380/450 nm filter combination is given in Figure 3-8b for the replicates of all nine metal ions with the three polymers, indicating strong differential response patterns from the polymers.

The resultant data set was subjected to linear discriminant analysis (LDA) and principal component analysis (PCA). The two-dimensional LDA and PCA scores plots of the raw data set displayed very good, albeit incomplete separation of all nine divalent metal cations. However, analysis of the corresponding loadings plot showed that many instrumental measurements were redundant, contributing nothing but noise to the overall performance of the array. The two-dimensional plots of LDA and PCA scores for the raw 500 pM data set are presented in Figure 3-9. The corresponding LDA loadings plot is presented in Figure 3-10.

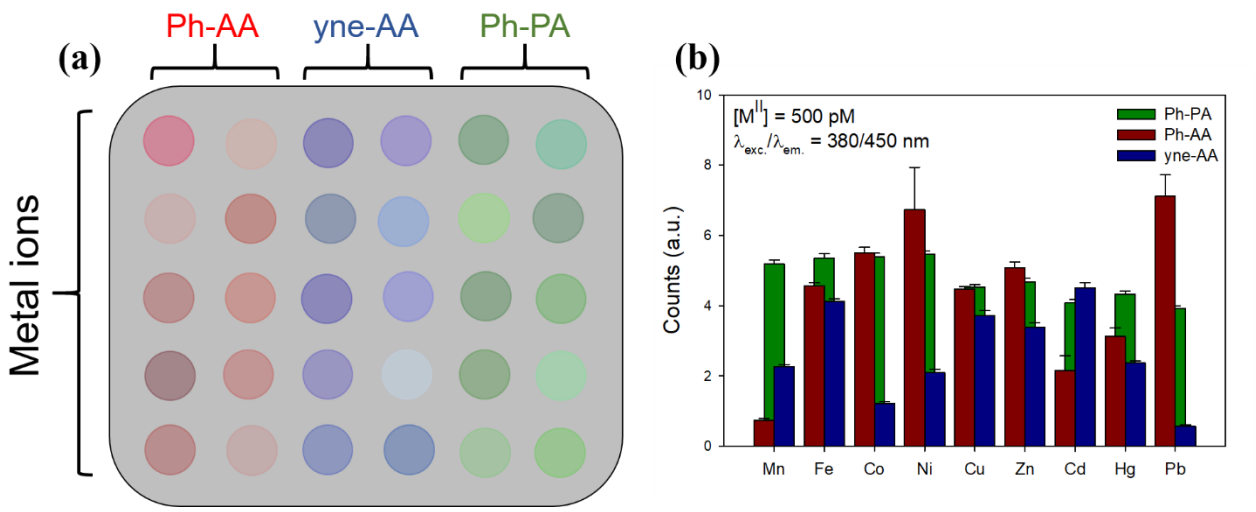

Figure 3-8 (a) A general schematic of a multi-well microplate used for a typical multivariate experiment. Red circles: wells containing **Ph-AA**:metal samples; blue circles: wells containing **yne-AA**:metal samples; green circles: wells containing **Ph-PA**:metal samples. (b) Raw experimental fluorescence data for the **Ph-AA**, **yne-AA**, and **Ph-PA** polymers in the presence of metal cations ($[M^{II}]$ = 500 pM), using the following band-pass filter combination: $\lambda_{exc.}$ = 380 ± 10 nm, $\lambda_{em.}$ = 450 ± 25 nm. The reported values are the averages of 12-16 replicate samples after removal of outlier data points.

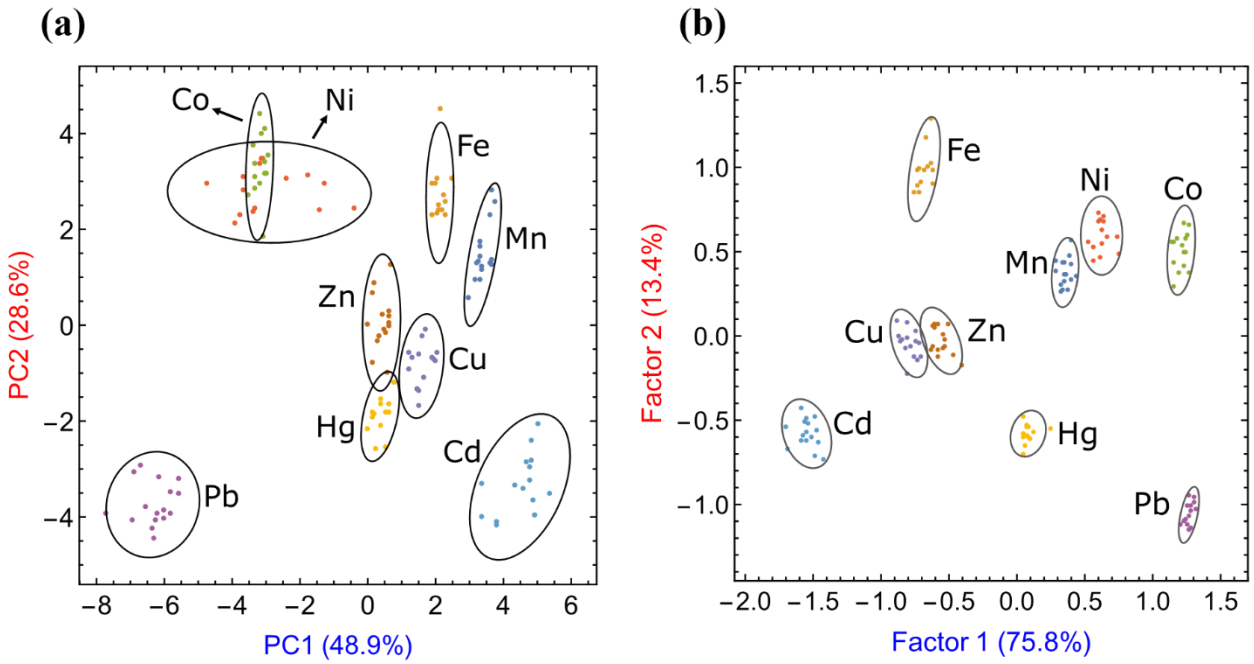

Figure 3-9 (a) Two-dimensional plot of the PCA scores for the attempted differentiation of nine divalent metal ions using all instrumental measurements in the raw data set ([metal] = 500 pM). (b) Two-dimensional plot of LDA scores for the differentiation of nine divalent metal ions using

the same data set. The experiment was conducted in 50:50 water:1,4-dioxane buffered to pH 7.4 with 25 mM HEPES. All confidence ellipsoids are drawn to 95% confidence level.

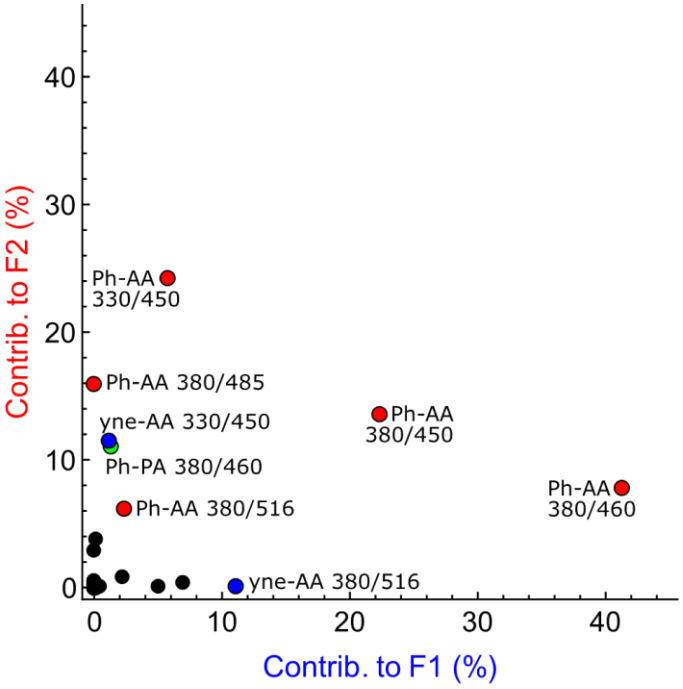

Figure 3-10 Two-dimensional plot of LDA loadings from the scores plot in Figure 3-9b, displaying the high amount of superfluous instrumental measurements that could be removed (black circles). Red circles: contributions from fluorescence measurements of **Ph-AA**; blue circles: **yne-AA**; green circles: **Ph-PA**.

To improve the array's discriminatory power, variable reduction was carried out, removing all instrumental variables whose overall weighted contribution to all LDA factors was less than 1%. This is graphically represented in Figure 3-11. This procedure removed 14 superfluous variables that were contributing only noise to the data set, thereby worsening the differentiation; this left only the ten most important measurements; namely the fluorescence emission at 330/450, 380/450, 380/460, 380/485, and 380/516 nm for **Ph-AA**; and fluorescence emission at 330/450, 380/450, 380/460, 380/485, and 380/516 nm for the **yne-AA** polymer. The resultant data set was subjected to multivariate analysis (LDA and PCA) and dimensionality reduction by retaining only the first two factors from the LDA analysis. The resulting

two-dimensional plots of LDA scores and loadings are shown in Figure 3-12. Indeed, the removal of 14 non-contributing measurements greatly improved the LDA scores plot: all metal ions were now clearly differentiated. Furthermore, the two-dimensional PCA scores plot, shown in Figure 3-13, also organized metal ion data points into much more distinct and well-separated clusters. As mentioned previously, PCA is an unsupervised pattern recognition technique that relies only on the variances contained in the data set for analyte classification. Therefore, it is often run to ensure that the results from the LDA analysis are representative of underlying chemical differences within the data. In fact, a strong improvement in the PCA results is a more direct indication of better overall quality of the reduced measurement data set, even if the final results of the PCA analysis are generally not as effective for analytical discrimination as the LDA results.

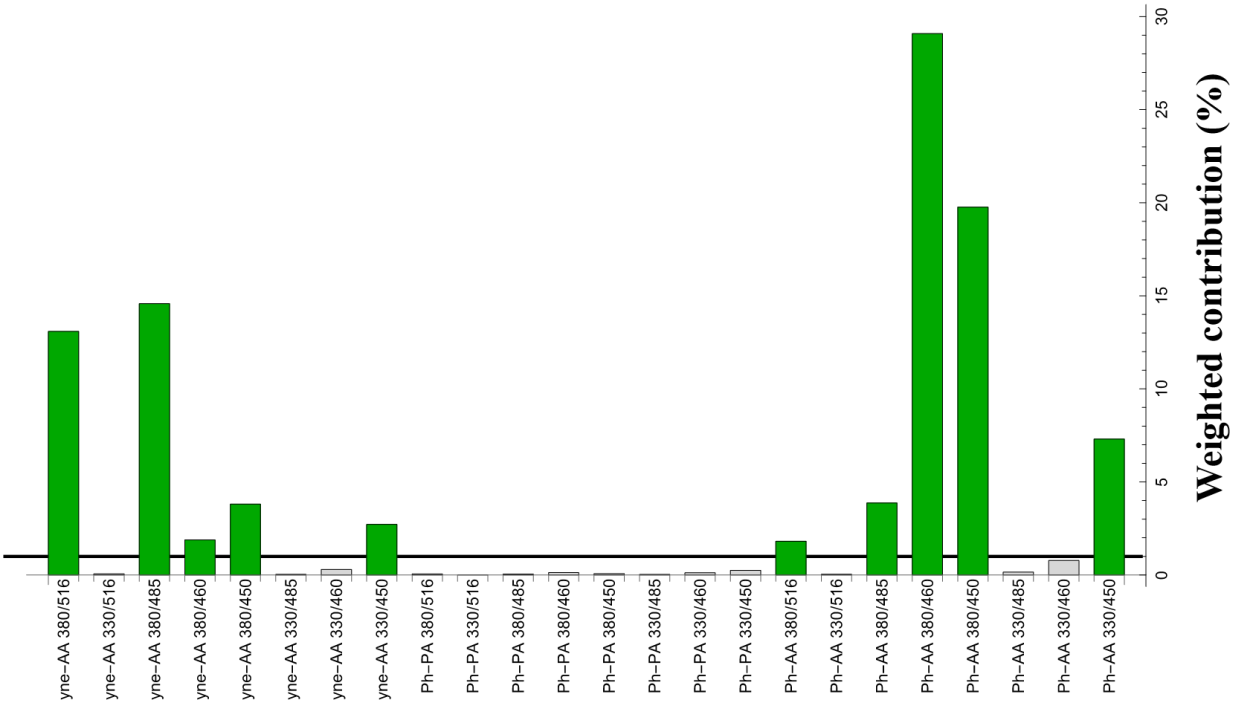

Figure 3-11 A graphical representation of the process by which we removed 14 instrumental measurements from the raw 500 pM data set. The black line at 1% designates our chosen threshold. Contributions from measurements whose importance was higher than the 1% threshold are shown as green bars and were retained for further analysis. Contributions from measurements that were less than 1%, shown as light grey bars, were removed from the data set.

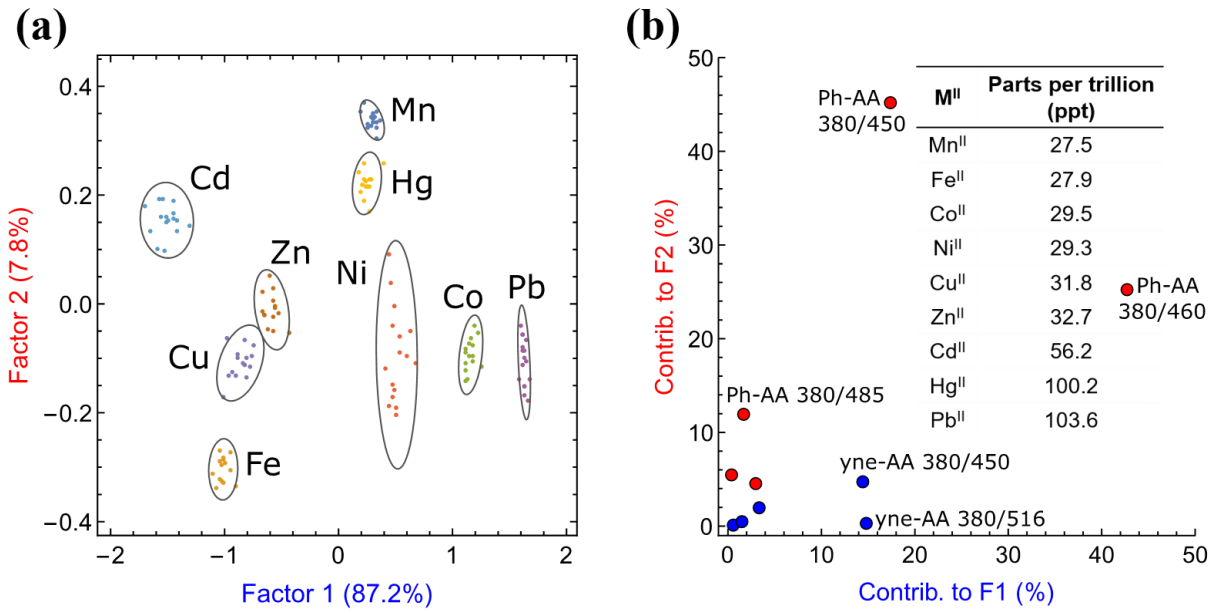

Figure 3-12 (a) Two-dimensional plot of the LDA scores for the successful differentiation of nine divalent metal cations at 500 pM using only the **Ph-AA** and **yne-AA** polymers. The plot was generated using *only the ten most important instrumental measurements* and captures 95.0% of the total information in the raw data set. All confidence ellipsoids are drawn to 95% confidence level. (b) Corresponding LDA loadings plot for the differentiation of divalent metal ions at 500 pM, indicating the relative contributions of each instrumental measurement to the first two LDA factors. Red circles: contributions from fluorescence measurements of **Ph-AA**; blue circles: **yne-AA**. Inset: table of parts per trillion (ppt) values for each target metal cation at 500 pM.

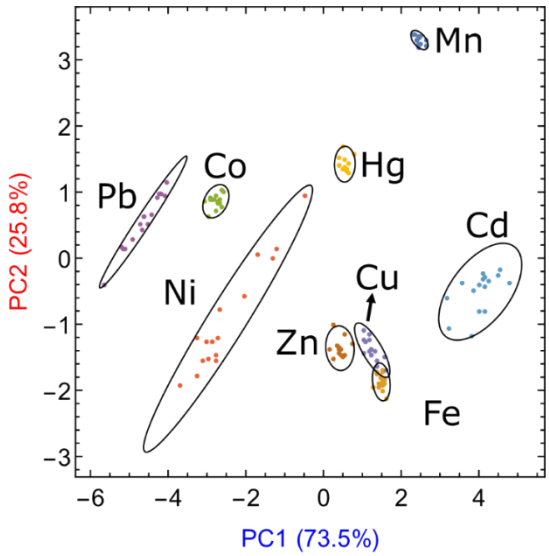

Figure 3-13 Two-dimensional plot of PCA scores for the differentiation of nine divalent metal cations at 500 pM, using the ten most important instrumental measurements. All confidence ellipsoids are drawn to 95% confidence level.

The factor loadings indicate that the **Ph-PA** polymer, carrying the iminodipropionate metal binding arms, contributed far less to the differentiation than the other two. In fact, variable reduction led to the removal of all fluorescence measurements from **Ph-PA**; only measurements from polymers **Ph-AA** and **yne-AA** (containing the EDTA-like iminodiacetate ligands) were retained. Moreover, polymers whose backbone contains either the *p*-phenylene ("Ph") or the ethynyl ("yne") spacers contribute in nearly equal proportions towards differentiation, an ideal situation in pattern recognition and an encouraging confirmation of the original hypothesis that differences in the conjugated backbone would provide a stronger contribution to differentiation at picomolar concentrations than differences in metal binding sites.

3.5 Detection in seawater samples

To test the array sensor in a more challenging analytical matrix, the same array was exposed to the same panel of dissolved metal ions, but this time in an environmental seawater sample collected during a scientific cruise on the Point Sur research vessel by our collaborator

Prof. Alan Shiller of the University of Southern Mississippi-Gulfport. The seawater samples we used came from the region in the Gulf of Mexico where the Deepwater Horizon platform used to be located. Sensing in this medium is often problematic due to the higher salinity (ca. 0.6 M NaCl) and level of chemical interferents, which often attenuate fluorescence properties by providing a variety of new pathways for non-radiative decay. However, the very strong fluorescence emission of these conjugated polyelectrolytes and the low impact of collisional (i.e. "random") quenching we found in our previous experiments at high [M^{II}] indicate that the latter would be of minimal concern even in a high salinity environment. Additionally, our previous experience with fluorene-based conjugated polyelectrolytes showed minimal quenching when used in high salinity media for azo dye detection.[78] The polymers' emission does not appear to be adversely affected by constituents of seawater (e.g. Na^+, Mg^{2+}, Cl^-).

The seawater samples were provided by Professor Alan Shiller's lab from the Department of Ocean Science and Engineering at the University of Southern Mississippi. A map of the Gulf Coast, pinpointing the geographic coordinates of the collected sample is shown in Figure 3-14a. All polymer solutions were prepared as described previously. Given the intrinsically higher complexity of seawater as a sensing medium, the targeted concentration of metal ions was 500 nM. Metal chloride stock solutions were prepared in DI water; small aliquots of these stock solutions were diluted in the seawater provided. All metal chloride solutions were diluted using seawater from a single homogeneous sample (labelled "Deepwater Horizon 3" by Dr. Shiller's lab, referred as "DWH3") to prevent unwanted effects stemming from compositional differences in environmental samples collected at different locations. The metal ions solutions were then added to the polymers and filled to volume, using the co-solvent system and conditions previously stated, before being deposited on a 384-well microplate. The same eight fluorescence

measurements were collected as mentioned previously. Figure 3-14b, once again, displays the raw fluorescence data ($\lambda_{exc.}/\lambda_{em.}$ = 380/450 nm) for the three conjugated polyelectrolytes in the presence of all nine metal ions in "DWH3" seawater.

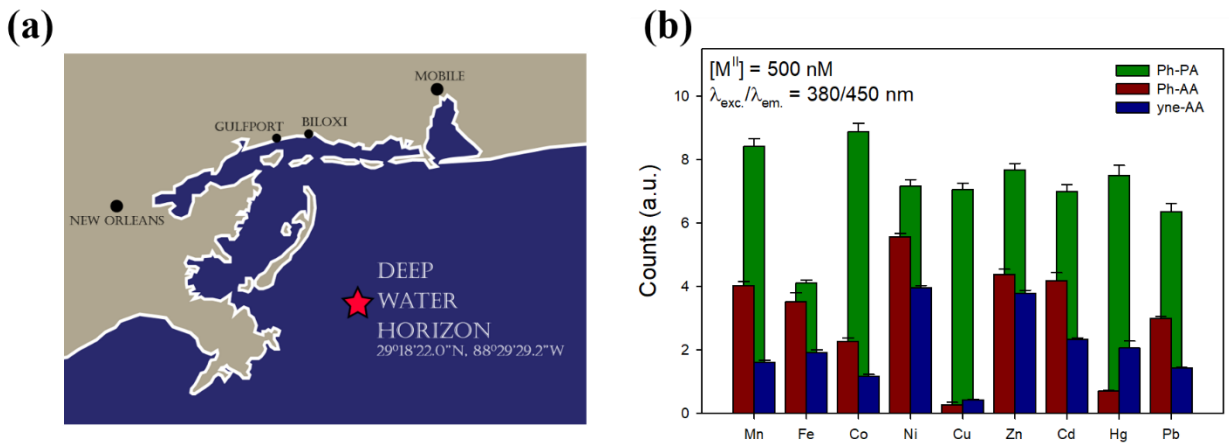

Figure 3-14 (a) A map of the Deepwater Horizon location in the Gulf of Mexico, identifying the coordinates of sample collection (red star, 29°18'22.0"N, 88°29'29.2"W) used as the matrix for metal ion sensing. (b) Raw experimental fluorescence data for the **Ph-AA**, **yne-AA**, and **Ph-PA** polymers in the presence of metal cations ($[M^{II}]$ = 500 nM) in Deepwater Horizon ("DWH3") seawater media, using the following band-pass filter combination: $\lambda_{exc.}$ = 380 ± 10 nm, $\lambda_{em.}$ = 450 ± 25 nm. The reported values are the averages of 12-16 replicate samples after removal of outlier data points.

After data collection, variable reduction was carried out as described previously; the resultant data set was subjected to LDA and dimensionality reduction to generate the two-dimensional scores and loadings plots shown in Figure 3-15. Despite the much more demanding conditions, the array displayed excellent discrimination of all nine divalent metal cations. Once again, the factor loadings revealed that the **Ph-PA** polymer did not contribute as much to the discrimination compared to the **Ph-AA** and **yne-AA** polymers. Interestingly, this time the **yne-AA** polymer was found to be the most important contributor under these harsher conditions. As mentioned before, it was gratifying to see that the PCA scores plot also provided complete separation of all nine metal ions in the "DWH3" seawater sample, indicating excellent

reproducibility and strong discriminatory power from the sensing array, given the much more complex and demanding conditions (see Figure 3-16).

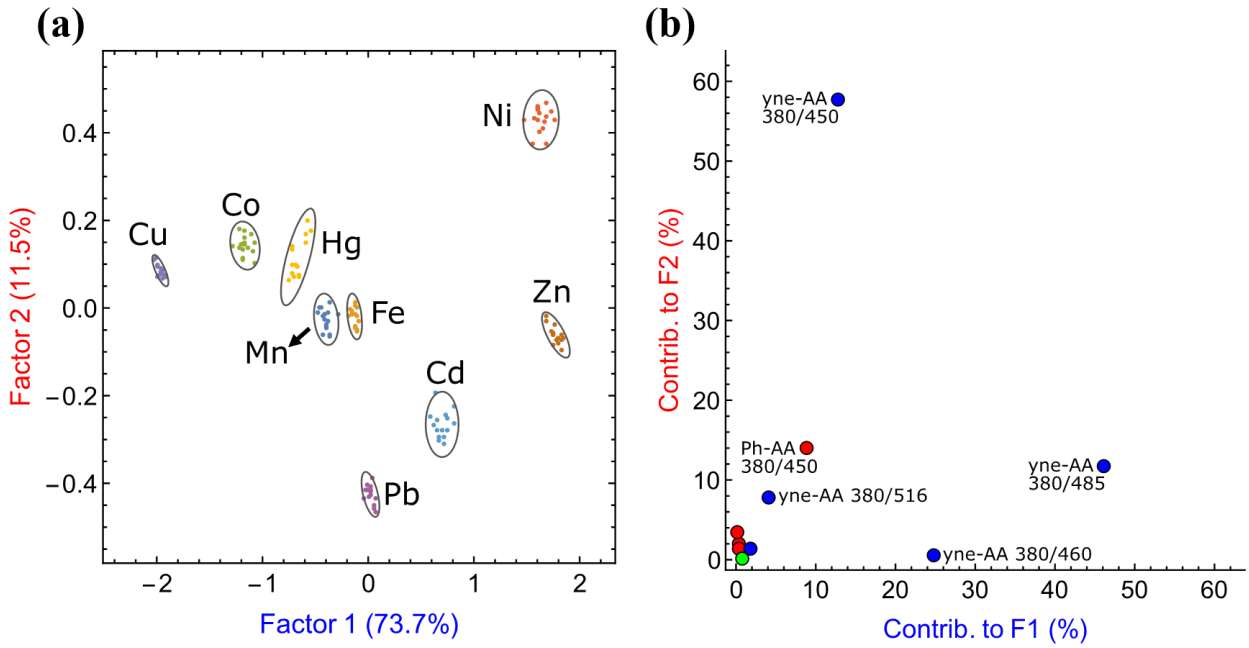

Figure 3-15 (a) Two-dimensional plot of LDA scores for the differentiation of nine divalent metal cations dissolved in a seawater sample matrix using conjugated polymers **Ph-AA**, **yne-AA**, and **Ph-PA** ([M^{II}] = 500 nM). The plot was generated using *only the ten most important instrumental measurements* and captures 85.2% of the total information in the raw data set. All confidence ellipsoids are drawn to 95% confidence level. (b) Corresponding LDA loadings plot, indicating the relative contributions of each instrumental measurement to the first two factors. Red circles: contributions from fluorescence measurements of **Ph-AA**; blue circles: **yne-AA**; green circles: **Ph-PA**.

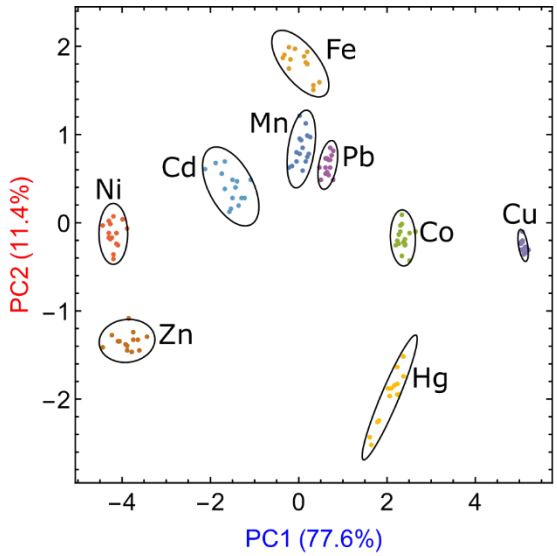

Figure 3-16 Two-dimensional plot of PCA scores for the differentiation of nine divalent metal cations at 500 nM in natural seawater, using the ten most important instrumental measurements. All confidence ellipsoids are drawn to 95% confidence level.

To ensure reproducibility of the sensing array and to explore the limit of differentiation of the system in seawater, further analysis was conducted in standard artificial seawater media (see Table 3-1 for its composition).[147]

Table 3-1 Constituents for a 1 kg artificial seawater solution prepared and used as a metal ion sensing medium.

Components	**g/kg sol'n**
NaCl	24.9
$MgCl_2$	5.21
Na_2SO_4	4.16
$CaCl_2$	1.18
KCl	0.724
$NaHCO_3$	0.150
KBr	0.104
$B(OH)_3$	0.027
$SrCl_2$	0.015
NaF	0.003

Initially, it was important to confirm that the array performed comparably in both seawater matrices at $[M^{II}]$ = 500 nM by reproducing the LDA scores plot that was obtained in

natural seawater. All conditions and array preparations were kept identical to those previously described and the same eight fluorescence measurements were taken for all three polymers, namely fluorescence emission at 330/450, 330/460, 330/485, 330/516, 380/450, 380/460, 380/485, and 380/516 nm. After multivariate analysis, variable and dimensionality reduction, a two-dimensional scores plot was obtained that separates all nine metal ions and is practically indistinguishable from the 500 nM experiment performed in the "DWH3" natural seawater matrix. Furthermore, the greatest contributors to differentiation in this experiment are similar to the natural seawater experiment (**yne-AA** > **Ph-AA** > **Ph-PA**). The LDA plots of factor scores and loadings at [M^{II}] = 500 nM in artificial seawater are presented in Figure 3-17.

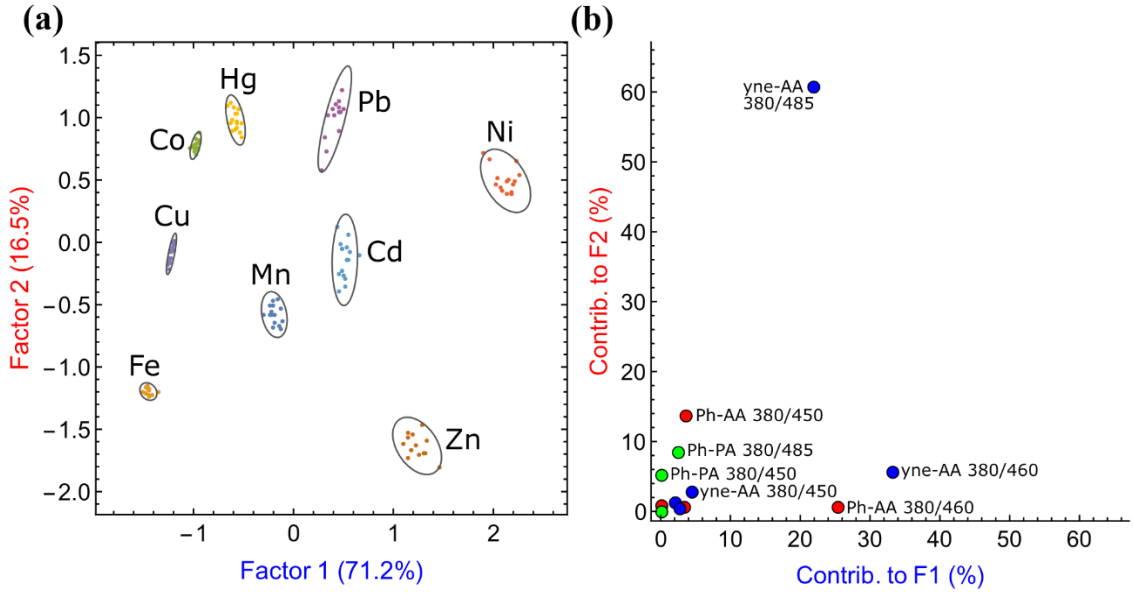

Figure 3-17 (a) Two-dimensional plot of LDA scores for the differentiation of nine divalent metal cations at 500 nM in artificial seawater media, using *the twelve most important instrumental measurements*. All confidence ellipsoids are drawn to 95% confidence level (b) Corresponding LDA loadings plot, indicating the relative contributions of each instrumental measurement to the first two factors. Red circles: contributions from fluorescence measurements of **Ph-AA**; blue circles: **yne-AA**; green circles: **Ph-PA**.

Given these results, the same experiment was repeated at a lower concentration ([M^{II}] = 100 nM) in the artificial seawater medium. Once again, multivariate analysis and

dimensionality reduction produced two-dimensional LDA and PCA scores plots that displayed good discrimination overall, albeit with slight overlap between the Cd^{II} and Pb^{II} clusters in both plots, even after removal of redundant instrumental measurements (variable reduction). Therefore, despite all other metal ion clusters being well-separated, the limit of differentiation was conservatively reported to be 100 nM for the current system. The two-dimensional plots of LDA scores and loadings at $[M^{II}]$ = 100 nM are given in Figure 3-18; the corresponding PCA scores plot is displayed in Figure 3-19. Under these more challenging conditions and lower metal ion concentration, the factor loadings indicate more uniform contributions from the three polymers; in fact, here the **Ph-PA** polymer displayed its most significant contribution so far, albeit still minor. Overall, the **yne-AA** and **Ph-AA** polymers were still the most important contributors to differentiation.

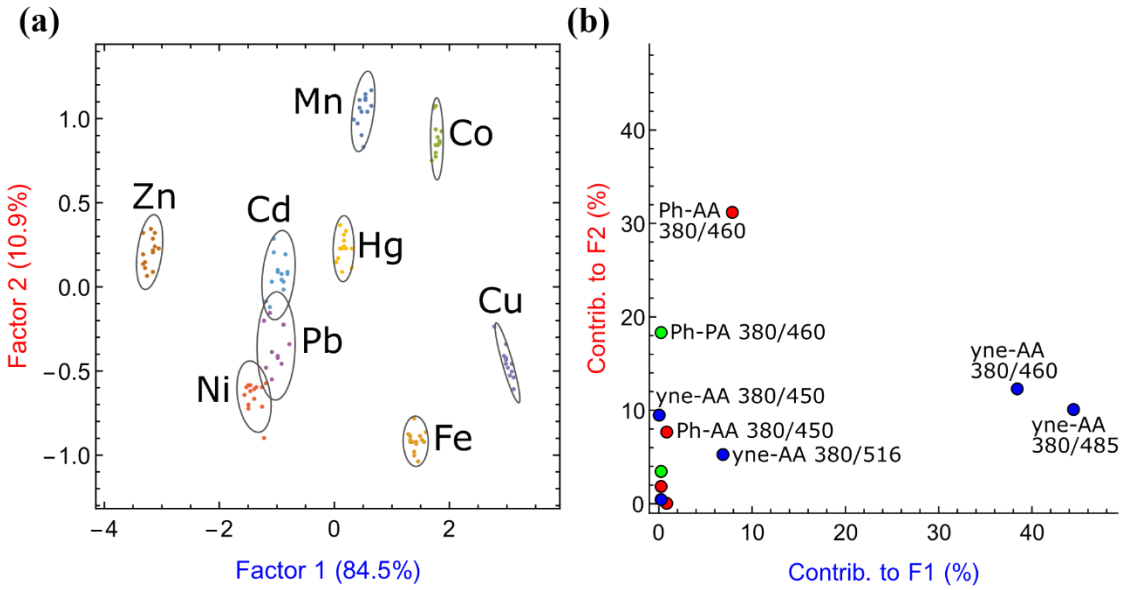

Figure 3-18 (a) Two-dimensional plot of LDA scores for the differentiation of nine divalent metal cations dissolved in an artificial seawater matrix using conjugated polymers **Ph-AA**, **yne-AA**, and **Ph-PA** ($[M^{II}]$ = 100 nM). The plot uses *only eleven of the most important instrumental measurements* and captures 95.4% of the total information in the raw data set. All confidence ellipsoids are drawn to 95% confidence level. (b) Corresponding LDA loadings plot, indicating the relative contributions of each instrumental measurement to the first two factors. Red circles: contributions from fluorescence measurements of **Ph-AA**; blue circles: **yne-AA**; green circles: **Ph-PA**.

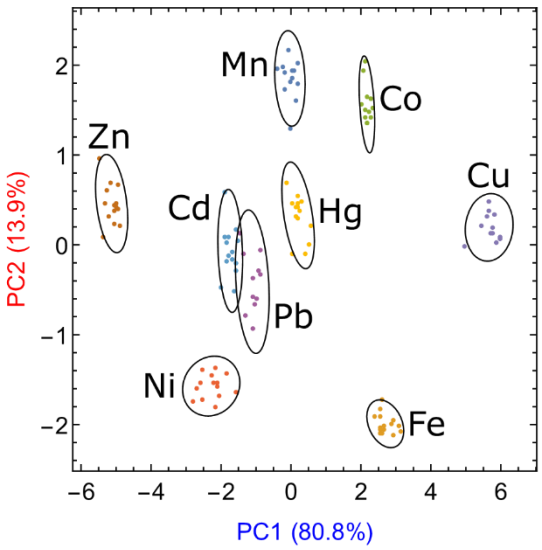

Figure 3-19 Two-dimensional plot of PCA scores for the differentiation of nine divalent metal cations at 100 nM in artificial seawater, using the 11 most important instrumental measurements. All confidence ellipsoids are drawn to 95% confidence level.

The minor overlap between the Cd^{II} and Pb^{II} replicate clusters at 100 nM was easily overcome by retaining more information (i.e. a third LDA factor) and generating a three-dimensional plot. The LDA analysis reports that the third factor contributed 4.0% of the overall information content in the $[M^{II}]$ = 100 nM data set. This relatively small addition, however, was sufficient to provide complete separation of the Pb^{II} and Cd^{II} clusters; indeed, these two metal clusters are clearly separated along the "Factor 3" axis. The three-dimensional LDA scores plot is presented in Figure 3-20.

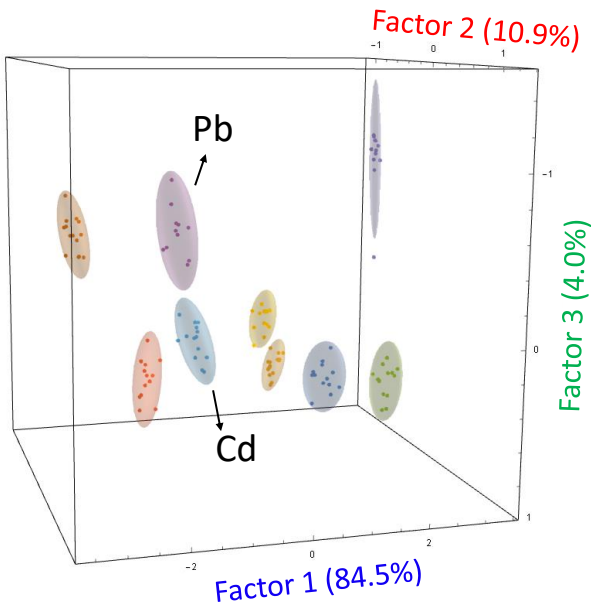

Figure 3-20 Three-dimensional plot of LDA scores for the differentiation of nine divalent metal cations at $[M^{II}]$ = 100 nM in artificial seawater media. The plot was generated using the same data set from the 2D plot shown in Figure 3-18a, using the eleven most important instrumental measurements, capturing 99.4% of the total information in the first three factors. Only the Pb^{II} and Cd^{II} clusters are labeled for clarity. All confidence ellipsoids are drawn to 95% confidence level.

The array presented here was highly successful with the detection of nine heavy metal cations at 100 nM in a single experiment; an achievement that would be very considerable even in neutral or buffered water, made more notable by the challenging high salinity, high interference analytical medium. It is noteworthy to mention again that concentrations of 100 nM (low ppb) in seawater are on par with the values reported by the EPA as safe for aquatic life.[124] The good reproducibility bodes well for future optimization work with these polymers in artificial seawater, which can be translated seamlessly to natural environmental samples. Future work will also attempt to apply this conjugated polyelectrolyte-based sensor to on-site detection of toxic metal ion pollutants in the Gulf of Mexico.

3.6 Conclusions

A series of water soluble conjugated polyelectrolytes biased towards heavy metal binding was designed and combined into a sensing array for ultra-sensitive detection (parts per trillion) of metal cations in aqueous media, including successful detection in challenging seawater media. Three strongly emissive fluorene-based conjugated polymers were used, each having their own distinct combination of conjugated spacer group and metal binding units; the former adjusted the electronic properties of the fluorene co-polymer, while the latter altered the affinity of the polymers towards metal ions. Optimal conditions were identified for high sensitivity metal identification, namely a 50:50 water:1,4-dioxane solution used to break up self-aggregation of the amphiphilic conjugated polyelectrolytes, buffered to pH 7.4 using 25 mM HEPES. A critical step to ensure repeatable operation was the use of standardized-emission solutions, prepared from easily attainable saturated solutions and then diluted to provide a reproducible and consistent fluorescence emission signal.

Preliminary metal ion titration studies indicated that these polyelectrolytes displayed differential quenching with a variety of divalent heavy metal ions, suggesting the manifestation of many quenching mechanisms, including amplified quenching, aggregation-induced quenching, metal ion-induced quenching, and collisional quenching. Thanks to their high sensitivity and their promiscuous yet differential quenching preferences, the polymers' complex response to metal ions could be interpreted by multivariate data analysis techniques, providing an exceedingly selective sensor at $[M^{II}]$ = 500 pM in low-salinity water. Analysis of the factor loadings revealed that differing electronic properties caused by changes in the conjugated spacer group (phenylene vs. ethynylene) were the most important contributor to the discriminatory power of this sensing array.

Given the strong and sensitive emission properties from these polymer receptors, and their relative insensitivity to potential quenchers in solution, these polymers were successfully put to use as receptors in highly interfering natural seawater media. Despite the high interferent level, the polymers' fluorescence emission intensity and differential quenching were only minimally affected, retaining their capabilities to discriminate the same divalent metal ions down to 100 nM in this complex analytical matrix. The easily tunable nature of these polyelectrolytes' electronic properties proved to be the most effective for differentiation, a characteristic that has rarely been applied to array sensing of metal ions. Moreover, the strong metal binding, EDTA-like, groups offered two novel conjugated polyelectrolytes and introduced a new class of polymeric materials for future array sensing endeavors. As the synthesis and functionality of conjugated co-polymers becomes more readily accessible, this work offers a guide for optimal array performance, using these materials as ultra-sensitive *and* selective metal ion sensors.

3.7 Experimental details

3.7.1 Materials

2-[4-(2-hydroxyethyl)piperazin-1-yl]ethanesulfonic acid (HEPES) and 1,4-dioxane were purchased from ICI Scientific and VWR, respectively, and used without further purification. All metal chloride salts were bought from Fluka. For consistency, all stock solutions of polymers and metal chloride salts were prepared fresh before each experiment. All experiments were carried out in a 50:50 water:1,4-dioxane solution buffered to 7.4 with 25 mM HEPES, prepared by adding an appropriate amount of HEPES free acid to deionized (DI) water; the pH was then adjusted to 7.4 by adding 1.0 M NaOH as needed and monitoring with a combined glass electrode, then bringing up to volume. To avoid unwanted absorption of water over time, any hygroscopic salts ($ZnCl_2$ and $CdCl_2$) were dried to constant weight in an oven set to 110 °C and

stored in a desiccator before use. All polymers in this study were synthesized and characterized by Dr. Joshua Tropp under the guidance of Prof. Jason Azoulay from the School of Polymer Science and Engineering at the University of Southern Mississippi.

3.7.2 Instrumentation

UV-vis experiments were performed on a Hewlett-Packard 8452A diode array UV-vis spectrophotometer. Benchtop steady-state fluorescence measurements were carried out with an ISS PC1 spectrofluorimeter. Excitation was carried out using a broad-spectrum high-pressure xenon lamp (CERMAX, 300W). Excitation correction was performed through a rhodamine B quantum counter with a dedicated detector. Excitation intensity was controlled by a manually operated iris (open/closed only). Spectral resolution was controlled by manually operated slits. Detection was through a Hamamatsu red-sensitive PMT. Experimental temperature (25 °C) was controlled by an external circulating water bath.

Multivariate data was acquired on a BioTek *Synergy II* multimode microwell plate reader, capable of measuring absorbance spectra through a monochromator and steady-state fluorescence intensity through a set of bandpass filters:

Excitation filters: (center/bandpass) 330/20 nm, 380/20 nm

Emission filters: (center/bandpass) 450/50 nm, 460/40 nm, 485/20 nm, 516/20 nm

The sample compartment in this instrument was electrically thermostatted to 25 °C. Detector gain on the plate reader was automatically adjusted to maximize the signal of the most emissive well on the plate. Experiments were laid out by hand using Eppendorf Research multichannel pipettors and disposable plastic tips into Aurora microwell plates with clear bottoms for fluorescence spectroscopy in a 384-well configuration. The plates were made of non-treated cyclo-olefin polymer (COP) with clear flat bottoms. Each well was filled with exactly

100 µL of sample solution for uniformity. Plates were read on the multimode plate reader immediately after preparation. Reading required about 20-30 minutes for each plate. In this time span, there appeared to be no evaporation of solvent (50:50 water:dioxane), therefore plates did not need to be sealed.

3.7.3 Benchtop titrations

All benchtop optical spectroscopic measurements, including metal binding titrations were performed in 50:50 water:1,4-dioxane buffered to pH 7.4 using 25 mM HEPES. Polymer stock solutions were prepared by suspending the solid polymer in the water:dioxane solvent and sonicating the suspension for 2-3 minutes. After cooling, each saturated polymer solution was then transferred to a centrifuge tube and centrifuged for 30 minutes at 3,300 rpm using a Fisher Scientific Centrific centrifuge, Model 228. After centrifugation, the saturated solution supernatant was removed. Any residual suspended solids were removed from it using a 13 mm syringe filter with 0.45 µm PTFE membrane (from VWR). Working polymer solutions were then diluted by adding an appropriate aliquot of this stock solution (200-400 µL) to pure 50:50 water1,4-dioxane solvent (buffered to pH 7.4 with 25 mM HEPES) in a 1 cm quartz cuvette. Absorbance and fluorescence emission measurements were then taken for the three polymers. Representative absorbance and fluorescence spectra are presented in Figure 3-21. Fluorescence emission spectra were collected by exciting the polymer at their most red-shifted spectral maximum.

All metal binding titrations were performed by adding a measured aliquot of the polymer stock solution into pure 50:50 water:1,4-dioxane (buffered to pH 7.4 with 25 mM HEPES) in a 1 cm quartz cuvette to obtain a working solution with the desired fluorescence intensity. Fluorescence emission measurements of each working polymer solution were then taken.

Subsequent additions (1-100 µL per addition) of a separately prepared titrant solution, containing a known concentration of metal chloride and the same concentration of polymer, were added to the cuvette. Fluorescence emission measurements were collected immediately after each addition of titrant solution.

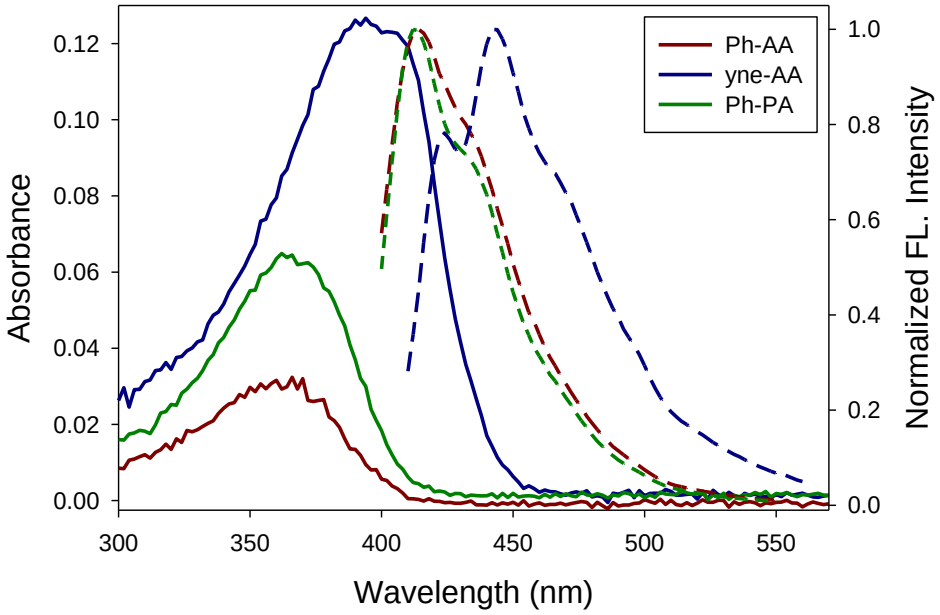

Figure 3-21 Representative absorbance (solid lines) and fluorescence spectra (dotted lines) for **Ph-AA** (red , $\lambda_{exc.}$ = 380 nm, 400 µL added stock solution), **yne-AA** (blue, $\lambda_{exc.}$ = 400 nm, 200 µL added stock solution), and **Ph-PA** (green, $\lambda_{exc.}$ = 380 nm, 400 µL added stock solution). Working solutions were prepared in a 1 cm quartz cuvette by adding the indicated amount (200-400 µL) of a saturated, stock polymer solution to 2.0 mL of pure co-solvent (50:50 water:1,4-dioxane buffered to pH 7.4 with 25 mM HEPES).

3.7.4 Multivariate data analysis

Linear Discriminant Analysis (LDA) and Principal Component Analysis (PCA) were used to interpret the data sets, common statistical treatments used for the interpretation of multidimensional data sets. All multivariate analyses were performed in the commercial *Mathematica* program (release 11.3) published by Wolfram Research Inc, using code developed in-house.

As a preliminary step to check for statistical outliers, principal component analysis was applied to each set of metal ion/polymer replicate points. Replicate points well outside a 95% confidence interval (CI) were considered outliers and removed from the raw data set. Figure 3-22 displays the results of this analysis for Cu(II) in the 500 pM data set as an example; in this case, data point 2 lies well outside the 95% confidence ellipsoid and was removed from the data set before further analysis.

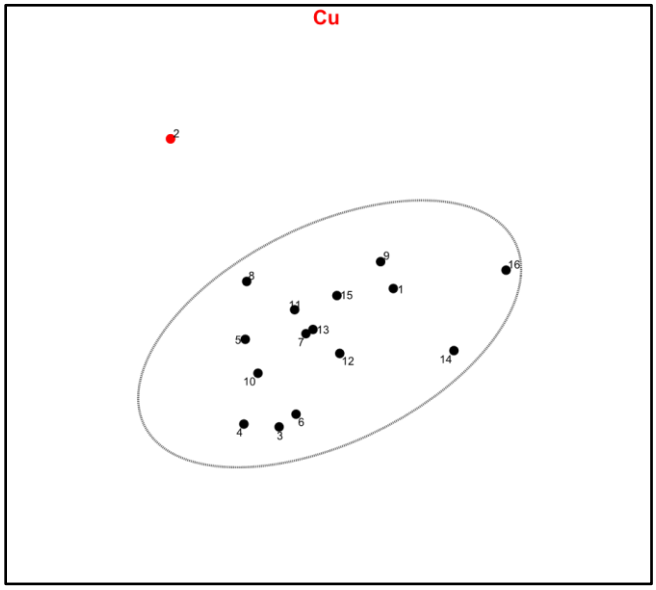

Figure 3-22 PCA score plot for replicates of the Cu(II) analyte in the 500 pM replicate data set, with a calculated 95% confidence ellipsoid shown as a grey line. Point 2 (indicated in red) is clearly well outside the confidence interval and was therefore removed from the data set before further analysis.

As a further preliminary step in addition to outlier data removal, the quality of information carried by each raw instrumental measurement was analyzed. LDA and PCA were run for a first time using all instrumental measurements and based on the analysis of the LDA loadings plot obtained from these results, many instrumental parameters were found to contribute very little to the overall differentiation. Thus, an optimal threshold was found, by which redundant measurements could be removed, while at the same time preserving the most

important ones. For all data sets in this study, the optimal threshold was determined to be between 0.5-1.0% of the *overall* weighted contribution among *all* factors in the transformed data set; i.e. any instrumental measurement whose percent contribution was below this set threshold was removed, and anything above was retained. For example, the optimal threshold for the 500 pM data set was 1%, which resulted in retention of only ten of the 24 total instrumental measurements; this variable filtering method for the 500 pM data set was graphically displayed in Figure 3-11 above.

CHAPTER 4

BINDING INTERACTIONS OF HYPERBRANCHED POLYELECTROLYTES WITH AROMATIC HYDROPHOBICS IN WATER

4.1 Introduction

For many years, globular polyelectrolytes, such as dendrimers and micelles, have been extensively studied as encapsulating agents for small organic molecules.[148-149] In particular, dendrimers are hyperbranched polymers containing a central core from which repeat units extend outwards. These macromolecular architectures were first introduced in the late 1970s by Vögtle et al.,[150] and since have led to a large variety of dendritic chemical structures.[151] One such class of dendrimers, poly(amidoamine) (PAMAM) dendrimers, first prepared in the early 1980s by Tomalia et al.,[152] consist of a variety of divalent cores, the most common being a 1,2-diaminoethane (ethylenediamine, *en*) core, with amidoamine repeating units and terminal primary amines representing further growth and branching points, with each new branching point starting a new generation of the dendrimer. Scheme 4-1 shows the chemical structure of a generation 1 (G1) PAMAM dendrimer. They are water soluble, commercially available, and highly ordered cationic polyelectrolytes that have received attention due to their interesting features, such as their well-defined globular structure and high loading capacity.[153-154]

In the Bonizzoni group, the multi-valent binding capacity associated with these polyelectrolytes has been exploited, making them effective supramolecular hosts for the detection of organophosphates and biological phosphates,[37-38] and of carbohydrates,[34] using optical spectroscopic methods. Given these promising results and wanting to attain a deeper

understanding of the processes involved in encapsulation of small molecules with these polymers,[155-157] our group embarked in studies to clarify these interactions with small-molecule analytes in water.

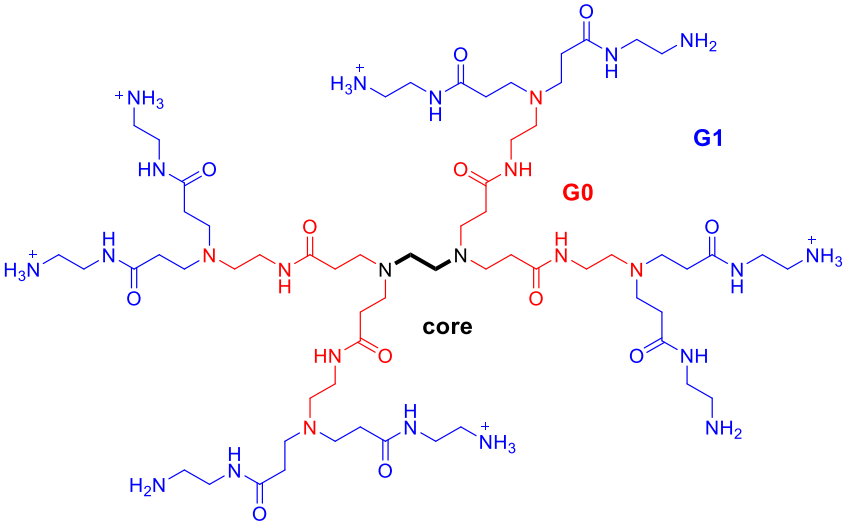

Scheme 4-1 Chemical structure of a first generation (G1) amine-terminated poly(amidoamine) (PAMAM) dendrimer.

The findings from this preliminary work, performed by Dr. Ashley Steelman, showed that electrostatic interactions provide most of the driving force for complex formation, with hydrogen bonding and interactions from the dendrimer arms with aromatic moieties (i.e. CH-π and cation-π interactions) in the guest molecule also providing more subtle differentiation in affinity between these dendrimers and small water-soluble species. The latter result was represented graphically using two trianion guests, trimesate and 1,3,5-cyclohexanetricarboxylate (CHTC), upon their addition to a 5,(6)-carboxyfluorescein (CF)-generation 5 (G5) PAMAM complex, displaying better displacement capability by trimesate.[156] The chemical structures of each small-molecule target and the fluorescence isotherm plots are presented in Figure 4-1. Starting with the dendrimer-fluorophore complex, the fluorophore (CF), is significantly quenched by the dendrimer. Upon the addition of the displacer (DP) guest molecules, the CF

molecules will be released from the dendrimer host, restoring its fluorescence signal. Given the similar charge density, it was proposed that the overall greater affinity was attributed to cation-π or CH-π interactions involving the aromatic core of the trimesate guest. In this chapter, we focus on the effects of this unexpected and important interaction of these dendrimers with small guest molecules with aromatic moieties. Fluorescent spectroscopic methods were used to probe the underlying interactions between amine-terminated PAMAM dendrimers with simple, yet analytically relevant, polycyclic aromatic hydrocarbon (PAH) targets.

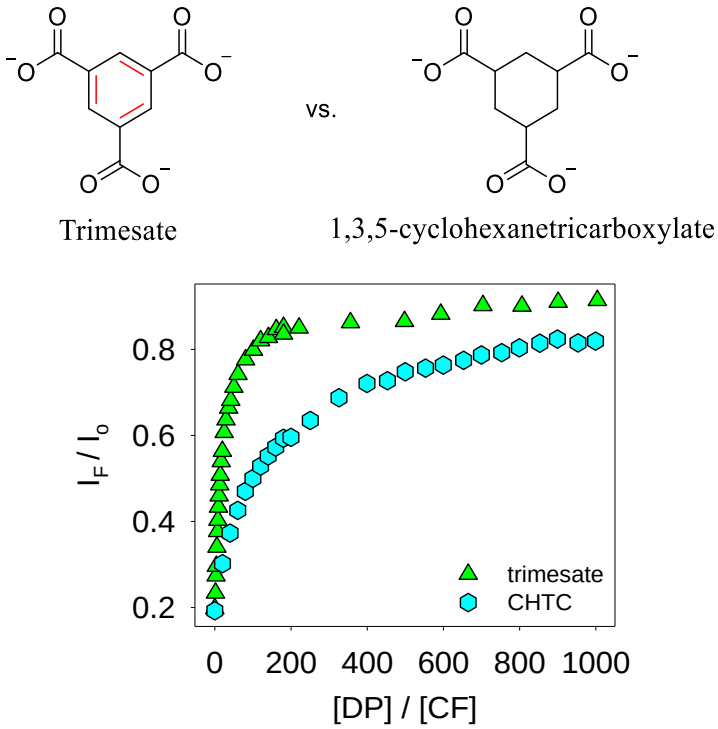

Figure 4-1 Fluorescence intensity isotherm from the titration of a G5-CF_n complex with trimesate and 1,3,5-cyclohexanetricarboxylate trianion displacers (DPs).[156] [CF] = 2.0 μM, [G5] = 0.45 μM in buffered H_2O (pH = 7.4 with 50 mM HEPES; $\lambda_{exc.}$ = 485/20 nm, $\lambda_{em.}$ = 560/40 nm).

Polycyclic aromatic hydrocarbons (PAHs) were chosen as a homogeneous family of hydrophobic aromatic compounds having pronounced and well-characterized fluorescence properties, providing a valuable and varied group of probes to study their interactions with these

macromolecules. PAHs are well-known as toxic environmental pollutants with mutagenic and carcinogenic properties, whose determination through non-covalent sensing methods is important for environmental and health applications,[158-162] so identifying their uptake into polymeric hosts could foster further applications towards their sensing and remediation. These compounds occur from many natural sources, however, emissions from pyrogenic sources such as fossil fuels and industrial manufacturing lead to their unwanted introduction into the environment.[163-164] Thus, many research efforts aim to address the detection of these compounds, despite their uncharged and non-polar nature, featureless chemical structure, and lack of heteroatom containing functional groups.[165] In addition to chemical detection applications, understanding the interactions between PAHs and PAMAM dendrimers would also impact other problems, such as hydrophobic drug dissolution and bioavailability, and problems in separation science.

For this study, the fluorescence emission response of anthracene and pyrene (Scheme 4-2) was investigated upon their interaction with amine-terminated PAMAM dendrimers. These PAHs were chosen as representative examples for their relatively simple chemical structure, their ready availability, and their intense, well-characterized fluorescence emission properties.[166-167] To evaluate the uptake of PAH guests by dendrimer host in neutral water despite the PAH's low solubility in this medium, a dissolution testing method was used, a common technique often used for the determination of solubility properties of pharmaceuticals.[168] Preliminary thin-film dissolution experiments and results, conducted by Dr. Steelman, are presented in the following section.

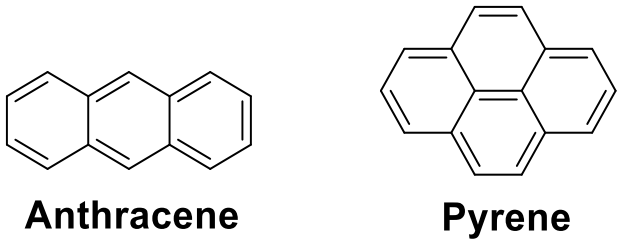

Scheme 4-2 Chemical structures of anthracene (left) and pyrene (right) as representative PAHs used as guest binding probes with amine-terminated PAMAM dendrimers.

4.1.1 Thin-film dissolution experiments

For this method, hexanes stock solutions of PAH guests were prepared, and small aliquots (200-300 µL) of these solutions were added to multiple cuvettes and the solvent removed under a stream of nitrogen to deposit a constant amount of PAH in each cuvette. Care was taken to deposit an amount of hydrocarbon much greater than what can be solubilized by water alone, and large enough to ensure that only a fraction of the available PAH would be brought into solution by the polyelectrolyte, ensuring that the free dissolved PAH would always be maintained at a constant concentration by each PAH's natural dissolution equilibrium in the presence of the solid thin film. To the cuvettes were added buffered aqueous solutions containing increasing concentrations of three generations of PAMAM dendrimer (G3-G5). Dendrimer generations were chosen because they strike an optimal balance between large size and affordable cost, making the findings more relevant for practical applications. In fact, dendrimers smaller than G3 do not display high enough affinity to be viable in the desired applications.[169] On the other hand, larger dendrimers might perform better than those reported here, however they are exponentially more expensive than the smaller sized generations due to greater difficulty obtaining them in high purity. All aqueous solutions were buffered to pH 7.4 using 50 mM HEPES since we were interested in aqueous conditions relevant to physiological and environmental applications.

Once prepared, the cuvettes were then allowed to equilibrate overnight at room temperature, and a fluorescence spectrum of each solution taken, upon excitation at 350 nm. The results obtained with anthracene, shown in Figure 4-2 and Figure 4-3, were promising, with a linear increase in the fluorescence emission signal for anthracene as the concentration of amine-terminated PAMAM dendrimer was increased, indicating that more anthracene was being brought into solution as the dendrimer was added. This result, although encouraging, may also have been influenced by the slight change in the solvent composition as larger quantities of dendrimer stock solution were added (since dendrimer stock solutions are made up in methanol), with a concomitant reduction in solvent polarity. Moreover, higher generations of PAMAM dendrimer caused proportionally greater quantities of anthracene to dissolve from the thin film into solution (see Figure 4-2, right) Once again, a slightly larger amount of MeOH was added in with the larger dendrimers: therefore these conditions could not yet confirm that the observed effect was completely due to the polymer.

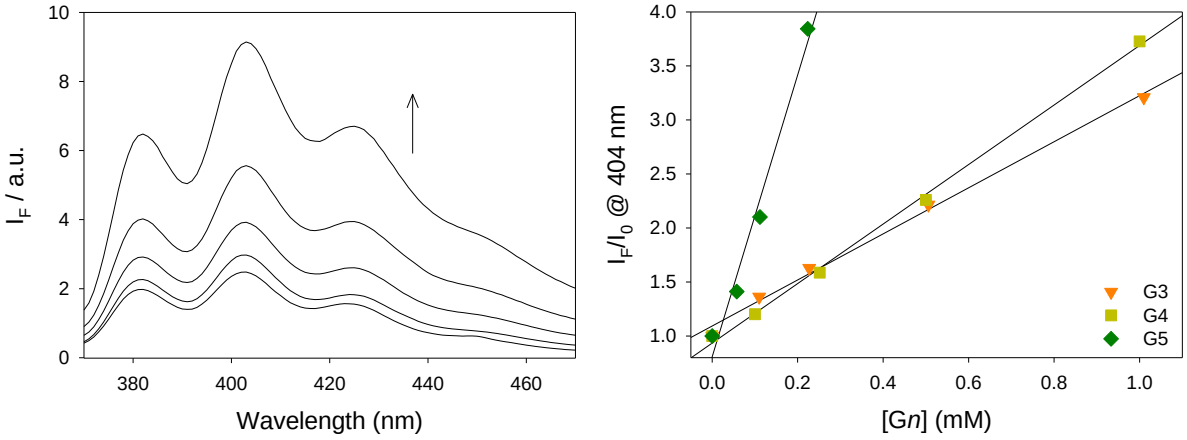

Figure 4-2 Left: Representative fluorescence spectra of anthracene brought into solution from a thin film in buffered water (pH = 7.4 using 50 mM HEPES) as a function of increasing concentration of G4 amine-terminated PAMAM dendrimer. Right: Comparing fluorescence emission profiles for anthracene as a function of increasing concentration of G3-G5 PAMAM added; the black solid lines were obtained from linear regression analysis ($\lambda_{exc.}$ = 350 nm,

$\lambda_{em.}$ = 404 nm; total deposited anthracene = 1.12 μmoles). The corresponding fluorescence emission spectra with G3 and G5 PAMAM dendrimers are presented in Figure 4-3.

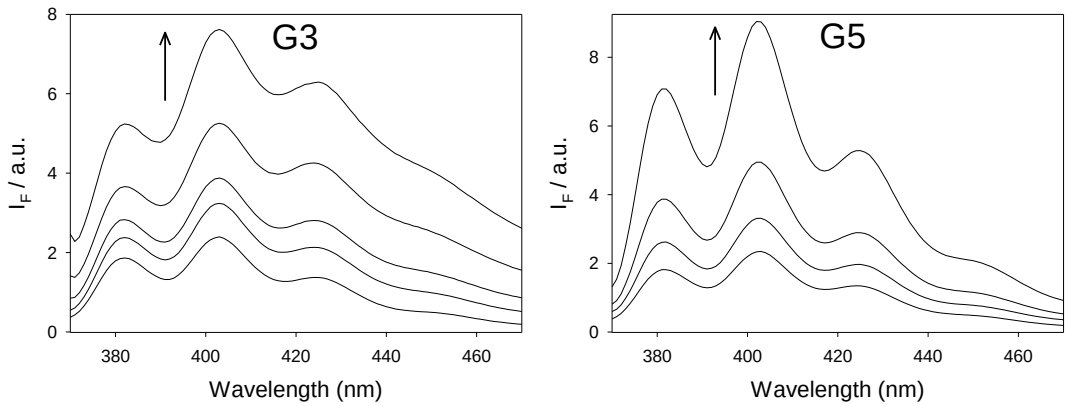

Figure 4-3 Fluorescence spectra for anthracene brought into solution from a thin film in H_2O buffered to pH 7.4 with 50 mM HEPES as a function of increasing concentrations of G3 PAMAM (left) and G5 PAMAM (right) dendrimers ($\lambda_{exc.}$ = 350 nm, total deposited anthracene = 1.12 μmol).

Pyrene was used as a second fluorescent probe with unique and well-known emission characteristics. Specifically, pyrene is known to form excited-state dimers (excimers) when concentrations are high enough to permit an excited-state pyrene to come into close proximity with another ground-state molecule.[166] In water, however, the natural solubility of pyrene in neutral buffered water is too low for free pyrene in solution to exhibit excimer emission under the experimental conditions outlined above. Therefore, observation of the pyrene excimer species centered at ($\lambda_{em.}$ = 470 nm) in the presence of PAMAM dendrimers would be a direct indication that pyrene molecules have been forced into closer proximity through binding to the dendrimer; in other words, it would be direct evidence of binding multiple pyrene molecules to the polyelectrolyte.

Thin-film dissolution experiments were conducted for pyrene according to the same procedure previously described for anthracene. As G3-G5 PAMAM dendrimer was added, a noticeable excimer band was formed in the fluorescence emission spectrum, upon excitation at

338 nm, which was otherwise not observed for free pyrene in water solution without the dendrimer. Moreover, the intensity of the excimer band was linearly dependent on the PAMAM concentration, with a more pronounced dependence for higher generations of PAMAM. These results for pyrene, presented in Figure 4-4 and Figure 4-5, display a clear emergence of the excimer band, which strongly supported the hypothesis that the increase in fluorescence emission signal of PAH was due to supramolecular complex formation between PAH and dendrimer, leading to a net increase in PAH solubilization in water. In this context, pyrene is a particularly useful "dual-channel" probe: its monomer emission, around 390 nm, reports on the concentration of free pyrene in solution; as shown in Figure 4-4 and Figure 4-5, this concentration is controlled by the probe's thermodynamic dissolution equilibrium so its monomeric emission signal changes minimally with added dendrimer concentration, since solid pyrene is still present on the walls of the experimental vessel. On the other hand, the excimer emission at 470 nm reports on the amount of pyrene bound to the dendrimer, whose molecules are forced closer together, enough for excited-state complexes to form.; this emission signal increases markedly with the addition of dendrimer hosts, with the slope of this increasing trend being a measurement of the relative "loading capacity" of each dendrimer generation.

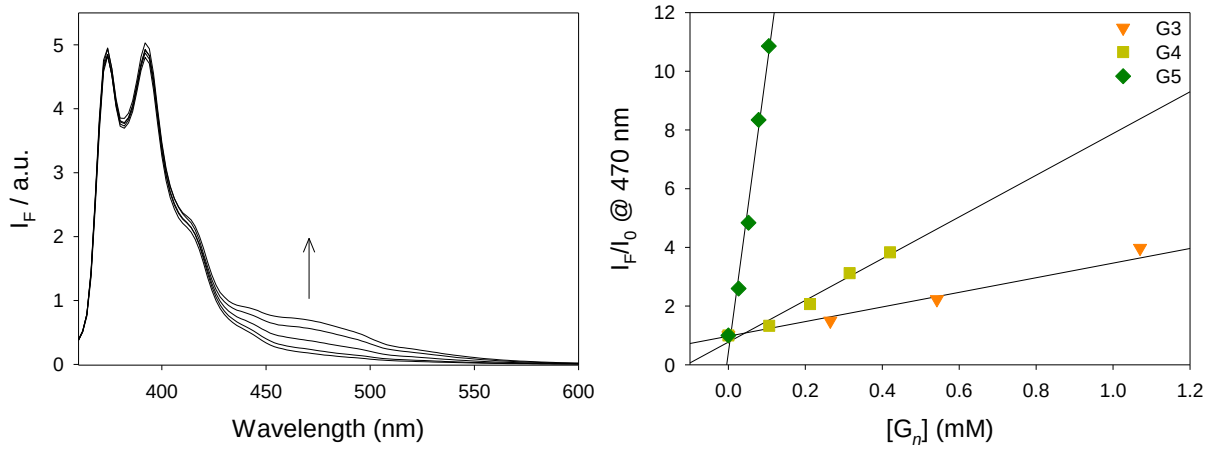

Figure 4-4 Left: Representative fluorescence emission spectra of pyrene brought into solution from a thin film in buffered water (pH = 7.4 using 50 mM HEPES) as a function of increasing concentration of G4 amine-terminated PAMAM dendrimer. Right: Profiles of the normalized fluorescence emission of pyrene's excimer as a function of increasing concentration of G3-G5 PAMAM ($\lambda_{exc.}$ = 338 nm, $\lambda_{em.}$ = 470 nm; total deposited pyrene = 1.07 µmol). The corresponding fluorescence emission spectra with G3 and G5 PAMAM dendrimers are presented in Figure 4-5.

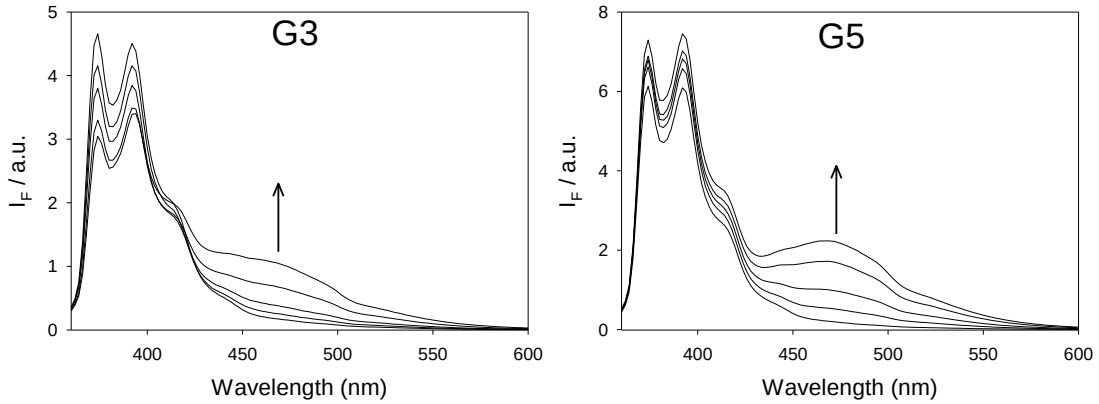

Figure 4-5 Fluorescence spectra of pyrene brought into solution from a thin film in H_2O buffered to pH 7.4 with 50 mM HEPES as a function of increasing concentrations of G3 PAMAM (left) and G5 PAMAM (right) dendrimers ($\lambda_{exc.}$ = 338 nm, total deposited pyrene = 1.07 µmol).

Based on our group's previous experience with the polyelectrolytes with hydrophilic guests,[156] it was proposed that the most important interactions responsible for the observed effects with anthracene were cation-π or CH-π interactions between the aromatic anthracene and positively charged ammonium groups at the dendrimer's surface, rather than interactions

between the non-polar hydrocarbon guest and the hydrophobic interior of the dendrimer. These interactions were responsible for hydrocarbon uptake into a complex with the polymer, which in turn caused the further dissolution of anthracene from the thin film reservoir, as required by anthracene's natural dissolution equilibrium in water. However, ionic strength of the solution from added polyelectrolytes was also considered as a possible cause for the increase in anthracene's emission. However, higher electrolyte concentrations are known to decrease the solubility of anthracene and other aromatics in aqueous solutions,[170-171] which would, in fact, *lower* the observed emission signal, and yet in this experiment, an *increase* in that signal was observed.

Preliminary results confirmed that an increase in ionic strength alone would not enhance PAH fluorescence by repeating the same experiment using a polyanionic carboxylate-terminated PAMAM dendrimer. Such carboxylate terminated dendrimers are referred to as "half-generation" PAMAM (e.g. G4.5 is the carboxylate-terminated, negatively charged equivalent of the amine-terminated polycationic G5). The similarly sized polycarboxylate PAMAM G3.5 and polyammonium G4 dendrimers were both probed using anthracene and pyrene under the same experimental conditions described above. Although they have opposite charges, the two dendrimers represent similar generations and are otherwise comparable in structure, size, and mass (64 surface groups; 14.2 kDa and 12.9 kDa for G4 and G3.5, respectively). The results, shown in Figure 4-6, indicated that the presence of G3.5 PAMAM dendrimer caused a *decrease* in anthracene's emission signal, attributed to the increased ionic strength in solution, which caused the amount of free anthracene in solution to decrease by changing the properties of the bulk solvent. For anthracene, these observations were a

completely opposite from those made with G4 PAMAM, whose emission clearly increased in the presence of this dendrimer (Figure 4-2).

On the other hand, similar experiments with pyrene displayed similar quenching behaviors when pyrene saturated solutions were exposed to either cationic G4 vs. anionic G3.5 (Figure 4-6, right), indicating that the peripheral functional groups on the dendrimers were less involved in their interaction with pyrene to these dendrimers and, at the same time, that the hydrocarbon is bound in a position more accessible to the tertiary amine quenchers, found within the inner layers of these dendrimers. Taken together, the preliminary results provided by Dr. Steelman suggested that the main driving force for the binding of pyrene to these dendrimers was likely hydrophobic interactions, instead of the cation/CH-π interactions hypothesized for anthracene. In fact, such charge/polar-π interactions in these systems are limited to the region of the dendrimer near the surface, exposed to the solvent, where the charged ammonium ions participating in these interactions are found.[172]

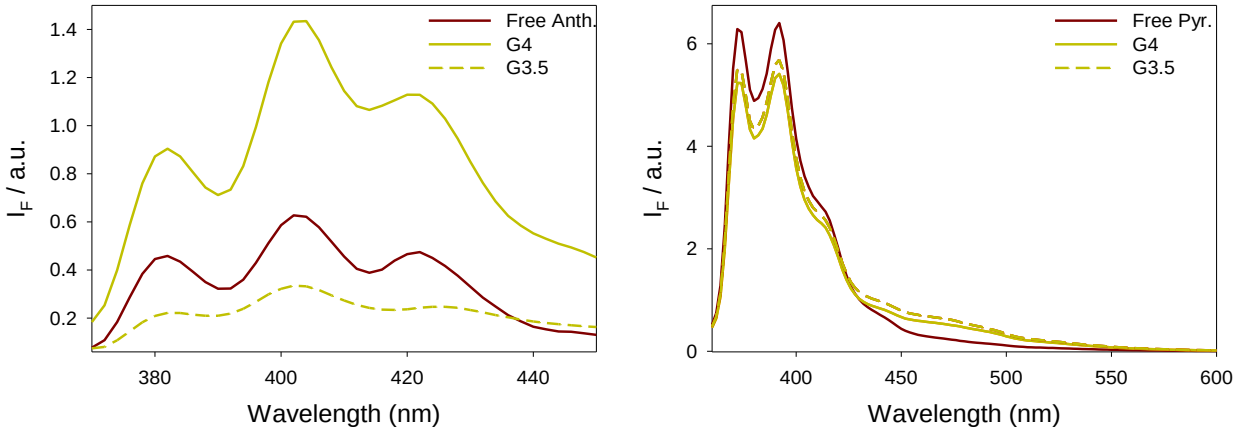

Figure 4-6 Thin film experiments of anthracene (left) and pyrene (right), comparing the effectiveness of positively (G4) and negatively (G3.5) charged poly(amidoamine) (PAMAM) dendrimers ([G*n*] = 0.10 mM for anthracene experiment, [G*n*] = 0.23 mM for pyrene experiment). The emission spectrum from a saturated solution of free PAH is included as a reference. All measurements were conducted in H_2O solution buffered to pH 7.4 in 50 mM HEPES (total deposited anthracene = 16.9 µmol, pyrene = 5.24 µmol; anthracene $\lambda_{exc.}$ = 350 nm; pyrene $\lambda_{exc.}$ = 338 nm).

4.2 Strict control of bulk solution properties

As mentioned in the introductory section, because PAMAM stock solutions are made up in MeOH and have different concentrations for each generation, increasing the concentration of PAMAM also resulted in an unwanted and concomitant increase in concentration of MeOH in the bulk solution, which may skew the reported results. To confirm that anthracene uptake was not a simple side-effect of the reduction in solution polarity caused by the MeOH, the same thin film dissolution experiments were carried out a constant concentration of G3-G5 dendrimer after adjusting the MeOH concentration in each solution to the same value, thereby eliminating any bulk solvent polarity effect. Results from these experiments are presented in Figure 4-7. For anthracene, an increase in fluorescence emission was observed, which strongly suggests anthracene binding and uptake by the dendrimer. For pyrene, on the other hand, an opposite trend was observed; i.e. there is a noticeable reduction of pyrene's emission in the presence of the PAMAM dendrimer. Furthermore, the excimer emission signal was no longer visible in these conditions.

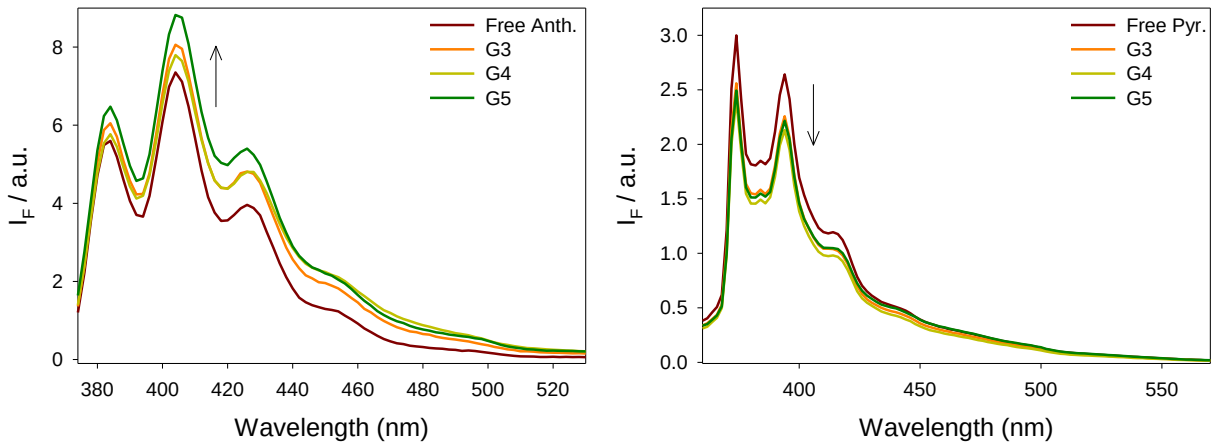

Figure 4-7 Fluorescence emission spectra of anthracene (left) and pyrene (right) solution in equilibrium with a thin film of the respective solid in H_2O buffered to pH 7.4 with 50 mM HEPES in the presence of a constant concentration of dendrimer and methanol ([G*n*] = 0.10 mM,

7.2% MeOH; total deposited anthracene = 1.90 µmol, pyrene = 1.56 µmol; anthracene $\lambda_{exc.}$ = 350 nm, pyrene $\lambda_{exc.}$ = 338 nm).

These results of thin film experiments with solutions that have the same solvent composition indicated that further investigation was needed to determine the modes of interaction of these cationic dendritic hosts with hydrophobic aromatics, including PAHs. We therefore turned to steady-state fluorescence anisotropy, time-resolved fluorescence measurements, and selective quenching experiments to probe the location and mode of binding.

4.3 Fluorescence anisotropy

Fluorescence anisotropy experiments were conducted to confirm binding of the PAH probes to cationic PAMAM dendrimers. If bound to the larger dendrimer, the PAH probe's anisotropy signal was expected to increase relative to that of the free small-molecule fluorophore. Free rotation of small molecules in solution occur about 2 orders of magnitude faster than the intrinsic fluorescence lifetime of the PAH fluorescent probes used here. Thus, these small fluorophores will have isotropic polarization of their fluorescence emission, when free in solution and excited by plane polarized light (i.e. this will give a low anisotropy signal). However, the rotational diffusion rate of the complex formed by these fluorescent probes upon binding to the much larger PAMAM macromolecule is dominated by the slower tumbling rate of the larger host, resulting in higher anisotropic polarization of the fluorescence emission of the complex (i.e. a higher anisotropy signal will be observed).

Thin film dissolution experiments were carried out at a constant G3-G5 PAMAM concentration ([G*n* = 0.1 mM). Four 1 cm quartz cuvettes were prepared containing a thin film of each PAH probe, obtained by evaporation a hexanes solution as described in the previous section; each cuvette was filled to a constant volume with buffer and a calculated amount of

G3-G5 dendrimer stock solution in methanol was added to each cuvette to achieve [dendrimer] = 0.10 mM. Once again, care was taken to ensure that each cuvette solution contained the same percent volume of methanol (7.2% MeOH in this experiment). We also ensure that the dendrimer concentration was low enough to prevent interference from the PAMAM dendrimers' weak intrinsic emission,[173-175] which may interfere with anisotropy measurements. As shown in Figure 4-8 smaller G3 and G4 PAMAM dendrimers display weak intrinsic fluorescence emission at relatively high concentrations, upon excitation at 338 nm.

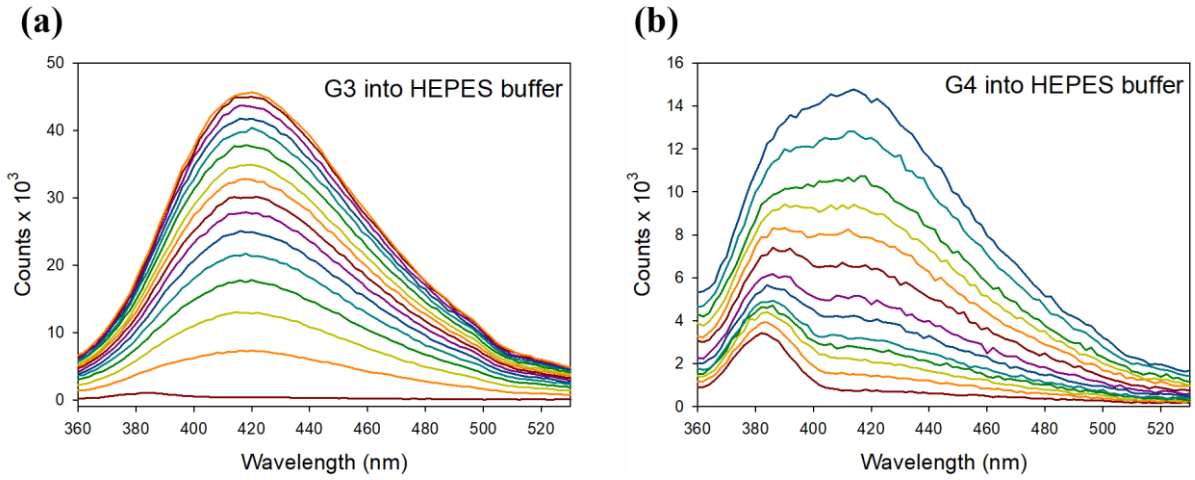

Figure 4-8 Intrinsic fluorescence emission spectra of PAMAM dendrimers upon excitation at 338 nm: families of fluorescence emission spectra of a water solution buffered to pH 7.4 with 50 mM HEPES, upon the addition of (a) G3 PAMAM (0-1.90 mM) and (b) G4 PAMAM (0-0.12 mM) dendrimers.

Based on these results, it was apparent that, at millimolar concentrations, these lower generation PAMAM dendrimers contribute a significant portion of their emission signal in the region where the PAH probes' emission is found. Due to their size, the macromolecule's emission would be highly polarized, interfering with the determination of fluorescence anisotropy of the PAH probes by artificially increasing the fluorescence polarization signal. Results from the first, potentially flawed, fluorescence anisotropy experiments using high G3 PAMAM concentrations are displayed in Figure 4-9. These exhibited a noticeable increase in

anisotropy signal for both PAHs with increasing dendrimer concentration, reaching saturation at relatively high [G3 PAMAM], in the millimolar range, where G3 PAMAM contributes significantly to the overall emission signal. Thus, it was unclear how much of the observed anisotropy signal came from the bound PAH vs. the dendrimer itself using this method.

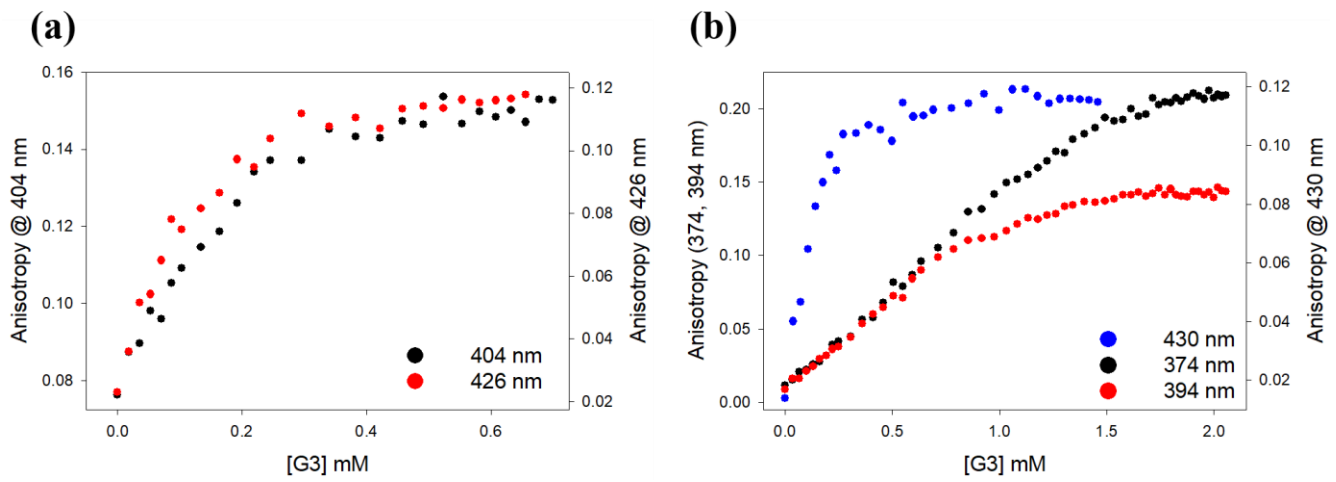

Figure 4-9 Fluorescence anisotropy of (a) anthracene at 404 nm (black) and 426 nm (red) and (b) pyrene at 374 nm (black), 394 nm (red), and 430 nm (blue), upon the addition of G3 PAMAM dendrimer. All measurements were conducted in water buffered to pH 7.4 with 50 mM HEPES (anthracene $\lambda_{exc.}$ = 350 nm; pyrene $\lambda_{exc.}$ = 338 nm).

To overcome this problem, thin film dissolution experiments were modified to use a constant low dendrimer concentration. These modified conditions guaranteed that emission from the dendrimers would be negligible and it would not interfere with the measurement of the anisotropy of PAH probes themselves, ensuring that a high anisotropy signal could be safely ascribed to the bound fluorophore probe bound to the dendrimer.

Once the four thin film experimental cuvettes were prepared for each PAH, the solutions were stored at room temperature overnight to reach equilibrium, as described previously in this chapter. Multiple anisotropy measurements were then taken for each cuvette, with the results presented in Figure 4-10. For both fluorescent probes, anthracene and pyrene, there is a clear increase in fluorescence anisotropy going from free PAH to higher PAMAM dendrimer

generations (G3 to G5). The observed trend provided further evidence that each PAH probe was bound to the dendrimer. This increasing trend in anisotropy of each PAH probe with G3 vs. G4 vs. G5 PAMAM dendrimers agrees with expectation; the larger higher generation PAMAM dendrimers can accommodate more PAH guest molecules, increasing the fraction of total PAH that is bound to the polymer, which causes a corresponding increase in fluorescence anisotropy signal.

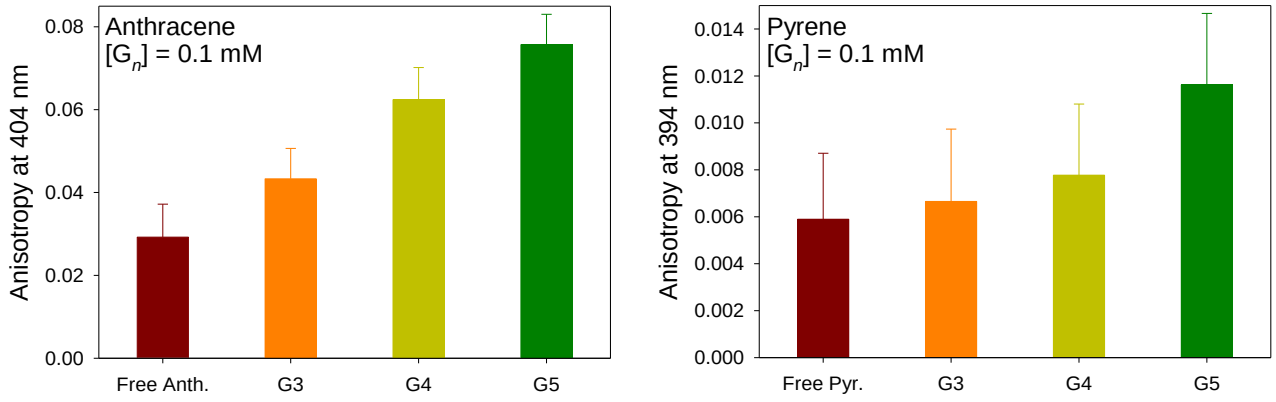

Figure 4-10 Fluorescence anisotropy data for anthracene (left) and pyrene (right), with constant concentration of G3-G5 PAMAM dendrimer ([G*n*] = 0.1 mM). Each solution contained buffered H_2O (pH = 7.4 with 50 mM HEPES) and 7.2% MeOH by volume (anthracene $\lambda_{exc.}$ = 350 nm, pyrene $\lambda_{exc.}$ = 338 nm).

The relatively low absolute values of the measured anisotropy signal for both PAH probes are likely due to the presence of free probe in solution, dissolved from the thin film deposited on the cuvette's walls according to its solubility equilibrium. The small unbound fluorophore probes themselves have a very low anisotropy signal, and since the solution's overall anisotropy is an average over all emitting forms of each probe, weighted by their molar fractions. Thus, the relatively high proportion of unbound probe in solution, with its low anisotropy signal, considerably depresses the ensemble average reading. It is also noteworthy that, counterintuitively, the anisotropy signal for the smaller anthracene probe is higher than the

slightly larger pyrene's anisotropy signal. This can be attributed to either tighter binding for anthracene than for pyrene, which increases the fraction of anthracene bound overall, increasing its relative contribution to the anisotropy signal; to the possibility of different degrees of internal mobility in each probe's complex, with pyrene having more freedom to move even while bound; or, ultimately, to a higher intrinsic anisotropy of anthracene vs. pyrene.[166,176-178] Fortunately, the absolute value of the anisotropy signal is not important here, but the trends are, and the information gleaned from these experiments also supports tight binding of these hydrocarbon probes to the PAMAM cationic polyelectrolytes.

4.4 Time-resolved fluorescence

Fluorescence lifetime determinations were carried out on the complexes of these PAH probes with G3-G5 PAMAM dendrimers as well. Four cuvettes were prepared and equilibrated overnight with an equal concentration of PAMAM dendrimer for each generation ([G*n*] = 0.10 mM), as outlined in previous sections. Time-resolved fluorescence measurements were then conducted to determine the fluorescence emission lifetimes of the PAH probes with and without the dendrimer. The exponential decay profiles for both PAHs with G3-G5 PAMAM dendrimers are displayed in Figure 4-11. Fitting of the decay profiles for both PAHs was achieved using a tri-exponential decay model (eq. 2). Indeed, fitting decay profiles of simple PAHs to a multi-exponential decay in water solution is not uncommon; in fact two emitting species are often observed, corresponding to the free PAH (shortest lifetime) and a hydrate aggregate cluster species (typically longer-lived);[179-182] these PAH probes in particular also have the potential for excimer and exciplex formation, emitting species with significantly longer lifetimes.[166]

$$\text{Intensity} = \mathrm{I} + \mathrm{A} \cdot \mathrm{e}^{\left(-\frac{t}{\tau_1}\right)} + \mathrm{B} \cdot \mathrm{e}^{\left(-\frac{t}{\tau_2}\right)} + \mathrm{C} \cdot \mathrm{e}^{\left(-\frac{t}{\tau_3}\right)} \qquad (\mathrm{eq.}\,2)$$

For anthracene, contributions were ascribed to two shorter-lived emitting species and one longer-lived one, although the latter had a significantly smaller contribution to the overall emission (ca. 1%, Table 4-1). Upon addition of dendrimer, little change was observed in the excited state lifetimes of the two shortest-lived contributors to the overall fluorescence emission (i.e. free anthracene in solution and its hydrated aggregate, respectively), suggesting that the dendrimer was incapable of acting as a dynamic (i.e. collisional) quencher of free anthracene in solution. The contribution of the longer-lived emitter increased somewhat in the presence of dendrimer, but its lifetime was the most significantly reduced of the three.

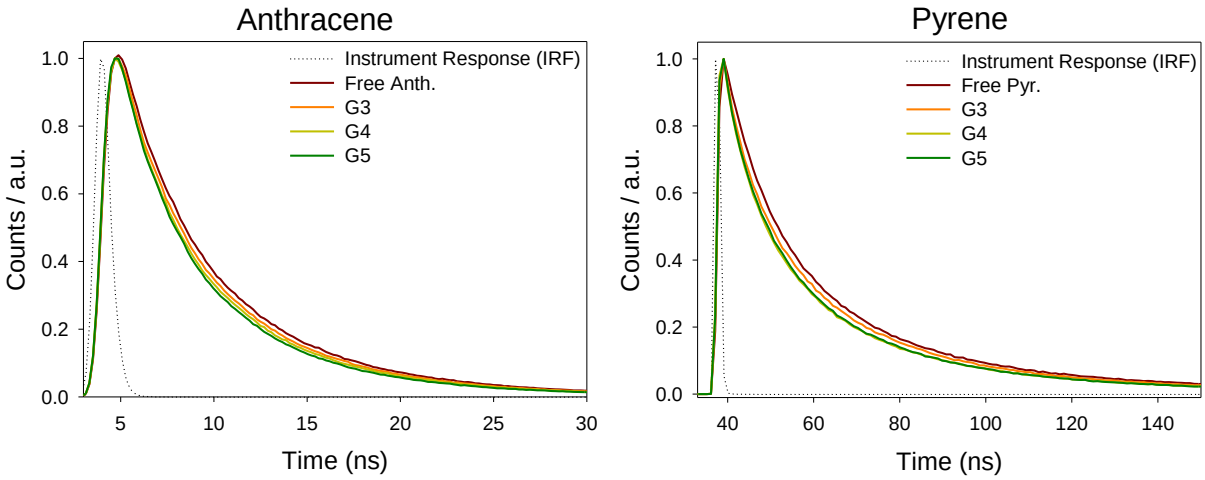

Figure 4-11 Time-resolved fluorescence decay profiles for anthracene (left) and pyrene (right) with constant concentrations of G3-G5 PAMAM dendrimer ([G*n*] = 0.10 mM, 7.2% MeOH by volume in H_2O solution buffered to pH 7.4 with 50 mM HEPES).

Table 4-1 Time-resolved fluorescence decay parameters from tri-exponential fittings of the emission decay profile data for anthracene and pyrene in Figure 4-11 ([G*n*] = 0.1 mM).

G*n*	τ_1 (ns)	τ_2 (ns)	τ_3 (ns)	$\%_1$	$\%_2$	$\%_3$
Free Anth.	3.36 ± 0.03	7.41 ± 0.04	28 ± 1	38	61	1
G3	3.06 ± 0.03	6.93 ± 0.04	21.4 ± 0.6	34	64	2
G4	2.75 ± 0.03	6.59 ± 0.04	18.7 ± 0.5	30	67	3
G5	2.86 ± 0.03	6.66 ± 0.04	20.2 ± 0.5	36	61	3

Free Pyr.	10.1 ± 0.1	29.1 ± 0.2	101.7 ± 0.4	21	56	23
G3	8.2 ± 0.1	28.0 ± 0.2	91.1 ± 0.4	18	62	20
G4	7.80 ± 0.09	27.0 ± 0.2	86.5 ± 0.4	20	59	21
G5	8.0 ± 0.1	27.0 ± 0.2	79.5 ± 0.4	20	59	21

Contrary to anthracene, pyrene's longest-lived component with an excited state lifetime around 80-100 ns (Table 4-1), corresponding to the excimer's emission, provided a much greater relative contribution, consistent with our observations in steady-state fluorescence emission experiments. It is interesting to note, however, that in these conditions the longer-lived excimer's contribution is evident even in the absence of the dendrimers. Among the monomer lifetime components, the shorter-lived species for pyrene displayed a greater decrease in their lifetimes (τ_1 and τ_2) upon interaction with PAMAM than anthracene's, albeit the overall change in lifetime was relatively small for both PAH probes. Nevertheless, the more pronounced decrease in pyrene's emitter lifetimes with the dendrimers suggests that the dynamic quenching effects are more prominent for pyrene; this is consistent with our previous observations of pyrene's steady-state emission (Figure 4-7).

Overall, the decay profiles for each PAH probe in the presence of [PAMAM] = 0.10 mM, i.e. the same concentration used in the steady-state work described above, were similar across all dendrimer generations, shown in Figure 4-11. This is a particularly important observation in the case of the pyrene probe, given that pyrene's emission is quenched in the presence of the dendrimer (Figure 4-7), which may suggest adventitious interactions between the dendrimer and PAH, leading to collisional quenching. However, pyrene's excited state lifetime was found to be essentially unaffected by the added dendrimer, effectively disproving this collisional quenching

possibility and indicating that the observed steady-state quenching was due to the formation of a ground-state complex between pyrene and the dendrimer (i.e. static quenching).

Fluorescence lifetime measurements were also carried out at high concentration of dendrimer (0.84 mM) with both PAH probes, to highlight the different behavior of the two fluorescent PAH probes upon interaction with the same dendritic host. G4-PAMAM was used for this study, representing the mid-point in generation and size among those we selected for this work. Indeed, at higher concentrations of G4-PAMAM dendrimer, we observed a much more significant change in the decay curve of the free vs. bound species for both PAH probes., as shown in Figure 4-12. The corresponding lifetime parameters obtained from a multi-exponential fit (Table 4-2) clearly shows that there is a more substantial decrease in the lifetimes for all emissive species at this higher dendrimer concentration; expectedly, pyrene displays the greatest change in lifetime compared to anthracene, indicating that pyrene is more susceptible to dynamic quenching with these dendrimers. We hypothesize that this is indicative of its more interior position within the hydrophobic core of these dendrimers upon binding, which leaves it more susceptible to dynamic quenching by the dendrimer's internal tertiary amines. Given these results, we tested our hypothesis further by conducting selective quenching experiments to more directly probe the location of these PAH fluorophores when bound to the dendrimers.

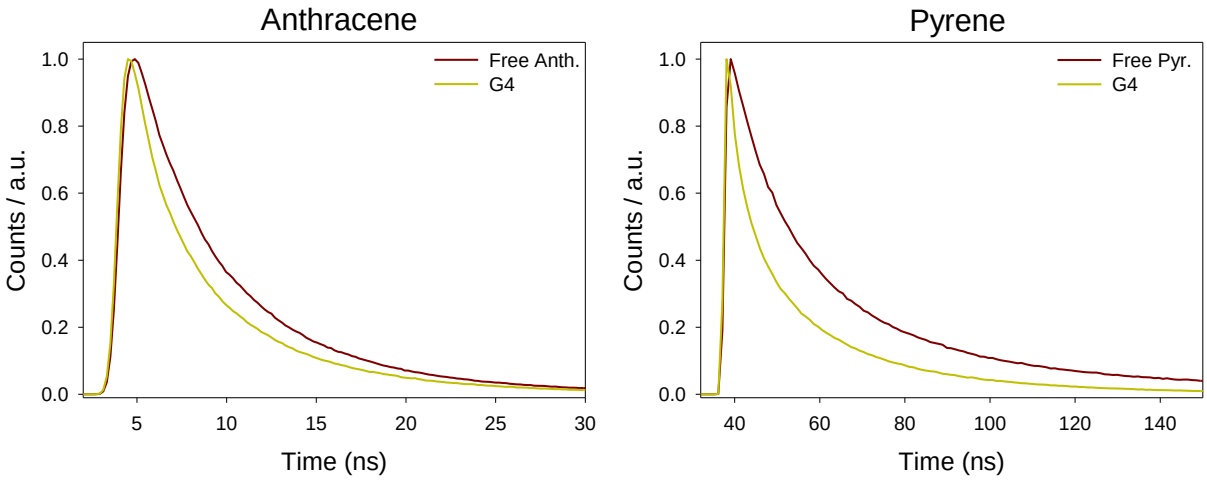

Figure 4-12 Fluorescence emission decay profiles for anthracene (left) and pyrene (right) with and without G4 PAMAM dendrimer (gold and red lines, respectively; [G4] = 0.84 mM). Each solution contained 15% MeOH by volume in H_2O solution buffered to pH 7.4 with 50 mM HEPES.

Table 4-2 Time-resolved fluorescence decay parameters from tri-exponential fitting of the emission decay profiles for anthracene and pyrene in Figure 4-12 ([G*n*] = 0.84 mM).

	τ_1 (ns)	τ_2 (ns)	τ_3 (ns)	$\%_1$	$\%_2$	$\%_3$
Free Anth.	3.31 ± 0.03	7.33 ± 0.05	24 ± 1	36	63	1
G4 + Anth.	1.86 ± 0.02	5.88 ± 0.04	13.6 ± 0.2	27	65	8
Free Pyr.	10.1 ± 0.2	29.3 ± 0.3	107.7 ± 0.4	18	52	30
G4 + Pyr.	3.16 ± 0.05	15.5 ± 0.2	38.8 ± 0.2	19	43	38

4.5 Selective quenching experiments

The experimental results discussed so far strongly suggest distinct interaction modes between each of the two hydrophobic fluorescent guests and the polycationic PAMAM hosts. Based on the steady-state and time-resolved fluorescence measurements discussed previously, the dendrimer is a more effective quencher for pyrene's fluorescence emission than that for anthracene, an effect we ascribe to the positioning of pyrene upon binding to the dendrimer's hydrophobic core, leading to better quenching of the pyrene's excited state through photoinduced

electron transfer from the tertiary amine groups present in the interior of the dendrimer.[171] To independently probe the location of binding of the anthracene and pyrene fluorophores to the dendrimer in support of this hypothesis, we conducted cesium(I) selective quenching experiments on complexes of these probes with G3-G5 PAMAM dendrimers.

If binding of the fluorescent aromatic hydrocarbon probes were driven primarily by cation/CH-π interactions, which involve the protonated primary amines of the dendrimer, found only at the surface of the macromolecule, then even when bound to PAMAM, the participating fluorescent probes would be located close to the dendrimer's surface, exposed to bulk solution. Therefore, a hydrophilic cationic quencher such as Cs^+, which would be able to access the solvent-exposed surface of the dendrimer, but not its core, should effectively quench the fluorescence emission of the PAH even when bound, regardless of the presence of the dendrimer.

On the other hand, if the PAH probe were encapsulated deeper inside the dendrimer's core upon binding, the Cs^+ cationic quencher would be far less likely to reach the fluorophore, due to electrostatic repulsion between the positively charged ammonium groups and the Cs^+ ions, leading to considerably less effective quenching of the PAH fluorophore in the presence of dendrimer vs. in its absence (see Scheme 4-3). Similar experiments have been conducted to study PAH interactions with various quenching agents in the presence of carboxylate-terminated PAMAM dendrimers.[183-184]

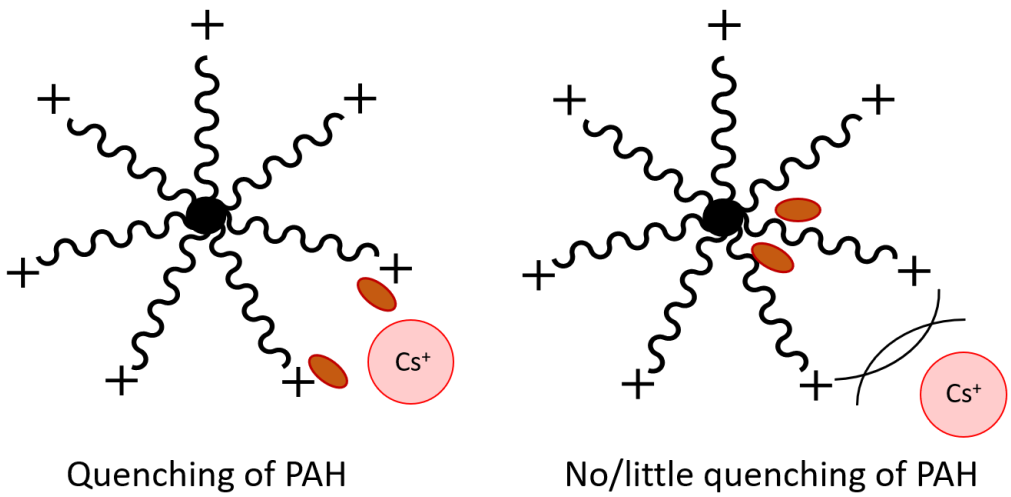

Scheme 4-3 A representation of the possible interaction modes between Cs^+ with a surface-bound PAH probe (left) vs. an internally encapsulated probe (right). Given the polycationic nature of the amine-terminated PAMAM dendrimers at neutral pH, PAHs inside the dendrimer would be more effectively shielded from the fluorescence quenching effect of Cs^+ cations.

For these titrations, a saturated solution of each PAH probe in buffered water containing a constant amount of MeOH (7.2% MeOH by volume) was prepared using the same method from the thin film experiments described above and added to a clean 1 cm quartz cuvette for titration with Cs^+. Separately, a CsCl titrant solution was prepared in the same solvent system. Aliquots (25-100 µL) of this solution were then added to each cuvette and steady-state fluorescence emission measurements were taken after each addition. The resultant profiles of emission intensity at the wavelength of maximum emission for the monomer form of each PAH (404 nm for anthracene and 394 nm for pyrene) vs. increasing [Cs^+] are presented in Figure 4-13. The results clearly show that larger, higher generation PAMAM dendrimers more effectively protect pyrene's excited state from quenching by added Cs^+ ions. Anthracene also displayed a similar trend with increasing PAMAM generation, albeit to a lesser extent. In accordance with our hypothesis, these results indicate that anthracene binds preferentially to the exterior of the

dendrimer, likely through cation-π or CH-π interactions, whereas pyrene is encapsulated within the hydrophobic confines of the dendrimer. This difference is particularly pronounced for the larger G4 and G5 dendrimers.

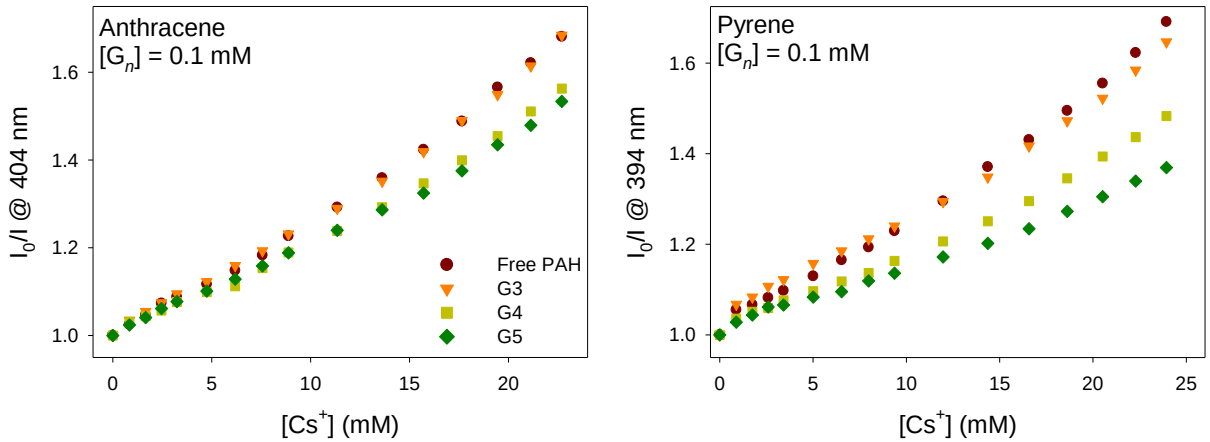

Figure 4-13 Stern-Volmer plots for anthracene (left) and pyrene (right) containing equal concentrations of G3-G5 PAMAM dendrimer ([G*n*] = 0.10 mM), upon the titration of CsCl. All measurements were conducted in a solution containing 7.2% MeOH by volume in H_2O buffered to pH 7.4 with 50 mM HEPES (anthracene $\lambda_{exc.}$ = 350 nm, pyrene $\lambda_{exc.}$ = 338 nm).

We repeated the Cs^+ quenching experiments at higher G4 PAMAM concentrations used above for fluorescence lifetime experiments The CsCl titrant solution was prepared using equal H_2O:methanol ratios as the cuvettes (75% H_2O:15% MeOH by volume, buffered to pH 7.4 with 50 mM HEPES). Fluorescence emission spectra were taken after each addition of aliquots (25-100 µL) of this CsCl titrant solution. The results from these titrations are presented in Figure 4-14. Based on these plots, it is apparent at this higher dendrimer concentration that pyrene was completely shielded from the quenching effects of Cs^+ ions. On the other hand, the higher G4 PAMAM concentration did not reduce the quenching of anthracene by Cs^+ ions; in fact, the anthracene probe displayed essentially no difference in the presence of the lower and higher G4 PAMAM dendrimer concentrations used in this study (i.e. [G4 PAMAM] = 0.10 vs. 0.84 mM).

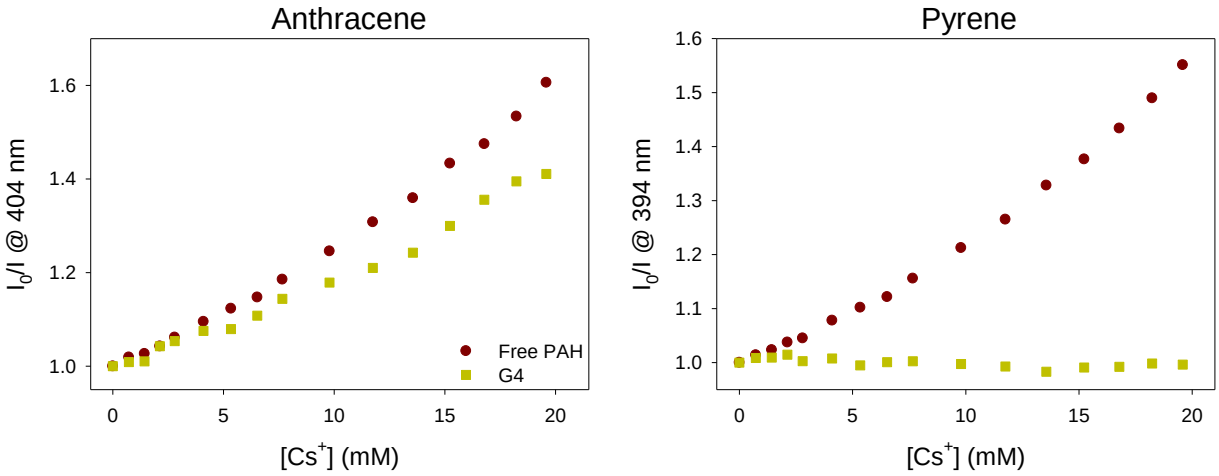

Figure 4-14 Stern-Volmer plots for anthracene (left) and pyrene (right), upon the titration of CsCl in the presence (gold squares) vs. absence (red circles) of G4 PAMAM dendrimer ([G4] = 0.84 mM). All measurements were conducted in a solution containing 15% MeOH by volume in H_2O buffered to pH 7.4 with 50 mM HEPES (anthracene $\lambda_{exc.}$ = 350 nm, pyrene $\lambda_{exc.}$ = 338 nm).

These results for two fluorescent aromatic hydrocarbon probes, pyrene and anthracene, display interestingly different trends in their binding modes to amine-terminated PAMAM dendrimers, both as a function of the dendrimer generation and concentration. This strongly suggests that pyrene is encapsulated deep within the polymer upon binding, whereas anthracene is bound closer to the dendrimer surface, at the interface with the bulk solution; there it interacts with the protonated termini, presumably through cation-π or CH-π interactions. These binding preferences are interesting and quite distinct, considering the similar chemical structure and properties of these relatively featureless hydrophobic aromatic molecules.

4.6 Conclusions

Poly(amidoamine) (PAMAM) dendrimers were proven to be capable of binding featureless polycyclic aromatic hydrocarbons (PAHs). By taking advantage of the probe's intrinsic fluorescence emission properties, a series of fluorescence-based experiments were carried out to investigate the extent to which these polymers can be envisioned as supramolecular

hosts for such hydrophobic hydrocarbons in aqueous media, expanding on Dr. Steelman's preliminary findings that these macromolecules exhibited enhanced affinity for guests containing aromatic moieties over their aliphatic counterparts.[156] In particular, we were also interested in establishing a baseline for Dr. Steelman's initial observations, using PAMAM dendrimer hosts for improved water solubility of this class of compound, possibly concentrating them out of solution, with an attention to future applications in sensing and remediation.

Fluorescence anisotropy experiments positively confirmed that spectral changes observed upon the interaction of these small-molecule fluorescent probes with PAMAM dendrimers in water stem from binding through a telltale increase in anisotropy signal upon addition of PAMAM, which was also sensitive to the macromolecules' size (generation). Time-resolved fluorescence emission experiments were also conducted, resulting in a greater change in lifetime for pyrene upon interaction with PAMAM, which was ascribed to pyrene's deeper encapsulation within the dendrimer upon binding, and thus, in closer proximity to the tertiary mine groups in the PAMAM structure, known to be effective dynamic quenchers for simple aromatic fluorophores.

The hypothesis of different binding locations for anthracene vs. pyrene was probed using selective quenching experiments with hydrophilic Cs^+ which, although an effective quencher, could only access the solvent-facing surface of the PAMAM dendrimer. The results from these experiments confirmed that anthracene was quenched more effectively by Cs^+, independent of dendrimer generation and concentration, whereas pyrene's emission was significantly less affected by Cs^+ ions for higher dendrimer generation and concentration. This was convincing evidence for the different binding modes *and* binding locations of these PAH probes to PAMAM

dendrimers. General considerations also indicate that these results should also apply to further members of this family of compounds.

In summary, our results suggest that these dendrimers offer interesting and varied binding modes for poorly water-soluble hydrocarbons in neutral water solution. The different binding modes observed for these two PAHs alone warrant further exploration into similar dendritic interactions with other PAH ring systems and chemical structures. This work opens the door to PAMAM dendrimers' further use as supramolecular hosts for otherwise featureless aromatic guests. Future work will also aim at understanding the exact nature of these interactions, e.g. between anthracene and PAMAM dendrimers (i.e. cation-π vs. CH-π interactions). These properties bode well for the development of pattern-based chemical fingerprinting systems for such polycyclic aromatic hydrocarbons, whose toxicological and environmental importance, which varies significantly within their family, make them valuable analytical targets for differentiation and quantitation attempts. Furthermore, the differential binding features of these PAHs, outlined in this chapter, can be exploited for many other applications, such as chemical separation and applications in controlled delivery of poorly water-soluble active ingredients.

4.7 Experimental details

4.7.1 Materials

Amine-terminated poly(amidoamine) (PAMAM) dendrimers with 1,2-diaminoethane (ethylenediamine, *en*) core were manufactured by Dendritech, Inc. and purchased from Sigma-Aldrich as methanol solutions at different concentrations depending on the dendrimer generation. Dendrimer solutions were stored at 4°C in a refrigerator. For each dendrimer generation, all experiments were carried out using the same batch (lot number) of dendrimer. Anthracene and pyrene were purchased from Sigma-Aldrich and used as received.

2-[4-(2-hydroxyethyl)piperazin-1-yl]ethanesulfonic acid (HEPES) was purchased from ICI Scientific. All experiments were carried out using a 50 mM HEPES aqueous solution buffered to pH 7.4, prepared by adding an appropriate amount of HEPES free acid to deionized (DI) water; the pH was then adjusted to 7.4 by adding 1.0 M NaOH as needed and monitoring with a combined glass electrode, then bringing up to volume. The HEPES concentration was diluted slightly (to between 40-50 mM), depending on the amount of PAMAM dendrimer stock solution (in MeOH) that was added to each cuvette.

4.7.2 Instrumentation

All experiments were conducted at 25°C, using an external circulating water bath. Steady-state fluorescence measurements were conducted with an ISS PC1 spectrofluorimeter. Excitation was carried out using a broad-spectrum high-pressure xenon lamp (CERMAX, 300W). Excitation correction was performed through a rhodamine B quantum counter with a dedicated detector. For anthracene, excitation was performed at 350 nm; for pyrene at 338 nm. Emission was recorded over a wavelength range of 370-600 nm for anthracene and 360-600 nm for pyrene. Excitation and emission wavelength selection were carried out by computer-controlled monochromators with manual slits for wavelength resolution control (for anthracene: 8 nm bandwidth for excitation, 4 nm for emission; for pyrene: 8 nm bandwidth for excitation, 2 nm for emission). Detection was through a Hamamatsu red-sensitive PMT. Computer-controlled high-aperture Glan-Thompson calcite polarizers were used in the excitation and emission channels to measure steady-state fluorescence anisotropy.

Fluorescence lifetimes were measured with an Edinburgh Photonics Mini-Tau time-resolved fluorometer using the time-correlated single photon counting technique (TC-SPC). Samples were excited by a picosecond-pulsed LED emitting at 310 nm (EPLED series) with a

pulse width of 900 ps. For experiments with anthracene and pyrene, a pulse repetition rate was set to 2 MHz and 0.5 MHz, respectively. Control of the excitation power was achieved through a continuously variable neutral density filter wheel to collect 2-3% excitation photons per second. A long-pass filter with a 450 nm cut-on wavelength was used for emission selection. Photons were detected by a high-sensitivity photomultiplier tube over a time range of 200 ns (for anthracene) and 1 μs (for pyrene). Decay curves were accumulated for 180 s (3 min.) and the resultant decay data was fit using the multi-exponential iterative reconvolution fit in the Edinburgh T900 software.

4.7.3 Thin film experimental setup

Stock solutions of anthracene and pyrene were prepared by adding about 25 mg of solid fluorophore to 25 mL of hexanes. Aliquots (200-300 μL) of fluorophore stock solution were transferred to a 1 cm quartz cuvette and the hexanes was carefully blown off via nitrogen stream. Care was taken so that the deposition of PAH was below the position of the impinging optical beam of the spectrofluorimeter. Aliquots of water buffered to pH 7.4 with 50 mM HEPES were then added to cuvettes containing the deposited solid PAH, followed by an appropriate aliquot of dendrimer stock solution in methanol. At this point, any deviation from pH 7.4 was corrected by adding a small amount of ~1 M HCl (ca. 3-7.5 μL) before filling to volume (3.0 mL) with more HEPES, to give [PAMAM] = 0.10 mM or 0.84 mM, depending on the experiment. Each cuvette was then sealed tight with Parafilm and stored in the dark at room temperature overnight, letting each solution reach dissolution equilibrium. The cuvettes were then subjected to steady-state fluorescence emission, time-resolved fluorescence lifetime, and fluorescence anisotropy measurements.

For Cs^+ quenching experiments, the supernatant from each equilibrated cuvette was removed and added to a clean 1 cm quartz cuvette. A stock solution of cesium chloride was prepared separately by adding the solid salt to 5 mL HEPES buffer, to give a ca. 0.35 M solution. The Cs^+ titrant solution was made by taking an aliquot of the CsCl stock solution (about 1 mL), adding to HEPES buffer, and then filling to volume with appropriate amounts of buffer and methanol to achieve the same content of MeOH as the cuvette solutions (% by volume). Small aliquots of this Cs^+ titrant solution were added to the cuvette, and a fluorescence emission measurement taken after each addition (excitation at 350 nm for anthracene; at 338 nm for pyrene).

CHAPTER 5

ARRAY SENSING OF OPTICALLY DENSE COMPOUNDS USING THE INNER-FILTER EFFECT

5.1 Introduction

In the previous chapter, we discussed the interactions between polycyclic aromatic hydrocarbons (PAHs) with poly(amidoamine) (PAMAM) dendrimers. The systems discussed there have applications in hydrophobic solubilization and drug dissolution and delivery.[149,185-186] Moreover, these findings pave the way for interesting applications in separation science, such as these polyelectrolytes' preferential affinity of aromatic compounds over aliphatics.[156] However, the driving force for differentiation, i.e. cation-π interactions are relatively weak, and they are likely not selective enough for sensing of unmodified PAHs. Chemical sensing of these uncharged, non-polar, and relatively featureless compounds represents a major challenge. Specialized techniques such as liquid and gas chromatography (LC and GC), and capillary electrophoresis are commonly used for PAH separation and detection.[187-192] These methods often require complex sample preparation (i.e. extraction and analyte pre-concentration), specialized equipment and personnel, and extra time for sample transport and processing to a lab facility. Therefore, significant problems in environmental science, such as source, environmental transport modes, and exposure tracing are complicated by the lack of effective in situ detection methods for these powerful pollutants.

While several PAH receptors have been reported, such as cyclodextrins (CDs),[193] calix[n]arenes,[194] and cationic cyclophanes,[195] their affinity and selectivity are highly dependent

on the size and shape of their non-polar cavity. Any one receptor would be selective, at best, for only a few specific PAHs of a given size. Achieving high discriminatory power for many PAHs would require a series of specialized distinct hosts, operated in parallel. Instead of using the subtle structural differences of simple PAHs (mass, polarity, size), more distinctive optical properties of each PAH could be more easily leveraged for discrimination. In particular, fluorescent conjugated polymer scaffolds used in Chapter 3 were selected as excellent candidates thanks to their high sensitivity to environmental conditions and bright fluorescence. In general, fluorescent sensors based on conjugated polymers operate through analyte- and aggregation-induced phenomena outlined previously, which serve to manipulate exciton migration and modulate the fluorescence response.[69-70] As a complement to typical fluorescent conjugated polymer probes that require polymer-analyte interactions via molecular recognition elements along the polymer backbone, the inner filter effect (IFE) was proposed as an alternative approach. The inner filter effect, typically considered a drawback in fluorescence studies, generates a reduction of a target fluorophore's emission signal, caused by the absorption of light by another chromophore in solution, either by preventing incident photons from exciting the target fluorophore (primary IFE, pIFE), or by absorbing the fluorophore's emitted light (secondary IFE, sIFE).[196]

In this chapter, the IFE is demonstrated, in combination with conjugated polymer-based array sensing, as an effective approach for the discrimination of 16 PAH compounds listed as priority pollutants by the Environmental Protection Agency (EPA).[197] To this end, a series of neutral conjugated polymers were synthesized, based on the fluorene co-polymer scaffolds used previously in our metal ion detection work (Chapter 3). To provide the greatest spectral overlap with the target PAH analytes allowing for an optimal IFE, specific optical modifiers were added

to the polymer backbone. This system takes advantage of intrinsic spectroscopic properties of each individual PAH, circumventing the need for specially made receptors for these chemically inert, featureless hydrocarbons. Finally, the promising results from this PAH detection work led to the development of a comparable detection system based on the IFE and similar conjugated polymers for the discrimination of 12 textile azo dyes in water.

5.2 Polymer design and optical characterization

The conjugated polymer receptors were prepared by the Azoulay research group from the University of Southern Mississippi. Much like the polymeric receptors discussed previously, the polymer's backbone was designed around a common fluorene core with varying conjugated spacer groups incorporated in an alternating fashion. Covalently attached to the fluorene was either a 2-phenylbenzimidazole optical modifier group or an ethylene glycol group; the former group being structurally similar to UV-absorbing agents commonly added to sunscreen and offering good spectral overlap between the absorbance of the polymer and PAH analytes. In total, six polymers were designed to provide a broad range of distinct structures and optical properties (see Scheme 5-1).

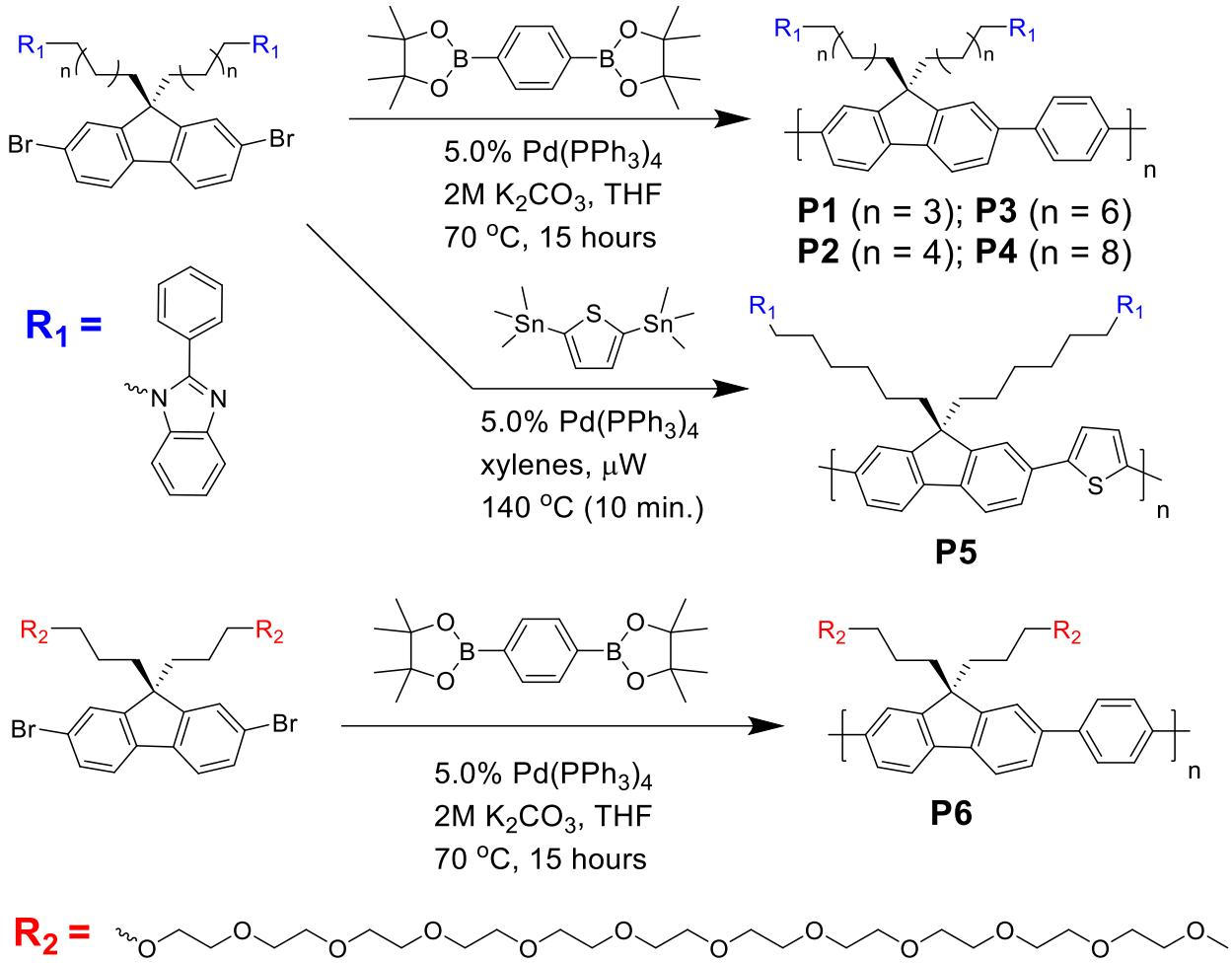

Scheme 5-1 Chemical structure and synthetic scheme of conjugated polymers, **P1-P6**, used for the detection of PAHs.

Polymers **P1-P4** demonstrate a systematic lengthening of the spacer groups between the 2-phenylbenzimidazole group and the conjugated polymer backbone, with 5, 6, 8, and 10 methylene units, respectively, leading to distinct differences in their optical spectra. Polymer **P5** incorporated a thiophene conjugate spacer group, leading to a red-shifted absorbance and emission maxima. Finally, **P6** was constructed by replacing the optical modifier side group with an ethylene glycol group, whose absorption spectrum lacks the higher energy band ($\lambda_{max.}$ = 290 nm). The normalized absorption and fluorescence spectra for all six polymers are displayed in Figure 5-1.

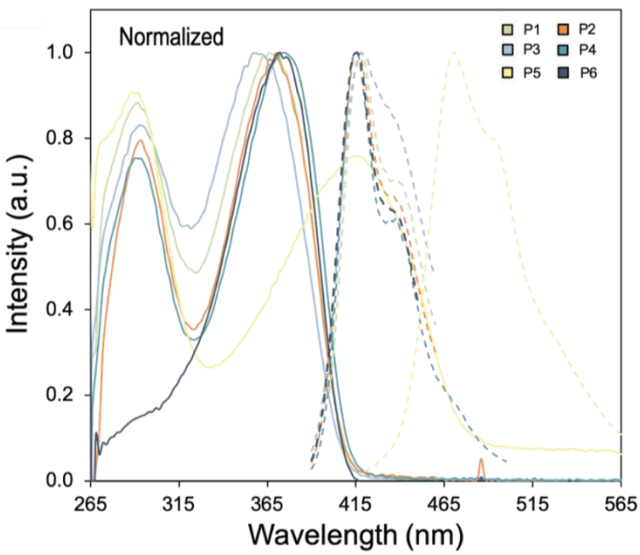

Figure 5-1 Normalized absorbance and fluorescence emission spectra of **P1-P6** in DMF.

As a representative example, polymer **P2** exhibits an absorption maximum of 374 nm, providing optimal spectral overlap in the regions of maximum absorption for a variety of PAHs, in the range of 250-500 nm. Figure 5-2a illustrates this spectral overlap between **P2** and anthracene, leading to significant observed quenching of the polymer's emission as anthracene is added to **P2** (Figure 5-2b). Specifically, anthracene acts as a "chemical filter" in this case, blocking the incident light from reaching the conjugated polymer. Therefore, as more anthracene was added, excitation of **P2** at 374 nm led to a stark decrease in the polymer's fluorescence emission ($\lambda_{em.}$), centered around 415 nm.

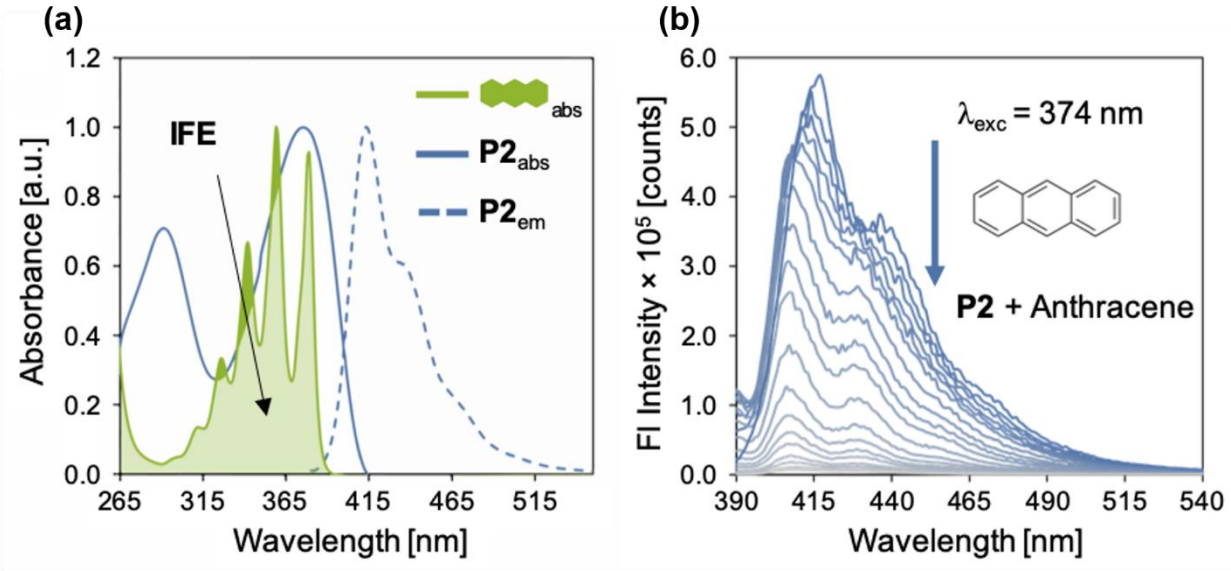

Figure 5-2 (a) Overlap between excitation and emission spectra of **P2** with the absorbance spectrum of anthracene ([anthracene] = 10 µM; [**P2**] = 15 mg L^{-1}), providing the basis for an IFE. (b) Representative fluorescent spectra of **P2** (15 mg L^{-1}) upon the titration with anthracene ([anthracene] = 0-9.4 mM; $\lambda_{exc.}$ = 374 nm). All spectra were recorded in *N*,*N*-dimethylformamide (DMF).

Several representative PAHs were titrated into **P1**-**P4** to study the effect of each PAH on the emission of each polymer. Thus, three PAHs, anthracene, acenaphthylene, and pyrene were chosen, representing a range of ring fusion and optical properties (i.e. molar absorptivity and position of the absorption maximum) in the family of PAHs. Small but noticeable differences in quenching efficiency were observed when polymers **P1**-**P4** interacted with each PAH, suggesting that even subtle structural modifications affected the fluorescence response. More dramatic differential responses were observed among the PAHs, which can be explained by the differences in molar absorptivity for each PAH at a given wavelength. The resultant titration profiles and wavelength dependence of the molar extinction coefficients are presented in Figure 5-3, in which the polymer emission is quenched differentially by the presence of the selected PAHs via the IFE. For instance, at excitation wavelength of 374 nm, anthracene has the greatest molar extinction coefficient, and as such, was the most efficient quencher of the three

PAHs. In fact, the molar absorptivity values at 374 nm for these PAHs directly correlate with the observed degree of quenching.

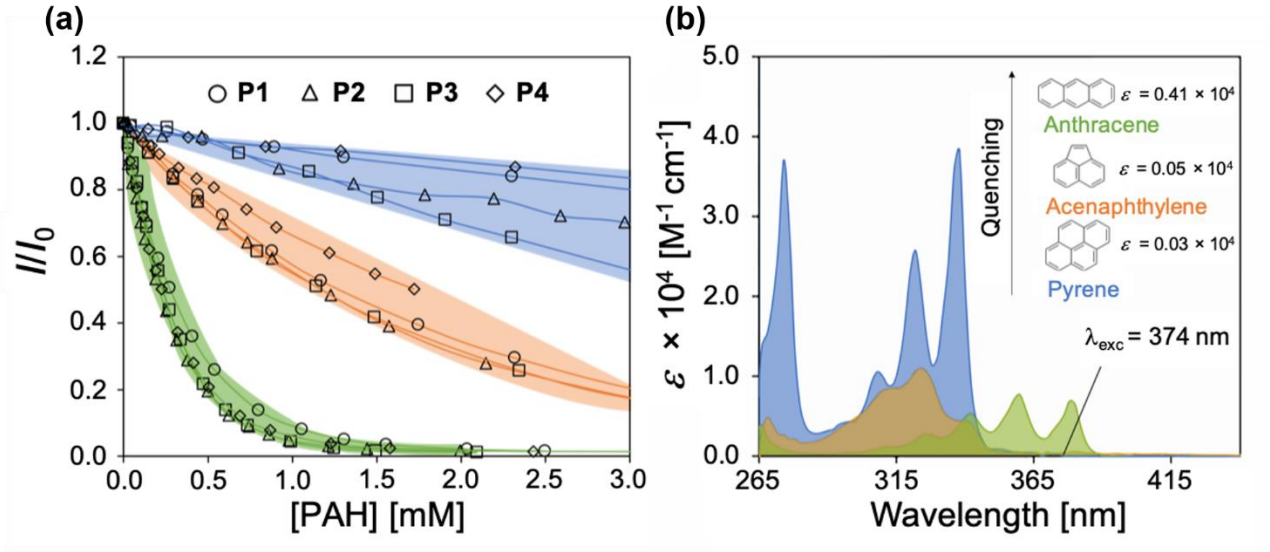

Figure 5-3 (a) Fluorescence titration profiles of **P1-P4** upon the addition of aliquots of anthracene, acenaphthylene, and pyrene in DMF ($\lambda_{exc.}$ = 374 nm, $\lambda_{em.}$ = 418 nm). (b) Wavelength dependence of molar extinction coefficient for anthracene, acenaphthylene, and pyrene. The colors indicate the PAH involved.

5.3 Evidence for the IFE

To elucidate the mechanism of fluorescence quenching, a variety of experiments were conducted to rule out other possible quenching pathways. As mentioned previously, the absorbance spectra of each PAH span a range of wavelengths from 250-500 nm, overlapping with the absorbance and emission spectra of **P1-P6**. This spectral overlap opens the possibility for fluorescence resonance energy transfer (FRET),[166] or the IFE, both of which are possible under these circumstances. To determine the mechanism of quenching for this system, fluorescence lifetime measurements were performed for anthracene in the absence and presence of **P2** as a representative example. If the observed quenching occurs via energy transfer processes, then a distinct change in the lifetime decay profile should be evident when the polymer is added.[198-199] Furthermore, the absorbance spectrum of the **P2**-anthracene mixture was

additive, completely matching with the calculated sum of the individual absorbances of each component. This ruled out aggregation and the formation of a ground-state complex between **P2** and anthracene. These measurements are presented in Figure 5-4.

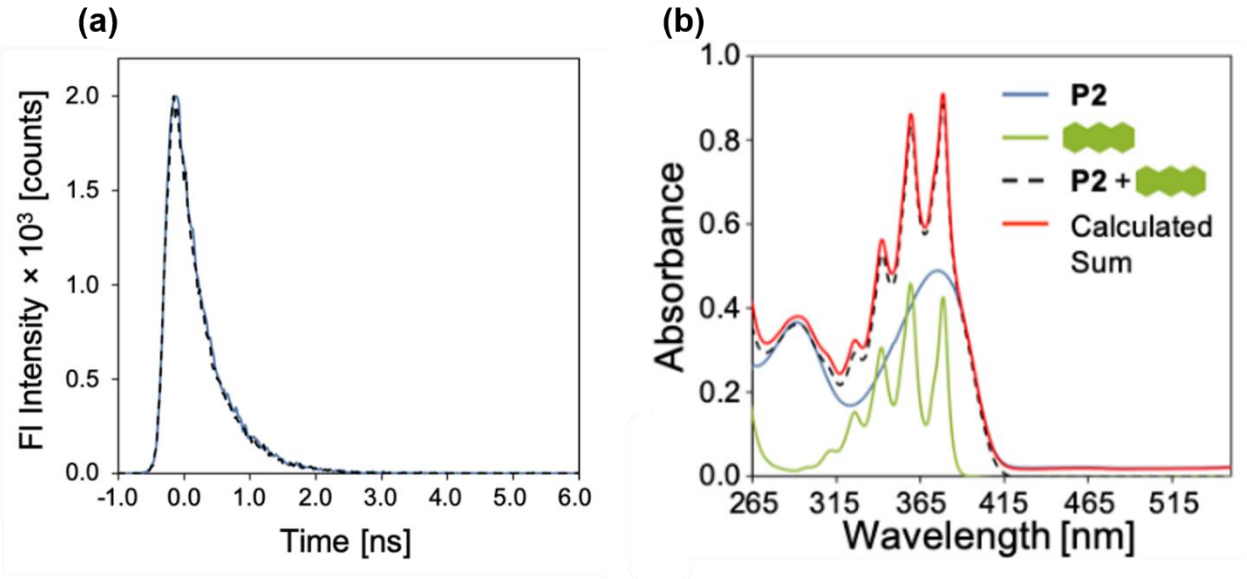

Figure 5-4 (a) Emission decay of **P2** (15 mg L^{-1}) before and after the addition of anthracene (500 µM) in DMF. (b) UV-vis absorption spectra of **P2**, anthracene, a mixture of **P2** and anthracene, compared to a simulated spectrum, calculated from sum of the individual experimental absorbance spectra.

Fluorescence anisotropy experiments were also conducted to investigate whether direct binding took place between the PAH analyte and these polymers. As mentioned in the previous chapter, a strong increase in fluorescence anisotropy indicates a slower rotational diffusion rate of a small fluorophore due to binding to a larger molecule.[166] For these experiments, **P5** was titrated into a solution of anthracene ([anthracene] = 100 µM in DMF). Polymer **P5** was chosen as the representative example because its emission spectrum is free of overlap with that of anthracene. Therefore, changes in anthracene's tumbling rate in solution could be directly and independently observed. As shown in Figure 5-5, no increase in fluorescence anisotropy was observed for anthracene's emission as more **P5** was added, suggesting that there was no binding

between anthracene and **P5**. Given all of these experimental results, the IFE is the most likely quenching mechanism of these polymers in the presence of PAH analytes.

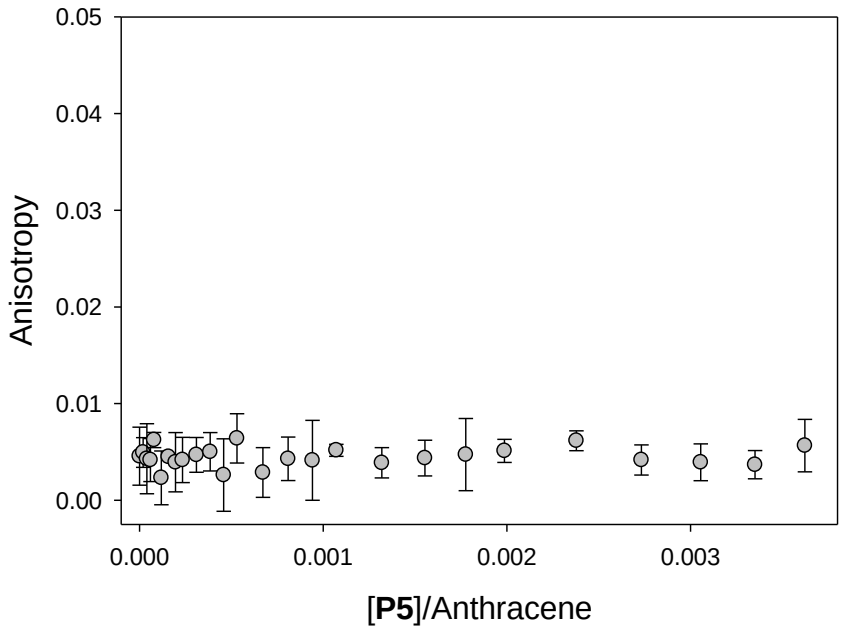

Figure 5-5 Fluorescence anisotropy as **P5** is titrated into anthracene (100 µM) in DMF. If binding occurred, a significant increase in fluorescence anisotropy would have been observed ($\lambda_{exc.}$ = 350 nm).

5.4 Pattern recognition of PAHs using conjugated polymers

The 16 PAH compounds identified as priority pollutants by the EPA were chosen as target analytes (Scheme 5-2). Each PAH demonstrates varying spectral overlap with these polymers. Figure 5-6 illustrates the unique spectral overlap between **P2** and **P6** and all 16 PAHs, providing the basis for differential quenching through the IFE. The minor structural variations between each polymer, in combination with the distinct relationship of molar absorptivity and wavelength for each PAH, provided a library of differential response that could be used for discrimination using pattern recognition techniques.

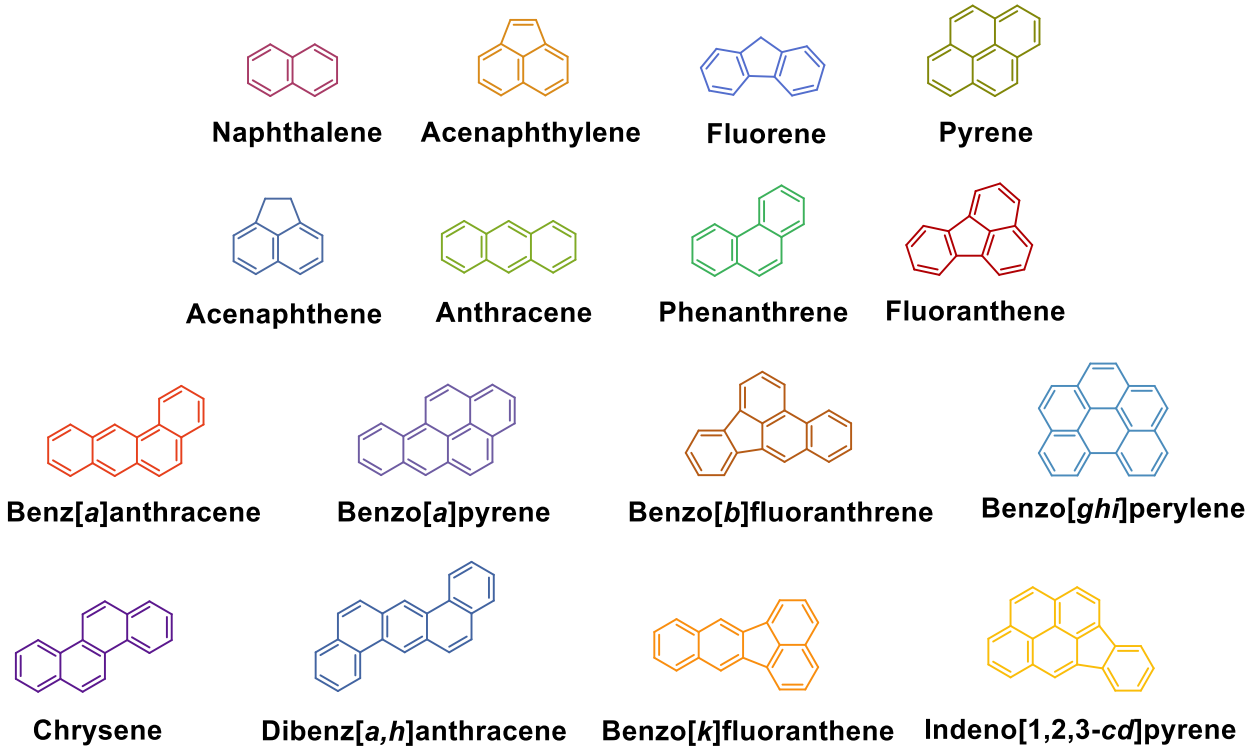

Scheme 5-2 The chemical structures of all 16 PAH analytes identified by the EPA as priority pollutants of interest.

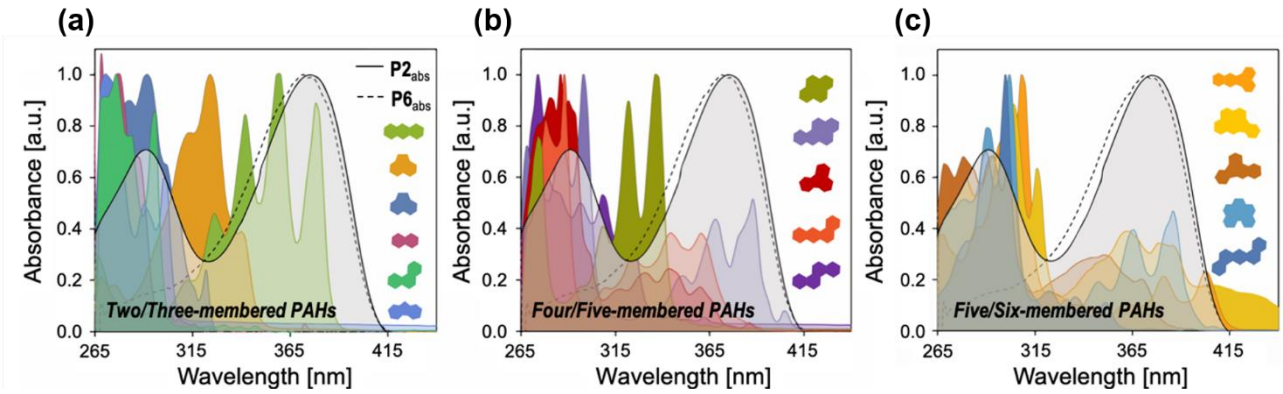

Figure 5-6 Normalized UV-vis absorption spectra of **P2** (solid line, [**P2**] = 15 mg L^{-1}) and **P6** (dashed line, [**P6**] = 15 mg L^{-1}) overlaid with the absorption spectra of (a) two- and three-membered PAHs, (b) four- and five-membered PAHs, and (c) five- and six-membered PAHs in DMF ([PAHs] = 10 µM).

Solutions of **P1-P6** in DMF (15 mg L^{-1}) were arranged on 384-well microplates and were exposed to 500 µM solutions of the 16 PAHs mentioned earlier as persistent pollutants by the

EPA.[200] Each PAH-polymer combination was prepared in replicates of 12 and multiple spectroscopic measurements were collected on a microwell plate reader. In total, 21 absorbance measurements, between 280-700 nm, were collected and six fluorescence measurements were collected using the following filter combinations ($\lambda_{exc.}/\lambda_{em.}$): 330/460 nm, 330/485 nm, 330/516 nm, 380/460 nm, 380/485 nm, and 380/516 nm, which correspond to the regions of greatest spectral overlap between the polymers and each PAH analyte.

After data collection, any superfluous instrumental measurements were removed from the original data set if their contribution to PAH discrimination was confirmed to be negligible, i.e. in the case of absorbance measurements above 500 nm. After initial removal of these absorbance measurements, the optical responses of **P1-P6** in the presence of each PAH were exposed to linear discriminant analysis (LDA), as outlined previously. Complete differentiation of 16 PAHs was observed, while retaining 78.0% of the total information from the original data set. Displayed in Figure 5-7 are the resulting plots of LDA scores and loadings. Replicate points of the same PAH were found to cluster tightly together, indicating excellent reproducibility. On the other hand, replicate clusters from different PAHs were very well-separated, demonstrating the strong discriminatory power of the conjugated polymer-based array.

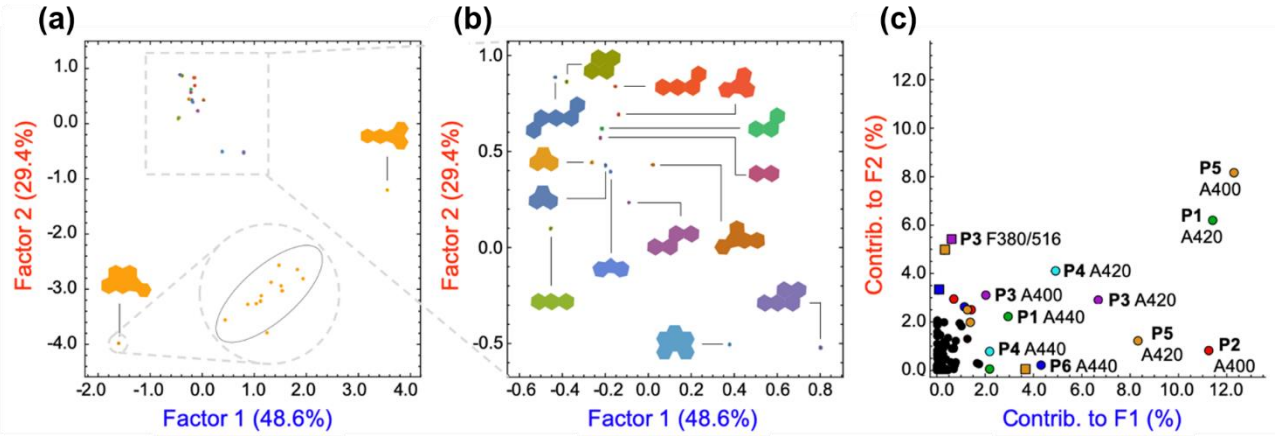

Figure 5-7 (a) Two-dimensional plot of LDA scores for the differentiation of 16 PAHs with **P1-P6** ([PAH] = 500 µM; [**P1-P6**] = 15 mg L^{-1}). The plot was generated using 114 instrumental measurements and captures 78.0% of the total information in the raw data set. The inset displays an example of the tight intra-cluster spacing of replicate samples for indeno[1,2,3-*cd*]pyrene. (b) Zoom-in on the LDA scores plot from Figure 5-7a for 14 PAHs, displaying less-than-ideal inter-cluster spacing for these analytes. All confidence ellipsoids are drawn to 95% confidence level. (c) LDA loadings plot for the differentiation of 16 PAHs shown in Figure 5-7a, displaying the relative contributions of each instrumental measurement to the first two LDA factors. Colored squares: contributions from fluorescence measurements. Colored circles: contributions from absorbance measurements.

Based on the LDA loadings plot (Figure 5-7c), the most important contributors to differentiation were absorbance signals in the range of 420-480 nm, arising from two PAHs in particular; namely benzo[*k*]fluoranthene and indeno[1,2,3-*cd*]pyrene. These two PAHs alone display unique, low-energy absorbance in this region and thus are overrepresented in the discrimination. Due to the disproportionately high weighting for these two PAHs in the LDA analysis, the other 14 are forced unnecessarily closer together, degrading the quality of their separation. In fact, the absorbance measurements for each polymer between 420-480 nm contain mostly noise with very little coherent signal, relative to the absorbance at lower wavelengths (< 420 nm). This is best represented by a visual overview of the quality of the information conveyed by each instrumental measurement, as presented in Figure 5-8. Based on this analysis, these absorbance measurements were removed from the data set and LDA was repeated.

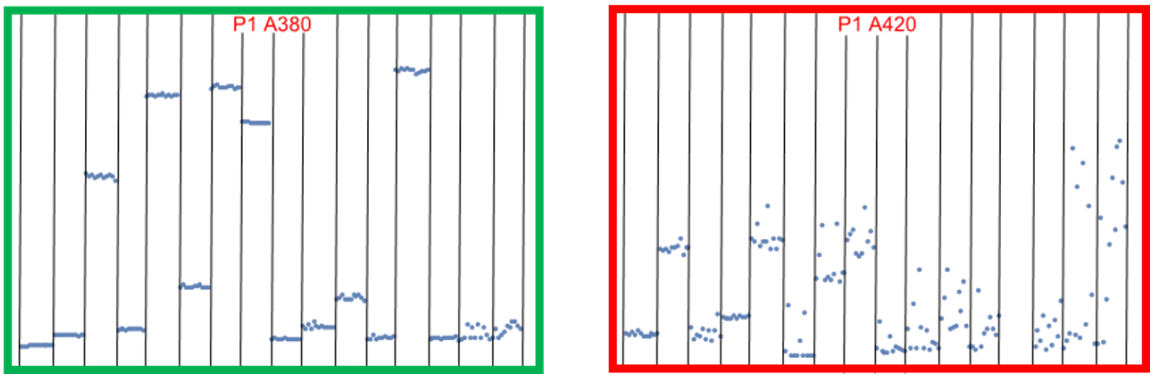

Figure 5-8 A representative example of one information-rich (green, < 420 nm) vs. an information-poor (red, ≥ 420 nm) measurement channel for all 16 PAH analytes; each horizontal "section" in the plot corresponds to replicate responses from one of the 16 PAH analytes (each PAH is separated by vertical lines).

After removal of the information-poor absorbance measurements between 420-480 nm, the resultant data set was subjected to LDA and subsequent data reduction, providing a significant improvement and better overall performance in the discriminatory power of the array. Furthermore, the corresponding LDA loadings plot revealed a reduced importance of absorbance signals, with fluorescence measurements being the most important contributors to discrimination, as we had hoped. An array-based sensor that relies on fluorescence of fluorene-based co-polymers is highly desirable given the high quantum efficiency of these materials, potentially leading to low limits of differentiation using these optical properties, as has been seen in previous chapters. The plots of LDA scores and loadings for this optimized data set is displayed in Figure 5-9.

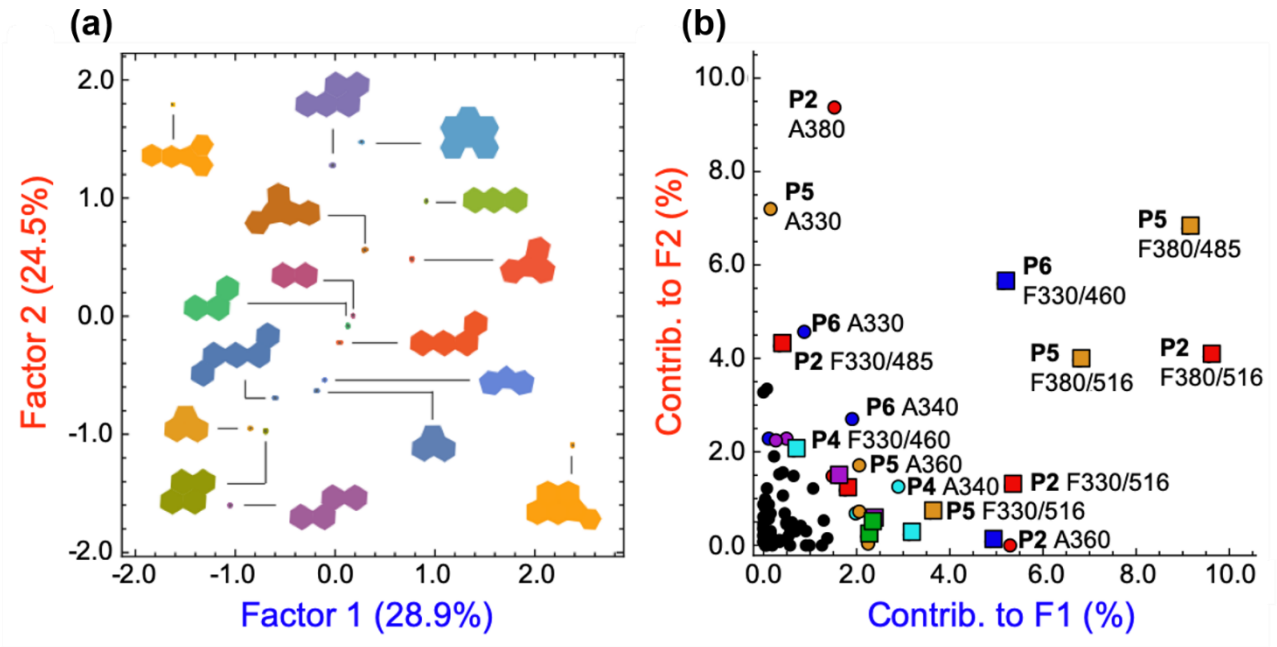

Figure 5-9 (a) Two-dimensional plot of LDA scores for the differentiation of 16 PAHs with polymers **P1-P6** ([PAH] = 500 µM); [**P1-P6**] = 15 mg L^{-1}). This plot was generated using the 79 most important instrumental measurements and captures 53.4% of the total information in the raw data set. All confidence ellipsoids are drawn to 95% confidence level. (b) LDA loadings plot for the differentiation of 16 PAHs shown in Figure 5-9a, displaying the relative contributions of each instrumental measurement to the first two LDA factors. Colored squares: contributions from fluorescence measurements. Colored circles: contributions from absorbance measurements.

Despite the vast improvement in discriminatory performance of the array, only half of the total information was retained in the first two factors (53.4%). Indeed, simply including the third factor and plotting the results in three dimensions allowed retention of an additional 21.3% of the total information. As shown in Figure 5-10, the three-dimensional LDA scores plot now retains 74.7% of the total information contained in the original data set and displayed even better inter-cluster separation than the corresponding 2D plot. Notably, the information content was distributed evenly among the three factors, indicating that multiple independent instrumental measurements contributed significantly to discrimination, an ideal situation in pattern recognition.

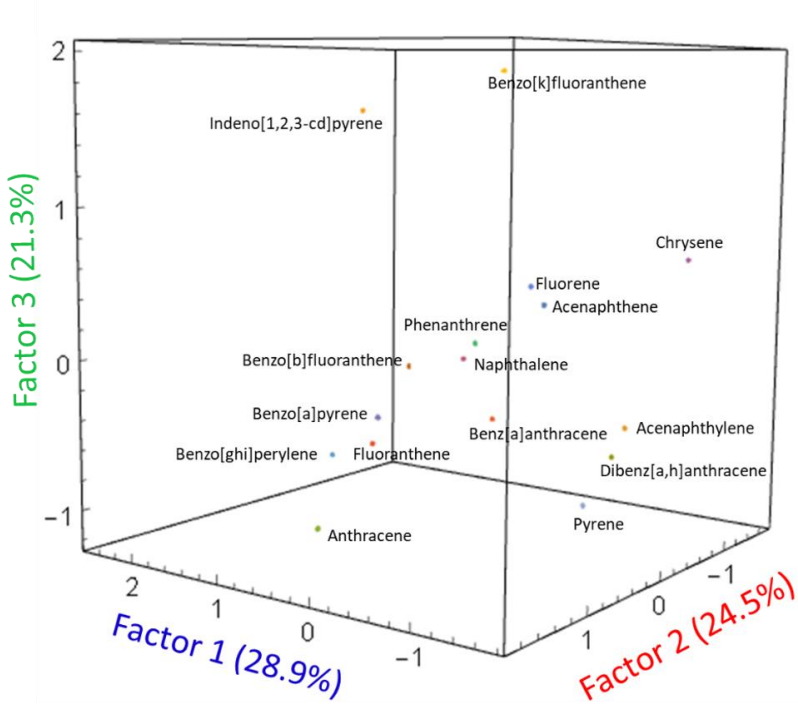

Figure 5-10 Three-dimensional plot of LDA scores for the differentiation of 16 PAHs with polymers **P1-P6**. The plot captures 74.7% of the total information contained in the raw data set ([PAH] = 500 µM; [**P1-P6**] = 15 mg L^{-1}). All confidence ellipsoids are drawn to 95% confidence level.

As a control experiment, the role of **P1-P6** was investigated by analyzing a data set containing absorbance and fluorescence measurements from only the PAHs, without the polymers. LDA analysis of this data set showed that complete separation of all 16 PAHs was *not* achieved on the basis of their optical responses alone. In fact, any discrimination of PAHs in these conditions was, once again, mostly reliant on the absorbance measurements. Incomplete discrimination could be ascribed to their similar absorbance features and their lack of signal in relevant spectroscopic regions. Thus, the naphthalene, fluorene, acenaphthene, and phenanthrene clusters were completely overlapped and could not be differentiated without modulating their effect on the **P1-P6** fluorescence. The plots of LDA scores and loadings from this control experiment are displayed in Figure 5-11.

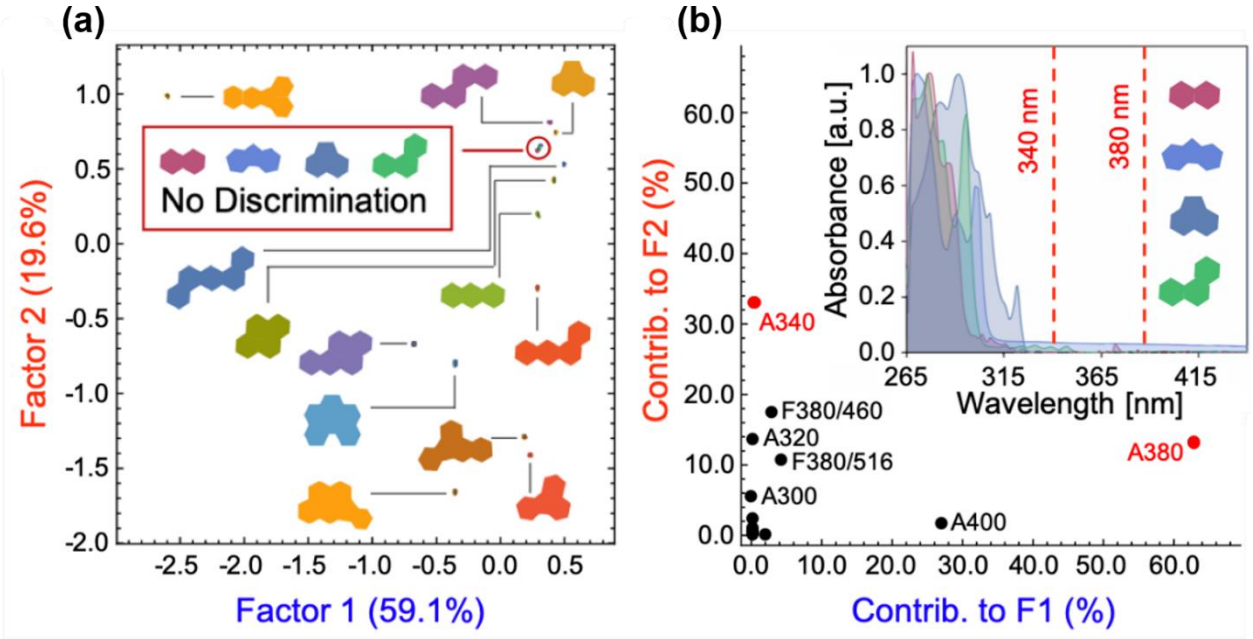

Figure 5-11 (a) LDA scores plot for the attempted differentiation of 16 PAHs without the inclusion of the polymers, **P1-P6** ([PAH] = 500 µM). All confidence ellipsoids are drawn to 95% confidence level. (b) LDA loadings plot for the attempted differentiation of 16 PAHs without the polymers shown in Figure 5-11a. Inset: UV-vis absorbance spectra of naphthalene, fluorene, acenaphthene, and phenanthrene; red points in the loadings plot denote the most important absorbance measurements, between 340-380 nm, where little signal is observed for these four PAHs.

Finally, the data set was also analyzed by principal component analysis (PCA). As mentioned previously, PCA provides an unsupervised representation of the variance in the data set. The two-dimensional PCA plots with and without the use of the polymers are displayed in Figure 5-12. The PCA analysis also gives complete separation of all 16 PAHs with very tight intra-cluster distances, retaining 70.7% of the total information in the first two principal components (PCs). Moreover, just like the LDA analysis, PCA was able to differentiate all 16 PAHs only when the polymers were used.

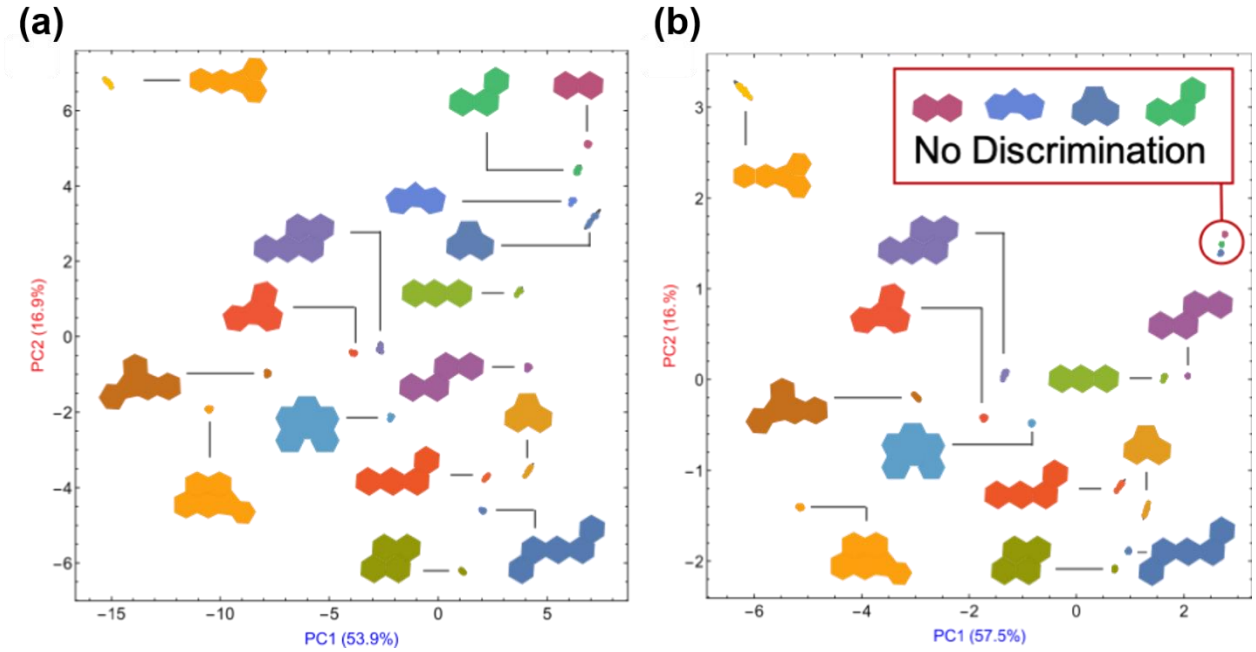

Figure 5-12 Two-dimensional PCA scores plot for the (a) differentiation of 16 PAHs using **P1-P6** and (b) attempted differentiation of 16 PAHs without **P1-P6** ([PAH] = 500 µM; [**P1-P6**] = 15 mg L^{-1}). All confidence ellipsoids are drawn to 95% confidence level.

In short, we have reported a highly tunable platform using an array of six conjugated polymers and optical modifiers, designed to have good spectral overlap with 16 PAH analytes, allowing for their complete detection through the inner filter effect (IFE) in a single experiment. These results were published in 2019 and laid the groundwork for an extension into discrimination of these relatively featureless hydrocarbons and other pollutants with high optical densities.[165]

5.5 Azo dye detection using conjugated polymers and the IFE

Given the positive results for PAH detection using conjugated polymers and the IFE, the same methods were extended to azo dye discrimination. Azo dyes are a ubiquitous class of synthetic dyes that contain one or more azo linkages (-N=N-), accounting for more than 50% of the global dye production.[201] These materials make up over 700,000 tons of manufactured dyes annually and are widely applied to textile fibers, plastics, leathers, cosmetics, and other

consumer products.[202-203] They are classified as persistent pollutants in wastewater discharge which readily elude industrial treatment processes.[204-205] They possess high chemical stability in the environment, they are resistant toward chemical or biological degradation, and when they do react, cleavage of the azo linkage is known to produce carcinogenic or mutagenic aniline by-products, making the disposal of these dyes a severe threat to human, biota, and ecosystem health.[206-207] In fact, current detection methods rely on the detection of the aromatic amine by-products,[208-209] leading to lengthy pre-treatment procedures before specialized techniques are used, such as gas and liquid chromatography coupled to mass spectrometry (GC-MS and LC-MS),[210-211] and high-performance liquid chromatography (HPLC).[212] Important questions regarding source attribution, environmental effects, and toxicology of these azo dye pollutants would benefit from rapid, portable, high-throughput, and cost-effective methods to improve their detection in the field (e.g. wastewater treatment plants for routine water quality monitoring).[213]

Like PAHs, many azo dye compounds are relatively featureless, except the azo group, with many chemical and structural similarities between different dyes. Given that azo dyes are strongly colored, they were selected as excellent candidates as analytes in a conjugated polymer-based array using the inner filter effect (IFE). Although several fluorescence sensors have been developed for the detection of azo dyes using the IFE, they were not able to offer complete and selective differentiation of multiple dyes given their very similar optical absorption profiles.[214-215] Thus, a series of conjugated polymer receptors were specially designed to provide effective spectral overlap for the IFE and combined with pattern recognition techniques to give complete discrimination of 12 azo dyes.

A set of three anionic conjugated polyelectrolytes (CPEs) were, once again, synthesized by the Azoulay group at the University of Southern Mississippi based on fluorene co-polymer

scaffolds, as used in previous sections. The three fluorene co-polymers were designed to have three distinct conjugated spacer groups in an alternating fashion, as outlined in Scheme 5-3. As discussed previously, incorporation of these ethynyl (**P7**), thiophene (**P8**), and 2,2'-bithiophene (**P9**) groups within the polymer backbone resulted in a systematic red-shift in the polymers' absorbance and fluorescence emission maxima, going from **P7** to **P9**. This allowed for strong and differential overlap with the absorption features of many common azo dyes. As a representative example, the absorbance and emission spectra for the **P8** polymer are displayed in Figure 5-13, overlaid with the absorbance of Congo Red (CR), a toxic, carcinogenic benzidine-based azo dye.[216] The good spectral overlap allows Congo Red to behave as a "chemical filter" causing apparent quenching of the **P8** polymer's fluorescence through the IFE. Additional design features included peripheral anionic butanesulfonate groups which promote water solubility and reduce aggregation of the conjugated polyelectrolytes. Perhaps more importantly, the multiple negative charges along the polymer backbone prevent direct interaction of the polymers with the negatively charged azo dyes, thereby restricting other possible quenching mechanisms, such as energy transfer processes, and promoting IFE effects.

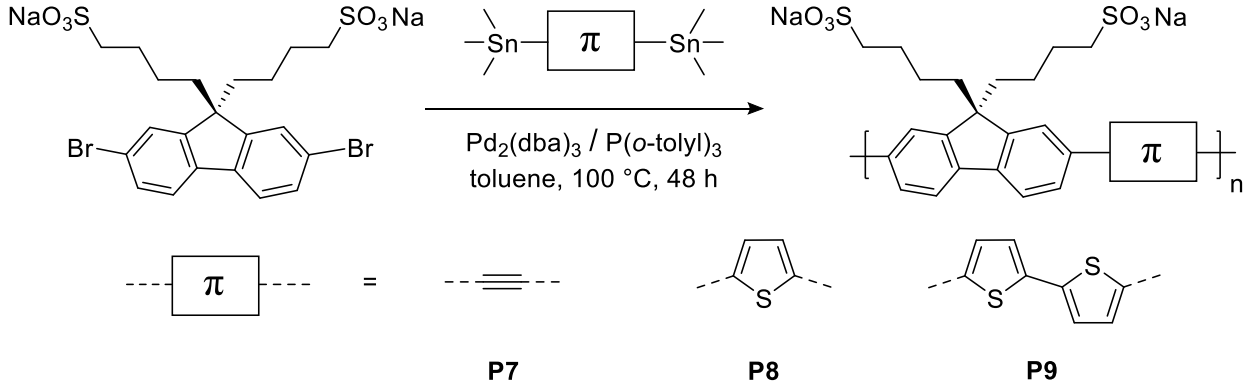

Scheme 5-3 Chemical structures and synthetic scheme of conjugated polyelectrolytes, **P7-P9**, used for the detection of azo dyes.

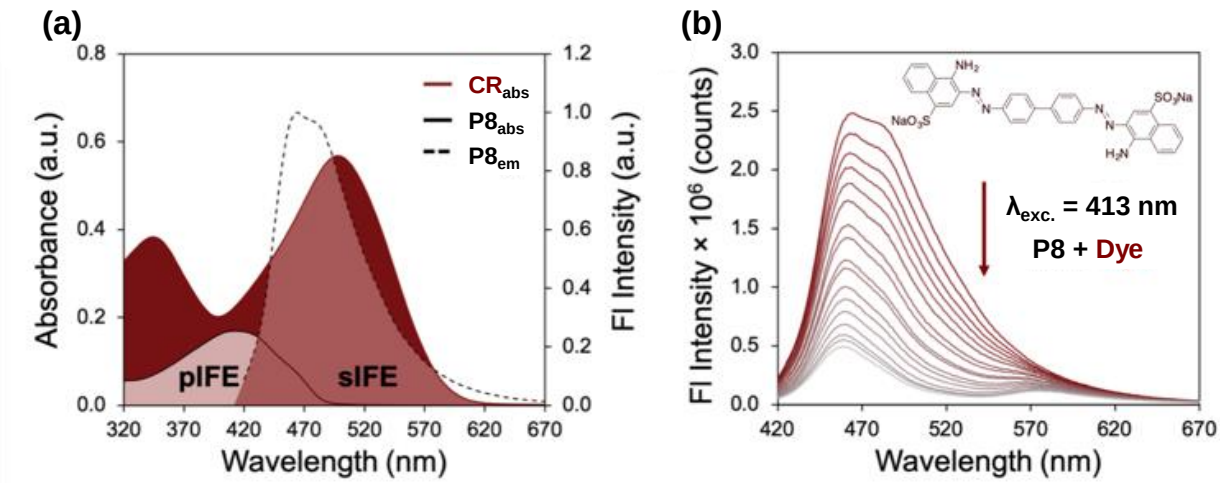

Figure 5-13 (a) Normalized excitation and emission spectra of **P8** overlaid with the absorbance spectrum of Congo Red ([CR] = 15 µM; [**P8**] = 10 µM), providing a good basis for the IFE. (b) Fluorescence spectra of **P8** (10 µM) upon the titration with Congo Red in deionized (DI) water ($\lambda_{exc.}$ = 413 nm).

The absorbance and fluorescence spectra of all three polymers, **P7-P9**, falls within the region of maximum absorbance for Congo Red, allowing the opportunity for the pIFE and sIFE, i.e. Congo Red prevents incident light from exciting the polymer (pIFE), or Congo Red absorbs the polymer's emitted light (sIFE). The absorbance and emission spectra of each polymer, overlaid with the absorbance spectrum of Congo Red are presented in Figure 5-14, along with the corresponding emission profiles at the wavelength of maximum fluorescence emission for each polymer in the presence of increasing Congo Red concentrations. When **P7** was excited at its absorption maximum (ca. 360 nm), it demonstrated the least efficient quenching, due to the weakest absorbance (pIFE) and emission overlap (sIFE) with Congo Red. Polymer **P8** demonstrated the best sIFE with Congo Red; however, there was only minor involvement from the pIFE, as the absorbance signals of **P8** and Congo Red have minimal overlap. **P9** showed the greatest contributions from both the pIFE and sIFE and, therefore, displayed the most efficient quenching.

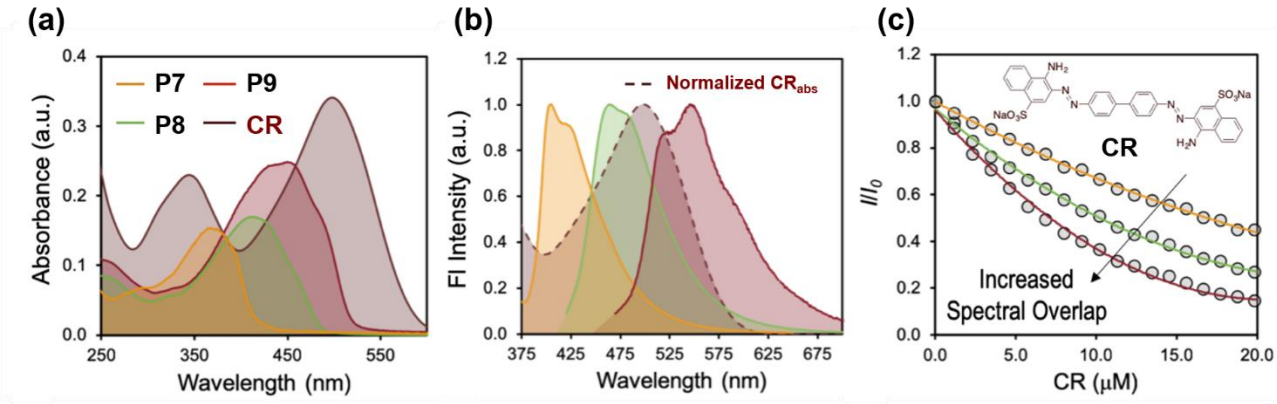

Figure 5-14 (a) Absorbance spectra of **P7-P9** ([polymer] = 10 μM) overlaid with that of Congo Red ([CR] = 10 μM). (b) Normalized emission spectra of **P7-P9** ([polymer] = 10 μM) compared to the normalized absorbance spectrum of Congo Red ([CR] = 10 μM). (c) Fluorescence titration profiles for **P7-P9**, upon the addition of aliquots of Congo Red. The excitation and emission wavelengths ($\lambda_{exc.}/\lambda_{em.}$) used were the wavelengths of maximum absorbance and emission for each polymer.

Displayed in Figure 5-15 are the chemical structures of 12 common azo dyes that were selected for inclusion in a sensing array, along with a comparison of each dye's molar absorptivity spectra, illustrating the fact that these dyes absorb light in a similar region of the spectrum, yet with varying intensity. These dyes were chosen for their related optical features and potential for toxic and carcinogenic by-products.[206,217] The absorbance and emission of **P7-P9** were designed to fall within this spectral region (250-550 nm), offering the opportunity for differential quenching of the conjugated polyelectrolytes via the pIFE and sIFE. As had been the case in our previous work with PAHs, minor variations in chemical structure and optical spectra among different azo dye analytes, in combination with each dye's unique relationship with the optical properties of the polymers, provided an assortment of differential responses in the emission behavior of the conjugated polymers that could be used for discrimination.

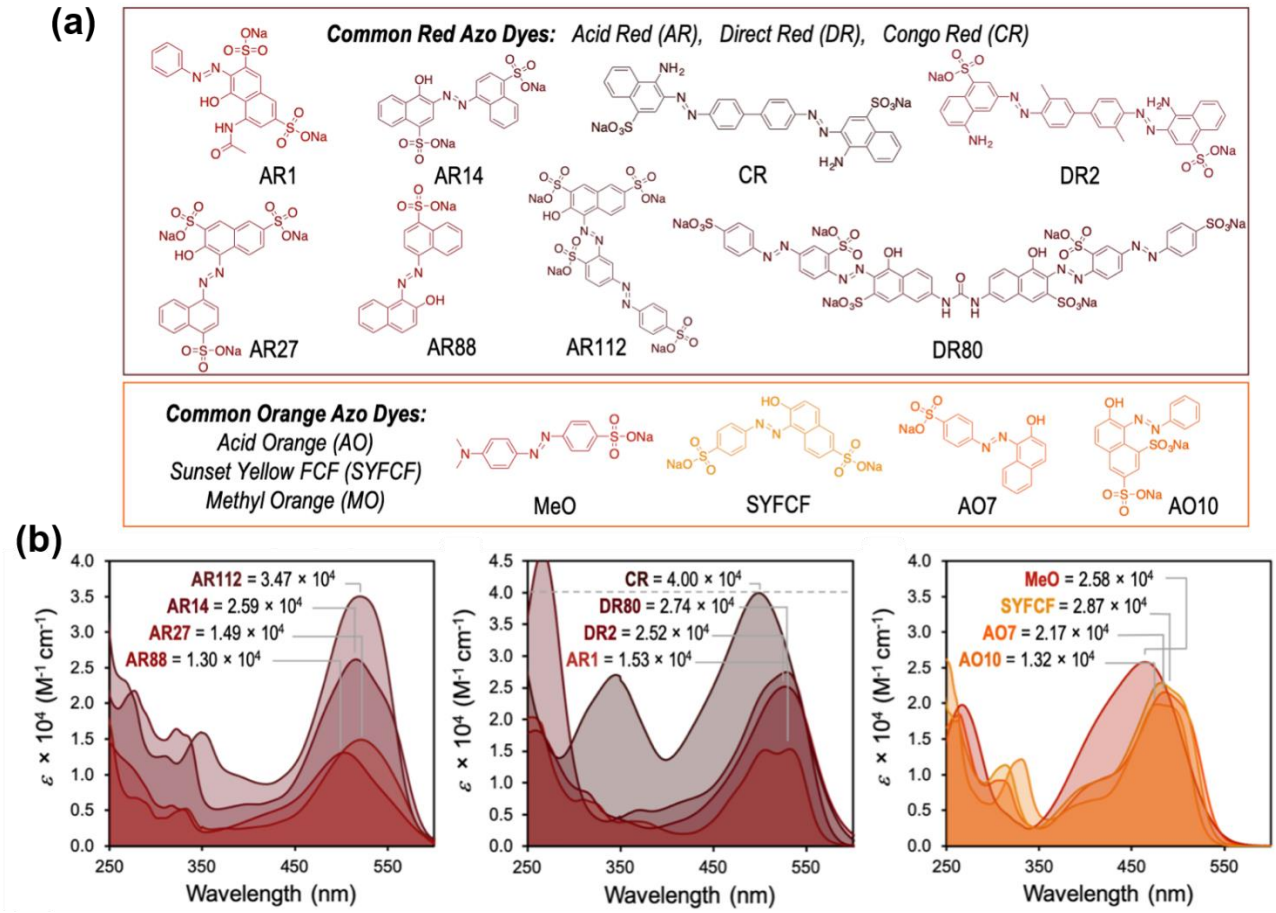

Figure 5-15 (a) Chemical structures of 12 target azo dye analytes identified as hazardous pollutants. (b) Wavelength dependence of molar absorptivity for 12 target azo dye analytes in aqueous solution. Extinction coefficients at each dye's absorbance maximum ($\lambda_{max.}$) are annotated.

The mechanism of fluorescence quenching was investigated using steady-state absorbance and time-resolved fluorescence measurements. Between 200-600 nm, there is clear spectral overlap between the dyes' absorption peaks and the excitation and emission bands of **P7-P9**. Therefore, there is the possibility of fluorescence resonance energy transfer (FRET) as an alternative quenching mechanism instead of the IFE.[166] The fluorescence lifetime of the polymers was measured in the absence and presence of Congo Red, chosen as a representative example. Based on Figure 5-16a, it is evident that the lifetime of **P8** does not display any significant change upon the addition of Congo Red (15 μM), ruling out the possibility that the

decreased emission of the polymers in its presence could be due to a dynamic quenching mechanism.[198-199,218] The fluorescence lifetimes for **P7**-**P9**, with and without Congo Red, are presented in Table 5-1, displaying negligible change upon the addition of the azo dye. Furthermore, the absorption spectrum of a mixture of **P8** and Congo Red is completely additive, matching the sum of the individual spectra of dye and polymer, ruling out the formation of a ground-state complex between the polymer and Congo Red and, consequently, the possibility of static quenching (see Figure 5-16b). Similar behavior was observed with **P7** and **P9**, shown in Figure 5-17. Considering these results, the IFE was the most probable mechanism for quenching of the polymer's emission with azo dyes.

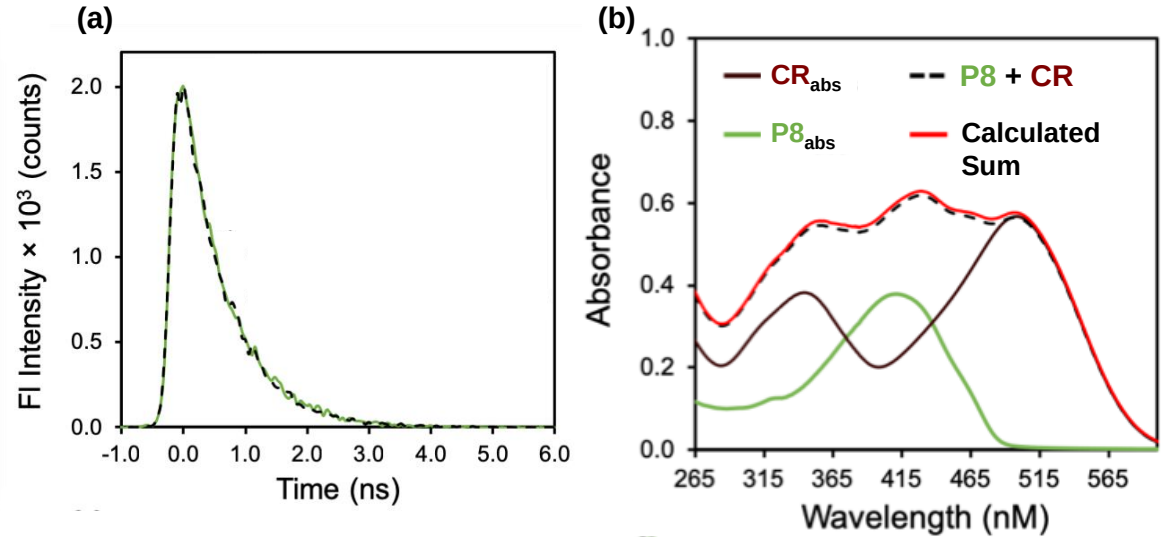

Figure 5-16 (a) Emission decay profile of **P8** (10 µM) before and after the addition of Congo Red (CR) (15 µM) in DI H_2O. (b) UV-vis absorption of **P8** (20 µM), CR (15 µM), and a mixture of **P8** and CR, compared to a simulated spectrum calculated from the sum of the individual experimental spectra.

Table 5-1 Time-resolved fluorescence decay parameters from single exponential fitting of the decay profile data for **P7**-**P9** and a mixture of each polymer and Congo Red (CR).

τ_1 (ns)	P7	P8	P9
Polymer	0.841	0.893	0.525
Polymer + CR	0.788	0.893	0.578

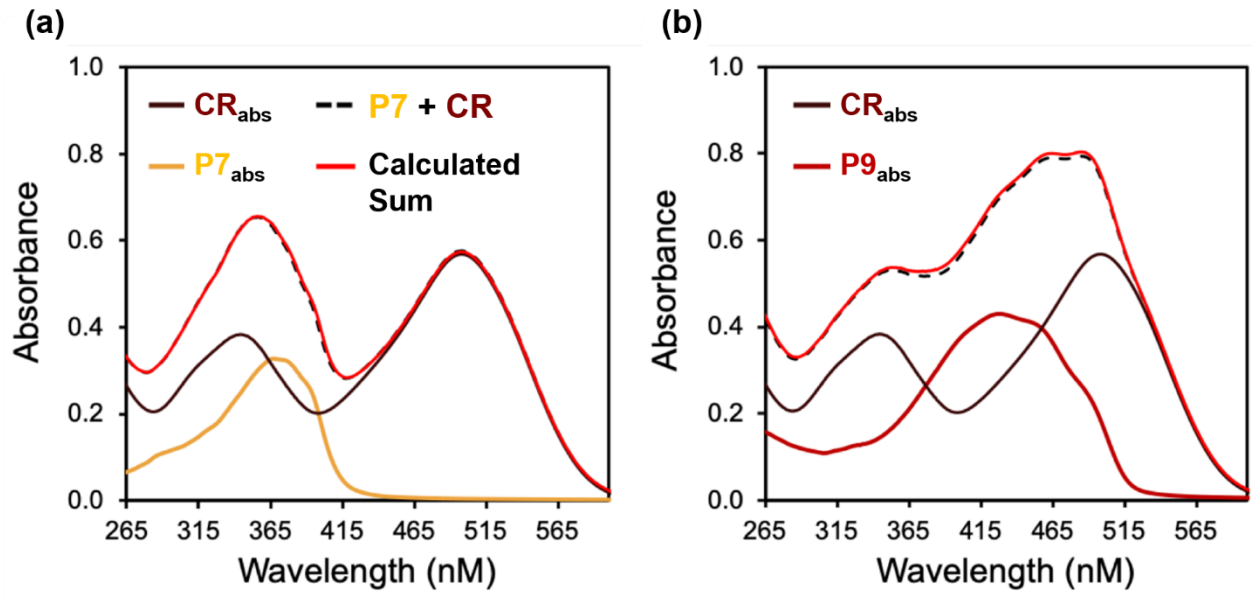

Figure 5-17 (a) UV-vis absorption of **P7** (20 µM), Congo Red (CR) (15 µM), and a mixture of **P7** and CR, compared to a simulated spectrum calculated from the sum of the individual experimental spectra. (b) UV-vis absorption of **P9** (20 µM), CR (15 µM), and a mixture of **P9** and CR, compared to a simulated spectrum calculated from the sum of the individual experimental spectra.

5.6 Pattern recognition of azo dyes

Once again, rapid data acquisition was achieved by arranging aqueous solutions of **P7-P9** (10 µM) on a 384-well microplate and exposing them to the 12 azo dyes. Each polymer-dye combination was prepared in replicates of 14 in this case, and multiple absorbance and fluorescence measurements were collected on a microwell plate reader, corresponding to the regions of greatest spectral overlap between the polymers and dyes. At [azo dye] = 15 µM, a total of 25 fluorescence measurements were collected for each polymer-dye sample. The resultant data set was then subjected to multivariate analysis (LDA and PCA), and the corresponding two-dimensional plots of LDA scores and loadings were generated (Figure 5-18).

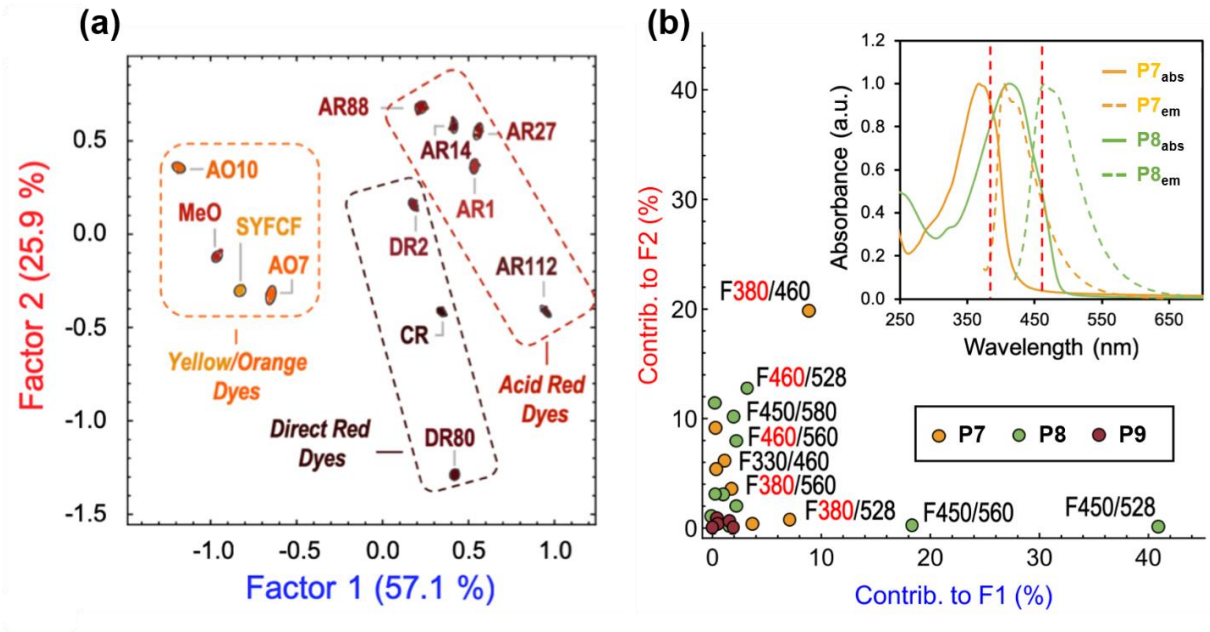

Figure 5-18 (a) Two-dimensional plot of LDA scores for the differentiation of 12 azo dyes with **P7-P9** in DI H_2O ([dye] = 15 µM, [**P7-P9**] = 10 µM). The plot was generated using the 23 most important fluorescence measurements and captures 83.0% of the total information in the raw data set. All confidence ellipsoids are drawn to 95% confidence level. (b) Corresponding LDA loadings plot for the differentiation of 12 azo dyes, indicating the relative contributions of each instrumental measurement to the first two LDA factors. Inset: Absorbance and emission spectra of **P7** and **P8**, with the wavelengths of maximum contribution outlined (red dotted lines, spanning 380-460 nm).

Each azo dye was well-separated, with small intra-cluster distances and large inter-cluster spacing. Altogether, 83.0% of the information in the original data set was retained in the first two factors. The factor loadings from the LDA analysis, i.e. the contributions of the instrumental measurements, indicate that the fluorescence of **P8** contributed the most to discrimination. In fact, the wavelengths of maximum excitation/emission for **P8** displayed the greatest differences in spectral overlap with each dye's absorbance maximum (see Figure 5-18, inset).

As usual, the corresponding two-dimensional PCA scores plot (Figure 5-19) was also analyzed and was found to successfully discriminate all 12 azo dyes, indicating good data quality for this system; i.e. the discrimination via the supervised LDA analysis is retained using the

unsupervised PCA analysis, and thus the separation is solely due to existing features of the data, reporting on underlying interactions of the array components.

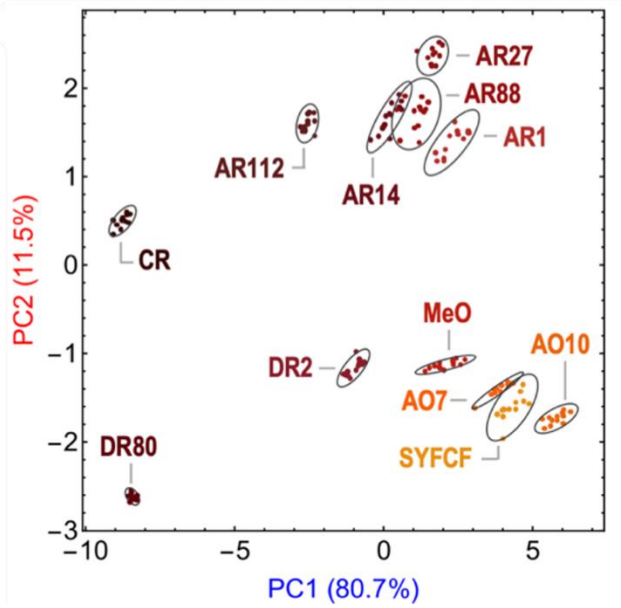

Figure 5-19 Two-dimensional PCA scores plot for the differentiation of azo dyes at 15 µM using **P7-P9** (10 µM). The plot was generated using the 23 most important fluorescence measurements in the original data set. All confidence ellipsoids are drawn to 95% confidence level.

At a concentration of 15 µM, using only fluorescence data was a good test of the polymer's capabilities, since most azo dyes showed significant absorbance signal at this concentration. Thus, using any absorbance data would either be redundant or inconclusive regarding the polymers' importance towards differentiation. Given the high significance of the polymers' fluorescence, the array was tested at sub-micromolar azo dye concentrations, often encountered in environmental samples such as rivers and wastewater.[205] The array was exposed to azo dyes at 500 nM, in which the absorbance signals of the dyes are no longer detectable. When the polymers were incorporated, the information obtained from the combined absorbance and fluorescence measurements from **P7-P9** ([polymer] = 375 nM) allowed us to achieve differentiation of all 12 azo dyes at these "optically silent" azo dye concentrations. Figure 5-20 displays the LDA and PCA scores plot at 500 nM dye concentration in the presence of the

conjugated polyelectrolyte sensors: replicates of the same azo dye sample clustered tightly together, and clusters from different analytes were clearly separated. In the polymer-based differentiation experiments, the factor loadings showed that fluorescence measurements were the most important contributors to the discrimination (Figure 5-21). Given that the azo dye analytes are not fluorescent,[219] the high significance of fluorescence data indicates the prominent role of **P7-P9** to the successful analytical separation of these dyes at nanomolar concentrations in aqueous solution. Particularly, the emission data from **P9** was the most important because its absorption and emission bands had the most extensive overlap with the dye's absorbance bands between 450-600 nm (see Figure 5-21, inset).

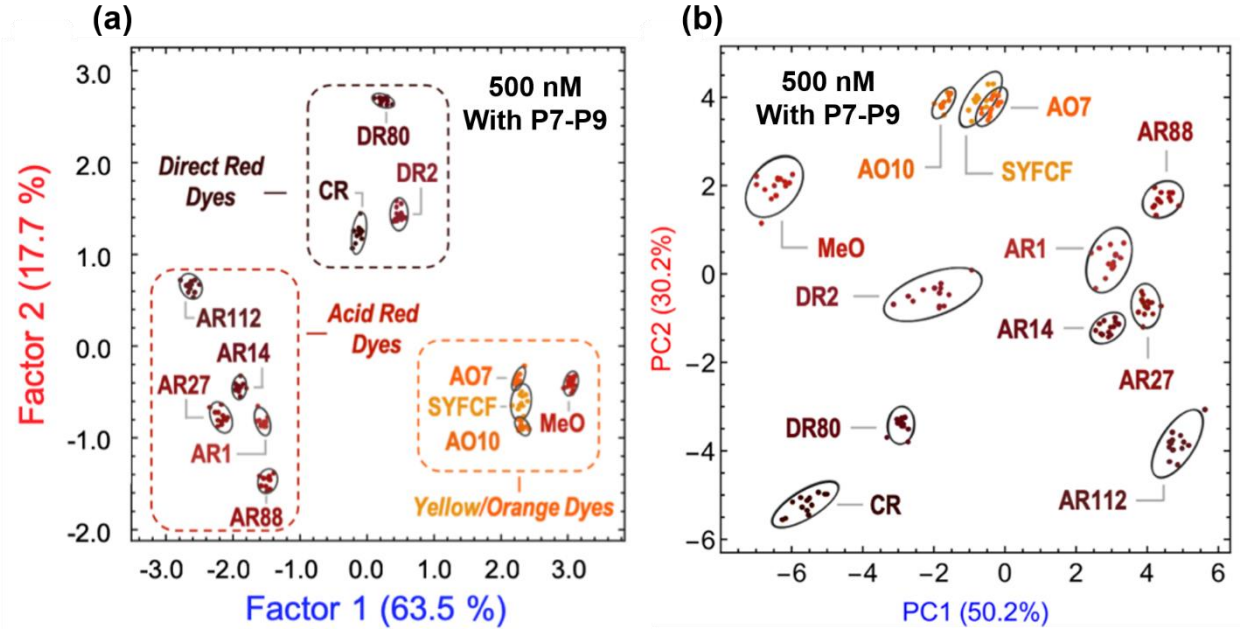

Figure 5-20 (a) Two-dimensional plot of LDA scores for the differentiation of 12 azo dyes ([dye] = 500 nM) with **P7-P9** ([polymer] = 375 nM) in DI H_2O. The plot was generated using 29 absorbance and fluorescence measurements and captures 81.2% of the information in the original data set. (b) Two-dimensional plot of PCA scores for the differentiation of 12 azo dyes with **P7-P9** at 500 nM in DI H_2O, using 29 absorbance and fluorescence measurements. All confidence ellipsoids are drawn to 95% confidence level.

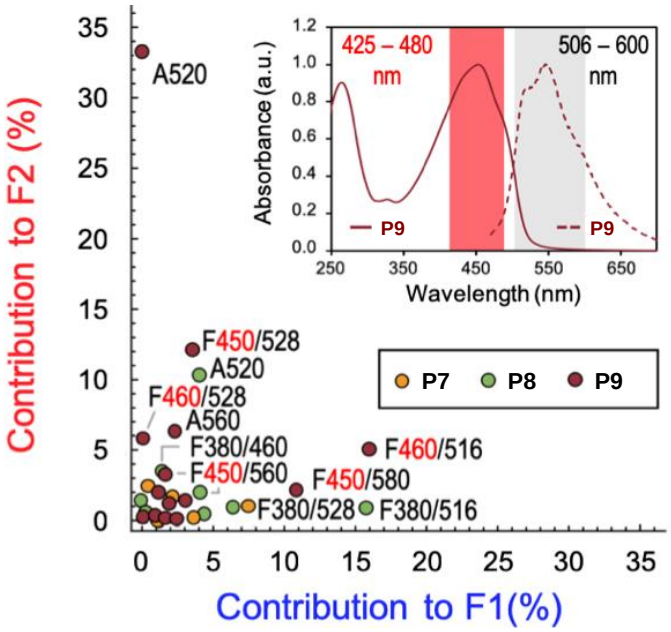

Figure 5-21 LDA loadings plot for the differentiation of 12 azo dyes shown in Figure 5-20a, indicating the relative contributions of each instrumental measurement to the first two LDA factors. Inset: UV-vis absorbance and fluorescence spectra of **P9**, highlighting the spectral regions of maximum contribution, expressed as the bandwidth of the corresponding optical filter sets. ($\lambda_{exc.}$ in red, $\lambda_{em.}$ in grey).

As a control experiment to further highlight the polymers' importance, the same 12 azo dye analytes ([azo dye] = 500 nM) were added to a 384-well microplate without the polymers in DI water, and 14 absorbance measurements were taken between 300-560 nm in 20 nm increments. Multivariate analysis (LDA and PCA), followed by variable and dimensionality reduction of the resultant data set led to the scores plots shown in Figure 5-22. Given that the absorbance signals of the azo dyes were too low at this concentration, differentiation based simply on the absorbance data alone was incomplete; classification of the azo dyes was limited only to grouping within their color index. For instance, the closely related red dyes (AR14 and AR27), as well as yellow/orange dyes (AO10 and SYFCF) are not well separated in the LDA scores plot. Moreover, the PCA scores plot at [azo dye] = 500 nM displayed even more

significant overlap between the red and yellow/orange dyes when only absorbance measurements were used without **P7-P9**.

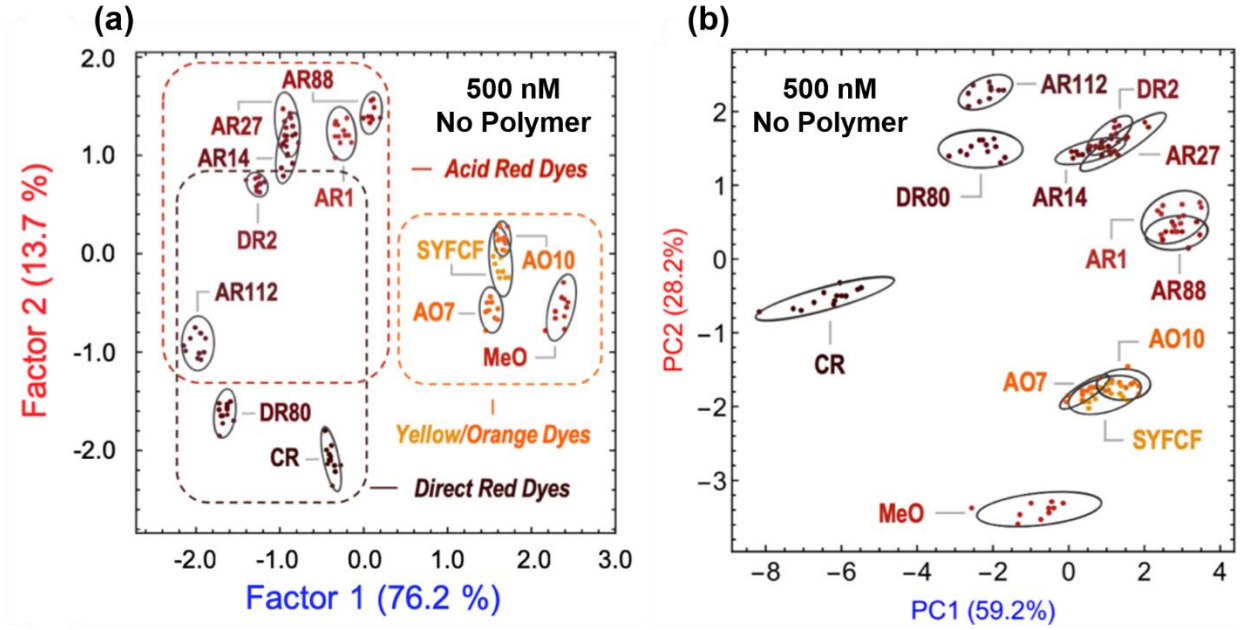

Figure 5-22 (a) Two-dimensional plot of LDA scores for the attempted differentiation of 12 azo dyes without **P7-P9** at 500 nM in DI H_2O. The plot was generated using the 11 most important absorbance measurements and captures 89.9% of the information in the original data set. (b) Two-dimensional plot of PCA scores for the attempted differentiation of 12 azo dyes without **P7-P9** at 500 nM in DI H_2O, using 11 absorbance measurements. All confidence ellipsoids are drawn to 95% confidence level.

Given the excellent discriminatory ability in low-salinity water, we examined the utility of the array in artificial seawater, to represent a more challenging analytical matrix. As mentioned previously, seawater is particularly demanding for optical detection platforms due to its high salinity, and presence of many chemical interferents that may attenuate fluorescence signals through electron and energy transfer processes.[69] However, highly fluorescent conjugated polyelectrolytes have been shown here and elsewhere to avoid such quenching phenomena and retain their strong fluorescence signal.[78] Given the more demanding matrix, we returned to the same experimental conditions that were used for the [azo dye] = 15 µM array ([polymer] = 10 µM). Using the same artificial seawater mentioned previously for metal ion

sensing with conjugated polyelectrolytes (Table 3-1),[147] six azo dyes (AR1, AR14, AR27, DR80, AO10, and SYFCF, 15 µM), which showed good solubility in seawater at 15 µM, were dissolved in this medium, and added to the array. For this experiment, we went back to collecting both absorbance and fluorescence measurements since absorbance signals could once again be reliably detected at [polymer] = 10 µM and [azo dye] = 15 µM. Like the 15 µM array in low-salinity water, we first attempted to use only fluorescence measurements for differentiation. After multivariate analysis, followed by variable and dimensionality reduction, we obtained the two-dimensional LDA and PCA scores plots, displayed in Figure 5-23. Good discrimination was only obtained using LDA as PCA led to poor differentiation. To improve the PCA results, absorbance measurements were included in the data set to achieve better discrimination and less noise from the unsupervised PCA technique in seawater. Multivariate analysis followed by subsequent variable and dimensionality reduction generated the LDA and PCA scores plots shown in Figure 5-24, displaying clear differentiation of all six azo dyes in artificial seawater.

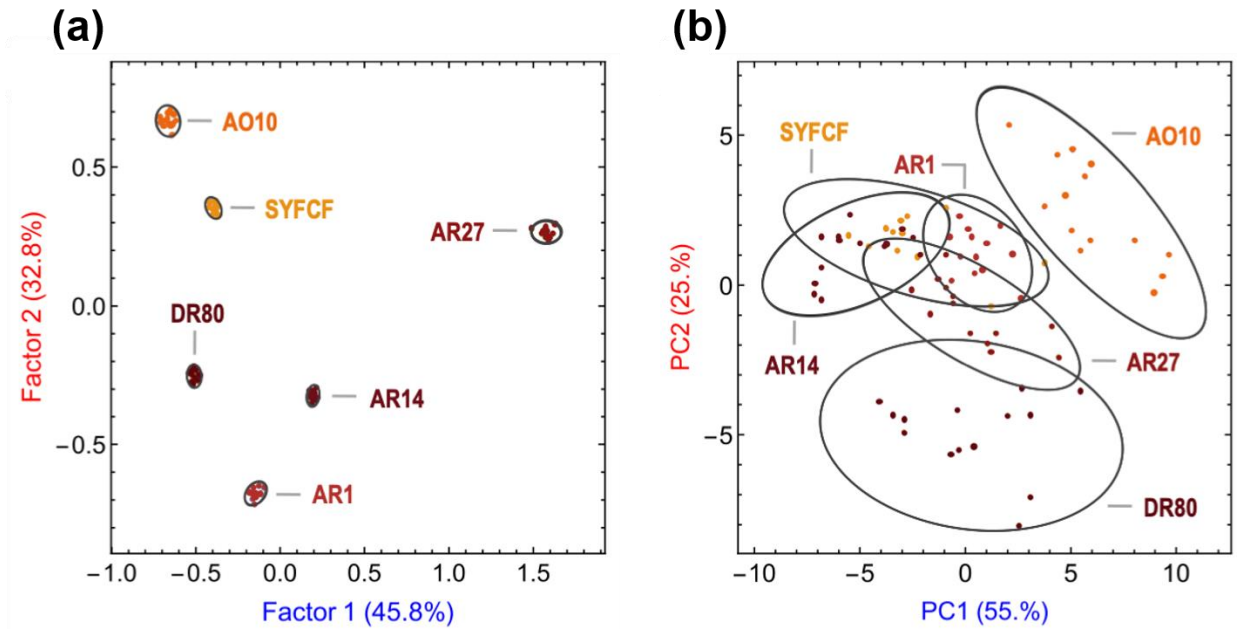

Figure 5-23 Two-dimensional plot of the (a) LDA and (b) PCA scores for the attempted differentiation of six azo dyes at 15 µM using **P7-P9** (10 µM) in artificial seawater media. The

plots use *the 30 most important fluorescence measurements* in the original data set. In this case, the LDA analysis successfully discriminates all azo dye analytes, but the corresponding PCA scores plot only clearly differentiates two of the six dyes, with a high degree of overlap observed throughout. All confidence ellipsoids are drawn to 95% confidence level.

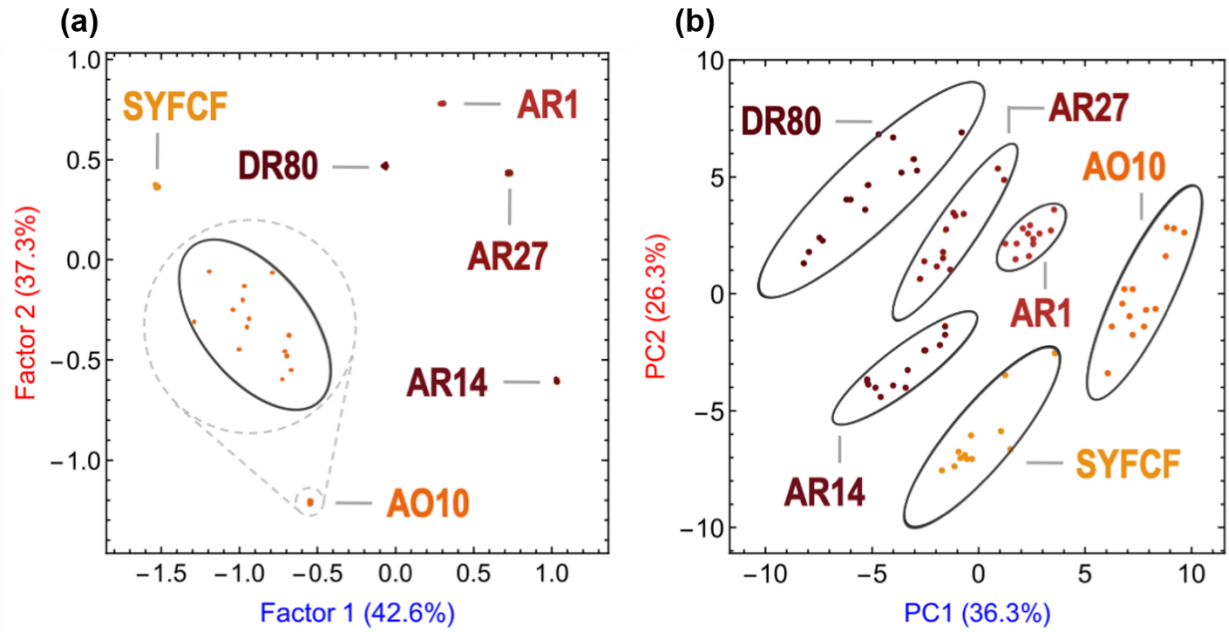

Figure 5-24 (a) Two-dimensional plot of LDA scores for the differentiation of six azo dyes at 15 µM using **P7-P9** (10 µM) in artificial seawater media using the 58 most important absorbance and fluorescence measurements in the original data set. (b) Corresponding PCA scores plot for the differentiation of azo dyes at 15 µM in artificial seawater using the same 58 instrumental measurements. All confidence ellipsoids are drawn to 95% confidence level.

5.7 Conclusions

In summary, the discrimination of 16 PAHs and 12 azo dyes were separately demonstrated using highly fluorescent modified conjugated fluorene co-polymers, using the inner filter effect as the means for detection. Because of their otherwise relatively featureless chemical structures, the optical absorption properties of the analytes were exploited as effective chemical filters, providing a range of differential responses. Multivariate pattern recognition strategies were used to generate two-dimensional scores plots to affect their analytical separation

using simple, common, and cost-effective instrumentation (UV-vis absorption and fluorescence spectroscopy).

PAH detection was achieved using a six-membered array with a series of fluorescent conjugated polymers prepared with tunable optical modifiers in their side chains, designed to have good spectral overlap with the target analytes. Similarly, azo dye detection was achieved using a three-polymer array, designed to have polyanionic side chains, to prevent host-guest interactions and to promote the IFE. The system was also successful in seawater, conditions that are otherwise inaccessible through traditional methods.

In short, the IFE was used as a robust approach to discriminate chemically featureless but high-absorbing compounds, circumventing some of the inherent challenges associated with systems operating through host-guest interactions, such as competing electrostatic and hydrogen bonding interactions, especially for similar analytes lacking suitable functional groups. These results lay the groundwork for qualitative and quantitative sensing strategies based on an array of conjugated fluorescent polymers for highly colored pollutants.

5.8 Experimental details

5.8.1 Materials

PAHs analytes were purchased from Sigma-Aldrich, and azo dyes were purchased from Strem Chemicals. Spectral grade *N*,*N*-dimethylformamide (DMF) was purchased from EMD Chemicals Inc. and used as received. All polymers were prepared and characterized in the Azoulay lab in the School of Polymer Science and Engineering at the University of Southern Mississippi.

5.8.2 Instrumentation

UV-vis measurements were performed using a Hewlett-Packard 8452a diode-array spectrophotometer. Benchtop steady-state fluorescence measurements were conducted with an ISS PC1 spectrofluorimeter. Excitation was carried out using a broad-spectrum high-pressure xenon lamp (CERMAX, 300W). Excitation correction was performed through a rhodamine B quantum counter with a dedicated detector. Excitation intensity was controlled by a manually operated iris (open/closed only). Spectral resolution was controlled by manually operated slits. Detection was through a Hamamatsu red-sensitive PMT. Experimental temperature (25°C) was controlled by an external circulating water bath on both instruments. Time-resolved fluorescence lifetime measurements presented in this chapter were carried out by our collaborators in the Azoulay lab.

Multivariate data was acquired on a BioTek *Synergy II* multimode microwell plate reader, capable of measuring absorbance spectra through a monochromator and steady-state fluorescence intensity through a set of bandpass filters. The sample compartment in this instrument is electrically thermostatted to 25 °C. Detector gain on the plate reader was automatically adjusted to maximize the signal of the most emissive well on the plate. Experiments were laid out by hand using Eppendorf Research multichannel pipettors and disposable plastic tips into microwell plates with clear flat bottoms for UV absorbance and fluorescence spectroscopy in a 384-well configuration. For PAH experiments, Aurora microwell plates were used, made of non-treated cyclo-olefin polymer (COP) because of this material's resistance to the DMF solvent; azo dye experiments were carried out in Greiner BioOne non-treated polystyrene microwell plates. Each well was filled with exactly 100 µL of sample solution for uniformity. Plates were read on the multimode plate reader immediately after

preparation. Reading time required about 20-30 minutes for each plate. In this time span, there appeared to be no evaporation of solvent (DMF or water), therefore plates did not need to be sealed.

5.8.3 Benchtop titration design

All PAH and azo dye optical spectroscopic and titration experiments were performed in DMF and DI H_2O, respectively. Polymer and dye stock solutions were prepared separately, then the polymer solutions (2 mL) were added to a 1 cm quartz cuvette, and absorbance and fluorescence spectra were collected for all polymers. Fluorescence emission spectra were collected by exciting the polymer at their most red-shifted spectral maximum. Titrations were carried out by adding appropriate aliquots (1-100 µL per addition) of dye solution to the polymers and taking fluorescence measurements after each addition.

5.8.4 Multivariate data analysis

To interpret the resultant data sets for PAH and azo dye experiments, LDA and PCA were performed, as described previously in the *Mathematica* program (release 11.3) published by Wolfram Research Inc, using code developed in-house. As a first step towards data analysis, each variable in the raw experimental data was mean-centered and standardized, a common practice in multivariate analysis, particularly in the case of input data spanning very different dynamic ranges, such as absorbance and fluorescence raw intensity data in this case.

For outlier detection, PCA was first applied to each dye/polymer replicate points. Points well outside the 95% confidence interval were considered outliers and removed from the data set. Representative examples for the PAH and azo dye data are shown in Figure 5-25 for the pyrene and AR27 dye analytes. In each case, data points 12 and 14, respectively, lie well outside

the 95% confidence interval (CI) and were removed from their corresponding data set before further analysis.

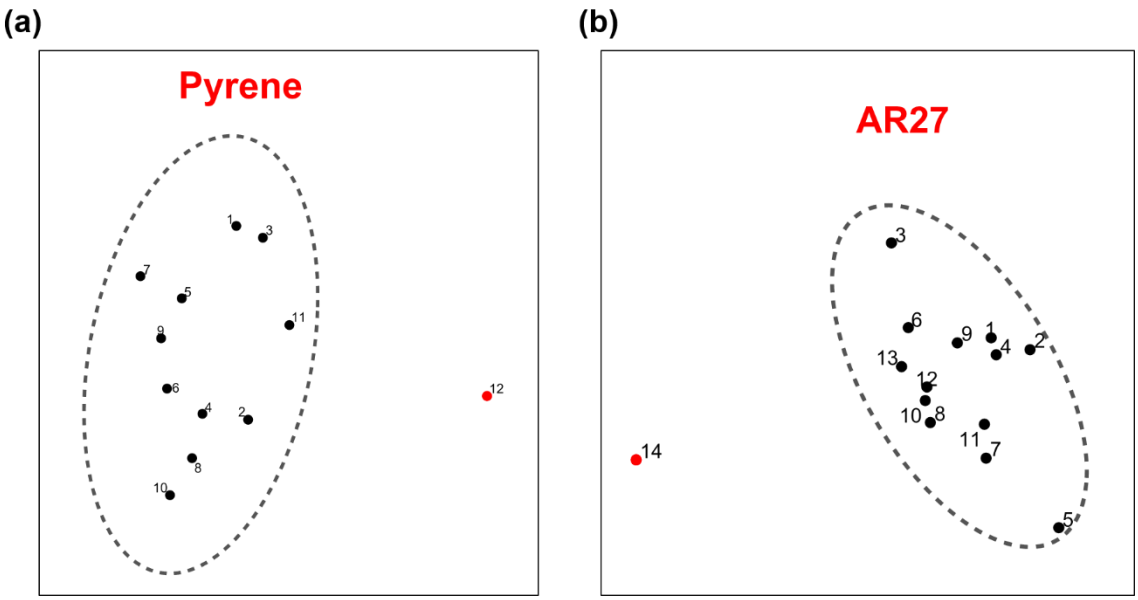

Figure 5-25 PCA scores plot of the (a) pyrene and (b) AR27 replicate sets, with 95% confidence ellipsoids shown as a dashed line. Points 12 and 14 (indicated in red), are clearly outside the confidence interval, and they were removed from the corresponding data set.

After outlier removal, variable reduction was carried out, to remove instrumental measurements that did not contribute to the discriminatory power of the array, introducing unwanted experimental noise. As an example, Figure 5-8 shown before is a visual overview the PAH data set, displaying good vs. poor information quality contained in two absorbance measurements (absorbance. at 380 nm and 420 nm, respectively) for the **P1** polymer.

For the azo dye experiments, fluorescence measurements were collected using 25 filter combinations ($\lambda_{exc.}/\lambda_{em.}$): 330/450 nm, 330/460 nm, 330/485 nm, 330/516 nm, 330/528 nm, 330/560 nm, 330/580 nm, 380/450 nm, 380/460 nm, 380/485 nm, 380/516 nm, 380/528 nm, 380/560 nm, 380/580 nm, 380/645 nm, 450/516 nm, 450/528 nm, 450/560 nm, 450/580 nm, 450/645 nm, 460/516 nm, 460/528 nm, 460/560 nm, 460/580 nm, and 460/645 nm. Absorbance measurements were collected from 300-560 nm at 20 nm increments. Individual measurements

were chosen for immediate removal from the data set if they could not contribute any information due to spectral mismatch. For example, any fluorescence measurements for the **P7** polymer carried out at $\lambda_{exc.}$ = 450-460 nm was removed, since this excitation wavelength was well outside the **P7** polymers' optimal excitation range, therefore producing no usable signal. A visual overview for the "P7 450/528" instrumental variable is depicted in Figure 5-26, representing an information-poor measurement; such measurements that were immediately removed are also represented in blue in Table 5-2.

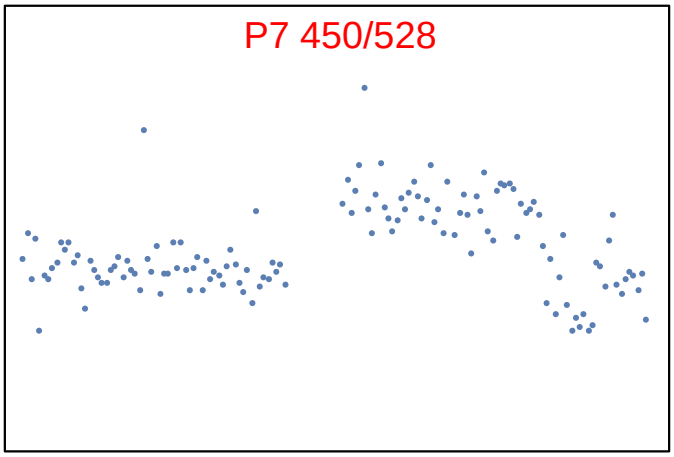

Figure 5-26 A representative visual example of an information-poor instrumental measurement ("P7 450/528") for all 12 azo dye analytes, containing more experimental noise than discriminatory capacity.

Multivariate analysis was then performed to further determine which instrumental measurements did not contribute enough to the discriminatory power of the array. At this stage, individual measurements were removed from the data set if they contributed <1% to factors 1 and 2. As an example, these measurements are shown for the 15 µM data set in Table 5-2 (shown in red). Finally, further removal of any measurement whose *overall* weighted contribution among *all* factors was <1% was also removed. Once again as an example, this final variable selection is depicted in Figure 5-27 (grey bars were removed) for the 15 µM data set (these measurements are represented in grey in Table 5-2). Thus, the final 15 µM data set was reduced from 75

fluorescence measurement descriptors to 23 selected ones. Similar data processing was carried out on the 500 nM and seawater data sets to produce appropriately reduced data sets; i.e. first removing measurements whose contributions were <1% to factors 1 and 2, then removing all remaining measurements whose overall weighted contributions were <1% among all factors.

Table 5-2 Individual fluorescence measurements for each polymer in the 15 µM data set and their corresponding percentage contributions to factors 1 and 2. Measurements that were immediately removed from the data set because of spectral mismatch are indicated in blue. Measurements that contributed <1% to factors 1 *and* 2 are indicated in red. Of the remaining 32 measurements, nine additional fluorescence measurements were filtered out whose overall weighted contributions were less than 1% among all factors (indicated in grey). The remaining measurements used in the final LDA analysis are displayed in green.

P7 ($\lambda_{exc.}/\lambda_{em.}$)	F1	F2	P8 ($\lambda_{exc.}/\lambda_{em.}$)	F1	F2	P9 ($\lambda_{exc.}/\lambda_{em.}$)	F1	F2
330/450	2	1	330/450	0	0	330/450	N/A	N/A
330/460	4	3	330/460	0	0	330/460	N/A	N/A
330/485	0	0	330/485	0	0	330/485	N/A	N/A
330/516	1	1	330/516	0	0	330/516	0	0
330/528	0	0	330/528	0	0	330/528	0	0
330/560	0	0	330/560	0	0	330/560	0	0
330/580	0	0	330/580	0	0	330/580	0	0
380/450	0	0	380/450	1	2	380/450	N/A	N/A
380/460	11	23	380/460	1	1	380/460	N/A	N/A
380/485	1	6	380/485	0	5	380/485	0	0
380/516	6	0	380/516	1	3	380/516	0	1
380/528	5	0	380/528	3	0	380/528	1	0
380/560	1	3	380/560	0	0	380/560	3	0
380/580	1	3	380/580	0	0	380/580	1	0
380/645	0	0	380/645	0	0	380/645	0	0
450/516	N/A	N/A	450/516	3	1	450/516	0	0
450/528	N/A	N/A	450/528	19	0	450/528	3	1
450/560	N/A	N/A	450/560	4	0	450/560	6	0
450/580	N/A	N/A	450/580	3	13	450/580	2	2
450/645	N/A	N/A	450/645	0	0	450/645	0	0
460/516	N/A	N/A	460/516	0	10	460/516	0	0
460/528	N/A	N/A	460/528	10	9	460/528	1	0
460/560	N/A	N/A	460/560	2	2	460/560	1	1
460/580	N/A	N/A	460/580	0	0	460/580	0	1
460/645	N/A	N/A	460/645	0	0	460/645	0	1

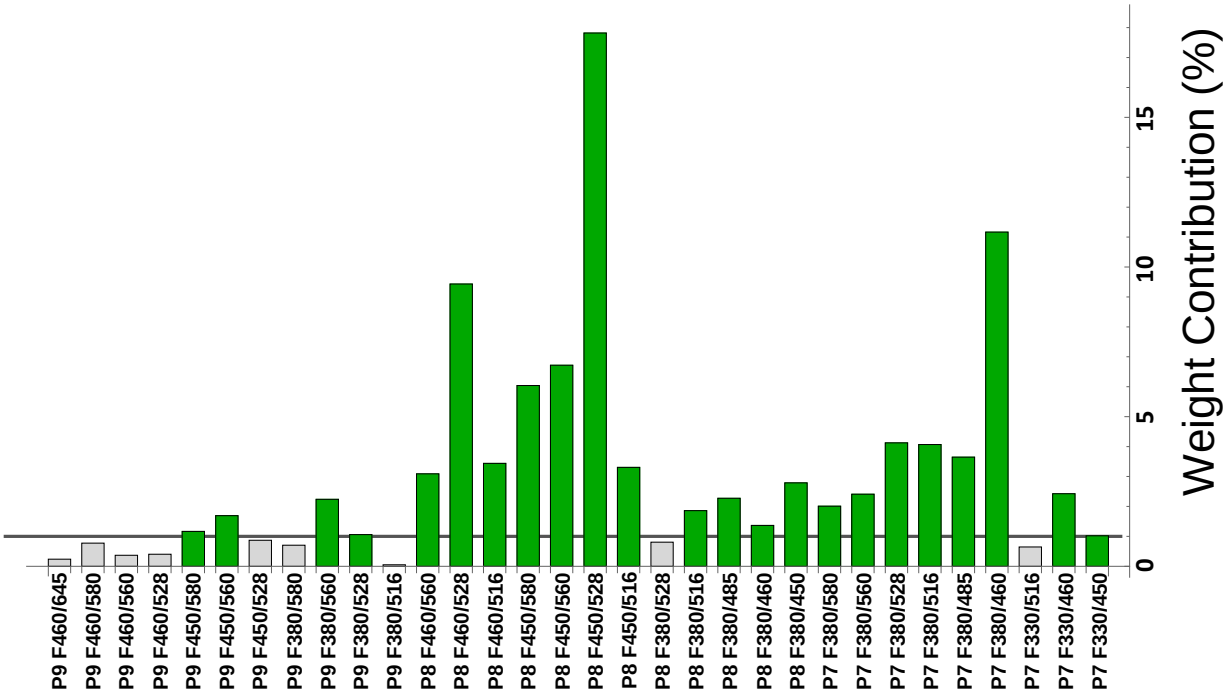

Figure 5-27 A graphical representation of the process by which we removed nine fluorescence measurements from the 15 µM data set. The grey line at 1% designates our chosen threshold. Contributions from measurements whose importance was higher than the 1% threshold are shown as green bars and were retained for further analysis. Contributions of less than 1%, shown as light grey bars, were removed from the data set.

CHAPTER 6

SUMMARY AND PERSPECTIVE

6.1 Summary

This original research successfully used supramolecular array sensing methods to detect a variety of relevant analytes, such as metal ions, polycyclic aromatic hydrocarbons, and azo textile dyes. These cross-reactive arrays were composed of off-the-shelf organic dyes and purpose-made conjugated polymer sensors, whose interactions to the target analytes produced detectable signal changes using simple optical spectroscopic methods (UV-vis absorption and fluorescence spectroscopy), and provided distinct response patterns that could be interpreted using well-known multivariate algorithms, such as linear discriminant analysis (LDA) and principal component analysis (PCA). We used different approaches to generate the required chemical interactions, including incorporation of metal-ligand coordinative interactions, as well as non-binding physical interactions, such as the inner filter effect.

We also showed a viable approach to solving the "problem of mixtures" that often plague chemical fingerprinting sensors, a particularly challenging problem in this field. By rigorously ensuring that all components (signal transduction, instrumental response, and data processing) respond linearly throughout the process, we showed that the overall response from pattern-based recognition methods can be used to identify the composition of mixtures for which the system had not been specifically trained.

We also contributed to fundamental knowledge regarding the nature and location of interaction sites for the binding of hydrophobic guests to water soluble polyelectrolytes, using cationic amine-terminated poly(amidoamine) (PAMAM) dendrimers as a representative example of this interesting class of macromolecular materials. The binding modes and locations of two well-characterized polycyclic aromatic hydrocarbons, anthracene and pyrene, were probed using a variety of information-rich fluorescence-based methods. Findings from this work showed unequivocally that these hydrophobic aromatic structures, although chemically very similar, displayed highly distinct binding preferences to the polyelectrolyte hosts.

6.2 Perspective

The conjugated fluorene polymer scaffold that proved so versatile and successful in this work will see further use by being decorated with other targeting receptors to expand the scope of ultra-sensitive pattern-based recognition beyond metal ions and polycyclic aromatic hydrocarbon analytes. The innovative approach to fingerprinting untrained-for mixtures of analytes by planning for and strictly ensuring linear response throughout the “toolchain” will also be applied to other systems, first to further prove its generality, and then to tackle difficult separation problems in an innovative and less resource-intensive way. Finally, applications of our fundamental findings regarding the internal structure and binding modes of polyelectrolytes, such as PAMAM dendrimers, will hopefully spur further application of these systems as supramolecular hosts in our group and beyond.

REFERENCES

(1) Steed, J. W.; Atwood, J. L. *Supramolecular chemistry*; Wiley: Chichester, 2012.

(2) Anslyn, E. V. Supramolecular analytical chemistry. *J. Org. Chem.* **2007**, *72*, 687-699.

(3) Lehn, J.-M. Toward complex matter: Supramolecular chemistry and self-organization. *Proc. Natl. Acad. Sci. U. S. A.* **2002**, *99*, 4763-4768.

(4) Lehn, J.-M. Perspectives in supramolecular chemistry: from molecular recognition towards self-organization. *Pure Appl. Chem.* **1994**, *66*, 1961-1966.

(5) Anslyn, E. V.; Dougherty, D. A. *Modern physical organic chemistry*; Univ. Science Books: Sausalito, Calif., 2008.

(6) Rowan, S. J.; Cantrill, S. J.; Cousins, G. R. L.; Sanders, J. K. M.; Stoddart, J. F. Dynamic covalent chemistry. *Angew. Chem., Int. Ed.* **2002**, *41*, 899-952.

(7) Li, B.; He, T.; Fan, Y.; Yuan, X.; Qiu, H.; Yin, S. Recent developments in the construction of metallacycle/metallacage-cored supramolecular polymers via hierarchical self-assembly. *Chem. Commun.* **2019**, *55*, 8036-8059.

(8) Cook, T. R.; Stang, P. J. Recent Developments in the Preparation and Chemistry of Metallacycles and Metallacages via Coordination. *Chem. Rev.* **2015**, *115*, 7001-7045.

(9) Chakrabarty, R.; Mukherjee, P. S.; Stang, P. J. Supramolecular Coordination: Self-Assembly of Finite Two- and Three-Dimensional Ensembles. *Chem. Rev.* **2011**, *111*, 6810-6918.

(10) Ma, J. C.; Dougherty, D. A. The Cation-π Interaction. *Chem. Rev.* **1997**, *97*, 1303-1324.

(11) Spiwok, V. CH/π interactions in carbohydrate recognition. *Molecules* **2017**, *22*, 1038/1031-1038/1011.

(12) Nishio, M.; Hirota, M. *The CH/pi interaction: evidence, nature and consequences*; Wiley: New York, N.Y, 1998.

(13) Martinez, C. R.; Iverson, B. L. Rethinking the term "pi-stacking". *Chem. Sci.* **2012**, *3*, 2191-2201.

(14) Steed, J. W.; Turner, D. R.; Wallace, K. J. Core concepts in supramolecular chemistry and nanochemistry. **2007**.

(15) Anzenbacher, P., Jr.; Lubal, P.; Bucek, P.; Palacios, M. A.; Kozelkova, M. E. A practical approach to optical cross-reactive sensor arrays. *Chem. Soc. Rev.* **2010**, *39*, 3954-3979.

(16) Swager, T. M. The Molecular Wire Approach to Sensory Signal Amplification. *Acc. Chem. Res.* **1998**, *31*, 201-207.

(17) Wright, A. T.; Anslyn, E. V. Differential receptor arrays and assays for solution-based molecular recognition. *Chem. Soc. Rev.* **2006**, *35*, 14-28.

(18) Collins, B. E.; Wright, A. T.; Anslyn, E. V. Combining molecular recognition, optical detection, and chemometric analysis. *Top. Curr. Chem.* **2007**, *277*, 181-218.

(19) Folmer-Andersen, J. F.; Kitamura, M.; Anslyn, E. V. Pattern-based discrimination of enantiomeric and structurally similar amino acids: an optical mimic of the mammalian taste response. *J. Am. Chem. Soc.* **2006**, *128*, 5652-5653.

(20) Munger, S. D.; Leinders-Zufall, T.; Zufall, F. Subsystem organization of the mammalian sense of smell. *Annu. Rev. Physiol.* **2009**, *71*, 115-140.

(21) Liberles, S. D.; Buck, L. B. A second class of chemosensory receptors in the olfactory epithelium. *Nature* **2006**, *442*, 645-650.

(22) Wilson, A. D.; Baietto, M. Applications and advances in electronic-nose technologies. *Sensors* **2009**, *9*, 5099-5148.

(23) Roeck, F.; Barsan, N.; Weimar, U. Electronic Nose: Current Status and Future Trends. *Chem. Rev.* **2008**, *108*, 705-725.

(24) Anzenbacher, P.; Palacios, M. A. Array-Based Sensors. 2011, p 345-368.

(25) Wright, A. T.; Griffin, M. J.; Zhong, Z.; McCleskey, S. C.; Anslyn, E. V.; McDevitt, J. T. Differential receptors create patterns that distinguish various proteins. *Angew. Chem., Int. Ed.* **2005**, *44*, 6375-6378.

(26) Li, Z.; Askim, J. R.; Suslick, K. S. The Optoelectronic Nose: Colorimetric and Fluorometric Sensor Arrays. *Chem. Rev.* **2019**, *119*, 231-292.

(27) Wei, X.; Chen, Z.; Tan, L.; Lou, T.; Zhao, Y. DNA-Catalytically Active Gold Nanoparticle Conjugates-Based Colorimetric Multidimensional Sensor Array for Protein Discrimination. *Anal. Chem.* **2017**, *89*, 556-559.

(28) Sarkar, T.; Selvakumar, K.; Motiei, L.; Margulies, D. Message in a molecule. *Nat. Commun.* **2016**, *7*, 11374.

(29) You, L.; Zha, D.; Anslyn, E. V. Recent Advances in Supramolecular Analytical Chemistry Using Optical Sensing. *Chem. Rev.* **2015**, *115*, 7840-7892.

(30) Tropp, J.; Ihde, M. H.; Williams, A. K.; White, N. J.; Eedugurala, N.; Bell, N. C.; Azoulay, J. D.; Bonizzoni, M. A sensor array for the discrimination of polycyclic aromatic hydrocarbons using conjugated polymers and the inner filter effect. *Chem Sci* **2019**, *10*, 10247-10255.

(31) Pushina, M.; Farshbaf, S.; Shcherbakova, E. G.; Anzenbacher, P. A dual chromophore sensor for the detection of amines, diols, hydroxy acids, and amino alcohols. *Chem. Commun.* **2019**, *55*, 4495-4498.

(32) Wang, B.; Han, J.; Bojanowski, N. M.; Bender, M.; Ma, C.; Seehafer, K.; Herrmann, A.; Bunz, U. H. F. An Optimized Sensor Array Identifies All Natural Amino Acids. *ACS Sens.* **2018**, *3*, 1562-1568.

(33) Huang, W.; Bender, M.; Seehafer, K.; Wacker, I.; Schroeder, R. R.; Bunz, U. H. F. A Tetraphenylethene-Based Polymer Array Discriminates Nitroarenes. *Macromolecules* **2018**, *51*, 1345-1350.

(34) Liang, X.; Bonizzoni, M. Boronic acid-modified poly(amidoamine) dendrimers as sugar-sensing materials in water. *J. Mater. Chem. B* **2016**, *4*, 3094-3103.

(35) Askim, J. R.; Li, Z.; La Gasse, M. K.; Rankin, J. M.; Suslick, K. S. An optoelectronic nose for identification of explosives. *Chem. Sci.* **2016**, *7*, 199-206.

(36) Minami, T.; Esipenko, N. A.; Zhang, B.; Isaacs, L.; Anzenbacher, P. "Turn-on" fluorescent sensor array for basic amino acids in water. *Chem. Commun.* **2014**, *50*, 61-63.

(37) Mallet, A. M.; Liu, Y.; Bonizzoni, M. An off-the-shelf sensing system for physiological phosphates. *Chem. Commun.* **2014**, *50*, 5003-5006.

(38) Liu, Y.; Bonizzoni, M. A Supramolecular Sensing Array for Qualitative and Quantitative Analysis of Organophosphates in Water. *J. Am. Chem. Soc.* **2014**, *136*, 14223-14229.

(39) Lin, H.; Jang, M.; Suslick, K. S. Preoxidation for Colorimetric Sensor Array Detection of VOCs. *J. Am. Chem. Soc.* **2011**, *133*, 16786-16789.

(40) Kitamura, M.; Shabbir, S. H.; Anslyn, E. V. Guidelines for pattern recognition using differential receptors and indicator displacement assays. *J. Org. Chem.* **2009**, *74*, 4479-4489.

(41) Zhang, C.; Suslick, K. S. A colorimetric sensor array for organics in water. *J. Am. Chem. Soc.* **2005**, *127*, 11548-11549.

(42) Li, Z.; Suslick, K. S. Colorimetric Sensor Array for Monitoring CO and Ethylene. *Anal. Chem.* **2019**, *91*, 797-802.

(43) Joy, N. A.; Rogers, P. H.; Nandasiri, M. I.; Thevuthasan, S.; Carpenter, M. A. Plasmonic-based sensing using an array of Au-metal oxide thin films. *Anal. Chem.* **2012**, *84*, 10437-10444.

(44) Rakow, N. A.; Suslick, K. S. A colorimetric sensor array for odor visualization. *Nature* **2000**, *406*, 710-713.

(45) Pode, Z.; Peri-Naor, R.; Georgeson, J. M.; Ilani, T.; Kiss, V.; Unger, T.; Markus, B.; Barr, H. M.; Motiei, L.; Margulies, D. Protein recognition by a pattern-generating fluorescent molecular probe. *Nat. Nanotechnol.* **2017**, *12*, 1161-1168.

(46) Sun, W.; Lu, Y.; Mao, J.; Chang, N.; Yang, J.; Liu, Y. Multidimensional Sensor for Pattern Recognition of Proteins Based on DNA-Gold Nanoparticles Conjugates. *Anal. Chem.* **2015**, *87*, 3354-3359.

(47) Xu, S.; Lu, X.; Yao, C.; Huang, F.; Jiang, H.; Hua, W.; Na, N.; Liu, H.; Ouyang, J. A Visual Sensor Array for Pattern Recognition Analysis of Proteins Using Novel Blue-Emitting Fluorescent Gold Nanoclusters. *Anal. Chem.* **2014**, *86*, 11634-11639.

(48) Mahmoudi, M.; Lohse, S. E.; Murphy, C. J.; Suslick, K. S. Identification of Nanoparticles with a Colorimetric Sensor Array. *ACS Sens.* **2016**, *1*, 17-21.

(49) Ngernpimai, S.; Geng, Y.; Makabenta, J. M.; Landis, R. F.; Keshri, P.; Gupta, A.; Li, C.-H.; Chompoosor, A.; Rotello, V. M. Rapid Identification of Biofilms Using a Robust Multichannel Polymer Sensor Array. *ACS Appl. Mater. Interfaces* **2019**, *11*, 11202-11208.

(50) Zamora-Olivares, D.; Kaoud, T. S.; Zeng, L.; Pridgen, J. R.; Zhuang, D. L.; Ekpo, Y. E.; Nye, J. R.; Telles, M.; Anslyn, E. V.; Dalby, K. N. Quantification of ERK Kinase Activity in Biological Samples Using Differential Sensing. *ACS Chem. Biol.* **2020**, *15*, 83-92.

(51) Hatai, J.; Motiei, L.; Margulies, D. Analyzing Amyloid Beta Aggregates with a Combinatorial Fluorescent Molecular Sensor. *J. Am. Chem. Soc.* **2017**, *139*, 2136-2139.

(52) Rochat, S.; Gao, J.; Qian, X.; Zaubitzer, F.; Severin, K. Cross-Reactive Sensor Arrays for the Detection of Peptides in Aqueous Solution by Fluorescence Spectroscopy. *Chem. - Eur. J.* **2010**, *16*, 104-113, S104/101-S104/136.

(53) Collins, B. E.; Anslyn, E. V. Pattern-based peptide recognition. *Chem. - Eur. J.* **2007**, *13*, 4700-4708.

(54) Lavigne, J. J.; Savoy, S.; Clevenger, M. B.; Ritchie, J. E.; McDoniel, B.; Yoo, S.-J.; Anslyn, E. V.; McDevitt, J. T.; Shear, J. B.; Neikirk, D. Solution-Based Analysis of Multiple Analytes by a Sensor Array: Toward the Development of an "Electronic Tongue". *J. Am. Chem. Soc.* **1998**, *120*, 6429-6430.

(55) Brereton, R. G. Chemometrics: data driven extraction for science. **2018**.

(56) Roggo, Y.; Duponchel, L.; Huvenne, J. P. Comparison of supervised pattern recognition methods with McNemar's statistical test. Application to qualitative analysis of sugar beet by near-infrared spectroscopy. *Anal. Chim. Acta* **2003**, *477*, 187-200.

(57) Hughes, A. D.; Glenn, I. C.; Patrick, A. D.; Ellington, A.; Anslyn, E. V. A pattern recognition based fluorescence quenching assay for the detection and identification of nitrated explosive analytes. *Chem. - Eur. J.* **2008**, *14*, 1822-1827.

(58) Germain, M. E.; Knapp, M. J. Discrimination of Nitroaromatics and Explosives Mimics by a Fluorescent Zn(salicylaldimine) Sensor Array. *J. Am. Chem. Soc.* **2008**, *130*, 5422-5423.

(59) Zhang, T.; Edwards, N. Y.; Bonizzoni, M.; Anslyn, E. V. The Use of Differential Receptors to Pattern Peptide Phosphorylation. *J. Am. Chem. Soc.* **2009**, *131*, 11976-11984.

(60) Miranda, O. R.; You, C.-C.; Phillips, R.; Kim, I.-B.; Ghosh, P. S.; Bunz, U. H. F.; Rotello, V. M. Array-Based Sensing of Proteins Using Conjugated Polymers. *J. Am. Chem. Soc.* **2007**, *129*, 9856-9857.

(61) Jolliffe, I. T. *Principal component analysis*; Springer: New York; London, 2011.

(62) Jambu, M. *Exploratory and multivariate data analysis*; Academic Press: Boston, 2010.

(63) Palacios, M. A.; Wang, Z.; Montes, V. A.; Zyryanov, G. V.; Anzenbacher, P., Jr. Rational Design of a Minimal Size Sensor Array for Metal Ion Detection. *J. Am. Chem. Soc.* **2008**, *130*, 10307-10314.

(64) Zhou, H.; Baldini, L.; Hong, J.; Wilson, A. J.; Hamilton, A. D. Pattern Recognition of Proteins Based on an Array of Functionalized Porphyrins. *J. Am. Chem. Soc.* **2006**, *128*, 2421-2425.

(65) Bolto, B.; Gregory, J. Organic polyelectrolytes in water treatment. *Water Res.* **2007**, *41*, 2301-2324.

(66) Zhou, Z.; Shen, Y.; Tang, J.; Jin, E.; Ma, X.; Sun, Q.; Zhang, B.; Van Kirk, E. A.; Murdoch, W. J. Linear polyethyleneimine-based charge-reversal nanoparticles for nuclear-targeted drug delivery. *J. Mater. Chem.* **2011**, *21*, 19114-19123.

(67) Farinato, R. S. Applications of polyelectrolytes in aqueous media. *ACS Symp. Ser.* **2006**, *937*, 153-168.

(68) McQuade, D. T.; Pullen, A. E.; Swager, T. M. Conjugated polymer-based chemical sensors. *Chem. Rev.* **2000**, *100*, 2537-2574.

(69) Mako, T. L.; Racicot, J. M.; Levine, M. Supramolecular Luminescent Sensors. *Chem. Rev.* **2019**, *119*, 322-477.

(70) Wu, W.; Bazan, G. C.; Liu, B. Conjugated-Polymer-Amplified Sensing, Imaging, and Therapy. *Chem* **2017**, *2*, 760-790.

(71) Thomas, S. W., III; Joly, G. D.; Swager, T. M. Chemical sensors based on amplifying fluorescent conjugated polymers. *Chem. Rev.* **2007**, *107*, 1339-1386.

(72) Zhou, Q.; Swager, T. M. Fluorescent chemosensors based on energy migration in conjugated polymers: the molecular wire approach to increased sensitivity. *J. Am. Chem. Soc.* **1995**, *117*, 12593-12602.

(73) Zhou, Q.; Swager, T. M. Method for enhancing the sensitivity of fluorescent chemosensors: energy migration in conjugated polymers. *J. Am. Chem. Soc.* **1995**, *117*, 7017-7018.

(74) Swager, T. M.; Gil, C. J.; Wrighton, M. S. Fluorescence Studies of Poly(p-phenyleneethynylene)s: The Effect of Anthracene Substitution. *J. Phys. Chem.* **1995**, *99*, 4886-4893.

(75) Burrows, H. D.; Knaapila, M.; Fonseca, S. M.; Costa, T. Aggregation properties of conjugated polyelectrolytes. Wiley-VCH Verlag GmbH & Co. KGaA: 2013, p 127-167.

(76) Jiang, H.; Zhao, X.; Schanze, K. S. Amplified Fluorescence Quenching of a Conjugated Polyelectrolyte Mediated by Ca^{2+}. *Langmuir* **2006**, *22*, 5541-5543.

(77) Rochat, S.; Swager, T. M. Conjugated Amplifying Polymers for Optical Sensing Applications. *ACS Appl. Mater. Interfaces* **2013**, *5*, 4488-4502.

(78) Tropp, J.; Ihde, M. H.; Crater, E. R.; Bell, N. C.; Bhatta, R.; Johnson, I. C.; Bonizzoni, M.; Azoulay, J. D. A Sensor Array for the Nanomolar Detection of Azo Dyes in Water. *ACS Sens.* **2020**, *5*, 1541-1547.

(79) Liu, H.; Wang, Y.; Mo, W.; Tang, H.; Cheng, Z.; Chen, Y.; Zhang, S.; Ma, H.; Li, B.; Li, X. Dendrimer-Based, High-Luminescence Conjugated Microporous Polymer Films for Highly Sensitive and Selective Volatile Organic Compound Sensor Arrays. *Adv. Funct. Mater.* **2020**, *30*, 1910275.

(80) Yin, M.; Zhang, C.; Li, J.; Li, H.; Deng, Q.; Wang, S. Highly sensitive detection of benzoyl peroxide based on organoboron fluorescent conjugated polymers. *Polymers* **2019**, *11*, 1655.

(81) Wang, C.-H.; Nesterov, E. E. Amplifying fluorescent conjugated polymer sensor for singlet oxygen detection. *Chem. Commun.* **2019**, *55*, 8955-8958.

(82) Chiang, C.-H.; Pangeni, D.; Nesterov, E. E. Higher Energy Gap Control of Fluorescence in Conjugated Polymers: Turn-On Amplifying Chemosensor for Hydrogen Sulfide. *Macromolecules* **2017**, *50*, 6961-6966.

(83) Jang, G.; Kim, J.; Kim, D.; Lee, T. S. Synthesis of triphenylamine-containing conjugated polyelectrolyte and fabrication of fluorescence color-changeable, paper-based sensor strips for biothiol detection. *Polym. Chem.* **2015**, *6*, 714-720.

(84) Rochat, S.; Swager, T. M. Fluorescence Sensing of Amine Vapors Using a Cationic Conjugated Polymer Combined with Various Anions. *Angew. Chem., Int. Ed.* **2014**, *53*, 9792-9796.

(85) Shan, Y.; Yao, W.; Liang, Z.; Zhu, L.; Yang, S.; Ruan, Z. Reaction-based AIEE-active conjugated polymer as fluorescent turn on probe for mercury ions with good sensing performance. *Dyes Pigm.* **2018**, *156*, 1-7.

(86) Sen, C. P.; Valiyaveettil, S. Conjugated polyphenols: Investigation of structure-property relationships and complexation with zinc ions. *Eur. Polym. J.* **2017**, *87*, 99-112.

(87) Luo, C.; Liu, Y.; Zhang, Q.; Cai, X. Hyperbranched conjugated polymers containing 1,3-butadiene units: metal-free catalyzed synthesis and selective chemosensors for Fe^{3+} ions. *RSC Adv.* **2017**, *7*, 12269-12276.

(88) Fegley, M. E. A.; Sandgren, T.; Duffy-Matzner, J. L.; Chen, A.; Jones, W. E., Jr. Detection and differentiation of ferrous and ferric ions using fluorescent metallopolymer and oligomer chemosensors. *J. Polym. Sci., Part A: Polym. Chem.* **2015**, *53*, 951-954.

(89) Li, Z.; Acharya, R.; Wang, S.; Schanze, K. S. Photophysics and phosphate fluorescence sensing by poly(phenylene ethynylene) conjugated polyelectrolytes with branched ammonium side groups. *J. Mater. Chem. C* **2018**, *6*, 3722-3730.

(90) Willis-Fox, N.; Gutacker, A.; Browne, M. P.; Khan, A. R.; Lyons, M. E. G.; Scherf, U.; Evans, R. C. Selective recognition of biologically important anions using a diblock polyfluorene-polythiophene conjugated polyelectrolyte. *Polym. Chem.* **2017**, *8*, 7151-7159.

(91) Wang, S.; Zeman, C. J.; Jiang, J.; Pan, Z.; Schanze, K. S. Intercalation of Alkynylplatinum(II) Terpyridine Complexes into a Helical Poly(phenylene ethynylene) Sulfonate: Application to Protein Sensing. *ACS Appl. Mater. Interfaces* **2017**, *9*, 33461-33469.

(92) Zhang, P.; Lu, H.; Chen, H.; Zhang, J.; Liu, L.; Lv, F.; Wang, S. Cationic conjugated polymers-induced quorum sensing of bacterial cells. *Anal. Chem.* **2016**, *88*, 2985-2988.

(93) Brookins, R. N.; Schanze, K. S.; Reynolds, J. R. Base-Free Suzuki Polymerization for the Synthesis of Polyfluorenes Functionalized with Carboxylic Acids. *Macromolecules* **2007**, *40*, 3524-3526.

(94) Stork, M.; Gaylord, B. S.; Heeger, A. J.; Bazan, G. C. Energy transfer in mixtures of water-soluble oligomers: Effect of charge, aggregation, and surfactant complexation. *Adv. Mater.* **2002**, *14*, 361-366.

(95) Anantha-Iyengar, G.; Shanmugasundaram, K.; Nallal, M.; Lee, K.-P.; Whitcombe, M. J.; Lakshmi, D.; Sai-Anand, G. Functionalized conjugated polymers for sensing and molecular imprinting applications. *Prog. Polym. Sci.* **2019**, *88*, 1-129.

(96) Pu, K.-Y.; Wang, G.; Liu, B. Design and synthesis of conjugated polyelectrolytes. Wiley-VCH Verlag GmbH & Co. KGaA: 2013, p 1-64.

(97) Harrison, B. S.; Ramey, M. B.; Reynolds, J. R.; Schanze, K. S. Amplified Fluorescence Quenching in a Poly(p-phenylene)-Based Cationic Polyelectrolyte. *J. Am. Chem. Soc.* **2000**, *122*, 8561-8562.

(98) Chen, L.; McBranch, D. W.; Wang, H.-L.; Helgeson, R.; Wudl, F.; Whitten, D. G. Highly sensitive biological and chemical sensors based on reversible fluorescence quenching in a conjugated polymer. *Proc. Natl. Acad. Sci. U. S. A.* **1999**, *96*, 12287-12292.

(99) Tan, C.; Pinto, M. R.; Schanze, K. S. Photophysics, aggregation and amplified quenching of a water-soluble poly(phenylene ethynylene). *Chem. Commun.* **2002**, 446-447.

(100) Tilley, A. J.; Danczak, S. M.; Browne, C.; Young, T.; Tan, T.; Ghiggino, K. P.; Smith, T. A.; White, J. Synthesis and Fluorescence Characterization of MEHPPV Oligomers. *J. Org. Chem.* **2011**, *76*, 3372-3380.

(101) Thomas, S. W., III; Amara, J. P.; Bjork, R. E.; Swager, T. M. Amplifying fluorescent polymer sensors for the explosives taggant 2,3-dimethyl-2,3-dinitrobutane (DMNB). *Chem. Commun.* **2005**, 4572-4574.

(102) Wong, K. S.; Wang, H.; Lanzani, G. Ultrafast excited-state planarization of the hexamethylsexithiophene oligomer studied by femtosecond time-resolved photoluminescence. *Chem. Phys. Lett.* **1998**, *288*, 59-64.

(103) Yeung, M. C.-L.; Yam, V. W.-W. Luminescent cation sensors: from host-guest chemistry, supramolecular chemistry to reaction-based mechanisms. *Chem. Soc. Rev.* **2015**, *44*, 4192-4202.

(104) Yoshino, T.; Murakami, S.; Ogura, K. Equilibriums of iron(III) complexes with xylenol orange and methylthymol blue. *J. Inorg. Nucl. Chem.* **1979**, *41*, 1011-1013.

(105) Murakami, S.; Yoshino, T. Correlation between the hard and soft character and the visible absorption spectra of Xylenol Orange and Methylthymol Blue complexes with bivalent metal ions. *Talanta* **1981**, *28*, 623-625.

(106) Sasaki, Y.; Minamiki, T.; Tokito, S.; Minami, T. A molecular self-assembled colourimetric chemosensor array for simultaneous detection of metal ions in water. *Chem. Commun.* **2017**, *53*, 6561-6564.

(107) Xu, W.; Ren, C.; Teoh, C. L.; Peng, J.; Gadre, S. H.; Rhee, H.-W.; Lee, C.-L. K.; Chang, Y.-T. An Artificial Tongue Fluorescent Sensor Array for Identification and Quantitation of Various Heavy Metal Ions. *Anal. Chem.* **2014**, *86*, 8763-8769.

(108) Wang, Z.; Palacios, M. A.; Anzenbacher, P., Jr. Fluorescence Sensor Array for Metal Ion Detection Based on Various Coordination Chemistries: General Performance and Potential Application. *Anal. Chem.* **2008**, *80*, 7451-7459.

(109) Mayr, T.; Igel, C.; Liebsch, G.; Klimant, I.; Wolfbeis, O. S. Cross-Reactive Metal Ion Sensor Array in a Micro Titer Plate Format. *Anal. Chem.* **2003**, *75*, 4389-4396.

(110) Mallet, A. M.; Davis, A. B.; Davis, D. R.; Panella, J.; Wallace, K. J.; Bonizzoni, M. A cross reactive sensor array to probe divalent metal ions. *Chem. Commun.* **2015**, *51*, 16948-16951.

(111) Lee, J.-S.; Lee, J. W.; Chang, Y.-T. Counterion Free Colorimetric Metal Cation Sensor Array. *J. Comb. Chem.* **2007**, *9*, 926-928.

(112) Burdette, S. C. Key Considerations for Sensing Fe(II) and Fe(III) in Aqueous Media. *Eur. J. Inorg. Chem.* **2015**, *2015*, 5728-5729.

(113) Flynn, C. M., Jr. Hydrolysis of inorganic iron(III) salts. *Chem. Rev.* **1984**, *84*, 31-41.

(114) Aragay, G.; Pons, J.; Merkoci, A. Recent trends in macro-, micro-, and nanomaterial-based tools and strategies for heavy-metal detection. *Chem. Rev.* **2011**, *111*, 3433-3458.

(115) Mattocks, J. A.; Ho, J. V.; Cotruvo, J. A., Jr. A Selective, Protein-Based Fluorescent Sensor with Picomolar Affinity for Rare Earth Elements. *J. Am. Chem. Soc.* **2019**, *141*, 2857-2861.

(116) Deng, H.-M.; Huang, L.-J.; Chai, Y.-Q.; Yuan, R.; Yuan, Y.-L. Ultrasensitive Photoelectrochemical Detection of Multiple Metal Ions Based on Wavelength-Resolved Dual-Signal Output Triggered by Click Reaction. *Anal. Chem.* **2019**, *91*, 2861-2868.

(117) Suherman, A. L.; Ngamchuea, K.; Tanner, E. E. L.; Sokolov, S. V.; Holter, J.; Young, N. P.; Compton, R. G. Electrochemical Detection of Ultratrace (Picomolar) Levels of Hg^{2+} Using a Silver Nanoparticle-Modified Glassy Carbon Electrode. *Anal. Chem.* **2017**, *89*, 7166-7173.

(118) Gao, L.; Li, L.-L.; Wang, X.; Wu, P.; Cao, Y.; Liang, B.; Li, X.; Lin, Y.; Lu, Y.; Guo, X. Graphene-DNAzyme junctions: a platform for direct metal ion detection with ultrahigh sensitivity. *Chem. Sci.* **2015**, *6*, 2469-2473.

(119) Zhu, G.; Li, Y.; Zhang, C.-y. Simultaneous detection of mercury(II) and silver(I) ions with picomolar sensitivity. *Chem. Commun.* **2014**, *50*, 572-574.

(120) Kotova, O.; Comby, S.; Gunnlaugsson, T. Sensing of biologically relevant d-metal ions using a Eu(III)-cyclen based luminescent displacement assay in aqueous pH 7.4 buffered solution. *Chem. Commun.* **2011**, *47*, 6810-6812.

(121) Wu, D.; Sedgwick, A. C.; Gunnlaugsson, T.; Akkaya, E. U.; Yoon, J.; James, T. D. Fluorescent chemosensors: the past, present and future. *Chem. Soc. Rev.* **2017**, *46*, 7105-7123.

(122) Geng, Y.; Peveler, W. J.; Rotello, V. M. Array-based "Chemical Nose" Sensing in Diagnostics and Drug Discovery. *Angew. Chem., Int. Ed.* **2019**, *58*, 5190-5200.

(123) *National primary drinking water regulations: inorganic chemicals*; United States Environmental Protection Agency, Office of Ground Water and Drinking Water, 1995.

(124) *National recommended water quality criteria*; United States Environmental Protection Agency, Office of Water, Office of Science and Technology, 2006.

(125) Joung, D.; Shiller, A. M. Trace Element Distributions in the Water Column near the Deepwater Horizon Well Blowout. *Environ. Sci. Technol.* **2013**, *47*, 2161-2168.

(126) He, F.; Tang, Y.; Wang, S.; Li, Y.; Zhu, D. Fluorescent Amplifying Recognition for DNA G-Quadruplex Folding with a Cationic Conjugated Polymer: A Platform for Homogeneous Potassium Detection. *J. Am. Chem. Soc.* **2005**, *127*, 12343-12346.

(127) Freudenberg, J.; Hinkel, F.; Jaensch, D.; Bunz, U. H. F. Chemical Tongues and Noses Based upon Conjugated Polymers. *Top. Curr. Chem.* **2017**, *375*, 1-49.

(128) Rana, S.; Elci, S. G.; Mout, R.; Singla, A. K.; Yazdani, M.; Bender, M.; Bajaj, A.; Saha, K.; Bunz, U. H. F.; Jirik, F. R.; Rotello, V. M. Ratiometric Array of Conjugated Polymers-Fluorescent Protein Provides a Robust Mammalian Cell Sensor. *J. Am. Chem. Soc.* **2016**, *138*, 4522-4529.

(129) Han, J.; Wang, B.; Bender, M.; Seehafer, K.; Bunz, U. H. F. Water-Soluble Poly(p-aryleneethynylene)s: A Sensor Array Discriminates Aromatic Carboxylic Acids. *ACS Appl. Mater. Interfaces* **2016**, *8*, 20415-20421.

(130) Han, J.; Bender, M.; Hahn, S.; Seehafer, K.; Bunz, U. H. F. Polyelectrolyte Complexes Formed from Conjugated Polymers: Array-Based Sensing of Organic Acids. *Chem. - Eur. J.* **2016**, *22*, 3230-3233.

(131) Wu, D.; Schanze, K. S. Protein Induced Aggregation of Conjugated Polyelectrolytes Probed with Fluorescence Correlation Spectroscopy: Application to Protein Identification. *ACS Appl. Mater. Interfaces* **2014**, *6*, 7643-7651.

(132) Maynor, M. S.; Deason, T. K.; Nelson, T. L.; Lavigne, J. J. Multidimensional response analysis towards the detection and identification of soft divalent metal ions. *Supramol. Chem.* **2009**, *21*, 310-315.

(133) Phillips, R. L.; Miranda, O. R.; You, C.-C.; Rotello, V. M.; Bunz, U. H. F. Rapid and efficient identification of bacteria using gold-nanoparticle-poly(para-phenyleneethynylene) constructs. *Angew. Chem., Int. Ed.* **2008**, *47*, 2590-2594.

(134) Kim, I.-B.; Bunz, U. H. F. Modulating the Sensory Response of a Conjugated Polymer by Proteins: An Agglutination Assay for Mercury Ions in Water. *J. Am. Chem. Soc*. **2006**, *128*, 2818-2819.

(135) Kim, I.-B.; Dunkhorst, A.; Gilbert, J.; Bunz, U. H. F. Sensing of Lead Ions by a Carboxylate-Substituted PPE: Multivalency Effects. *Macromolecules* **2005**, *38*, 4560-4562.

(136) Kim, I.-B.; Dunkhorst, A.; Bunz, U. H. F. Nonspecific Interactions of a Carboxylate-Substituted PPE with Proteins. A Cautionary Tale for Biosensor Applications. *Langmuir* **2005**, *21*, 7985-7989.

(137) Wu, Y.; Tan, Y.; Wu, J.; Chen, S.; Chen, Y. Z.; Zhou, X.; Jiang, Y.; Tan, C. Fluorescence Array-Based Sensing of Metal Ions Using Conjugated Polyelectrolytes. *ACS Appl. Mater. Interfaces* **2015**, *7*, 6882-6888.

(138) Ding, X.; Xie, H.; Kang, Y. J. The significance of copper chelators in clinical and experimental application. *J. Nutr. Biochem.* **2011**, *22*, 301-310.

(139) Waters, R. S.; Bryden, N. A.; Patterson, K. Y.; Veillon, C.; Anderson, R. A. EDTA chelation effects on urinary losses of cadmium, calcium, chromium, cobalt, copper, lead, magnesium, and zinc. *Biol. Trace Elem. Res.* **2001**, *83*, 207-221.

(140) Xu, Q.; An, L.; Yu, M.; Wang, S. Design and synthesis of a new conjugated polyelectrolyte as a reversible pH sensor. *Macromol. Rapid Commun.* **2008**, *29*, 390-395.

(141) Zeman, C. J.; Schanze, K. S. Elucidating the Effects of Solvating Side Chains on the Rigidity and Aggregation Tendencies of Conjugated Polymers with Molecular Dynamics Simulations Using DFT Tight Binding. *J. Phys. Chem. A* **2019**, *123*, 3293-3299.

(142) Jiang, H.; Taranekar, P.; Reynolds, J. R.; Schanze, K. S. Conjugated Polyelectrolytes: Synthesis, Photophysics, and Applications. *Angew. Chem., Int. Ed.* **2009**, *48*, 4300-4316.

(143) Burrows, H. D.; Tapia, M. J.; Silva, C. L.; Pais, A. A. C. C.; Fonseca, S. M.; Pina, J.; Seixas de Melo, J.; Wang, Y.; Marques, E. F.; Knaapila, M.; Monkman, A. P.; Garamus, V. M.; Pradhan, S.; Scherf, U. Interplay of Electrostatic and Hydrophobic Effects with Binding of Cationic Gemini Surfactants and a Conjugated Polyanion: Experimental and Molecular Modeling Studies. *J. Phys. Chem. B* **2007**, *111*, 4401-4410.

(144) Zhao, X.; Pinto, M. R.; Hardison, L. M.; Mwaura, J.; Mueller, J.; Jiang, H.; Witker, D.; Kleiman, V. D.; Reynolds, J. R.; Schanze, K. S. Variable Band Gap Poly(arylene ethynylene) Conjugated Polyelectrolytes. *Macromolecules* **2006**, *39*, 6355-6366.

(145) Menon, A.; Galvin, M.; Walz, K. A.; Rothberg, L. Structural basis for the spectroscopy and photophysics of solution-aggregated conjugated polymers. *Synth. Met.* **2004**, *141*, 197-202.

(146) Burrows, H. D.; Fonseca, S. M.; Silva, C. L.; Pais, A. A. C. C.; Tapia, M. J.; Pradhan, S.; Scherf, U. Aggregation of the hairy rod conjugated polyelectrolyte poly{1,4-phenylene-[9,9-bis(4-phenoxybutylsulfonate)]fluorene-2,7-diyl} in aqueous solution: an experimental and molecular modelling study. *Phys. Chem. Chem. Phys.* **2008**, *10*, 4420-4428.

(147) Millero, F. J. *Chemical oceanography*; CRC Press: Boca Raton, 2013.

(148) Chandra, S.; Dietrich, S.; Lang, H.; Bahadur, D. Dendrimer-Doxorubicin conjugate for enhanced therapeutic effects for cancer. *J. Mater. Chem.* **2011**, *21*, 5729-5737.

(149) Bae, Y.; Kataoka, K. Intelligent polymeric micelles from functional poly(ethylene glycol)-poly(amino acid) block copolymers. *Adv. Drug Delivery Rev.* **2009**, *61*, 768-784.

(150) Buhleier, E.; Wehner, W.; Voegtle, F. "Cascade"- and "nonskid-chain-like" syntheses of molecular cavity topologies. *Synthesis* **1978**, 155-158.

(151) Hawker, C. J.; Wooley, K. L.; Frechet, J. M. J. Unimolecular micelles and globular amphiphiles: dendritic macromolecules as novel recyclable solubilization agents. *J. Chem. Soc., Perkin Trans. 1* **1993**, 1287-1297.

(152) Tomalia, D. A.; Baker, H.; Dewald, J.; Hall, M.; Kallos, G.; Martin, S.; Roeck, J.; Ryder, J.; Smith, P. A new class of polymers: starburst-dendritic macromolecules. *Polym. J.* **1985**, *17*, 117-132.

(153) Smith, P. E. S.; Brender, J. R.; Durr, U. H. N.; Xu, J.; Mullen, D. G.; Banaszak Holl, M. M.; Ramamoorthy, A. Solid-State NMR Reveals the Hydrophobic-Core Location of Poly(amidoamine) Dendrimers in Biomembranes. *J. Am. Chem. Soc.* **2010**, *132*, 8087-8097.

(154) Klajnert, B.; Pastucha, A.; Shcharbin, D.; Bryszewska, M. Binding properties of polyamidoamine dendrimers. *J. Appl. Polym. Sci.* **2007**, *103*, 2036-2040.

(155) Jolly, A. M.; Bonizzoni, M. PAMAM dendrimers as supramolecular hosts through non-covalent interactions. *Supramol. Chem.* **2015**, *27*, 151-160.

(156) Jolly, A. M.; Bonizzoni, M. Intermolecular Forces Driving Encapsulation of Small Molecules by PAMAM Dendrimers in Water. *Macromolecules* **2014**, *47*, 6281-6288.

(157) Bonizzoni, M.; Long, S. R.; Rainwater, C.; Anslyn, E. V. PAMAM Dendrimer-Induced Aggregation of 5(6)-Carboxyfluorescein. *J. Org. Chem.* **2012**, *77*, 1258-1266.

(158) Yan, D.; Wu, S.; Zhou, S.; Tong, G.; Li, F.; Wang, Y.; Li, B. Characteristics, sources and health risk assessment of airborne particulate PAHs in Chinese cities: A review. *Environ. Pollut.* **2019**, *248*, 804-814.

(159) Du, W.; Li, X.; Chen, Y.; Shen, G. Household air pollution and personal exposure to air pollutants in rural China - A review. *Environ. Pollut.* **2018**, *237*, 625-638.

(160) Behera, B. K.; Das, A.; Sarkar, D. J.; Weerathunge, P.; Parida, P. K.; Das, B. K.; Thavamani, P.; Ramanathan, R.; Bansal, V. Polycyclic Aromatic Hydrocarbons (PAHs) in inland aquatic ecosystems: Perils and remedies through biosensors and bioremediation. *Environ. Pollut.* **2018**, *241*, 212-233.

(161) Adamkiewicz, G.; Choi, H.; Delgado Saborit, J. M.; Fharrison, P.; Harrison, R. M.; Henderson, R. F.; Jarvis, D.; Kaden, D. A.; Kelly, F. J.; Kephalopoulos, S.; Komulainen, H.; Kotzias, D.; Kreuzer, M.; Mandin, C.; Maynar, R. L.; McLaughlin, J.; Nielsen, G.; Nijhuis, N.; Penney, D. G.; Shinohara, N.; Wolkoff, P.; Krzyzanowski, M. *WHO guidelines for indoor air quality: selected pollutants*; World Health Organization Regional Office for Europe: Copenhagen, 2010.

(162) Menzie, C. A.; Potocki, B. B.; Santodonato, J. Exposure to carcinogenic PAHs in the environment. *Environ. Sci. Technol.* **1992**, *26*, 1278-1284.

(163) Kim, K.-H.; Jahan, S. A.; Kabir, E.; Brown, R. J. C. A review of airborne polycyclic aromatic hydrocarbons (PAHs) and their human health effects. *Environ. Int.* **2013**, *60*, 71-80.

(164) Mastral, A. M.; Callen, M. S. A Review on Polycyclic Aromatic Hydrocarbon (PAH) Emissions from Energy Generation. *Environ. Sci. Technol.* **2000**, *34*, 3051-3057.

(165) Tropp, J.; Ihde, M. H.; Williams, A. K.; White, N. J.; Eedugurala, N.; Bell, N. C.; Azoulay, J. D.; Bonizzoni, M. A sensor array for the discrimination of polycyclic aromatic hydrocarbons using conjugated polymers and the inner filter effect. *Chem. Sci.* **2019**, *10*, 10247-10255.

(166) Lakowicz, J. R. *Principles of Fluorescence Spectroscopy*; Springer: New York, NY, 2013.

(167) Duhamel, J. New Insights in the Study of Pyrene Excimer Fluorescence to Characterize Macromolecules and their Supramolecular Assemblies in Solution. *Langmuir* **2012**, *28*, 6527-6538.

(168) Gowthamarajan, K.; Singh, S. K. Dissolution Testing for Poorly Soluble Drugs: A Continuing Perspective. *Dissolut. Technol.* **2010**, *17*, 24-33.

(169) Fernandez, L.; Gonzalez, M.; Cerecetto, H.; Santo, M.; Silber, J. J. Solubilization and release properties of dendrimers. Evaluation as prospective drug delivery systems. *Supramol. Chem.* **2006**, *18*, 633-643.

(170) Arias-Gonzalez, I.; Reza, J.; Trejo, A. Temperature and sodium chloride effects on the solubility of anthracene in water. *J. Chem. Thermodyn.* **2010**, *42*, 1386-1392.

(171) Goodpaster, J. V.; McGuffin, V. L. Selective Fluorescence Quenching of Polycyclic Aromatic Hydrocarbons by Aliphatic Amines. *Anal. Chem.* **2000**, *72*, 1072-1077.

(172) Niu, Y.; Sun, L.; Crooks, R. M. Determination of the Intrinsic Proton Binding Constants for Poly(amidoamine) Dendrimers via Potentiometric pH Titration. *Macromolecules* **2003**, *36*, 5725-5731.

(173) Jasmine, M. J.; Kavitha, M.; Prasad, E. Effect of solvent-controlled aggregation on the intrinsic emission properties of PAMAM dendrimers. *J. Lumin.* **2009**, *129*, 506-513.

(174) Wang, D.; Imae, T.; Miki, M. Fluorescence emission from PAMAM and PPI dendrimers. *J. Colloid Interface Sci.* **2007**, *306*, 222-227.

(175) Wang, D.; Imae, T. Fluorescence Emission from Dendrimers and Its pH Dependence. *J. Am. Chem. Soc.* **2004**, *126*, 13204-13205.

(176) Bardi, B.; Krzeszewski, M.; Gryko, D. T.; Painelli, A.; Terenziani, F. Excited-State Symmetry Breaking in an Aza-Nanographene Dye. *Chem. - Eur. J.* **2019**, *25*, 13930-13938.

(177) Chen, Y.-C.; Wang, Z.; Yan, M.; Prahl, S. A. Fluorescence anisotropy studies of molecular imprinted polymers. *Luminescence* **2006**, *21*, 7-14.

(178) Marczyk, J.; Fetzer, J. C.; Szubiakowski, J.; Waluk, J. Luminescence anisotropy and linear dichroism studies of large polycyclic aromatic hydrocarbons based on the perylene chromophore. *J. Lumin.* **1997**, *72-74*, 517-519.

(179) Chan, K. M.; Xu, W.; Kwon, H.; Kietrys, A. M.; Kool, E. T. Luminescent Carbon Dot Mimics Assembled on DNA. *J. Am. Chem. Soc.* **2017**, *139*, 13147-13155.

(180) Ganguly, A.; Ghosh, S.; Guchhait, N. Modulated photophysics of an anthracene-based fluorophore within bile-salt aggregates: the effect of the ionic strength of the medium on the aggregation behavior. *Photochem. Photobiol. Sci.* **2015**, *14*, 2168-2178.

(181) Alonso, R.; Yamaji, M.; Jimenez, M. C.; Miranda, M. A. Enhanced Photostability of the Anthracene Chromophore in Aqueous Medium upon Protein Encapsulation. *J. Phys. Chem. B* **2010**, *114*, 11363-11369.

(182) Shiraishi, Y.; Tokitoh, Y.; Hirai, T. pH- and H_2O-Driven Triple-Mode Pyrene Fluorescence. *Org. Lett.* **2006**, *8*, 3841-3844.

(183) Wade, D. A.; Mao, C.; Hollenbeck, A. C.; Tucker, S. A. Spectrochemical investigations in molecularly organized solvent media: evaluation of pyridinium chloride as a selective fluorescence quenching agent of polycyclic aromatic hydrocarbons in aqueous carboxylate-terminated poly(amido) amine dendrimers and anionic micelles. *Fresenius' J. Anal. Chem.* **2001**, *369*, 378-384.

(184) Wade, D. A.; Torres, P. A.; Tucker, S. A. Spectrochemical investigations in dendritic media: evaluation of nitromethane as a selective fluorescence quenching agent in aqueous carboxylate-terminated poly(amidoamine) (PAMAM) dendrimers. *Anal. Chim. Acta* **1999**, *397*, 17-31.

(185) Savla, S.; Surjusee, A.; Rokade, V.; Sawant, S.; Kadu, P. Approaches to improve solubility of poorly water soluble drugs. *World J. Pharm. Pharm. Sci.* **2015**, *4*, 610-626.

(186) Tang, M.; Redemann, C. T.; Szoka, F. C., Jr. In Vitro Gene Delivery by Degraded Polyamidoamine Dendrimers. *Bioconjugate Chem.* **1996**, *7*, 703-714.

(187) Dost, K.; Ideli, C. Determination of polycyclic aromatic hydrocarbons in edible oils and barbecued food by HPLC/UV-Vis detection. *Food Chem.* **2012**, *133*, 193-199.

(188) Bojes, H. K.; Pope, P. G. Characterization of EPA's 16 priority pollutant polycyclic aromatic hydrocarbons (PAHs) in tank bottom solids and associated contaminated soils at oil exploration and production sites in Texas. *Regul. Toxicol. Pharmacol.* **2007**, *47*, 288-295.

(189) Toriba, A.; Kuramae, Y.; Chetiyanukornkul, T.; Kizu, R.; Makino, T.; Nakazawa, H.; Hayakawa, K. Quantification of polycyclic aromatic hydrocarbons (PAHs) in human hair by HPLC with fluorescence detection: A biological monitoring method to evaluate the exposure to PAHs. *Biomed. Chromatogr.* **2003**, *17*, 126-132.

(190) Sirimanne, S. R.; Barr, J. R.; Patterson, D. G., Jr.; Ma, L. Quantification of Polycyclic Aromatic Hydrocarbons and Polychlorinated Dibenzo-p-dioxins in Human Serum by Combined Micelle-Mediated Extraction and HPLC. *Anal. Chem.* **1996**, *68*, 1556-1560.

(191) Nie, S.; Dadoo, R.; Zare, R. N. Ultrasensitive fluorescence detection of polycyclic aromatic hydrocarbons in capillary electrophoresis. *Anal. Chem.* **1993**, *65*, 3571-3575.

(192) Takada, H.; Onda, T.; Ogura, N. Determination of polycyclic aromatic hydrocarbons in urban street dusts and their source materials by capillary gas chromatography. *Environ. Sci. Technol.* **1990**, *24*, 1179-1186.

(193) Zengin, A.; Tamer, U.; Caykara, T. SERS detection of polyaromatic hydrocarbons on a β-cyclodextrin containing polymer brush. *J. Raman Spectrosc.* **2018**, *49*, 452-461.

(194) Leyton, P.; Sanchez-Cortes, S.; Garcia-Ramos, J. V.; Domingo, C.; Campos-Vallette, M.; Saitz, C.; Clavijo, R. E. Selective molecular recognition of polycyclic aromatic hydrocarbons (PAHs) on calix[4]arene-functionalized Ag nanoparticles by surface-enhanced Raman scattering. *J. Phys. Chem. B* **2004**, *108*, 17484-17490.

(195) Dale, E. J.; Vermeulen, N. A.; Juricek, M.; Barnes, J. C.; Young, R. M.; Wasielewski, M. R.; Stoddart, J. F. Supramolecular Explorations: Exhibiting the Extent of Extended Cationic Cyclophanes. *Acc. Chem. Res.* **2016**, *49*, 262-273.

(196) Chen, S.; Yu, Y.-L.; Wang, J.-H. Inner filter effect-based fluorescent sensing systems: A review. *Anal. Chim. Acta* **2018**, *999*, 13-26.

(197) Mumtaz, M.; George, J. *Toxicological Profile for Polycyclic Aromatic Hydrocarbons (PAHs)*; 1995 ed.; U.S. Department of Health and Human Services, Agency for Toxic Substances & Disease Registry (ATSDR): Atlanta, 1995.

(198) Tanwar, A. S.; Patidar, S.; Ahirwar, S.; Dehingia, S.; Iyer, P. K. “Receptor free” inner filter effect based universal sensors for nitroexplosive picric acid using two polyfluorene derivatives in the solution and solid states. *Analyst* **2019**, *144*, 669-676.

(199) Tanwar, A. S.; Adil, L. R.; Afroz, M. A.; Iyer, P. K. Inner Filter Effect and Resonance Energy Transfer Based Attogram Level Detection of Nitroexplosive Picric Acid Using Dual Emitting Cationic Conjugated Polyfluorene. *ACS Sens.* **2018**, *3*, 1451-1461.

(200) Keith, L. H. The Source of U.S. EPA's Sixteen PAH Priority Pollutants. *Polycyclic Aromat. Compd.* **2015**, *35*, 147-160.

(201) Puvaneswari, N.; Muthukrishnan, J.; Gunasekaran, P. Toxicity assessment and microbial degradation of azo dyes. *Indian J. Exp. Biol.* **2006**, *44*, 618-626.

(202) Carmen, Z.; Daniela, S. Textile Organic Dyes – Characteristics, Polluting Effects and Separation/Elimination Procedures from Industrial Effluents – A Critical Overview. In *Organic Pollutants Ten Years After the Stockholm Convention - Environmental and Analytical Update*; Puzyn, T., Mostrag-Szlichtyng, A., Eds.; IntechOpen: 2012, p 55-86.

(203) Moosvi, S.; Kher, X.; Madamwar, D. Isolation, characterization and decolorization of textile dyes by a mixed bacterial consortium. *Dyes and Pigments* **2007**, *74*, 723-729.

(204) Mani, S.; Bharagava, R. N. Textile Industry Wastewater Environmental and Health Hazards and Treatment Approaches. In *Recent Advances in Environmental Management*; Bharagava, R. N., Ed.; CRC Press: Boca Raton, 2018.

(205) Chequer, F. M. D.; Oliveira, G. A. R. d.; Ferraz, E. R. A. c.; Cardoso, J. C.; Zanoni, M. V. B.; Oliveira, D. P. d. Textile Dyes: Dyeing Process and Environmental Impact. In *Eco-Friendly Textile Dyeing and Finishing*; Günay, M., Ed. 2013.

(206) Chung, K.-T. Azo dyes and human health: A review. *J. Environ. Sci. Health C* **2016**, *34*, 233-261.

(207) Şen, S.; Demirer, G. N. Anaerobic treatment of real textile wastewater with a fluidized bed reactor. *Water Res.* **2003**, *37*, 1868-1878.

(208) Sarkar, S.; Banerjee, A.; Halder, U.; Biswas, R.; Bandopadhyay, R. Degradation of Synthetic Azo Dyes of Textile Industry: a Sustainable Approach Using Microbial Enzymes. *Water. Conserv. Sci. Eng.* **2017**, *2*, 121-131.

(209) Nguyen, T.; Saleh, M. A. Detection of azo dyes and aromatic amines in women undergarment. *J. Environ. Sci. Heal. A* **2016**, *51*, 744-753.

(210) Otero, P.; Saha, S. K.; Hussein, A.; Barron, J.; Murray, P. Simultaneous Determination of 23 Azo Dyes in Paprika by Gas Chromatography-Mass Spectrometry. *Food Anal. Methods* **2017**, *10*, 876-884.

(211) Voyksner, R. D.; Straub, R.; Keever, J. T.; Freeman, H. S.; Hsu, W.-N. Determination of aromatic amines originating from azo dyes by chemical reduction combined with liquid chromatography/mass spectrometry. *Environ. Sci. Technol.* **1993**, *27*, 1665-1672.

(212) Pielesz, A.; Baranowska, I.; Rybak, A.; Włochowicz, A. Detection and Determination of Aromatic Amines as Products of Reductive Splitting from Selected Azo Dyes. *Ecotox. Environ. Safe.* **2002**, *53*, 42-47.

(213) Pinheiro, H. M.; Touraud, E.; Thomas, O. Aromatic amines from azo dye reduction: status review with emphasis on direct UV spectrophotometric detection in textile industry wastewaters. *Dyes and Pigments* **2004**, *61*, 121-139.

(214) Wu, M.; Sun, L.; Miao, K.; Wu, Y.; Fan, L.-J. Detection of Sudan Dyes Based on Inner-Filter Effect with Reusable Conjugated Polymer Fibrous Membranes. *ACS Appl. Mater. Interfaces* **2018**, *10*, 8287-8295.

(215) Sivasankaran, U.; Cyriac, S. T.; Menon, S.; Kumar, K. G. Fluorescence Turn off Sensor for Brilliant Blue FCF- an Approach Based on Inner Filter Effect. *J. Fluoresc.* **2017**, *27*, 69-77.

(216) Asses, N.; Ayed, L.; Hkiri, N.; Hamdi, M. Congo Red Decolorization and Detoxification by Aspergillus niger: Removal Mechanisms and Dye Degradation Pathway. *Biomed. Res. Int.* **2018**, 3049686.

(217) Brown, M. A.; De Vito, S. C. Predicting azo dye toxicity. *Crit. Rev. Env. Sci. Tec.* **1993**, *23*, 249-324.

(218) Tanwar, A. S.; Hussain, S.; Malik, A. H.; Afroz, M. A.; Iyer, P. K. Inner Filter Effect Based Selective Detection of Nitroexplosive-Picric Acid in Aqueous Solution and Solid Support Using Conjugated Polymer. *ACS Sens.* **2016**, *1*, 1070-1077.

(219) Puchtler, H.; Sweat, F.; Gropp, S. An investigation into the relation between structure and fluorescence of azo dyes. *J. R. Microsc. Soc.* **1967**, *87*, 309-328.